# Synthesis and Photophysical Investigation of Novel Supramolecular Lanthanide Luminescent Architectures

**Christophe Lincheneau**

**October 2010**

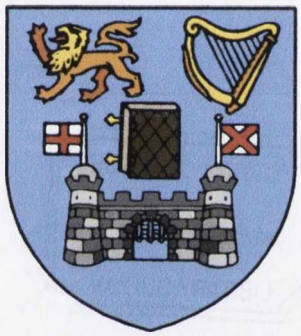

**University of Dublin**
**Trinity College**

**Based on research carried out under the direction of**
**Prof. Thorfinnur Gunnlaugsson**

***A thesis submitted to the School of Chemistry, University of Dublin, Trinity College for the degree of Doctor of Philosophy***

## Declaration

This thesis is submitted for the degree of Doctor of Philosophy to the University of Dublin, Trinity College and has not been submitted before for any degree or examination to this or any other university. Other than where acknowledged, all work described herein is original and carried out by the author alone. Permission is granted so that the Library may lend or copy this thesis upon request. This permission covers only single copies made for study purposes, subject to normal conditions of acknowledgment.

_____

**Abbreviattions:**

| | |
|---|---|
| Bipy | Bipyridine |
| CD | Circular dichroism |
| CT | Charge Transfer |
| CPL | Circular Polarised Luminescence |
| DCM | Dichloromethane |
| DMF | Dimethyl Formamide |
| DMAP | Dimethyl aminopyridine |
| DMSO | Dimethyl Sulfoxyde |
| Dpa | Dipicolinic acid |
| DOTA | 1,4,7,10-tetraazacyclododecane-tetraacetic acid |
| DTPA | Diethylen Triamine Pentaacetic acid |
| EDCI | 1-ethyl-3-(3-dimethylaminopropyl) carbodiimide) |
| Eq. | Equivalents |
| Eq. | Equation |
| EtOAc | Ethyl Acetate |
| ESI-MS | Electrospray Mass Spectrometry |
| HOBt | Hydroxybenzotriazole |
| ICT | Internal Charge Transfer |
| K | Stepwise Binding constant |
| MeCN | Acetonitrile |
| MeOH | Methanol |
| NMR | Nuclear Magnetic Resonance |
| RCM | Ring Closing Metathesis |
| RT | Room Temperature |
| THF | Tetrahydrofuran |
| TsCl | Tosyl Chloride |
| UV | Ultra-violet |

Abstract:

This thesis is entitled "Synthesis and photophysical investigations of novel supramolecular architectures" and is composed of five chapters. In the first chapter the photopysical and chemical properties of the lanthanide ions was described and this was followed by a discussion on the potential different methods in order to build highy geometric lanthanide complexes, using various approaches such as the use of macrocyclic ligands, podand and lanthanide directed formation of self-assemblies, which as been most particularly described.

In the second chapter, with the view of developing calixarene based luminescent hosts for lanthanide ions, the synthesis and the characterisation of 1:1 $Tb^{III}$ complexes using a family of calix-[4]-arenes alkylated on their lower with amido based pendant arms was described and their photophysical properties studied. These studies have shown the successful synthesis of the desired complexes in high yield. The formation of these self-assemblies was also investigated *in situ* using various spectroscopic methods and these have shown the quantitative formation of the desired 1:1 (M:L) in solution with high binding constants.

The third chapter of the manuscript developed the formation of monometallic chiral lanthanide luminescent self-assemblies. The formation of the molecular bundles has been investigated *in situ* using three different couples of enantiomers, either symmetric or asymmetric, and in each case, bearing one or two chiral polyaromatic antennae, the solution studies performed these systems have demonstrated that the chirality of the ligand was successfully transferred to the excited stated of the lanthanide ions, which gave rise to Circuarly polarised luminescence.

The induction of chiralty has been further investigated by the synthesis of bimetallic chiral luminescent triple stranded helicates, in the chapter 4, which described the synthesis and the formation of these helicates. The synthesis of enantiomerically pure ditopic ligand containing two diamidopyridine binding unit separated by a diaryl linker was first described. The synthesis of the 3:2 (L:M) complexes has been carried out and this gave rise to the desired helicates in high yield. The formation of the $\mathbf{L_3.Eu_2}$ helicates has also been investigated *in situ* and this showed the high stability of these self-assemblies in solution. Furthermore, the CD and the CPL analyses were performed demonstrating the enantiomerically pure formation of the triple stranded helicates.

Finally the last chapter of this PhD will be focused on the use of the lanthanide coordination geometry of lanthanide in order to attempt the synthesis of the first, to the best of our knowledge, fully interlocked [3]-catenane. This was undertaken following a lanthanide directed strategy following a triple clipping catnenation. Herein, we described the synthesis of two linear ligand based on a central diamido pyridine binding unit flanked on its 2- and 6-position with two flexible pendant arms. The first ligand was designed with alcohol terminal functions in order to induce the macrocyclisation using Williamsin ether synthesis and the second one bears allylic terminal moieties capable of ring closing metathesis. First, the complexation of $Ln^{III}$ by these ligand was studies and this have shown that three ligand self-assembled around the lanthanide ion. The catenation of the 1:3 (M:L) complexes, using Williamson ether synthesis and ring closing metathesis was undertaken and the characterisation of the resulting adduct are discussed.

Finally, in the final Chapter 6, details of the experimental details of the procedure discussed within this thesis are prvided.

## Table of contents


| | | Page |
|---|---|---|
| **CHAPTER 1:** | **INTRODUCTION** | |
| **1** | Introduction | **1** |
| **1.1** | Properties of Lanthanides | **1** |
| **1.1.1** | Photophysical and Spectroscopic Properties of $Ln^{III}$ | **1** |
| **1.1.2** | Electronic and Chemical properties of $Ln^{III}$ | **7** |
| **1.2** | Design and synthesis of lanthanide based complexes | **8** |
| **1.2.1** | Macrocyclic ligands to host lanthanide | **9** |
| **1.2.2** | Complexation of lanthanide with linear ligands | **15** |
| **I.2.2.1** | The podand approach | **15** |
| **I.2.2.2** | Lanthanide directed formation of supramolecular self-assemblies | **18** |
| | Organometallic clusters | **19** |
| | Mono-molecular lanthanide based self-assemblies: | **21** |
| | Lanthanide-based helicates | **24** |
| **I.3** | Work described in this thesis | **28** |
| **CHAPTER 2:** | **Calix-[4]-arene based hosts for $Tb^{III}$** | **31** |
| **2.1** | Introduction | **31** |
| | Previous work from Dr Eoin Quinlan: Design and Synthesis of Calix-[4]-arenes derivatives for $Ln^{III}$ complexation. | **32** |
| **2.2** | Synthesis and photophysical studies of luminescent Host-Guest systems: **42-45.Tb** | **35** |
| **2.2.1** | Synthesis and characterisation of the complexes **42-45.Tb** | **35** |
| **2.2.2** | Photophysical studies of the complexes **L.Tb** (L= **42-45**) | **38** |
| **2.2.3** | Investigation of the formation of the complexes **L.Tb** *in-situ* | **41** |
| **2.2.3.1** | Study of the formation of the complexes **L.Tb** (L= **42, 43**) *in situ* | **41** |
| **2.2.3.2** | Study of the formation of the complexes **L.Tb** (L= **44-45**) *in situ* | **43** |
| **2.2.3.3** | Fitting and calculation of the binding constants of the complexes **L.Tb** | **45** |
| **2.3** | Conclusion | **49** |
| **CHAPTER 3:** | **Chiral lanthanide luminescent monometallic self-assemblies** | **51** |
| **3.1** | Introduction | **51** |
| **3.1.1** | Previous work preformed in the Gunnlaugsson group | **52** |
| **3.2** | Formation of the Trinity Sliotar **27S-27R$_3$.Eu** in situ | **56** |
| **3.2.1** | UV-vis absorption and luminescence emission investigations | **56** |

| | | |
|---|---|---|
| 3.2.2 | Determination of the binding constants and the speciation distribution of the complexation process | 58 |
| 3.3 | Ln-directed formation in situ of molecular bundles containing tryptophanantennae | 61 |
| 3.3.1 | Photophysical properties of the **47L-47D$_2$.Eu** complexes in solution | 62 |
| 3.3.2 | Solution studies of the complexation of $Eu^{III}$ by **47L** and **47D** | 64 |
| 3.3.3 | Photophysical properties of the **47L-47D$_2$.Tb** complexes in solution | 66 |
| 3.3.4 | Solution studies of the complexation of $Tb^{III}$ by **47L** and **47D** | 68 |
| 3.4 | Formation of molecular bundles based on linear asymmetric ligands | 72 |
| 3.4.1 | Photophysical properties of the **51R-51S$_3$.Eu** complexes in solution | 72 |
| 3.4.2 | CD and CPL invstigations of the **51R-51S$_3$.Eu** complexes in solution | 74 |
| 3.4.3 | Solution studies of the complexation of $Eu^{III}$ with **51R-51S** | 76 |
| 3.50 | Conclusion | 78 |
| **CHAPTER 4:** | **Synthesis and photophysical studies of dimetallic chiral luminescent triple stranded helicates.** | 81 |
| 4.1 | Introduction | 81 |
| 4.2 | Design of the ligands | 83 |
| 4.3 | Synthesis and characterisation of ligands **53S-53R** and **54S-54R** | 84 |
| 4.4 | Synthesis and characterisation of the triple stranded helicates **L$_3$.Eu$_2$** | 85 |
| 4.5 | Photophysical studies of the helicates **L$_3$.Eu$_2$** (L= **53S-53R** and **54S-54R**) | 86 |
| 4.6 | CD and CPL analyses of the helicates **L$_3$.Eu$_2$** (L = **54S, 54R**) | 90 |
| 4.7 | Molecular Mechanics modelling studies of the helicates of the triple stranded helicates | 92 |
| 4.8 | Studies of the formation of the helicates **L$_3$.Eu$_2$** (L= **54R-54R**) *in situ* | 94 |
| 4.9 | Conclusion | 97 |
| **CHAPTER 5:** | **Lanthanide templated synthesis of [3]-catenanes** | 99 |
| 5.1 | Introduction | 99 |
| 5.1.1 | Synthesis of catenane using a Brownian approach | 100 |
| 5.1.2 | Synthesis of catenane *via* directed approach | 101 |
| 5.1.3 | Design of the ligands | 103 |
| 5.2 | Lanthanide directed synthesis of a [3]-catenane via triple Williamson ether synthesis | 104 |
| 5.2.1 | Synthesis and characterisation of Ligand **66** | 104 |
| 5.2.2 | Synthesis and characterisation of the lanthanide complexes **66$_3$.Ln** (Ln = $Eu^{III}$, $Tb^{III}$, $Lu^{III}$) | 105 |

| | | |
|---|---|---|
| 5.2.3 | Investigation of the photophysical properties of the lanthanide complexes **66$_3$.Ln** (Ln = $Eu^{III}$, $Tb^{III}$) | 106 |
| 5.2.4 | Studies of the formation of the complexes **66$_3$.Ln** *in situ* | 108 |
| 5.2.5 | Catenation *via* triple-Williamson ether synthesis of **66$_3$.Ln** | 111 |
| 5.3 | Synthesis of [3]-catenane using triple-ring closing metathesis | 117 |
| 5.3.1 | Introduction to ring-closing metathesis using Grubbs catalyst | 117 |
| 5.3.2 | Synthesis and charaterisation of ligand **71** bearing terminal allylic moieties | 118 |
| 5.3.3 | Synthesis and characterisation of the complexes **71$_3$.Eu** | 120 |
| 5.3.4 | Photophysical studies of the complex **71$_3$.Eu** | 122 |
| 5.3.5 | Study of the formation of the complexes **71$_3$.Eu** and **71$_3$.Tb** *in situ* | 123 |
| 5.3.6 | Catenation of **71$_3$.Eu** using a triple clipping using ring closing metathesis. | 126 |
| 5.4 | Study of the ring closing metathesis on the free ligand **71** | 133 |
| 5.4.1 | Investigation of formation of the complexes **72.Eu** *in situ* | 134 |
| 5.4.2 | Formation of the pseudo rotaxane **72.Eu.71$_2$** *in situ.* | 139 |
| 5.5 | Conclusion | 141 |

| | | |
|---|---|---|
| **CHAPTER 6:** | **Experimental section** | 145 |
| 6.1 | General Experimental Details | 145 |
| 6.2 | UV-Visible Spectroscopy | 146 |
| 6.3 | Luminescence Measurements | 146 |
| 6.5 | CD measurements | 147 |
| 6.6 | CPL measurements | 147 |
| 6.7 | Molecular mechanics modelling studies | 147 |
| 6.8 | General synthetic procedures | 148 |
| | **References** | 159 |
| | **Appendices** | |
| | **Publications** | |

**Acknowledgements:**

I would like to begin by thanking my supervisor, Prof. T. Gunnlaugsson for the help and the support that I have received during the accomplishment of my PhD. I am also very grateful for all the things he taught me, in many different ways. In just few words: Merci beaucoup Thorri.

I would like to thank the member of the TG group, past and present; Aline, Andrew, Flo, Cidalia, Claire, Doireann, Danni, Gary, Celia, Emma, Brian, Julien, Jon, Mihal, Dawn, for all the good moments we have share during the past few years. I will always remember, the various passionate talks and the laughter we got in and outside the lab. I want also to say a special thanks to Elaine, Laura, Rob and Dave for the massive help they gave me for the accomplishment of this manuscript. I want also to say a great thank you with a Capital… 'T' to Steve, Oxana, Sam and Rebecca for patiently, reading and correcting the drafts of this thesis. I'm sorry but my poor English vocabulary does not allow to really expressing how grateful I am for what you have done.

Thank you to the technical and administrative staff of the school of chemistry for their assistance within the years; Martin, Bernard, Fred, Patsy, Brenden, Mark, Teresa, Helen, Maria, Tess and Gill. And more particularly to John and Manual who have been of a great help with a endless enthiusasm for the NMR and so many 'Interesting' samples…

I want also to say thank you to Frank for his patience and to have listen to all my stories during the past year around a little Chinese or an Appache. And also a big thank you to the water-polo lads that was so great to play (and win and also party with you…).

Thank you to all my friends outside Trinity especially Polo, Sylvain, Romain, and Betz …

I want also to say a special thank you to my Mom, my Dad, Sandrine and Loic for all their love and their support (emotional and financial!) and also their constant encouragement during that experience.

And to Jen: From the deepest of my heart, thank you so much! I think you are beyond acknowledgements, Thank you to have been so patient, nice, kind, helpful, thank you to have been always here, thank you to make me happy!!!

# Chapter 1:
# Introduction

# 1. INTRODUCTION

The *4f* elements, from lanthanum ($^{57}$La) to lutetium ($^{71}$Lu) are called lanthanides or *rare earth metals* and benefit from unique magnetic and photophysical properties due to their electronic configuration.[1,2] These metals have in the past attracted large interest due to their wide applications in different research fields such as in material science with the development of catalysts[3], magnets,[4] optical devices[5,6], imaging agents and chemosensors.[7,8] During the past few decades the lanthanides have had a significant impact in the field of coordination and supramolecular chemistry. It was found that through simple designs, lanthanide complexes can be used as simple building blocks for the formation of functional supramolecular architectures with potential applications as novel contrast agents for magnetic resonance imaging (MRI), as luminescent contrast agents for *in cellulo* imaging as well as chemical sensors.[9-11] To date, the most highly luminescent lanthanide complexes are made with either europium ($Eu^{3+}$) or terbium ($Tb^{3+}$) ions.[11] This chapter presents a brief summary on the various spectroscopic and photophysical properties of the lanthanides and the utilisation of lanthanide ions to template the synthesis of luminescent supramolecular structures.

## 1.1 Properties of Lanthanides

### 1.1.1 Photophysical and spectroscopic properties of $Ln^{III}$

Most of the major applications of lanthanides are based on their unique optical properties.[5] However, unlike the chemical properties (detailed in Section I.2), which are quite similar for the whole series, their photophysical properties vary strongly through the series. Indeed, all of the lanthanides are luminescent except for $La^{III}$ and $Lu^{III}$. They can be fluorescent ($Pr^{III}$, $Nd^{III}$, $Ho^{III}$, $Er^{III}$, and $Yb^{III}$) or phosphorescent ($Sm^{III}$, $Eu^{III}$, $Gd^{III}$, $Tb^{III}$, $Dy^{III}$, $Tm^{III}$).[11] The electronic configuration of the lanthanides is composed of a *4f* open shell, which is protected by the filled $5s^2p^6$ subshells resulting in a weak influence of the chemical environment on the photophysical properties of the complexes.[12,13] According to the IUPAC rules regarding molecular luminescence spectroscopy, the term fluorescence refers to an emission occurring without spin conversion such as in the case of the transition $^4I_{13/2} \rightarrow {}^4I_{15/2}$ of $Er^{III}$, while phosphorescence refers to emission involving a change in the spin like $^5D_4 \rightarrow {}^7F_6$ seen for $Tb^{III}$ (and will be denoted as such in this thesis).[14]

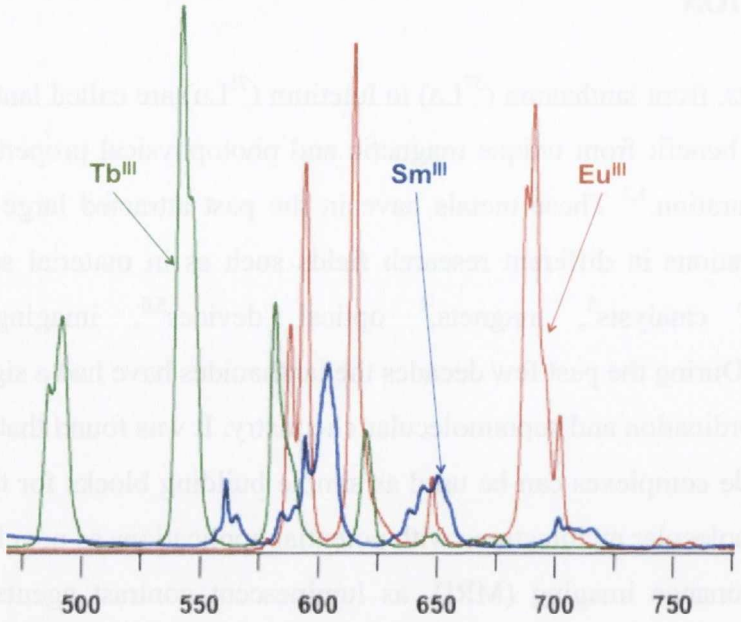


**Figure 1.1:** *Emission spectra of luminescent lanthanide complexes containing $Sm^{III}$, $Eu^{III}$, $Tb^{III}$.*

The lanthanide ions are easily recognisable by their characteristic emission spectra presenting narrow sharp line like emission bands. These *f-f* transitions involve a rearrangement of the electrons within the *4f* sub-shell and thus, are Laporte forbidden. Therefore, lanthanide ions are characterised by weak extinction coefficients (around 0.1 $M^{-1}cm^{-1}$.[15] Their emission covers the entire spectrum from the UV ($Gd^{III}$), to the visible region ($Tm^{III}$, $Tb^{III}$, $Dy^{III}$, $Sm^{III}$, $Eu^{III}$, $Ho^{III}$) as well as into the NIR regions ($Nd^{III}$, $Yb^{III}$). As an example, the characteristic emission spectra of terbium, europium, and samarium ions are shown in Figure 1.1. The electronic $[Xe]4f^n$ ($n$ = 0-14) configurations of lanthanide ions generate a rich variety of electronic levels. Furthermore, the intrinsic quantum yields of lanthanide emission are directly related to the energy gap between the lowest excited state and the highest vibronic level of the ground state (Figure 1.2). Thus, their emission efficiency is different from one element to the next along the series.[16] Indeed, the deactivation of the excited state of the lanthanide *via* light emission is essentially in competition with non-radiative processes, which usually occur through energy transfer to alternative vibrational modes (mostly small mechanical oscillators) matching more or less the energy state of the lanthanide ion. Therefore, the presence of high frequency oscillators such as –OH and –NH, present in various solvent molecules, binding to the metal centre can result in an efficient quenching of the lanthanide luminescence, by deactivating non-radiatively the energy of its excited state.[17,18] In terms of energy, the smaller the gap between the highest occupied (HOMO) and the lowest unoccupied (LUMO) molecular orbitals of the ion, the higher the probability for the metal

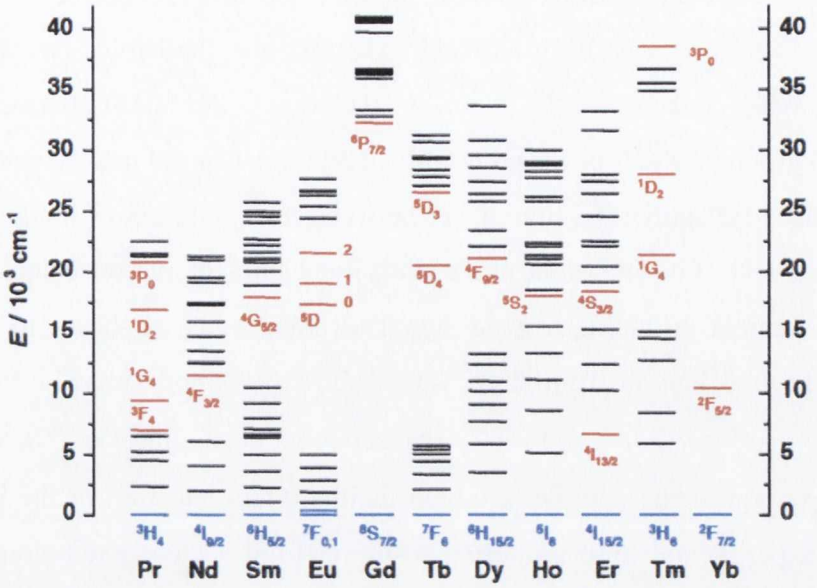


**Figure 1.2:** *Energy diagram of the lanthanide ions; the main luminescent levels are drawn in red, while the fundamental level is indicated in blue.*[5]

to undergo non-radiative deactivation of its excited state. As shown in Figure 1.2, $Eu^{III}$ and $Tb^{III}$ possess the highest luminescence efficiency and are ideal candidates to be incorporated as luminescent probes. Indeed, they have high energy transitions between their lower excited state and their ground state *ca.* $\Delta E_{Gd}(^6P_{7/2} \rightarrow {}^7F_6) = 32200\ cm^{-1}$, $\Delta E_{Eu}(^5D_0 \rightarrow {}^7F_6) = 12300\ cm^{-1}$ and $\Delta E_{Tb}(^5D_4 \rightarrow {}^7F_0) = 14800\ cm^{-1}$, which reduce the energy transfer toward high frequency oscillators and allow an easier population of their excited states *via* energy transfer from the triplet states of different organic chromophores.[19,20]

When the deactivation *via* non-radiative processes is minimised, the lanthanide ions possess a long-lived excited state, with luminescence decays going from the microsecond

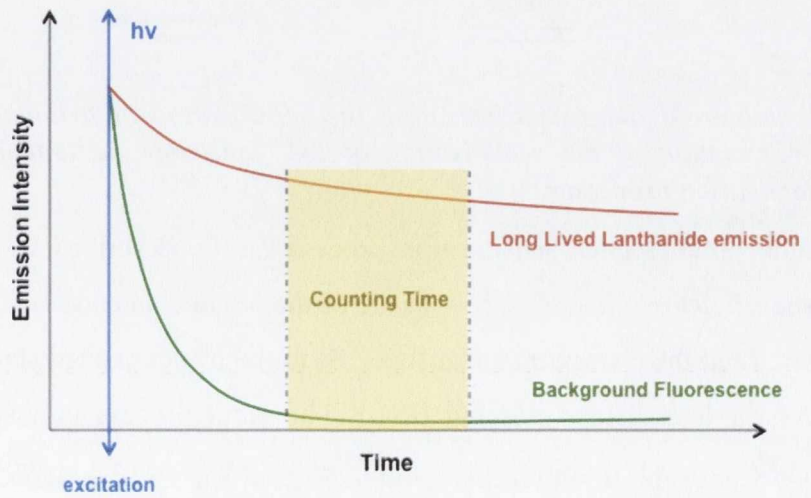


**Figure 1.3:** *Long-lived lanthanide emission in comparison to the emission of the biological background.*

(as in the case of Yb, Nd) to millisecond (as for $Eu^{III}$ and $Tb^{III}$) timescale.[21] This aspect of lanthanide luminescence has been utilised in numerous lanthanide-based systems as luminescent probes and sensors[8,11,22] as it overcomes the autofluorescence from a biological background, which has been established to exist in the nanosecond range. This technique is based on applying a time delay between the excitation of the lanthanide ions and the measurement of its emission, so the short lived auto-fluorescence does not interfere with the measurement providing a good signal to noise ratio, as shown in Figure 1.3.[15] Furthermore, the ions benefit from large Stokes shifts (*ca.* approximately $\Delta\nu \approx 320$ $cm^{-1}$ and $\Delta\nu \approx 250$ $cm^{-1}$ for $Eu^{III}$ and $Tb^{III}$, respectively, depending on the nature of the chromophore present in the complex), which facilitate the detection of the luminescence avoiding any experimental light scattering resulting from a close excitation wavelength. These unique photophysical properties make the lanthanide ions, such as $Tb^{III}$ and $Eu^{III}$, ideal candidates for a wide variety of luminescent systems for applications *in cellulo* (luminescent probes, sensors, time resolved imaging agent, etc.).[5,9]

The use of lanthanide ions in luminescent systems can be quite challenging due to the forbidden *f-f* transitions as previously mentioned.[11,23] However, the excited state of lanthanide ions can be populated from the triplet state of organic chromophores *via* energy transfer. This process is called the antenna effect and is shown schematically in Figure 1.4.

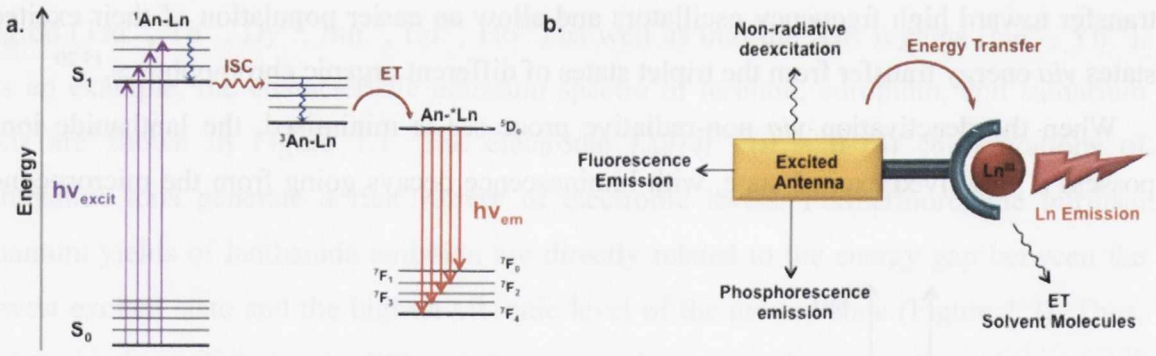


**Figure 1.4: a.** *Jablonski diagram illustrating the sensitisation of a lanthanide ion*[9] **b.** *Schematic representation of the sensitisation of* $Ln^{III}$ *emission via antenna effect and competitive deactivation processes.*

The lanthanide luminescence sensitisation process can be described to occur in four steps. Firstly, the singlet excited $^*S_1$ (or $^*S_2$) state of the organic antenna is populated upon direct excitation. Then the energy transfers from $^*S_1$ to the triplet excited state ($^*T_1$) of the organic antenna *via* intersystem crossing (ISC). The latter process is a spin forbidden process that can be induced by spin-orbit coupling in the presence of a heavy metal such as $Tb^{III}$ and $Eu^{III}$.[24] However, this process has to be fast enough (in the range of $10^{-7}$-$10^{-9}$ s) to compete with other pathways such as fluorescence emission and internal conversion

$S_1 \rightarrow S_0$, all of which deactivate the excited state, as shown in Figure 4.[25] The excited states of the lanthanide ion ($^5D_4$ for $Tb^{III}$ and $^5D_0$ for $Eu^{III}$) are then populated through energy transfer (ET) between the triplet excited state of the antenna and the accepting level of the metal ion, giving rise to the characteristic lanthanide emission *via* radiative de-excitation to one of the vibronic levels $^7F_J$ ($J$= 0-6 in the case of $Tb^{III}$ and $Eu^{III}$) related to the ground state of the metal ion. As depicted in Figure 4a, the energy transfer can take place from both the singlet and the triplet states.[19] However, energy transfer from the short-lived singlet states is usually inefficient except in the case of $Nd^{III}$ and $Er^{III}$.[26] Consequently, the ligand to metal energy transfer is considered to occur only from the triplet state of the antenna. The triplet state can be quenched *via* different deactivation processes such as the phosphorescence emission of the antenna, the population of the metal to ligand charge transfer (MLCT) and internal ligand charge transfer (ILCT) states, as well as through other radiationless back energy transfer to the ground state $S_0$. Also, the $^3\pi$-$\pi^* \rightarrow Ln^{III}$ energy transfer can be induced following two different mechanisms shown in Figure 1.5. The Dexter's (exchange) mechanism that involves a double electron transfer process, resulting in an exchange of electrons between the antenna and the metal (Figure 1.5a), occurs in a through-bond interaction, and as such requires an overlap between the energy levels of the donor and the acceptor.[19] This transfer is characterised by a strong dependence on the donor-acceptor distance ($r$) with a factor $e^{-r}$. Consequently, the process is more efficient when the distance $r$ between electron-donor and acceptor is minimal.[27] The second mechanism, called Förster (or dipole-dipole) energy transfer, requires that the dipole moment associated with the triplet state of the antenna couples with the one associated with the *4f* orbitals (Figure 1.5b).

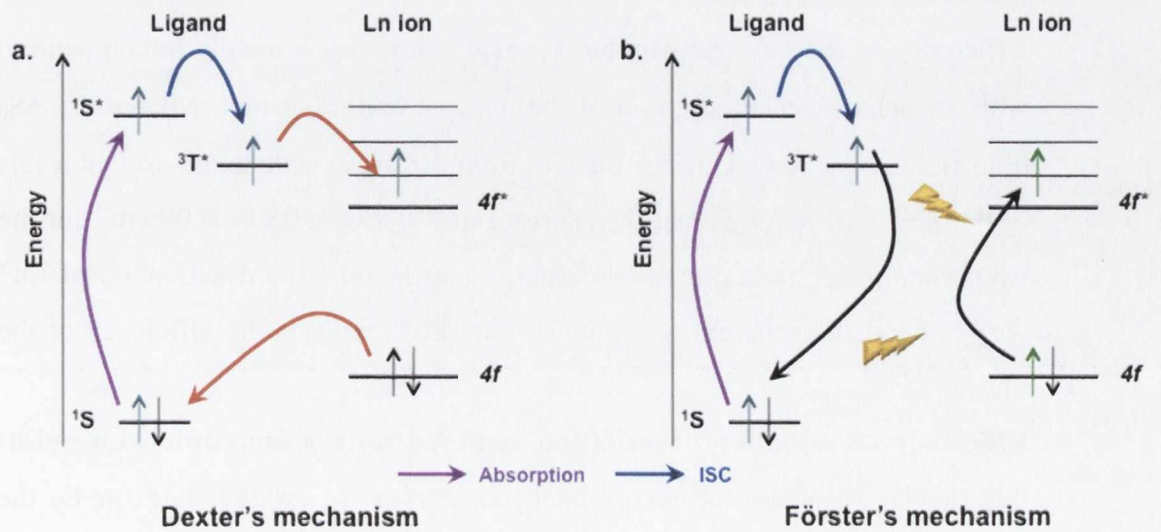


**Figure 1.5:** *Schematic representation of the Dexter (exchange a.) and the Förster (dipole-dipole b.) energy transfer mechanism.*[19]

This energy transfer operates through space with a dependence on the distance of $r^{-6}$ and the yield of the energy transfer is proportional to the overlap between the emission spectrum of the donor (*i.e.* triplet state of the antenna) and the absorption spectrum of the acceptor (lanthanide ion). As in the case of the Dexter energy transfer mechanism, the closer the antenna is to the lanthanide centre, the more efficient the Förster energy transfer is.[28] The presence of additional dipole-multipole interactions can also play an important role in the population of the lanthanide excited-state. These interactions and the Dexter mechanism are preferred during the ligand to metal energy transfer processes, whereas the Förster transfer happens mainly during metal-metal processes.[19] This is due to their respective dependence upon the donor-acceptor distance *r* according to which the Dexter and multipolar mechanism operate at shorter distance than the dipole-dipole interactions. Therefore, two main strategies are used to reach the ideal distance favourable for the energy transfer: 1) an external aromatic antenna is directly bound to the metal centre or 2) the chromophoric antenna is incorporated within the backbone of the ligand capable of binding the lanthanides. These strategies will be described more precisely in the next sections.[5,9,11,12,22]

In summary, lanthanide ions benefit from unique photophysical and spectroscopic properties, which are dependent on several factors. This can be summarised as being most dependent on:

- **Efficiency of the intersystem crossing $S_1 \rightarrow T_1$:** this competes mainly with fluorescence emission of the ligand and non-radiative internal-conversion processes. It has been established that efficient ISC from the singlet excited state of the ligand to the triplet state with the lowest energy occurs when $\Delta E(^1\pi\pi^*\text{-}^3\pi\pi^*)$ is around 5000 $cm^{-1}$.[29]
- **Efficiency of the energy transfer $T_1 \rightarrow Ln^*$:** this step is mainly in competition with phosphorescence emission of the antenna and other non-radiative $T_1 \rightarrow S_0$ transitions. An efficient energy transfer from the triplet state to the excited levels of the $Ln^{III}$ ions requires that the energy gap is between 2500-5000 $cm^{-1}$ for the whole lanthanide series; a smaller energy gap favours the deactivation of Ln* *via* back transfer whereas a larger $\Delta E(^3\pi\pi^*\text{-Ln}^*)$ reduces the efficiency of the transfer.[19]
- **Efficiency of radiative deexcitation centered on the lanthanide $Ln^* \rightarrow Ln$:** this can be quenched by energy back transfer to the excited states or by the action of mechanic oscillators such as the solvent molecules as developed in Section 1.2.

### 1.1.2 Electronic and chemical properties of $Ln^{III}$

Unlike the photophysical properties of lanthanide ion, which are diverse along the *4f* series, most lanthanide ions have a particular homogeneity in their chemical behaviour. As previously explained, their *4f* shell is protected by the $5s^2p^6$ shell, which makes the lanthanide ions relatively insensitive to the outer chemical environment.[8] Due to their general electronic configuration, ($[Xe]4f^n5d^1s^2$), the common most oxidation state of lanthanide ions is +3, which results from the depopulation of the *5d* and *5s* shells. However, some of the ions can be easily reduced to their +2 state such as $Sm^{III}$, $Eu^{III}$, $Tm^{III}$ and $Yb^{III}$ or oxidised to their +4 state as in the case of $Ce^{III}$, $Pr^{III}$ and $Tb^{III}$. Consequently, the $Ln^{III}$ cations possess a high charge density and a strong electrostatic nature, which makes them strong Lewis acids. For this reason, the lanthanide ions will interact preferentially with ligands containing strong donor atoms, such as oxygen and nitrogen, which act as Lewis bases. Therefore, combinations of carboxylate and amino moieties are commonly used in the formation of rare earth complexes. Furthermore, in order to synthesise lanthanide complexes that are thermodynamically stable as well as kinetically inert several donor atoms are needed,[30,31] particularly as the lanthanide have a high and variable coordination numbers, ranging from 3 to 12 in the solid state and 8- 9 in solution. Previous studies on the lanthanide solvation showed that in the absence of such ligands, the trivalent lanthanides naturally fill their first coordination sphere with nine solvent molecules, hence, the high enthalpy of solvation. However, the use of podands or multidentate ligands can facilitate the lanthanide complexation, where each of such ligand replaces several solvent molecules, which favours the complex formation, increasing the entropic factor.[9,10,22,32]

As mentioned previously in section 1.1, the main non-radiative deactivation of $Ln^*$ pathway is the dissipation of its energy by high frequency oscillators such as N-H and O-H, which possess vibrational energy that is in the same range as the energy levels of the lanthanide excited states. Consequently, the presence of solvent molecules within the first coordination sphere of the lanthanide ions can efficiently quench the lanthanide emission and dramatically affect the luminescence properties of the complex. The lifetimes and quantum yields can experience an important decrease.[11] However, numerous systems in the field of luminescent sensing utilise this detrimental aspect of lanthanide emission to their advantages, by tuning the efficiency of $Ln^{III}$ emission by displacing solvent molecules in the presence of a guest.[33-38] For this reason, most of the strategies envisaged with the purpose of developing luminescent probes based on lanthanide complexation are directed by an induced adjustment of the ligands shape, *i.e.* the ligand system wraps and organises

its geometry around the metal core to create the ideal cavity adapted to the size of the guest in order to shield the metal core from its environment. However, the coordination bonds have a strong ionic character and the geometry of the resulting complexes depends essentially on the steric repulsion within the ligand system.[1,5,13]

As a result, the design of ligands with the view of achieving highly emissive complexes is quite challenging and requires precise chemical conditions in order to minimize the occurrence of competitive processes. First of all, the choice of the antenna is crucial; the $^1T$ triplet state has to be close in energy from the excited states of the lanthanide ion in order to favour the energy transfer $^1T \rightarrow Ln^*$, as discussed above. The poly-aromatic chromophores can efficiently sensitise various lanthanide ions. Phenyl, pyridinyl and naphthyl antennae have all been utilised to sensitise ions such as $Eu^{III}$ and $Tb^{III}$, [9,39] whereas antennae such as quinolyl or benzimidazole moieties have been used in order to sensitise near-infrared (NIR) emitters such as $Nd^{III}$ or $Yb^{III}$ ions.[10,11]

**1.2 Design and synthesis of lanthanide based complexes**

The design of ligands for the complexation of lanthanide ions plays a crucial role in view of the success of the luminescent molecular system. Also, the lability and the high coordination number of the *4f* ions have rendered the complexation strategy more challenging for inorganic chemists. Regarding the conditions described during the previous section, the main feature of a ligand for a successful complexation of lanthanides and the sensitization of their photophysical properties are:

- The ability to form thermodynamically stable complexes with $Ln^{III}$
- The presence of an antenna (acting as a substituent within the organic ligand or as ligand itself directly coordinated to the metal) at an ideal distance from the lanthanide ion
- The ability to shield the ion from vibrational quenching

The lanthanides have been widely utilised as building blocks in the formation of supramolecular systems for luminescent sensing and as contrast agents for medical imaging.[5,9] These edifices are based on the optimisation of the complex geometry. The appropriate geometry can be constructed following the three main approaches shown in Figure 1.6. The first approach is based on the utilisation of preorganised macrocyclic ligands (Figure 1.6a).[40] The second strategy consists in the synthesis of linear multidentate ligands or podands or cryptands (Figure 1.6b). Finally, lanthanide complexes can be synthesised by using several smaller ligands that self-assemble around the lanthanide (Figure 1.6c).[41]

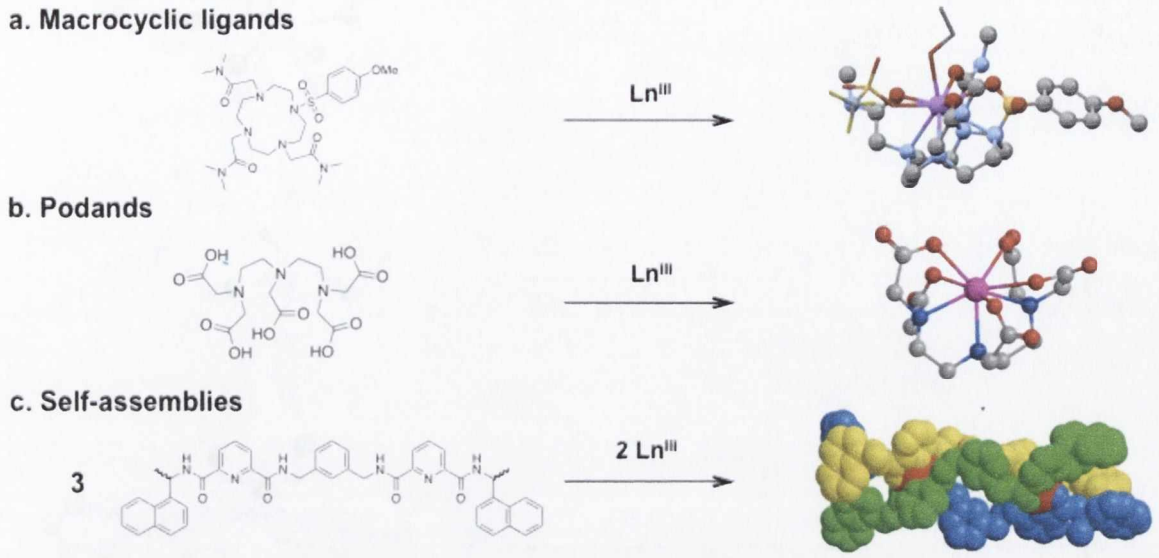


**Figure 1.6:** *Synthetic strategies to insert $Ln^{III}$ ions into supramolecular structures.* ***a.*** *Macrocyclic ligand illustrated by a DO3A derivative*[40] ***b.*** *Podand approach with DTPA, the structure obtained by MM2 calculations* ***c.*** *Metal directed formation of self-assemblies.*[41]

### 1.2.1 Macrocyclic ligands to host lanthanide

This strategy is based on the design of preorganised cavities, which minimize the reorganisation enthalpy upon the complexation to a metal ion.[42] Consequently, the utilisation of macrocyclic scaffolds such as coronands,[43] cryptands,[42] calixarenes,[44] or porphyrins,[11] can give rise to efficient luminescent probes, as shown by the examples in Figure 7, emitting from the UV-vis (Figure 7a, b)[45,46] to the NIR region (Figure 7c).[47] However, the success of this approach relies on the size of cavity with regard to the radius of the guest and on the ability of the ligand to shield the metal core from solvent molecules. Compound **1** and **2** provide an ideal hexadentate cavity to host lanthanide ions such as $Eu^{III}$ while fulfilling its coordination sphere with three solvent molecules. The tetradentate cavity in the porphyrin derivative **3** is, in comparison, too small in order to host the lanthanide ion, and so an additional dimethoxyethane (DME) molecule coordinated to the metal centre will minimize the emission quenching caused by the mechanical deactivation of the complex excited states.

Nonetheless, the design of a cavity matching precisely the diameter of a given lanthanide ion is almost impossible to achieve and this results in a poor selectivity along the lanthanide series. For example, with systems, such as **1**, the change of the cavity size occurs through the addition or the removal of a monomeric unit $CH_2$-$CH_2$-O provoking a variation of the macrocycle diameter of $\Delta d$(L)= 0.5-0.7Å,[48] which is greater than the variation of the size of the nucleus diameter between $La^{III}$ and $Lu^{III}$ ($\Delta d_i$(La-Lu) ≈ 0.36).[1] Moreover, the stability in water of most of these systems are quite low. Also, the synthesis

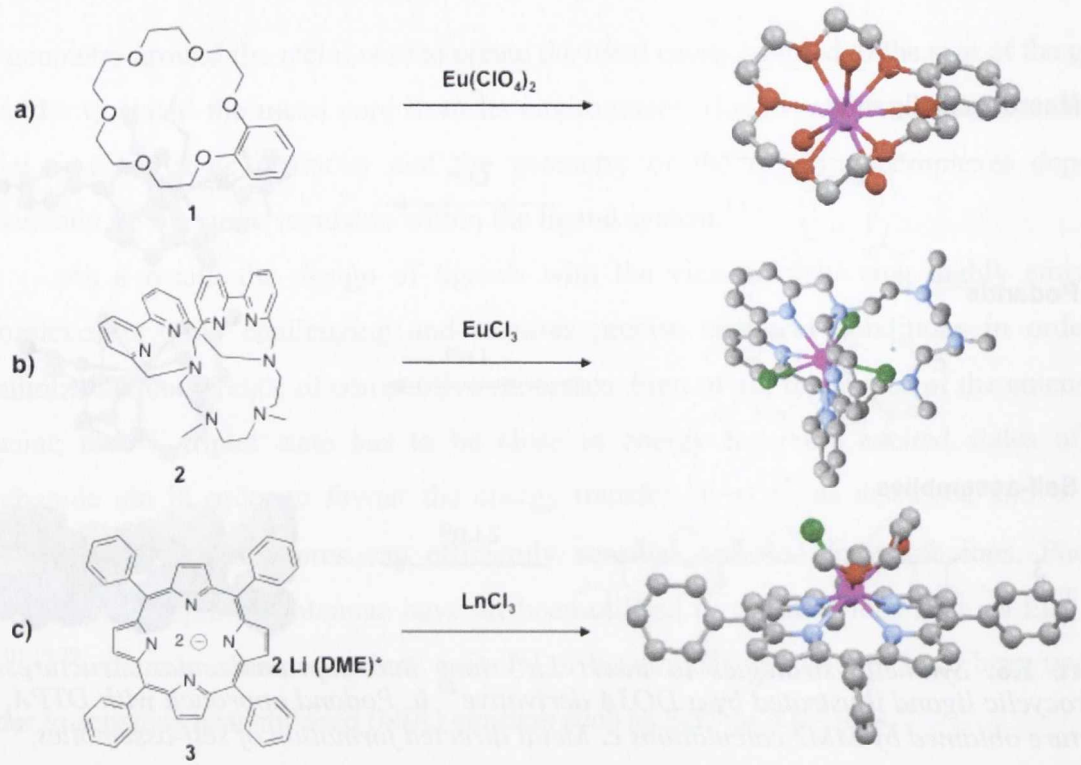


**Figure 1.7:** *Ligands and crystal structures of the resulting complexes obtained using the lock-and-key approach: a) **1** designed from coronand.*[46] *b) **2** designed from azacrown*[51] *c) **3** from porphyrin.*[52]

of these organic preorganised ligand is quite challenging. For these reasons, and in order to avoid the limitation caused by the use of preorganised receptors, another approach, inspired by the *induced fit* principle, has been widely utilised over the past decades.[5]

The "*induced fit*" strategy consists of designing more flexible predisposed receptors, which possess a cavity which can adapt to the size of the metal ion. Unfortunately, the conformational changes induced by the complexation cause an increase in the formation energy. However, this increase in energy, which is stronger than that of the enthalpy effect previously mentioned for the preorganised receptors, is usually compensated by the enthalpy gain due to the host-guest interaction.[49] Different types of design, following this approach have been developed over the past decades and some examples are shown in the Figure 1.8. The first approach consists in the synthesis of large flexible macrocycles such as coronands[50,51] and large calixarenes, which are capable of wrapping around the lanthanide ions. Also, this design has been of a great interest in the synthesis of bimetallic complexes as shown by Bünzli *et al.* for imaging in the NIR region.[52] Furthermore, the flexibility and the inherent preorganisation of the ligand, which can also be provided through functionalisation of its central macrocylic scaffold, is essential for the stability of the resulting complexes, reducing their energy of formation, due to the reorganization of the ligand upon complexation. In the system developed by Bünzli and coworkers shown in Figure 1.8a, compound **4** was designed from the coronand

[2,2]-(1,10-diaza-4,7,13,16-tetraoxacyclooctadecane), which provides a hexadentate cavity including two amino moieties. Firstly, the alkylation of the aza-macrocyclic scaffold with monodentate pendant arms gives a coordination environment of 8 with the two phenolic ester moieties both participating in the binding of the $Eu^{III}$ ion. The pendant arms also possess long aliphatic chains, necessary to form mesogenic complexes for their potential application as liquid crystals devices. This study showed that the formation of liquid crystals was dependent on the nature of the lanthanide salt employed and on the number of alkyl chains appended to the ligand.[53] As previously mentioned, the azacrowns were observed to be efficient receptors for lanthanide ions, and the 1,4,7,10-tetraazacyclododecane (cyclen) has been one of the most intensively investigated in the field of lanthanide coordination chemistry.[9,11,12,40] Indeed, this tetradentate macrocycle offers four potential sites for the functionalization with pendant arms.

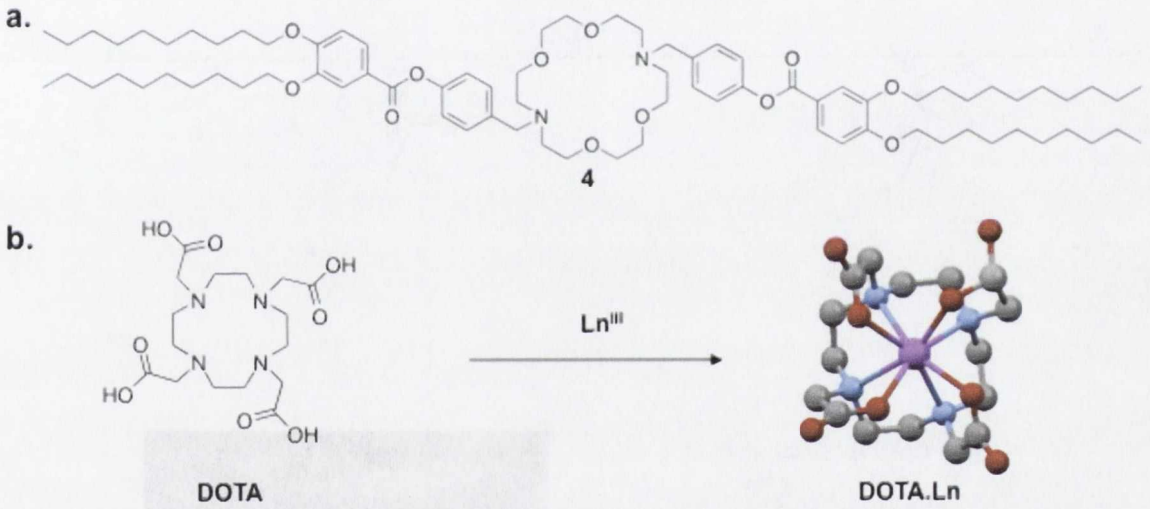


**Figure 1.8:** *Examples of ligands designed following the induced fit strategy for the a.) incorporation lanthanides ion in mesogenic systems (4).*[53] *and b.) 1,4,7,10-tetraazacyclododecane-tetraacetic acid (DOTA).*[57]

Following the wide utilisation of amino-carboxylate moieties for the coordination of *d*-elements, their incorporation into cyclen for lanthanide coordination has been studied in details and well established by numerous groups.[9,54-56] Furthermore, the complexes with DOTA (1,4,7,10-tetraazacyclododecane-tetraacetic acid) (Figure 1.8b) have been ranked among the most stable $Ln^{III}$ coordination compounds (with $Log\ \beta \approx 20\text{-}23$).[57] This is due to the flexibility given by the presence of the carboxylate arms, which allows an optimization of the geometry of the cavity, increasing the host-guest interaction.

Furthermore, the grafting of various pendant arms as part of the cyclen scaffold, offers a synthetic pathway, which facilitates the incorporation of other functional moieties as observed in the examples shown in Figure 1.9. Complex **5** was designed by Pope *et al.*

from the DO3A and contains a chromophoric bis-picolyl unit (orange), which can bind selectively $Zn^{II}$. This system has been observed to be responsive towards $Zn^{II}$ with variation of the luminescence intensity and lifetimes, occurring through a change in the solvation number changing from 1 to 2, in the presence of $Zn^{II}$.[58] Recent examples have shown that the lanthanide luminescence can also be modulated by the presence of anions and the development of luminescent anion sensors has been performed following two different strategies. The first approach, involves lanthanide complexes with unsaturated coordination spheres, which will be fulfilled with solvents molecules such as water, binding directly to the metal ion. In water, the recognition of the anion then occurs *via* displacement of these metal bound water molecules. This gives rise to less quenching in the lanthanide emission, as now the OH oscillator have been removed.

This strategy has been widely utilised for the recognition of anionic guests and

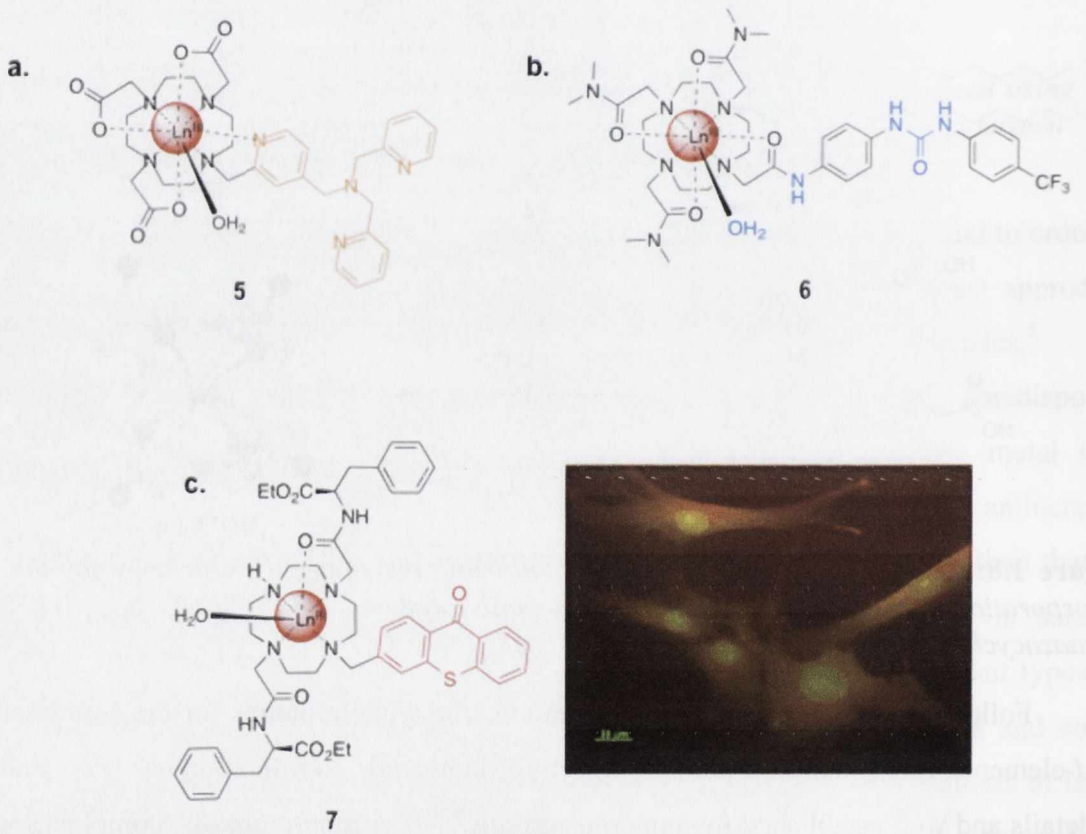


**Figure 1.9:** *Examples of luminescent functional DO3A derivatives:* ***a.*** *$Zn^{II}$ sensor[56]; **b.** Anion sensor[62] and **c.** Contrast agent for in cellulo imaging.*[63-65]

most particularly of carboxylic acid and phosphates derivatives.[9,59-61] However, efficient sensing can be performed through the utilisation of binding moieties, such as urea, that are grafted into an antenna. For example, structure **6**, developed within our research group, contains a phenolic-urea moiety, an amido -NH and a $H_2O$ molecule within the first coordination sphere of $Eu^{III}$ (in blue) and this sensor has shown a high sensitivity to anions such as acetate and phosphate.[62]

The functionalisation of the cyclen scaffold gave also rise to numerous examples of targeting lanthanide complexes for medical imaging such as magnetic resonance imaging (MRI) contrast agents, as well as NIR and visible emitters. The $Eu^{III}$ complex **7**, developed by Parker *et al.,* contains an azathioxanthone moiety and has been shown to possess the ability to stain selectively the nuclei of alive and fixed HeLa, HDF and NIH 3T3 cells making compound **7** an ideal candidate for *in vivo* imaging using time-resolved microscopy.[63-65]

Since the introduction of calixarenes, this family of compounds has been widely used in chemosensing, and in coordination chemistry,[66] as well as for the separation of heavy atoms such 5*d*, 4*f*, and 5*f* elements,[67,68] catalysis,[69] and in ion-channel mimetics.[70] The calixarene offers two possibilities for alkylation with different reactivity, on the lower rim bearing four alcohol moieties and on the upper rim. Due to their inherent cone preorganisation, the functionalisation upon the upper wider rim gives rise to a large cavity capable of hosting large guests, whereas the grafting of pendant arms upon the narrower rim forms a smaller cavity below the phenylic platform as shown in the examples depicted in Figure 1.10. The size of the cavity and the distance from the scaffold can be modified as a function of the nature of the pendant arms. For example, the calix-[4]-arene derivatives **8a** and **8b**, developed by Shinkai and coworkers, have demonstrated high selectivity towards large cations such as sodium cations as well as 4*f* metal ions. Indeed, the tetrameric scaffold has been alkylated with four bidentate pendant arms containing carboxylate or amido terminal functions (**8**) in order to fulfil the coordination requirement of lanthanide ion.[71,72] This flexibility, provided by the phenolic moieties and the methylene spacers, then allows an efficient collaboration of the four pendant arms forming an ideal cavity relatively close from the annulus, whereas, ligand **9** developed by Bünzli *et al.* forms a binding pocket sitting further from the phenylic scaffold.[1] The approach for the synthesis of these ligands gave rise to numerous ligands leading to 1:1 complexes with high binding constants $p\text{Ln} \sim 10$ for **8b**. For these systems, the polyaromatic annulus can act as an antenna to sensitise lanthanide emission.[71,72]

As a result, luminescent probes and contrast agents for use in the visible or in the NIR regions, such as **10a** and **10b**, have been developed from the tbu-calix-[4]-arene. However, the sensitisation process can be difficult. Shinkai and coworkers have demonstrated that the direct excitation of the annulus of compound **8-9** sensitised the terbium emission, whereas the sensitisation of europium needed the presence of an external antenna. Indeed, the complexation of $Eu^{III}$ results in the formation of a C=O to $Eu^{III}$ charge transfer band (CT), sitting between the $^3\pi\pi^*$ and the $^3n\pi^*$ excited states of the calixarene

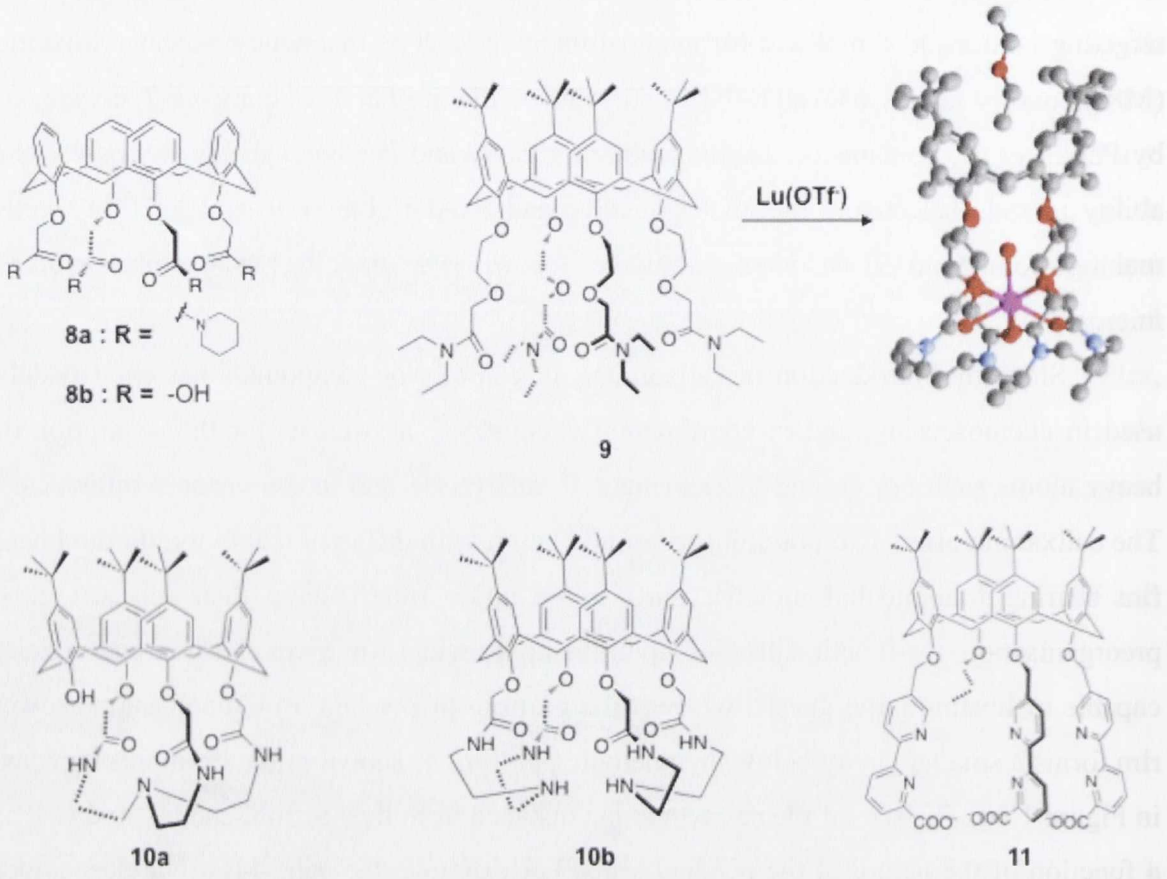


**Figure 1.10:** *Examples of ligands designed from calix-[4]-arenes forming 1:1 (metal:ligand) complexes with lanthanide ions.*

annulus. Consequently, the direct excitation of the calixarene scaffold provokes the population of the aforementioned CT band, which deactivates the complex excited states to the ground state, resulting in poor emission quantum yields.[1,71] Similar results have been published by Oueslati *et al.* for the NIR emitters **10a-b,** which demonstrated weak sensitisation abilities.[73] In order to avoid this issue, the utilisation of modified calixarenes, such as thia-calixarene, give rise to more luminescent and more water-soluble complexes mostly for *in cellulo* imaging.[74,75]

Most of those systems are also based on the alkylation of the lower rim of the calixarene. Finally, the incorporation of binding sites such as picolyl or bipyridyl moeties can give rise lanthanide complexes having a higher level of symmetry.[76] An example of this is the ligand **11**, designed by Ziessel *et al.,* which bears three bipyridyl moieties, known to form helical complexes with lanthanide ions, and can form the monometallic triple stranded helicate **11.Ln**. However, the formation of the $\mathbf{11_2.Ln_2}$ complex, containing two metal centres with a local helical geometry, was also observed for this system. This is due to the constraints inflicted by the size and the rigidity of the central scaffold, which provokes a difficult optimization of geometry around a single metal ion.[77,78] In order to

avoid this issue, the synthesis of lanthanide complexes was carried out following alternative approaches based on the utilisation of acyclic linear ligands, which could have a better ability to wrap around the lanthanides ions. This gave rise to novel supramolecular systems where the coordination requirement of the lanthanide ion was fulfilled *via* either the utilisation of podands or the formation of metal directed self-assemblies.

### I.2.2 Complexation of lanthanide with linear ligands

#### I.2.2.1 The podand approach

The design of suitable podands to bind lanthanide ions is based on the use of acyclic ligands, which contain several pendant arms attached to a central moiety. The ligand sustains a strong reorganisation upon the lanthanide complexation in order to shield the lanthanide ion from its environment. These two processes provoke a significant

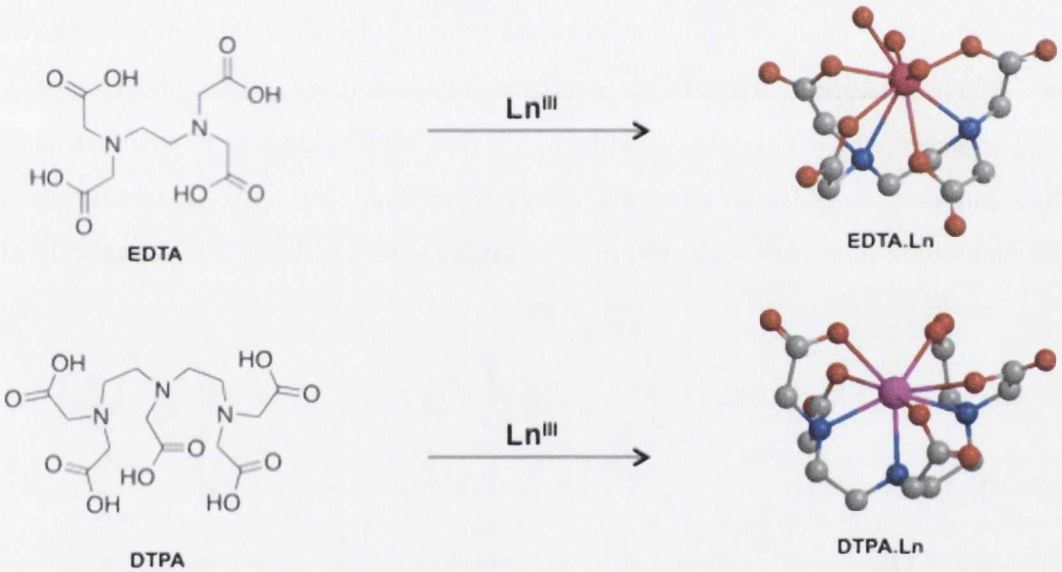


**Figure 1.11:** ***EDTA** and **DTPA** and MM2 calculations of the complexes **EDTA.Ln** and **DTPA.Ln***

increase in the enthalpy of formation of the complexes, which is compensated by the increase in the entropy of the systems due to the chelate effect. **EDTA** (ethylenediamine-tetraacetic acid) and **DTPA** (diethylenetriamine-pentaacetic acid) are examples of such ligands (Figure 1.11) gave rise to highly stable l:1 complexes with lanthanides *ca.* $\log\beta \approx$ 15-20[57] and $\log\beta \approx$ 19-22[1], respectively. Ligand **12** shown in Figure 1.12, developed by Glover *et al.* was designed on the **DTPA** motive, functionalised with bisamide thiophenol moieties, which offer two grafted donor sites capable of binding to other transition metals such as $Pt^{II}$, where the lanthanide complexation orientates the ligands in a hairpin shape, leaving the two thiol sites available for the $Pt^{II}$ binding. The resulting luminescent architecture was used to bind DNA.[79] Ligands similar to **12** were also used in order to incorporate lanthanide ions in luminescent molecular substructures such as nanoparticles[80]

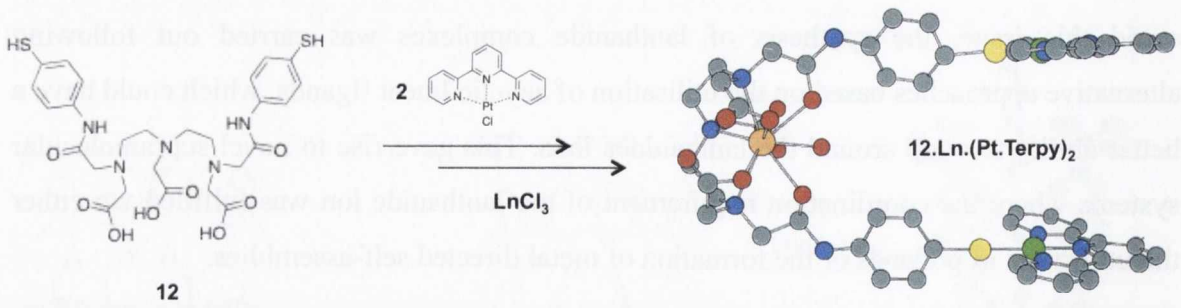


**Figure 1.12:** *Ligand 12 and molecular modeling of a lanthanide templated hairpin shaped DNA intercalator.*[79]

and single stranded DNA for immunoassays.[5] However, the design of ligands based on these kind of metal chelate derivatives gives rise, in most of the cases, to a "pocket-like" geometry limiting then the potential control of the complex geometry.

In order to facilitate conformational control, other alternatives to podand design have been developed, which consist in grafting multidentate pendant arms around smaller anchorage moieties, such as small aromatic rings, or even a single atom, as shown in Figure 1.13. For example, **13** was designed by Bünzli and coworkers and consists of a phenylic moiety, which acts as a platform for the four imidazole pendant arms. This structure interacts with lanthanide ions in water yielding 1:1 and 1:2 complexes with various lanthanide ions with high stability *ca.* $\log\beta_{11} \approx 13$ and $\log\beta_{12} \approx 23$, respectively.[81]

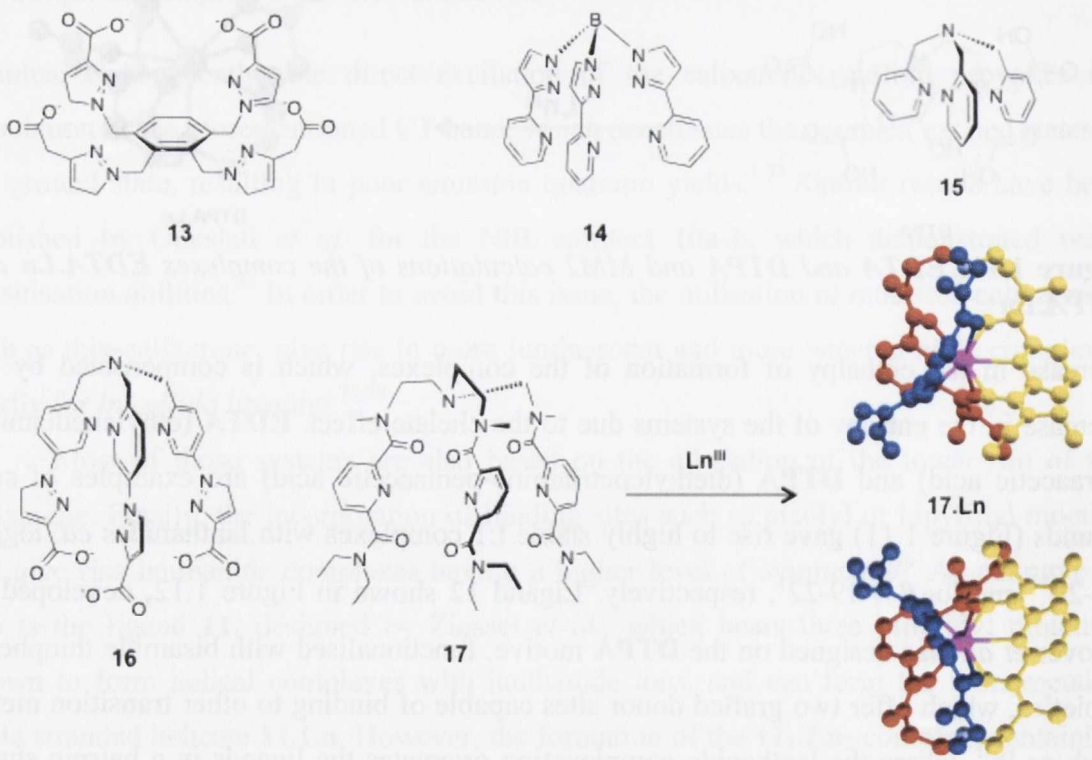


**Figure 1.13:** *Ligands developed following the podand approach:* ***13*** *with phenylic anchor,*[81] ***14*** *designed around boron.*[82] ***15, 16*** *and* ***17*** *around a nitrogen atom.*[83-85]

However, the cup shaped geometry of these systems is still dependent on the shape of the central scaffold. Consequently, numerous systems based on the incorporation of flexible multidentate pendant arms onto a single atom have also been developed. For the purpose of lanthanide complexation, trivalent elements such as boron or nitrogen are suitable as anchors due to their reactivity and their quasi-tetragonale directionality. The tripodate **14** was built around boron and provides 6 donor atoms through its pyrazol and pyridinyl moieties resulting in an efficient wrapping around the lanthanide ion. However, the utilisation of these bidentate moieties does not allow the saturation of the $Ln^{III}$ first coordination sphere, which can have a dramatic effect on the quantum yields of the system.[82] The utilisation of other polydentate moieties such as polypyridines can allow a better control of the geometry of the topology. However, the nature of their binding site is imperative for the easy formation of highly symmetric topologies such as helicates.[83,84] Compound **15** was developed by Charbonnière *et al.* and used as a nitrate sensor. This structure has three pyridine units and can bind lanthanides in a helical shape; The sensing process occurs by replacement of the solvent molecule present in the coordination sphere of the $Eu^{III}$ ion with $NO_3^-$ or $Cl^-$ anions, which provokes a large increase in the $Eu^{III}$ emission intensity.[84] For the purpose of geometry optimisation, the podand approach gave rise to numerous systems for time-resolved imaging in the visible or the NIR region,[10,12] and chemosensing.[37]

With the view of a better control of the complexes geometry, numerous tripodal systems containing tridentate moieties on more flexible arms have also been developed such as **16** and **17**. The ligand **16** possesses both carboxylate and pyrazol as well as pyridine moieties as pendant arms, all of which can provide up to three donor atoms to bind the lanthanide ion. The system provides a nonadentate cavity, shielding the lanthanide ion from the solvent molecules. This is due to the flexibility of the pendant arms, given by the ethylene spacers between the anchor and the binding site.[83] However, the example developed by Renaud *et al.* (ligand **17**, Figure 1.13) showed that, in this particular case, the flexibility of the arms plays a less important role than the nature of their binding site.[85] Molecular modelling calculations performed on this type of systems have shown poor efficiency of such systems for the sensitisation of the $Eu^{III}$ and $Tb^{III}$ excited states. The tripodal ligand **17**, which has been designed to complex a single lanthanide ion in a helical form, contains three pendant arms grafted on a single nitrogen atom.[85] Each arm contains a tridentate 6-(*N,N*-diethylcarbamoyl)pyridine-2-amido moiety, which is known to form helical complexes with $Ln^{III}$ in a $C_3$ overall geometry.[86] This provides nine donor atoms filling the coordination sphere of the lanthanide ion, while the pyridine unit acts as a

sensitizing antenna. The resulting lanthanide complexes were obtained as two cone-shaped triple-stranded helicates, which displayed opposite helicity, as shown in Figure 1.13. Furthermore, in acidic media, ligand **17** benefited from a remarkable preorganisation due to the protonation of the apical N atom. The authors showed that a trifurcated H-bond between the apical proton and the surrounding oxygen atoms stabilizes the *endo* conformation of the central nitrogen positioning the pendant arms in a ideal "dome" like configuration, which allowed to overcome the electrostatic repulsions occurring during the complexation process. It was concluded that the podand effect in conjunction with secondary weak intramolecular interactions allowed for a precise control of the coordination site geometry.[85] From the above discussion, it can be concluded that the podand approach is an efficient strategy to incorporate lanthanide ions into luminescent systems over the field of supramolecular chemistry and that the inherent preorganisation provided by this type of ligand allows the formation of highly symmetric and stable 1:1 complexes. However, the synthesis of ligands leading to polymetallic systems can be quite challenging and requires in most of the cases, the contribution of small subunits to fulfil the coordination environment of the lanthanide ion. In order to overcome these synthetic issues, the coordination chemists use a well known approach in the field of transition metals to synthesise polymetallic oligomers, namely the metal directed formation of self-assemblies.

### I.2.2.2 Lanthanide directed formation of supramolecular self-assemblies

This strategy takes advantage of both the high electric field of the lanthanide ions and weak intermolecular interactions in order to self-assemble several coordinating building blocks around one or several ions. This strategy gave rise to numerous mono- or ditopic ligands capable of self-assembling with transition metals in order to give rise to larger functional substructures, some example of which are depicted in Figure 1.14. Lanthanide ions, which possess a high coordination number (up to 10 coordination sites in solution as discussed above) and most often a soft tricapped coordination sphere, are suitable candidates to template the formation of supramolecular architectures such as triple stranded helicates and interlocked molecules as shown in the following sections.[83] Lanthanide ions have also been incorporated into metallo-supramolecular structures such as molecular boxes or inorganic clusters.[87-89] Over the past few decades, it has been well established that the complexation process *via* self-assembly occurs strictly under thermodynamic control.[48,83] For this reason the synthesis of luminescent systems involving the self-assembly of small coordinating units such as bipyridine or picolinic acid

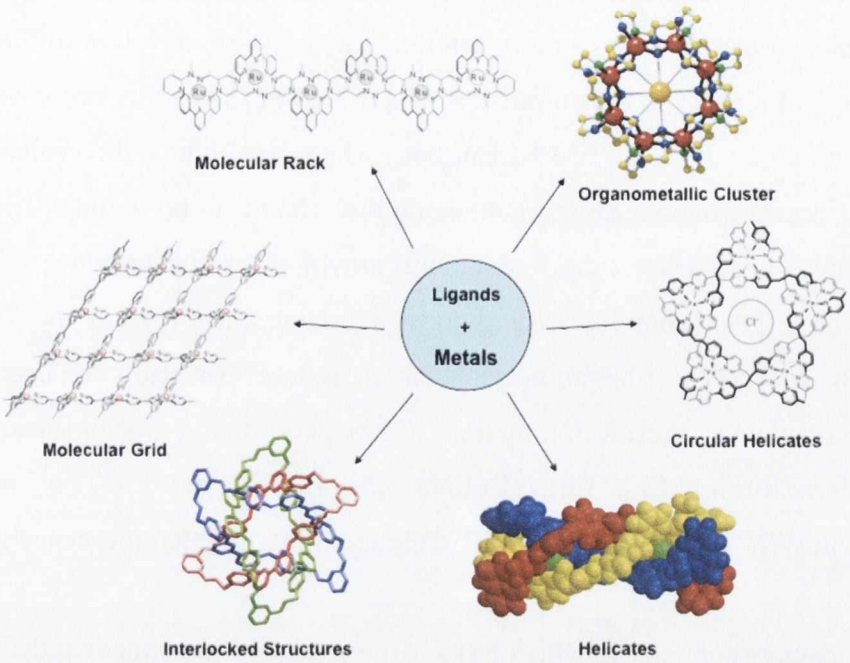


**Figure 1.14:** *Different metallo supramolecular structure which can be obtained via metal directed self-assemblies.*[83,87-89]

derivatives, around a lanthanide is straightforward and has given rise to numerous stable complexes in quasi quantitative yields.[83,88] Moreover, the grafting of the polyaromatic chromophores directly onto the metal ion allows the efficient sensitisation of the lanthanide emission facilitating the antenna effect. The lanthanide-directed formation of self-assemblies allowed either the incorporation of lanthanide ions into organometallic clusters or the formation supramolecular architectures such as helicates or bundles.

**Organometallic clusters:**

As indicated above, the choice of the coordinating subunit is essential to control the stoichiometry and the shape of the complexes as demonstrated by the systems in Figure 1.15. The ligands **18** and **19** are both tridentate and built on a 2,2′-bipyridyl framework. Ligand **18** was synthesised by Lama *et al.,* and contains a chiral pinene substituted with a carboxylate moiety, that forms 3:6 (M/L) trinuclear homochiral complexes with most of the lanthanide ions.[90] Ligand **19**, developed by Comby *et al.,* is based on the use of a phosphonic acid moiety, which gave rise to the formation of mononuclear complexes where three subunits self-assemble around the lanthanide ion.[91] The resulting complexes of **19** with lanthanides such as $Eu^{III}$ and $Nd^{III}$, have been shown to be stable with high binding constants *ca.* $\log\beta_{13} \approx 17.6$ and $\log\beta_{13} \approx 16.0$, respectively. This ligand efficiently sensitised the lanthanide excited states upon excitation of the bipyridyl moiety, with quantum yields up to 42.2% (for the terbium complex).[91] However, the solid state studies

performed on the self-assemblies of ligand **19** with lanthanides such as $Eu^{III}$, $Tb^{III}$, $Gd^{III}$ and $Er^{III}$, demonstrated that the configuration of the self-assembly was different than the one formed in solution. The crystallization of a 1:3 (M/L) ratio mixture gave rise to the formation of polymetallic cluster $\mathbf{19_{16}.Eu_9.Na_6}$, where the eight indiscernible lanthanide centres are disposed around a central lanthanide ion. The resulting 9:16 (M/L) architecture was stabilised by the electrostatic interactions provoked by the presence of six sodium ions, which have been demonstrated to have a predominant role in the self-assembly formation. The formation of hetero polylanthanide systems has also been investigated and has been demonstrated to result in a mixture of large coordination complexes, which have the same general formula $\mathbf{19_{16}.{}^1Ln_{9-x}.{}^2Ln_x.Na_6}$ (x = 4 or 5 with a $Eu^{III}/Yb^{III}$ mixture), and showed both the $Yb^{III}$ emission in the NIR region and the $Eu^{III}$ luminescence in the visible region.[92]

The tetradentate subunit **20,** which has a carboxylic acid substituent at the position two of the terpyridine moiety, self-assembles with various lanthanide ions to give rise to a large wheel-shaped self-assembled complex. The controlled synthesis of such a structure was

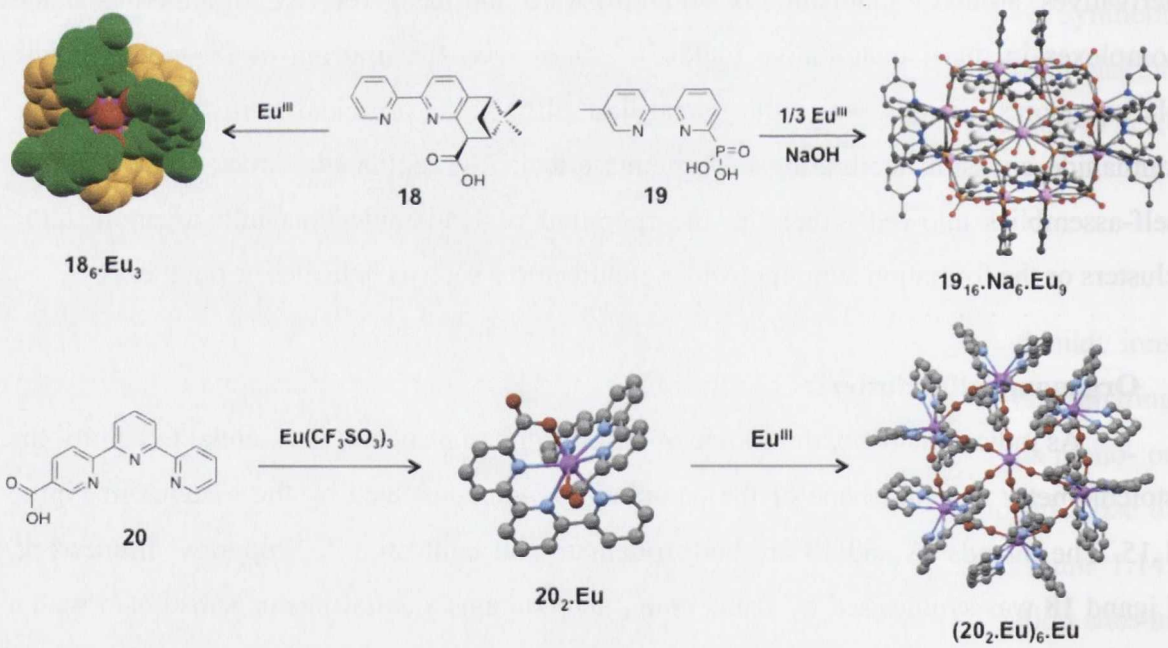


**Figure 1.15:** *Examples of sophisticated metallo supramolecular architecture formed via self-assemblies of small subunits based on bipyridine such as **18** and **19** [90-92] and on a terpyridine (**20**).*[93]

performed in two steps. Firstly, the complex $\mathbf{20_2.Ln}$ was synthesised, then six mono-metallic 1:2 (M/L) complexes were linked together *via* complexation of a seventh lanthanide ion. Mazanti *et al.* have also demonstrated that the formation of the polymetallic ring can be controlled by changing the ratio between the ligand and the cation.[93] The control of the supramolecular architecture can also occur by combining different binding

units as illustrated by the systems developed more lately by Wang *et al,* as shown in Figure 1.16.[94] The structure **21a,** which results from the self-assembly of the rigid pyridine-2-carboxylic acid and adipic acid in the presence of $Eu^{III}$, forms a 2-dimensional lanthanide coordination polymer in the solid state. Moreover, Wang *et al.* have also demonstrated that the functionalisation on the position five of the pyridine with another carboxylic moiety allows the formation of the tri-dimensional $Eu^{III}$ polymer **21b**.[94] The utilisation of small coordinative subunits offers a direct synthesis pathway leading to large supramolecular lanthanide coordination complexes. However, the synthesis of poly-lanthanide architectures with a high nuclearity remains quite challenging and yields in most cases to mixtures of different clusters as illustrated previously with ligand **19**.

In order to reduce the synthetic effort, the research in the field of mixed metallic supramolecular systems focused on simpler systems, such as the molecular square **22** developed by Guo *et al.*.[95] This structure, which has been isolated in high yields, consists of four divalent metal complexes, two $\mathbf{Ln(TTA)_3}$ and two $\mathbf{Ru(bipy)_2}$, assembled *via* four 4,4'-bipyridine linkers. It has also been demonstrated that the excitation in the visible

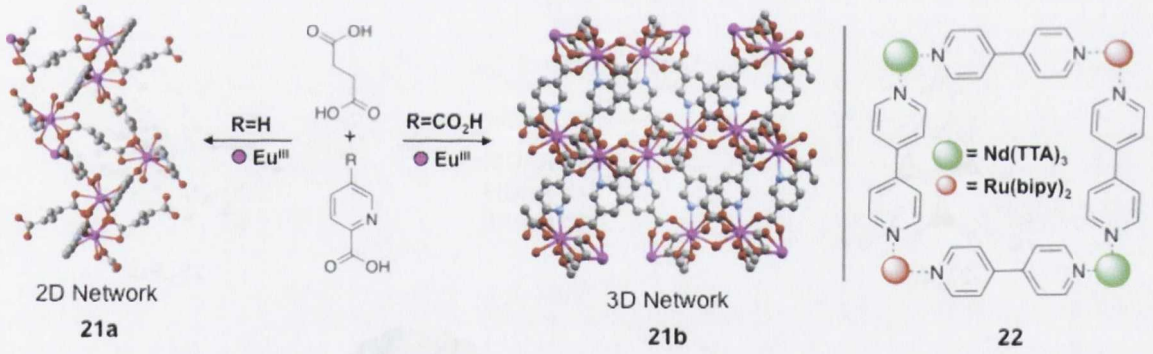


**Figure 1.16:** *2D (**21a**) and 3D (**21b**) lanthanide coordination polymer obtained via self assembly of rigid and flexible units in the presence of $Eu^{III}$.*[94] *Hetero polymetallic molecular box based on $Nd^{III}$ and $Ru^{II}$ complexes (**22**).*[95]

region (up to 500 nm) of the ruthenium centered antenna, which exhibits high intersystem crossing yields, enables the sensitisation of $Nd^{III}$ and $Yb^{III}$ luminescence in the NIR region.[95] The self-assembly approach using small binding units has been widely utilised in order to enhance the photophysical and magnetic properties of lanthanide ions, making them particularly interesting for the development of optical-fibres, molecular information storage and electroluminescent devices through their incorporation into thin films, or polymers.[48,51,96-98] The success of this strategy is due to the efficient control of the geometry of the system at the nanometre scale.

**Mono-molecular lanthanide based self-assemblies:**

The 2,6-diamidopyridine moiety **23** (Figure 1.17) possesses a tridentate cavity, which allows the formation of 1:3 complexes with trivalent lanthanide ions. Tanase *et al.* have shown that the lanthanide ion is completely shielded from the solvent molecules, by three units **23** forming a structure, which possesses a $C_3$ geometry. Furthermore, the pyridinyl unit provides an efficient antenna capable of populating the excited states of $Tb^{III}$ and $Eu^{III}$.[86] The series of ligands **24a-c** were alkylated on the 4-position of the dipicolinate moiety with a polyethylene-based pendant arm in order to facilitate their use in biological systems. Indeed, the presence of the long polyethoxyethylene chain can bring a better solubility in aqueous media but also offer the possibility for functionalisation at a considerable distance from the metal centre. The three ligands developed by Chauvin *et al.*, which bear different terminal moieties such as alcohol, methoxy or amine have been demonstrated to form thermodynamically stable complexes with *ca.* $\log\beta_{13} \approx 18\text{-}20$ for the whole lanthanide series. It has also been established that the nature of the terminal moiety

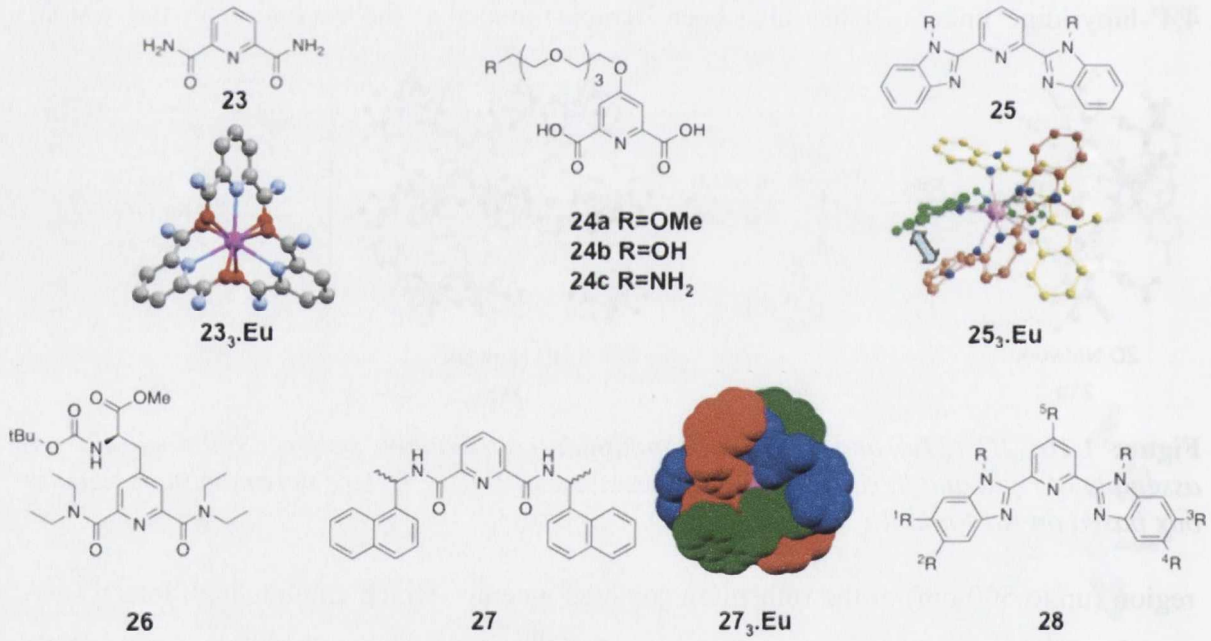


**Figure 1.17:** *acyclic ligands designed to form 1:3 mono-metallic systems upon lanthanide complexation:* ***23****,* ***24*** *and* ***25*** *are symmetrical and achiral;*[86, 99, 100] ***26*** *and* ***27*** *are chiral;*[101, 102] *and* ***28*** *building block for the synthesis of larger asymmetric ligands.*[1,103-105]

present on the pendant arms, has very little influence of the stability of the trivalent complexes. Indeed, the complexation of each ligand with $Eu^{III}$ gave rise to 1:3 complexes with $\log\beta_{13}$ between 20.3 and 21.[99]

The functionalisation of the subunit **23** has also been performed *via* alkylation of the groups present on the position 2 and 6 allowing the synthesis of symmetrical ligands such as **25-27** (Figure 1.17). As an example, ligand **25** provides a tridentate cavity through the

pyridine and the two benzimidazol moieties present in the position 2 and 6 of the pyridinyl scaffold. The benzimidazol moiety functions as an efficient sensitising antenna for $Tb^{III}$ and $Eu^{III}$ in the visible region and also for $Nd^{III}$ in the NIR region and can also generate inter-ligand interaction *via* π-π stacking. As demonstrated by the crystal structure of **25$_3$.Eu**, the presence of such intermolecular interactions (shown on the crystal structure with the blue arrow) coupled with the rigidity of the ligand results in the formation of a "squeezed" triple helical shaped complex presenting an overall $C_3$ geometry. Further alkylation of the benzimidazol moieties in the R-positions appeared to have an influence on the stability of the complexes and on the geometry of the resulting self-assembly structure.[100] However, by using **25** the authors have shown interesting discrimination properties towards the heavier lanthanide ions, which make the architecture **25$_3$.Ln** and its derivatives excellent building blocks for the synthesis of heterometallic helicates.[101]

On the purpose of developing more efficient contrast agent and in order to enhance their selectivity to different guests, the alkylation of small binding units have been widely used to add functionality to the lanthanide complexes. For examples, **26** and **27,** bear chiral pendant arms on the position 4 of the pyridine unit in the case of **26** or on the nitrogen atoms present on the amido moieties (in the case of **27**). The ligand **26** displayed similar coordinative properties than other systems developed from the dipicolinate framework, where the 1:3 stoichiometry is the most thermodynamically stable with *ca.* $\log\beta_{13} \approx$ 19-20 in acetonitrile. In addition, the rotary dispersion of the complex was ten times larger as the one of the ligand alone, which confirmed that a triple stranded monometallic helicate with a chiral emission was formed. The ligand **27** developed in our group has been observed to form the enantiomerically pure self-assembly **27$_3$.Eu**, which possesses also a $C_3$ geometry and triple stranded helicate shape. As the study of the formation of self-assemblies of **27** analogues with $Ln^{III}$ is the subject of Chapter 3, the analysis of the circularly polarised luminescence (CPL) of the $Eu^{III}$ complexes upon the excitation of the naphthyl moiety,[102] will be developed in details in section 3.1.

The functionalisation of the building blocks such as **28** can also have dramatic effects on the photophysical properties and on the shape of the resulting self-assembly. It has been demonstrated by Bünzli *et al.* that the functionalisation of **28** at the R-positions only affects the stability and the final shape of the topologies, whereas the substitution within the $^{1\text{-}5}$R-positions can also affect the electronic and physical properties of the resulting structure.[103-105] This strategy offers a simple synthetic pathway towards larger ligands capable of forming polymetallic systems, and also provides an important control of the shape of the resulting supramolecular architectures. For that reason, the metal-directed formation of

self-assembly has been widely used to yield high topologies with a level of symmetry such as helicates, which will be discussed in the next section.

**Lanthanide-based helicates**

Due to the inherent properties provided by polymetallic supramolecular structures, the synthesis of homo- and hetero-polymetallic helicates has been an active area of research during the past few decades.[106,107] More recently, numerous elegant examples of lanthanide based triple stranded helicates have been reported and in most of the cases the strategy employs the design of a ligand connecting several building blocks. As an example of this design is ligand **29** developed by Piguet *et al.*, which bears two tridentate pyridinyl-bis-benzimidazol moieties connected *via* a methylene linker, and it is, to the best of our knowledge, the first example of lanthanide directed triple-stranded helicate published in the literature (Figure 1.18).[108] These triple stranded dimetallic helicates were formed with three equivalents of ligand **29** wrapped around the two nine-coordinate $Ln^{III}$ ions in

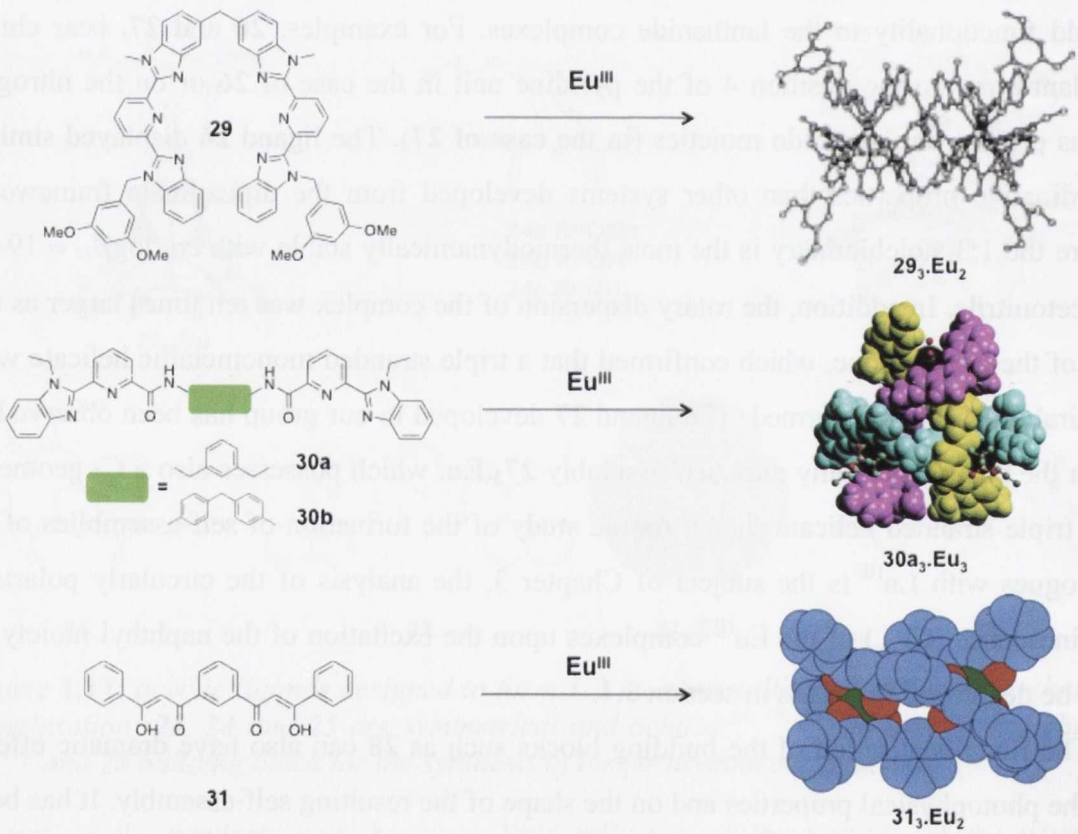


**Figure 1.18:** *Ligands synthesised for the formation of dimetallic triple stranded helicates based on different binding blocks such as pyridine-benzmidazol (ligands* ***29****[108,109] and* ***30a-b****)[110] and bis-β-diketonate (****31****).[111]*

pseudo-$D_3$ symmetry for the whole lanthanide series. Moreover, the complexes $\mathbf{29_3.Ln_2}$ and their stability were comparable to that of many DOTA derivatives.[1,22,108,109] However, the resulting architecture showed a poor solubility in water, preventing its potential use in

bio-related applications. The family **30** is another example of ligands designed to yield triple stranded helicates. For example, $\mathbf{30a_3.Ln_2}$ was formed in solution from a 2:3 Ln:**30a** ratio. The series of ligands **30** bear two pyridinyl-benzimidazole moieties linked *via* a phenylic **30a** or a para-diphenylic **30b** spacer. The authors demonstrated that in the solid state compound **30b** gave rise to the formation of a stable triple stranded helicates, whereas **30a** formed the circular single stranded trimetallic helicate $\mathbf{30a_3.Ln_3}$. This confirms that the nature of the linker separating the two building blocks can greatly affect the shape and the stoichiometry of the supramolecular assembly.[110] The same aspect of the helicate formation has also been observed with the family of ligand **32** developed by Horrocks and co-workers (Figure 1.19). Moreover, the influence of the spacer on the shape of the helical topology has also been studied on the functionalised chiral analogues of **33**, developed in our research group (see Chapter 4.).

The bis(β-diketonate) ligand **31** has been prepared by Pikramenou and coworkers and was used to form the homodimetallic triple stranded helicate $\mathbf{31_3.Ln_2}$ (Ln = $Nd^{III}$ or $Eu^{III}$). The formation of an anionic quadruple stranded dimetallic helicate $\mathbf{31_4.Eu_2}$ was also observed.[111] The formation of such supramolecular architecture has also been carried out using dipicolinate derivatives. The interest for this subunit lies in its solubility in aqueous media and in its capability to form stable lanthanide complexes with trigonal prismatic, $D_3$ geometry and either Δ or Λ chirality. The family of compound **32** developed by Horrocks and coworkers consists in the use of two tridentate chelating units linked by an organic diamine (4,4-diaminodiphenylmethane or 1,2-diaminocyclohexane, respectively for **32a** and **32b** in Figure 19).[106]

As the complexes $\mathbf{dpa_3.Ln}$ and other complexes of the same type racemise in solution, for **32b**, both of the *R,R* and *S,S* enantiomers were used in order to impose hardness to the architecture and to form a complex, which retains its optical activity (ΔΔ or ΛΛ) in solution. The solution studies performed on these systems coupled with molecular modelling calculations have been used to predict the structures of the dinuclear helicates, which has indicated the formation of the true helix form (ΔΔ or ΛΛ configuration at the metal centre) and also the formation of the side by side helicate (ΔΛ configuration).[106] The compound **33** has been designed in our research group from two similar tridentate dipicolinate moieties functionalized with a chiral antenna containing a naphthalene unit separated by a phenylic spacer, which provides more flexibility than the analogues with the 4,4-diaminodiphenylmethane linker. The photophysical studies of the complexation process have shown the quasi-quantitative formation (90% in presence of 0.66 eq of $Ln^{III}$) of the triple stranded helicate $\mathbf{33_3.Ln_2}$ with high binding constants ($\log \beta_{23} \approx 20$), where **Ln**

is $Eu^{III}$, $Tb^{III}$ or $Sm^{III}$. The excitation of the naphthyl moiety gave rise to the lanthanide luminescence in both the visible and the NIR regions. The studies and the MM2 simulations on the analogues **33** (which will be the object of section 4.1) containing a diphenylic spacer, have been shown to form a more "squeezed" topology than in the case of **33** and an enantiomerically pure europium centered emission which led them as ideal candidates for imaging contrast agent.[41,112]

The functionalisation of the helicate scaffold has recently been an active area of research in order to enhance the properties of the systems and to facilitate their incorporation into biological systems. The family of ligand **34** (only two example are shown in Figure 1.19, which are based on the same design as **29**), have been developed and studied by the group of Bünzli and Piguet in order to investigate the influence of diverse functionalisation of the ditopic ligand backbone on the shape and on the properties of the resulting architecture. It has been well established that the functionalisation of the position $R_2$ and $R_3$ affects the solubility, the biological coupling ability as well as the photophysical properties of the helicates whereas the substitution in the position $R_1$ affects mostly the coordination of the lanthanide ion.[113] For example the whole series of ligand **34a-c** formed

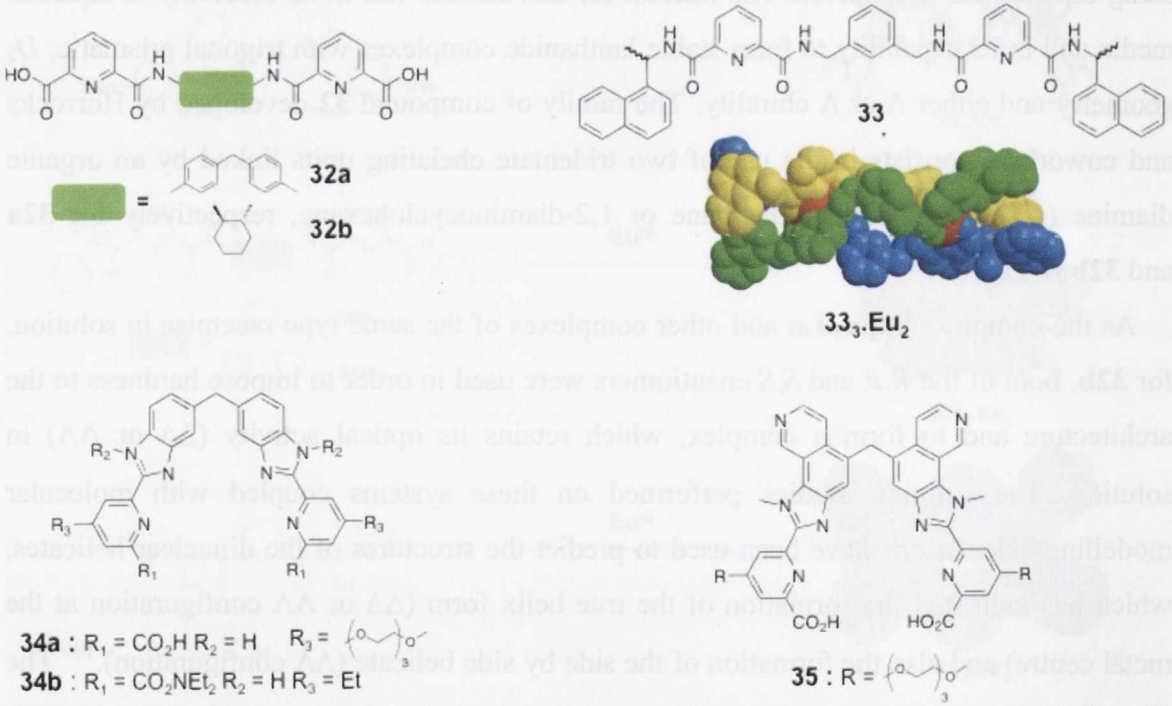


**Figure 1.19:** *Other example of ligand designs, based on pyridinyl functions, for the synthesis of dimetallic triple stranded helicates developed within Horrocks', Bünzli's and our group.*

stable ($\log\beta_{23} \approx 24$-$26$) dimetallic triple stranded helicates using various lanthanide ions. In this study, both lanthanide ions were nine coordinated in a prismatic trigonal $D_3$ symmetry but only **34a-b** and **35**, which contain long polyethoxyethylene chain, were soluble in

water allowing for their utilisation as luminescent in biological media. The helicate **35$_3$.Eu$_2$**, which bears naphatylene chromophores shown to be taken up by the cells by endocytosis and locates into the lysosomes showing a time resolved $Eu^{III}$ emission.[113,114] The functionalisation of $R_1$ has enabled for the formation of multitopic ligand, such as the examples shown in Figure 1.20. The selective modification of the terminal moiety of the ligand **36** by grafting of a benzimidazole at one $R_1$ position and a diethylamide moiety at the other, has allowed the formation of the hetero-bi-lanthanide triple stranded helicates. The research of Piguet and coworkers has demonstrated that the selectivity of the hetero-metallic self-assembly is governed by a combination of electrostatic and inter-strand interactions such as π-π stacking or H-bonding.[83] The selectivity of the hetero-pair is also dependant on the difference in the radius between the two lanthanide ions.

The bimetallic helicates **36$_3$.$^1$Ln.$^2$Ln** were formed with 90% selectivity in solution using $\Delta r$ = 0.1 Å. Consequently, the hetero-lanthanide triple stranded helicate containing the lanthanide pairs **$^1$Ln.$^2$Ln** (where $^1$Ln.$^2$Ln are La.Eu, La.Tb, Pr.Er and Pr.Lu) have been isolated *via* crystalisation from mixture containing equi-molar quantities of $^1$Ln and $^2$Ln. This approach gave also rise to elegant multi-topic systems such as the family of ligand

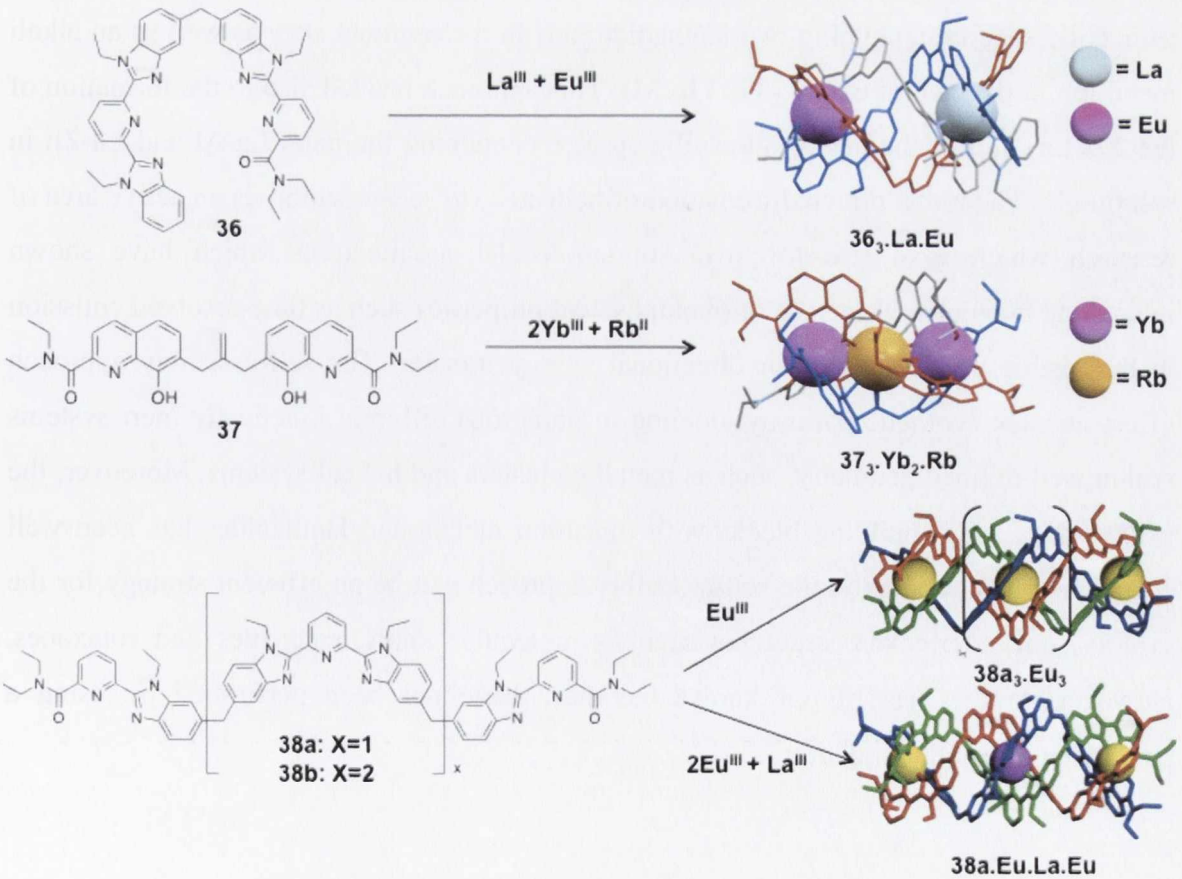


**Figure 1.20:** *Ligands designed to form heteropolymetallic triple stranded helicates based on pyridinyl-benzimidazole (such as **36** and **38a-b**)[9,110] and quinoxyline (**37**) moieties.*[115]

**38a-b** designed on the same principle as **36**, consisting of two terminal tridentate diethylenamidopyridine-benzimidazol binding units separated by one (**38a**) or two (**38b**) dibenzimidazole-pyridine central moieties. The self-assembly of **38a** in the presence of various lanthanide ions gave rise to the formation of homo-metallic tri-lanthanide triple stranded helicate $\mathbf{38a_3.Eu_3}$ in which the central cavity is different to that of the peripheral ones. The formation of such hetero metallic species has also been studied using the lanthanide series and have shown that the difference of affinity of the central and the terminal cavities provides a size discriminative effect with respect to the lanthanide ion radius. This favours the formation of the heterotrimetallic helicates containing the larger metal of the lanthanide pair within the central cavity, as shown by the crystal structure of **38a.Eu.La.Eu** (Figure 1.20).[9,110]

The ligand **37** has been designed by Albrecht *et al.* possesses two tridentate hydroxyquinoline moieties, which are known to be good NIR sensitiser, linked *via* a methylen-alkene bridge. The self-assembly of three ligands forms two nonadentate cavities capable of fulfilling the requirement of lanthanide coordination. In addition, the six alcohols moieties formed a hexadentate cavity, which can bind transition metal ions such as $Al^{III}$ and $Zn^{II}$, and alkali ions. The heterometallic studies have shown the formation of trimetallic species containing two lanthanide ions in the terminal sites as well as an alkali metal ion in the central cavity ($\mathbf{37_3.Yb_2.M}$). This approach has led also to the formation of the $\mathbf{37_3.Ln_2}$ and of the hetero-dimetallic species containing the pairs La-Al and La-Zn in solution.[115] The metal-directed formation of helicates *via* self-assembly is an active area of research which gave rise to novel supramolecular architectures which have shown interesting magnetic, electronic or photophysical properties such as time-resolved emission in the visible or NIR region or directional energy transfer. The self-assembly approach offers an easy synthetic pathway yielding to numerous different kinetically inert systems with a well-defined geometry, such as metallic clusters and helical systems. Moreover, the geometry of small building blocks with transition metals and lanthanides has been well established. Consequently, the self-assembly approach can be an efficient strategy for the synthesis of interlocked structures such as molecular knots, catenanes and rotaxanes. However, to the best of our knowledge these have not been performed by using a lanthanide directed templation.

## I.3. Work described in this thesis

As it has been illustrated within the previous sections, the complexation of lanthanide ions such as $Eu^{III}$ and $Tb^{III}$ offered an interesting approach for the development of lanthanide luminescent probes. It has been illustrated that several strategies can yield to the formation of luminescent complexes for their potential use as chemosensors and contrast agents for imaging. Furthermore, it has also been outlined that the lanthanide ions can be used in order to build functional luminescent self-assembly systems. With this in mind, the main focus of this thesis will be the development of lanthanide luminescent supramolecular architectures.

In the Chapter 2, the formation $Tb^{III}$ complexes with a family of for calix-[4]-arenes alkylated on their lower rim will be investigated. After assessing the photophysical properties of the 1:1 (M/L) complexes, their formation *in situ* will then be investigated using spectrophotometric titrations.

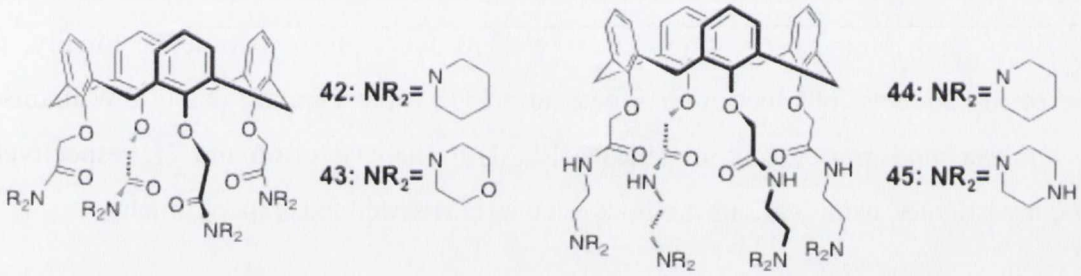


**Figure 1.21:** *Family of calix-[4]-arenes derivatives studied in Chapter 2.*

In Chapter 3, the formation and the investigation *in situ* of the photophysical properties novel monometallic chiral luminescent complexes containing either a chiral naphthyl or tryptophan antenna will be investigated, using different spectroscopic methods such as UV-vis absorption, time-resolved luminescence titrations. The influence of the design of the ligand on the overall chirality of the resulting $Ln^{III}$ complexes will also be studied using CD and CPL analyses.

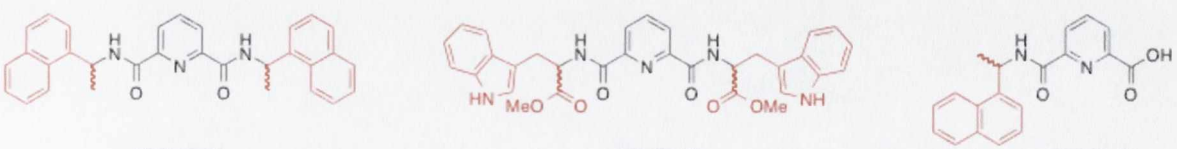

27S (S,S)
27R (R,R)

47L (L,L)
47D (D,D)

51R (L,L)
51S (D,D)

**Figure 1.22:** *Ligands studied in Chapter 3 for the formation of chiral lanthanide luminescent mono-metallic complexes*

In Chapter 4, the synthesis and the characterisation of the two chiral bis tridentate ligand **57S** and **57R** and their corresponding $Eu^{III}$ triple stranded helical complexes will be presented. Once characterised, their photophysical properties will be discussed and the formation *in situ* of the helicates will be investigated using different spectroscopic methods.

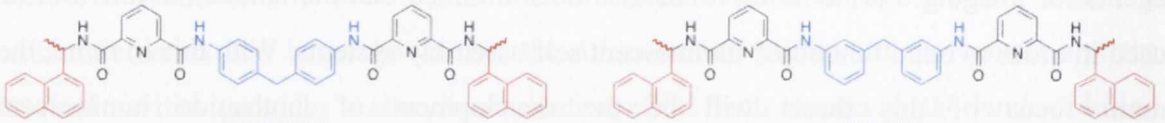

53S (S,S)
53R (R,R)

54S (S,S)
54R (R,R)

**Figure 1.23:** *Ditopic ligands developed in Chapter 4 for the formation of dimetallic triple-stranded helicates*

In Chapter 5, the lanthanide directed synthesis of a [3]-catenane, where each macrocycle is interlocked within the two others will be attempted. Firsty, the $Ln^{III}$-templation of the precursors will be studied using various spectroscopic methods such as $Ln^{III}$ UV-vis and luminescence titrations as well as Job's plot experiments. Finally, the nature of the adducts, obtained after a catenation via triple clipping using a Williamson ether synthesis and ring-closing metathesis (RCM) in the case of **66** and **71**, respectively, will be investigated using various methods such as NMR, and mass spectrometry.

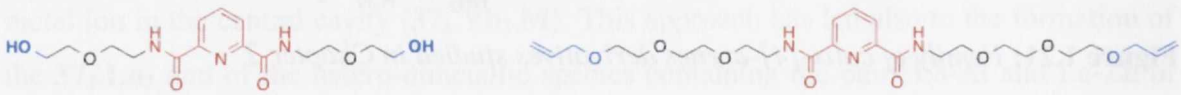

66

71

**Figure 1.24:** *Ligands designed for the formation of [3]-catenane in Chapter 5*

# Chapter 2:

# Calix-[4]-arenes based hosts for $Tb^{III}$

## Chapter 2: Calix-[4]-arene based hosts for $Tb^{III}$

### 2.1 Introduction

As previously mentioned in Chapter I, the chemistry of calixarenes is vast and wide-ranging, finding use across the breadth of supramolecular chemistry, including ion coordination and sensor chemistry.[66,116] These structures, due to their preorganised cavities have also found applications in areas including ion channel mimetics[117] and catalysis.[118] The calixarenes offer several unique features that make them attractive for host-guest chemistry such as the aforementioned preorganisation, due to their rigid phenylic annulus and the two different arrays of derivatisation, as shown in Figure 2.1.

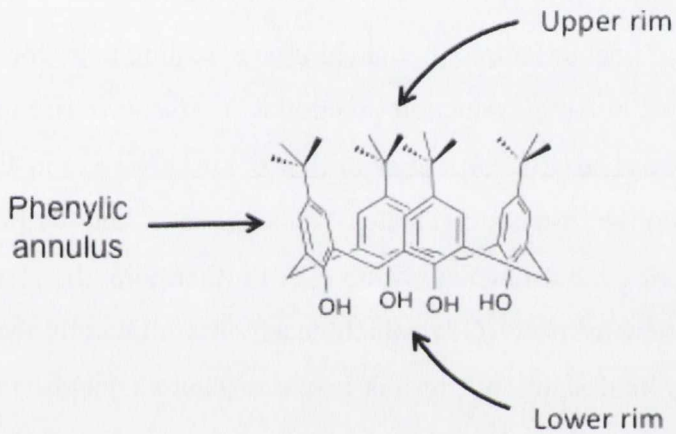


**Figure 2.1**: *Reactivity sites of the tbu-calix-[4]-arene scaffold*

The presence of hydroxyl groups on the lower rim allows an easy functionalisation of the calixarene scaffold *via* alkylation or acylation, whereas the presence of the tert-butyl moiety on the upper rim offers a second wider way of derivatisation. Calix-[4]-arenes derivatives have been utilized for the complexation of lanthanides with the aim of forming luminescent probes emitting in the visible and the NIR region.[73,75] The most popular way of achieving lanthanide binding is the alkylation of the phenol moieties with pendant arms containing carboxylate or amido functional groups, which allow the formation of a flexible cavity, and can host easily lanthanide ions such as $Eu^{III}$ or $Tb^{III}$. However, it has been demonstrated that the sensitization of the lanthanide emission can occur following two different pathways[71] as shown in Figure 2.2: The path A (in red, Figure 2.2) shows in the direct excitation of the calix-[4]-arene in order to populate the excited state scaffold provoking the lanthanide emission *via* energy transfer (E.T).

Due to the high energy level of the $^{1}\pi$-$\pi^*$ and $^{3}\pi$-$\pi^*$ excited state of the phenolic scaffold (in the range of 35-40 $\times 10^3$ $cm^{-1}$ and 25-30 $\times 10^3$ $cm^{-1}$, respectively), the sensitisation of the luminescence of lanthanides such as $Tb^{III}$ is favorable; the energy

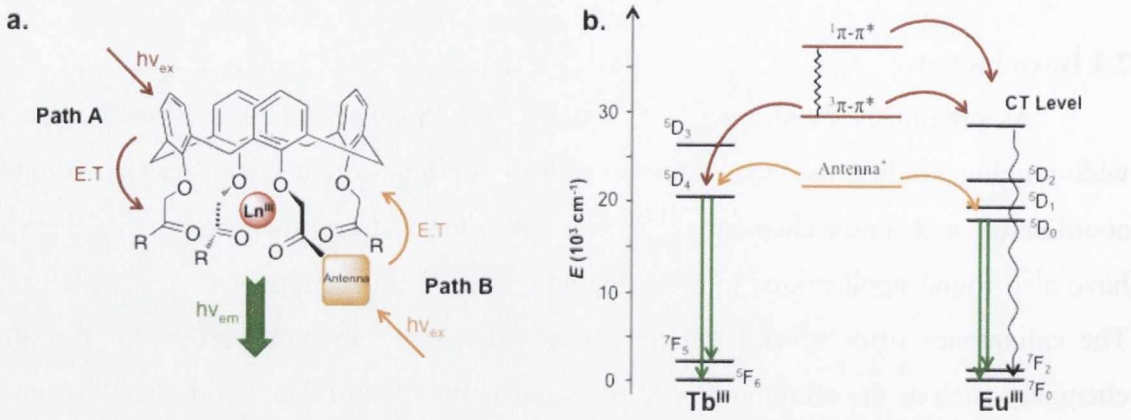


**Figure 2.2**: ***a.)*** *Different pathways leading to the sensitization of europium and terbium: via excitation of the calixarene scaffold (A) and use of another antenna (B).* ***b.)*** *Sensitization mechanism proposed by Shinkai and co-workers.*[71]

accepting levels of the terbium ion matching the requirement for an efficient energy transfer as discussed in the introduction (Section I.2). This gave rise to luminescent probes with high quantum yields (in the range of 10-20%). However, in the case of $Eu^{III}$, the energy gap between the $^3\pi$-$\pi^*$ triplet state of the calixarene and the $Eu(^5D_0)$ is large ($\Delta E \approx 13500\ cm^{-1}$)[71] altering the efficiency of the E.T. Furthermore, the presence of the C=O to europium charge-transfer band (CT), which deactivates efficiently the excited state of the complex to the ground state, and results in poor quantum yields. In order to overcome these issues, the action of another adequate antenna directly linked to the ligand or *via* the formation of ternary complexes- can be used, favoring the population of the lanthanide emissive state *via* Path B (in orange, Figure 2.2).[71] Finally, it has been also well established that different functionalisation can have an influence on the position of the excited states of the ligand and then change the efficiency of the energy transfer from the calixarene to the lanthanide.[29,72] The aim of this chapter was the synthesis and the investigation of the formation of novel terbium luminescent probes based on calix-[4]-arene derivatives previously synthesised by Dr Eoin Quinlan.[119]

**Previous work from Dr Eoin Quinlan: Design and Synthesis of Calix-[4]-arene derivatives for $Ln^{III}$ complexation.**

As discussed within the previous sections, the alkylation of the lower rim of calix-[4]-arene has allowed for the synthesis of efficient ligands for the binding of cationic guests. Following this strategy, the series of calix-[4]-arenes **42-46** was designed and synthesised within the Gunnlaugsson group in collaboration with Dr. Susan Matthews at UEA, UK, in order to provide an octadentate binding pocket capable of hosting lanthanide ions such as $Tb^{III}$.

In this previous work, the annulus of each calixarene was tetra-alkylated at the lower rim with four pendant arms, which provide an overall eight donor environment *via* the use of four phenolic oxygens linked to different amido derivatives such as -piperidine (**42**), -amido-morpholine (**43**), and -piperidine (**44**), amido-ethylen-piperazyl (**45**) -dimethylamine (**46**), respectively. Moreover, the phenolic and the amido moieties were separated by a methylene spacer inducing a better flexibility for the resulting "binding pocket", which was formed with the view of being able to adapt its geometry in order to increase its affinity to the $Tb^{III}$ ion.[119]

The calix-[4]-arene analogues were synthesised in three and four steps respectively for **42-43** and **44-46** from the *p-$^t$Bu*-phenol: First of all, the cyclic tetramer **39** was synthesised in 55% yield following a condensation reaction. Then, the cleavage of the *$^t$Bu* groups of compound **39** was then performed *via* retro Friedel-Craft reaction, yielding the precursor **40** (70% yield), which is the base of the synthesis of each calix-[4]-arene analogues. The first generation of ligand, calixarenes **42** and **43,** which bear shorter pendant arms, were synthesised *via* Williamson ether-synthesis with the appropriate α-bromoacetamide producing the ligands **42** and **43** in 48% and 66% yields, respectively. The calixarenes **44**, **45** and **46**, which contain longer and more flexible pendant arms, were synthesized following the route shown in Figure 2.3. The tetra-ester **41** was first isolated in high yields

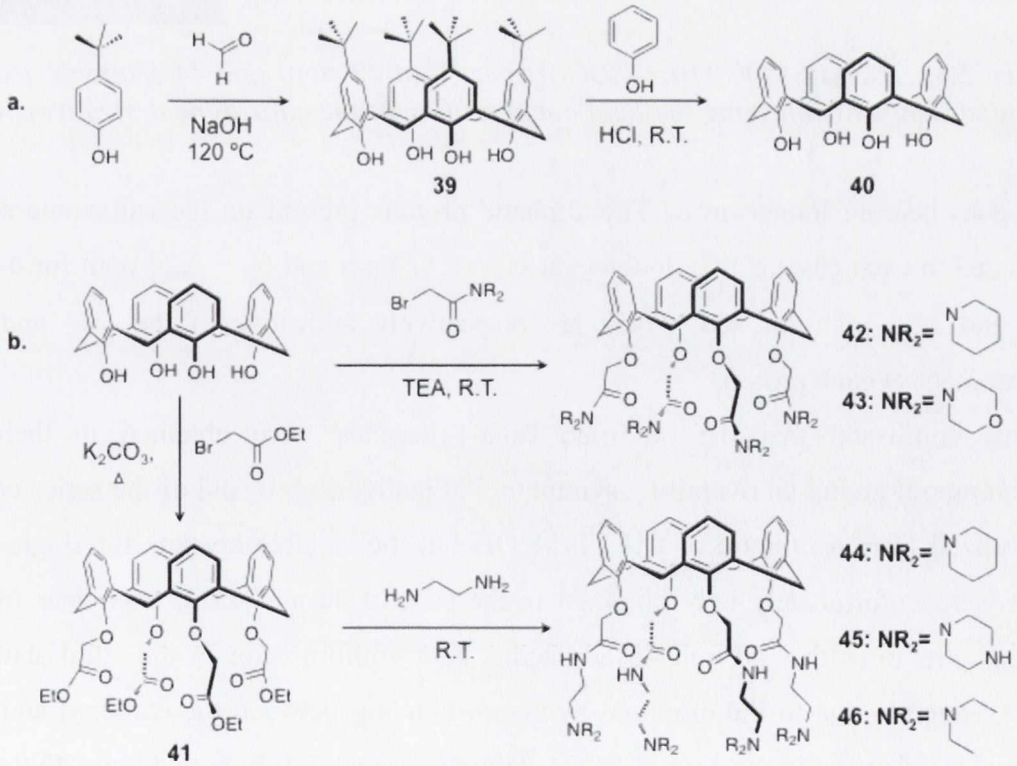


***Figure 2.3:a)*** *Synthesis of the precursor calix-[4]-arene,* ***b)*** *synthesis of the family of derivative* ***41-46*** *alkylated upon their lower rim.*

(71%) after reacting compound **40** with ethyl-bromoacetate. Then, the nucleophilic substitution of the ethoxy groups of **41** with the corresponding primary amine gave rise to the modified calix-[4]-arenes **44, 45** and **46** in 44%, 78% and 62% yields respectively.

Each ligand has been characterized using conventional spectroscopic methods and in each case, the $^1$H-NMR resonances (in $CDCl_3$) have been clearly attributed: For example, the aromatic protons coalesce as a multiplet between 6.60 and 6.70 ppm and the protons in α-position of the amido moiety, which are subjected to a strong shielding due to the presence of the phenolic ether and the amido moiety, were observed as a singlet around at $\delta_H$ = 4.90 ppm for each of the ligands with short pendant arms and at $\delta_H$ = 4.51 ppm for the

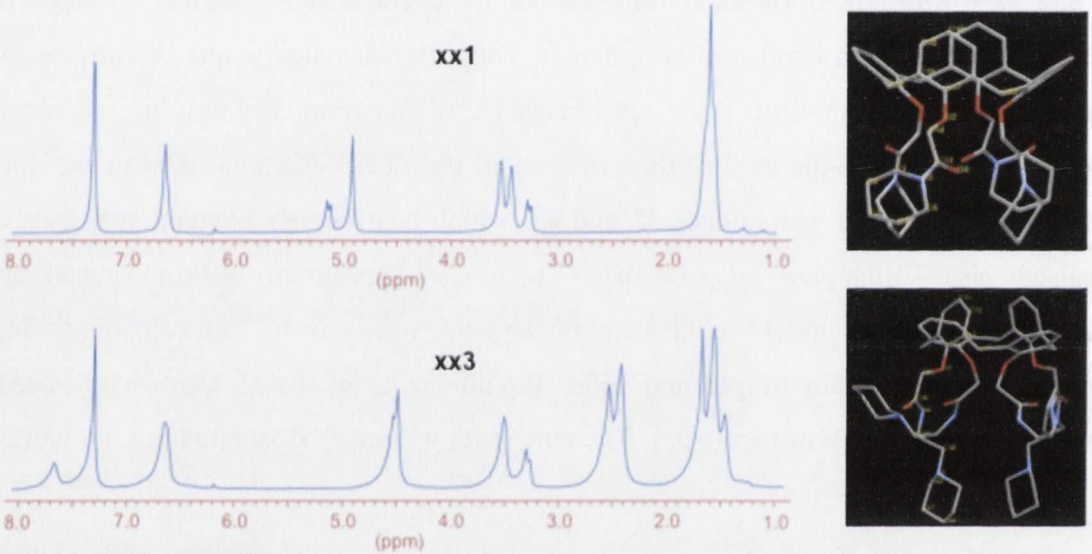


**Figure 2.4:** *$^1$H-NMR (400 MHz; $CDCl_3$) spectra of **42** (top) and **44** (bottom) and XRD crystal structures confirming the boat configuration of the calixarene derivatives, **44** and **45***

analogues bearing longer arms. The aliphatic protons present on the calixarene scaffold resonated in each case as two doublets at $\delta_H$ = 5.11 ppm and $\delta_H$ = 3.26 ppm for **44** ($\delta_H$ = 4.53 and 3.26 ppm for **45**), which are respectively indicative of the *exo-* and *endo-* environment of each proton.

This confirmed that the modified calix-[4]-arenes were obtained in their cone configuration, giving an overall $C_4$ symmetry.[66] Finally, each ligand of the series could be crystallized from a mixture of $CH_2Cl_2$/MeOH but the suitable crystals for single crystal XRD were unfortunately only obtained in the case of **44** and **45**. It was clear from the crystals structures that **44** and **45** adopted a boat conformation in the solid state. This effect, which is due to the observed hydrogen bonding between the carbonyl and amido protons, is enhanced in the case of **45**, as shown in Figure 2.4. In both **44** and **45** the solid-state structure showed an octadentate cavity of 6.4 Å (measured diagonally between the coordinating amido oxygens) suitable for the inclusion of a cationic guest such as $Tb^{III}$.[119]

In summary, the two novel synthetic pathways, discussed above for the functionalisation of calixarenes, were readily accessible and provide further support for the formation of different host-guest systems. With the view of developing terbium based luminescent probes, each ligand, provides an octadentate cavity at ideal distance from the calixarene scaffold to allow the sensitisation of terbium emission *via* excitation of the phenolic moiety. Consequently, the synthesis and the photophysical studies of the complexes **42-45.Tb** is the objective of the next section.

## 2.2 Synthesis and photophysical studies of luminescent Host-Guest systems: 42-45.Tb

### 2.2.1 Synthesis and characterisation of the complexes 42-45.Tb

As previously illustrated in Section 2.1, the sensitisation of the $Eu^{III}$ emission via excitation of the calixarene scaffold can be quite challenging due to its CT energy level.

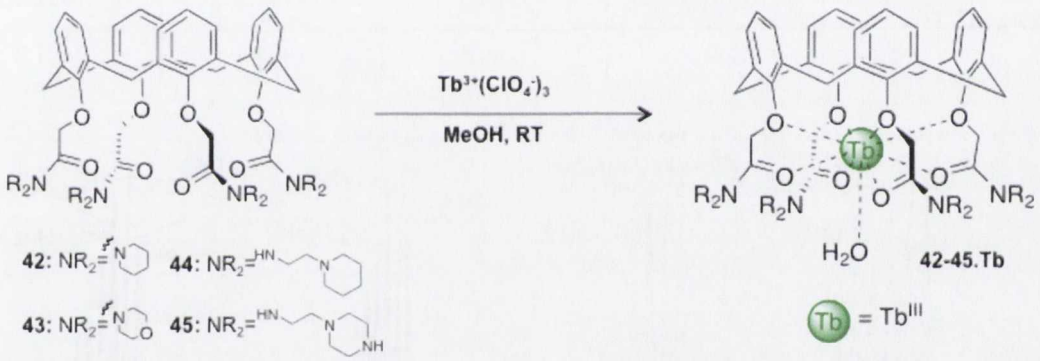


**Figure 2.5:** *General procedure for the synthesis of the complexes* ***L.Tb*** *(L = **42-45**)*

For this reason, our investigation will be focused on the utilisation of $Tb^{III}$, which can give rise to more efficient luminescent probes. The $Tb^{III}$ complexes **42-45.Tb** were synthesised following the general procedure shown in Figure 2.5: The calixarenes **42-45** were refluxed in the presence of an equimolar quantity of $Tb(ClO_4)_3$ in $CH_3OH$, as shown in Figure 2.5. The complex **42.Tb** was obtained in 67% yield as an off-white solid, precipitating out of solvent while the complexation occured. However, the complex **43.Tb**, which bears amido-morpholine terminal moieties, and its longer arm analogues, **44-45.Tb** showed a better solubility in MeOH, and were consequently isolated in quantitative yield (≈ 90-99%) after 12 hours, *via* precipitation from diethyl ether.

The characterisation of the complexes **L.Tb** (L = **42,45**) was achieved using conventional spectroscopic methods. Electrospray mass spectrometry analyses were performed in ESI+/ToF mode (MeOH) and each of the complexes **L.Tb** (L = **42, 43**) were detected as a mono- and di-charged fragment corresponding to $M^{3+}$ + 2 $ClO_4^-$ and $M^{3+}$ + $ClO_4^-$ ions, respectively. The complexes **L.Tb** (L = **44, 45**) containing longer arms were

found as a mono-charged ion corresponding to $M^{3+} + 3Cl^- + K^+$ (Table 2.1). Furthermore, for each one the characteristic isotopic distribution pattern of monometallic terbium complexes, shown in Figure 2.6, matched that of the calculated pattern indicating the successful formation of the 1:1 stoichiometry **Ln:L** complexes, in all cases.

**Table 2.1:** *Yield of complexation after purification and summary of the ions found in ESI+ Mass spectrometry*

| L.Tb (L= ) | | 42 | 43 | 44 | 45 |
|---|---|---|---|---|---|
| % yields | | 69 % | 99 % | 97 % | 95 % |
| +2 Charged | Calc. | **42.Tb + 2 $ClO_4^-$** 591.6 | **43.Tb + 2 $ClO_4^-$** 596.6 | N.O. | N.O. |
| | Found | 591.1 | 596.1 | N.O. | N.O. |
| +1 charged | Calc. | **42.Tb + 2 $ClO_4^-$** 1281.3 | **43.Tb + 2 $ClO_4^-$** 1289.2 | **44.Tb+3$Cl^-$+$K^+$** 1397.5 | **45.Tb+3$Cl^-$+$K^+$** 1401.4 |
| | Found | 1281.8 | 1289.8 | 1397.4 | 1401.2 |

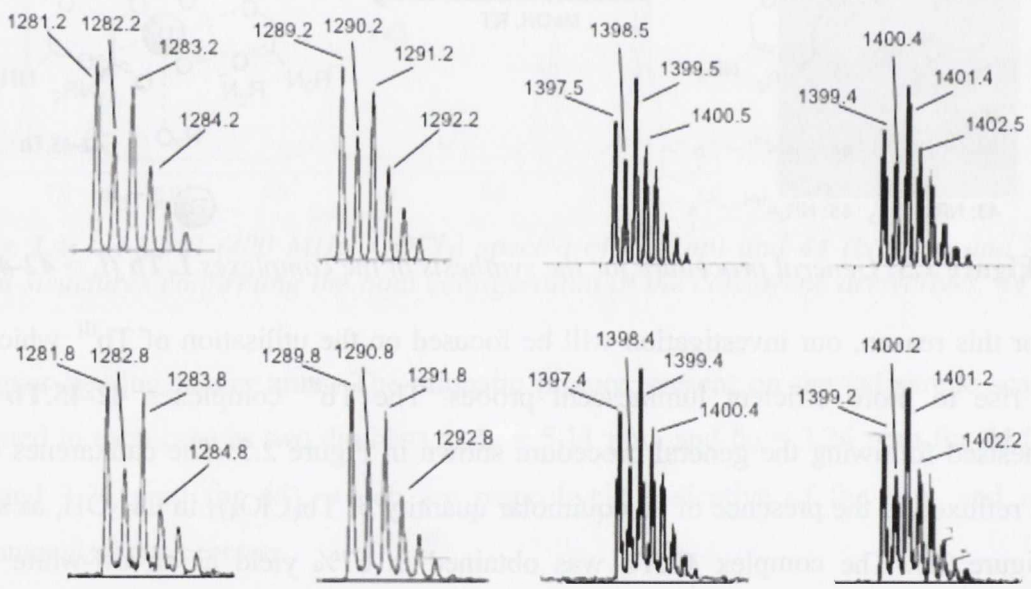


**Figure 2.6:** *Isotopic pattern calculated (top) and found (bottom) for the mono-charged fragment of the complexes* ***L.Tb***

The configuration of the complexes **L.Tb** was further investigated using $^1H$ NMR spectroscopy ($CD_3CN$, 400 MHz). In each case, the $^1H$ NMR spectrum (Figure 2.7) showed a high symmetry level suggesting that the resulting complexes possess $C_4$ symmetry, which is indicative of the retention of the *cone* configuration of the calixarene upon complexation to the lanthanide ion. However, the lack of shifts in all of these spectra is quite surprising as a pseudo-contact shifting is expected upon $Tb^{III}$ complexation, instead

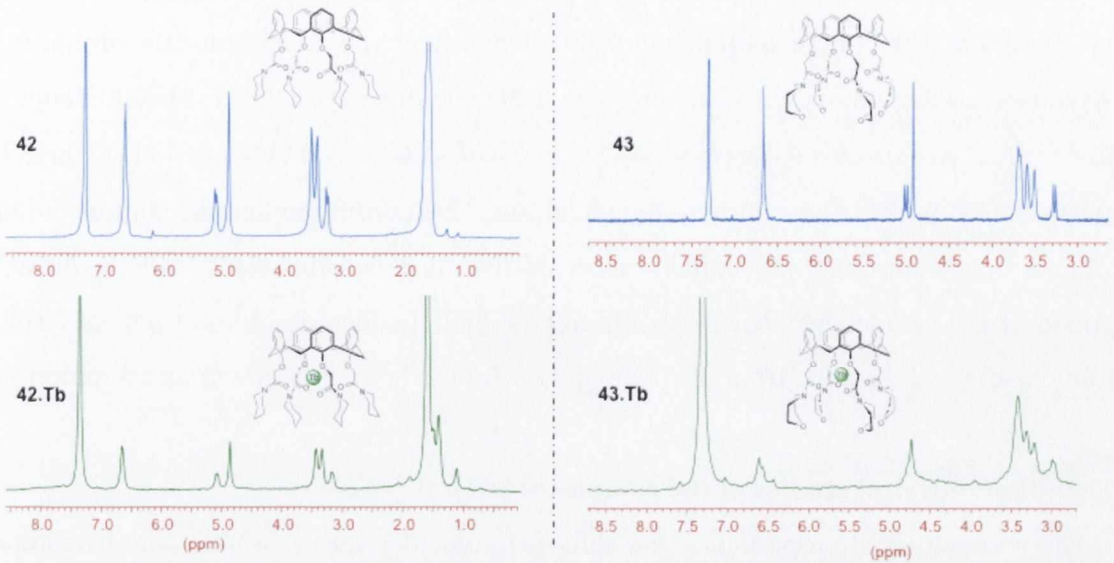


**Figure 2.7:** *$^1$H-NMR ($CD_3CN$, 400 MHz) of **42** and **45** (blue) and their resulting terbium complexes **L.Tb** (Green)*

of the broadening effect observed. However, the broadening in the $^1$H resonances of the ligand upon complexation such as for the protons in the α-$CH_2$ of the chain, could indicate that these protons are close to the metal ion. Furthermore, the significant resonance of the phenylic protons of the annulus and those of the terminal moieties experienced a weaker effect, suggesting that the terminal moieties are lying below the terbium centre.

Finally, the *endo-* protons of the methylene bridge of the calixarene scaffold broadened more intensively than those in the *exo-* position, which confirmed that the terbium ion was hosted below the calixarene scaffold, in the cavity formed between the 8 oxygen atoms provided by the pendant arms (as shown with the proposed binding mode in the inset of Figure 2.7 and Figure 2.13).

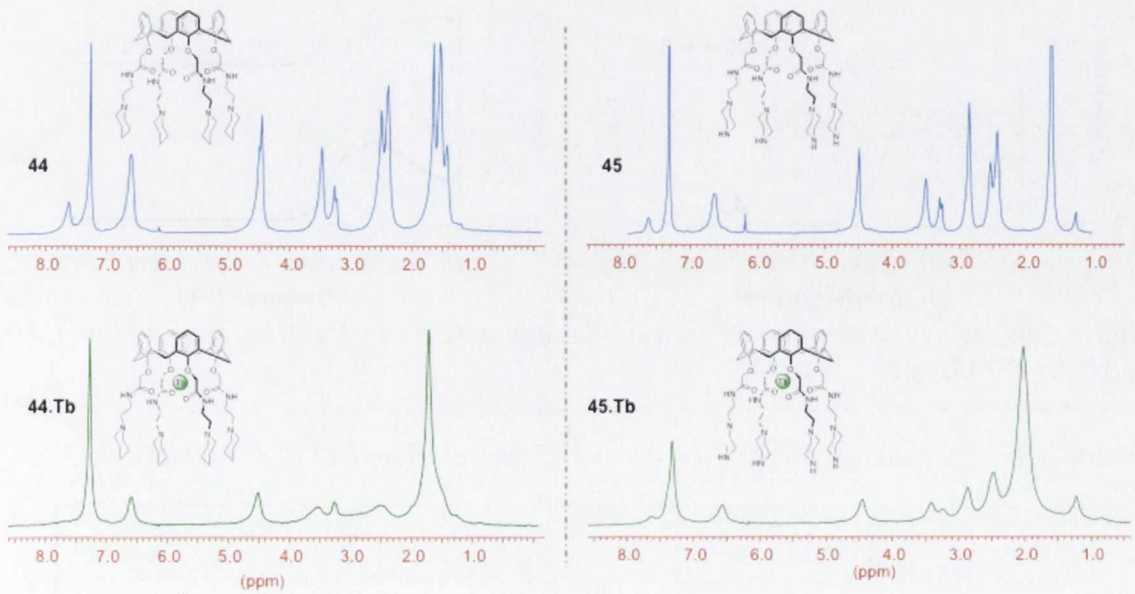


**Figure 2.8:** *$^1$H-NMR in $CH_3CN$ of **44** and **45** (blue) and their resulting terbium complexes (Green)*

In the case of the complexes **44.Tb** and **45.Tb,** shown in Figure 2.8, a similar behaviour was observed: The complexation gave rise to a significant broadening for the proton in the α-positions of the amide, while the protons of the annulus experienced weaker changes. A strong effect has also been observed in the chemical shifts of the ethylene linker ($\delta_H$ = 2.45 ppm), suggesting their proximity to the metal ion. This confirmed that the complexation of terbium occurs through the collaboration of the four pendant arms, which allow the formation of an adequate cavity to efficiently bind lanthanides ions, such as terbium, sitting at an ideal distance from the phenylic scaffold to be sensitised *via* its excitation.

### 2.2.2. Photophysical studies of the complexes L.Tb (L= 42-45)

The photophysical properties of the calix-[4]-arene derivatives **42-46** were investigated in solution. In each case, the UV-vis absorption spectrum showed a broad absorption band centred at $\lambda_{max}$ = 271 nm, which was characteristic of the π→π* transitions of the aromatic scaffold of the calixarenes.

The great similarity between UV-vis absorption spectra of **42** (Figure 2.9), which bears terminal piperidine moieties, and **43**, with morpholines, showed clearly that the nature of the tertiary amine has little influence on the position of the accepting excited state of the ligand. This is also confirmed by the spectra of **43** and **44**, which both have the same absorption band at 271nm. The molar extinction coefficients $\varepsilon_{271}$ were determined for each of the ligands and are summarized in Table 2.2. The analogues **44** and **45** possess lower

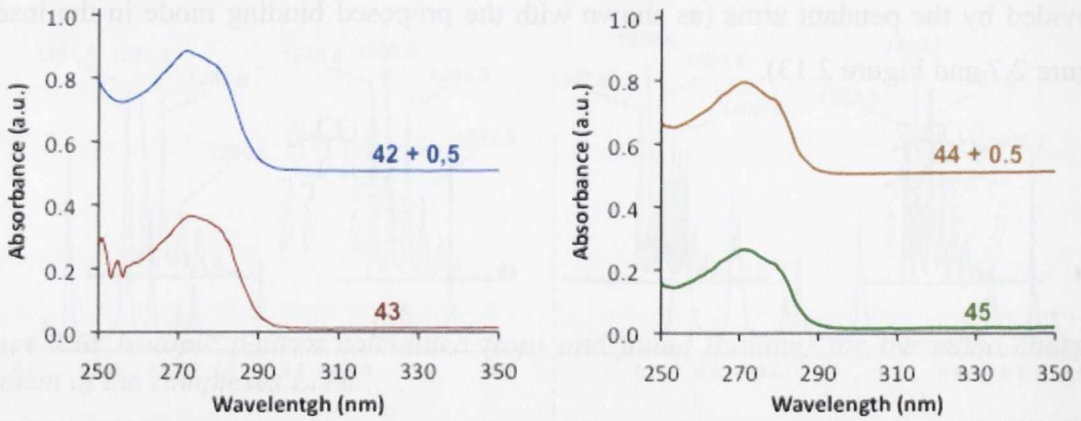


**Figure 2.9:** *UV-vis absorption spectra of the ligand **42-44** in MeOH (1,3,4) and in 4:1 DMSO/$H_2O$ (**43**) at C =2×10$^{-4}$M*

**Table 2.2:** *Absorptivity of ligand **42**, **44** and **45** in MeOH and **43** in 4:1 DMSO/$H_2O$*

| L | 42 | 43 | 44 | 45 |
|---|---|---|---|---|
| $\varepsilon_{271}$ | 2038.8 | 2006.3 | 1458.4 | 1388.3 |

coefficients (of *c.a.* 1500 $cm^{-1}M^{1}$ range) than ligand **42** and **43** ($\varepsilon_{271}$ in the range of 2500 $cm^{-1}M^{-1}$). This can possibly be due to the different geometry adopted by the calixarene derivatives containing longer pendant arms.[29] The excitation of the calixarene scaffold of ligand **42-45,** at 281 nm, gave rise to a weak broad fluorescence emission band centred at $\lambda$= 416 nm, which was less intense for ligands **44** and **45** than for **42** and **43**. This suggests that the majority of the energy absorbed by the ligand is released *via* non-radiative deactivation from either the singlet or the triplet excited states.

The UV-vis spectroscopic analysis of the complexes **L.Tb** have shown that in the case of the analogues **42** and **43** (bearing short pendant arms), the absorption band at $\lambda_{max}$ =271 nm, experienced a hypochromic effect upon complexation to terbium. The molar extinction coefficient of the complexes **42.Tb** and **43.Tb** decreased by *c.a.* 69.2% and 25.6% respectively in comparison to those obtained for the ligands. However, the UV-vis absorption spectra of the derivatives **L.Tb** (**L = 44,45**) showed only negligible changes in absorptivity, in $\Delta\varepsilon_{271}$ <10% range (respectively 5.9 and 4.7% for **44.Tb** and **45.Tb**). The

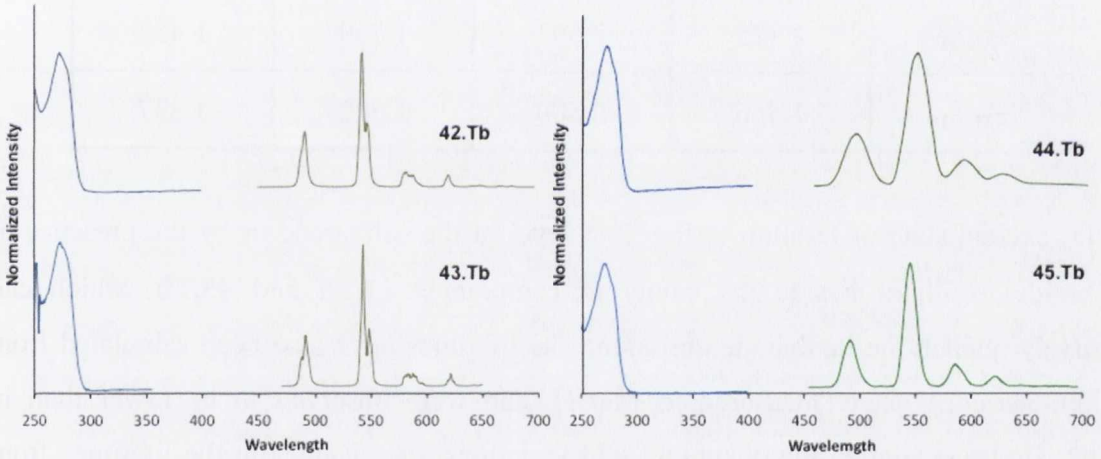


**Figure 2.10:** *Excitation (Blue; λem = 545 nm) and terbium luminescence spectra (green λex =281 nm) of the complexes* ***L.Tb****. in MeOH at C =2×10$^{-4}$ M.*

excitation of the calix-[4]-arene scaffold of each complex **L.Tb**, gave rise to the long lived terbium emission, Figure 2.10, and the recorded excitation spectra matched the UV-vis absorption bands of the corresponding ligand.

This confirms that the emission sensitisation process occurs *via* energy transfer from the excited states of the calixarene phenolic scaffold to the terbium centre.[25] The luminescence decays were measured for each complex in MeOH and in $d_4$-MeOD and were fitted to a mono-exponential decay $I = A_1\exp(-1/\tau_1)+C$ (appendix 2.1), which is indicative of the presence of only one configuration of luminescent cavity in solution. The lifetimes of the complexes **42,43.Tb** excited states in MeOD were longer ($\tau \approx$ 2.3-2.6 ms) than for **44, 45.Tb** ($\tau \approx$ 1.5-1.7 ms). It can be concluded from these results that the non-

radiative deactivation of the structure's excited states is more efficient for the complexes **44.Tb** and **45.Tb**, due to their longer pendant arms. This behaviour has been also illustrated by the luminescence quantum yield measurements, which in the case of **42.Tb** and **43.Tb** resulted in a highly luminescent terbium centred emission with $\Phi$ = 19 %[29,71] and $\Phi$ = 18.6 %, respectively, whereas in the case of **44.Tb** and **4.Tb** the complexes were significantly less luminescent ($\Phi$ < 1%, Table 2.3).

This difference in behaviour between the two families can be due to back transfer from

**Table 2.3:** *Summary of the photophysical properties of the complexes* ***L.Tb*** *(L=**42-45**) in MeOH*

| Complex | 42.Tb | 43.Tb | 44.Tb | 45.Tb |
|---|---|---|---|---|
| $\varepsilon_{271}$ | 627.2 | 1891.9 | 1289.2 | 1206.1 |
| $\phi$ | 19.0% | 18.6% | 0.5% | 0,2% |
| $\tau_{MeOD}$ | 2.325 | 2.593 | 1.759 | 1.457 |
| $\tau_{MeOH}$ | 1.566 | 2.500 | 1.322 | 1.337 |

the $^5D_n$ excited state of terbium to the $^3\pi\pi^*$ level of the calixarene or by the presence of NH amide oscillator beside the cavity in compounds **44.Tb** and **45.Tb**, which can effectively quench the lanthanide emission. The lifetimes have also been calculated from the luminescence decay measured in MeOH, and were observed to be lower than in MeOD. However, unlike the quantum yield variations, the changes in the lifetimes from deuterated to non-deuterated methanol seemed to be more dependent on the nature of the terminal moiety rather than the length of the pendant arms. Indeed, the luminescence lifetimes of **42.Tb** and **44.Tb** experienced a dramatic decrease in MeOH compared to that measured above in MeOD (*c.a.* $\Delta\tau$ = 32.7% and 24.9% respectively), whereas the lifetimes recorded for **43.Tb** and **45.Tb** were insignificantly affected ($\Delta\tau$ < 10 %). This can be due to the presence of solvent molecules bound to the metal core in order to fulfil the coordination requirement of terbium. In the case of the systems **43.Tb** and **45.Tb,** the last coordination site of terbium could be possibly filled by the extra donor atoms present on the terminal moiety through the morpholinyl and the piperazyl functions. Unfortunately, the number of solvent molecules bound to the terbium ion could not be determined accurately due to the uncertainty (± 1.5) of the formula enunciated by Steemers *et al*,

which does not take into consideration the potential back energy transfer $^5D_n \rightarrow {}^3\pi\pi^*$ in competition with the lanthanide centred emission.[29]

It can be concluded from these results that the calixarenes ligands **42-45** are suitable for terbium complexation and for the sensitization of its luminescence. It has been also illustrated that the nature of the pendant arms can have a significant effect on the photophysical properties of the resulting $Tb^{III}$ complexes, such as the quantum yields and the luminescent lifetimes were more affected by the size of the pendant arms rather than by the nature of their terminal amine moiety of **43** and **45**. However, the presence of extra donor atoms on the terminal moiety seems to influence the configuration of the binding site, which could possibly shield the access to the metal centre from solvent molecules.

### 2.2.3. Investigation of the formation of the complexes L.Tb *in-situ*

#### 2.2.3.1 Study of the formation of the complexes L.Tb (L= 42, 43) *in situ*

In order to further investigate the formation of the luminescent complex systems **L.Tb**, and to study what influence the design of these ligands has on the host-guest process, the formation of the complexes **L.Tb** (L = **42-45**) were also studied *in situ*, in MeOH, by monitoring the changes of the UV-vis absorption spectra and in the time delayed emission (delay = 0.1 ms) of the complexes while varying the concentration of terbium perchlorate salt, except in the case of **43**, which had poor solubility in methanol, for which a 4:1 DMSO/$H_2O$ mixture was used as solvent media.

The changes in the absorption spectra of **42** are shown in Figure 2.11a. The UV-vis absorption band at $\lambda$ = 271 nm of **42** experienced a hypochromic effect, which reached a plateau after the addition of 0.7 equivalents of terbium. This can be indicative of the formation of the $\mathbf{42_2.Tb}$ at low concentration of $Tb^{III}$. This effect was also seen by the results obtained in the luminescence titrations (Figure 2.11b), where the terbium luminescence of the complex became apparent, up to the addition of 0.7 equivalents of terbium perchlorate. This confirmed the initial formation of the 1:2 (M/L) stoichiometric species followed by a displacement of the equilibrium in solution towards the 1:1 species.

The changes obtained in the spectroscopic properties of **43** upon the variation of terbium concentration were different to that seen above and are shown in Figure 2.12. Firstly, in the 4:1 DMSO/$H_2O$ solvent system, no major changes were seen in the UV-vis absorption spectra upon terbium complexation. However, like in the case of ligand **42**, the lanthanide luminescence is successfully switched on upon the addition of 0→25 equivalents of $Tb^{III}$.

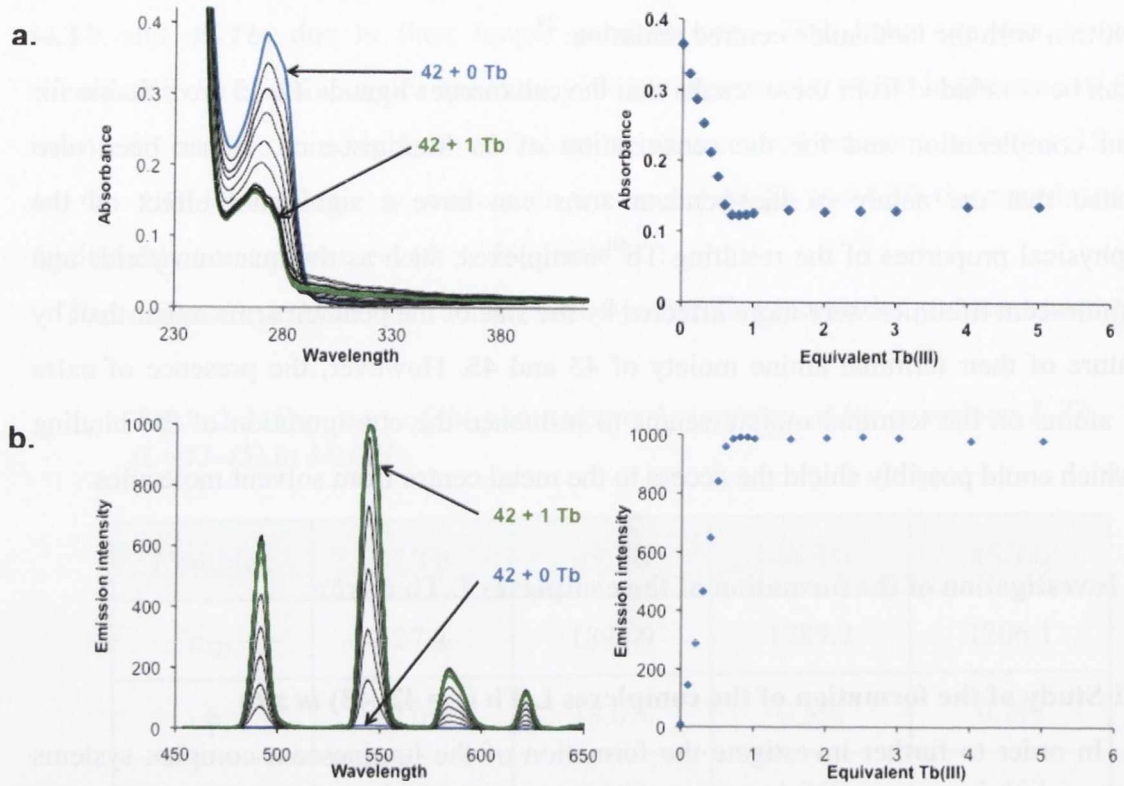


**Figure 2.11:** *Changes observed in the UV-vis spectrum (a) and emission spctrum (b) titrating* ***42*** *upon the addition of* $Tb(ClO_4)_3$ *in MeOH* $C = 2\times10^{-4}M$

Initially, the luminescence intensity increases efficiently upon the addition of 1 equivalent of $Tb^{III}$, which can be explained by the formation of the 1:1 L/Tb stoichiometry species also observed in the case of **42**. The changes were then less pronounced upon the

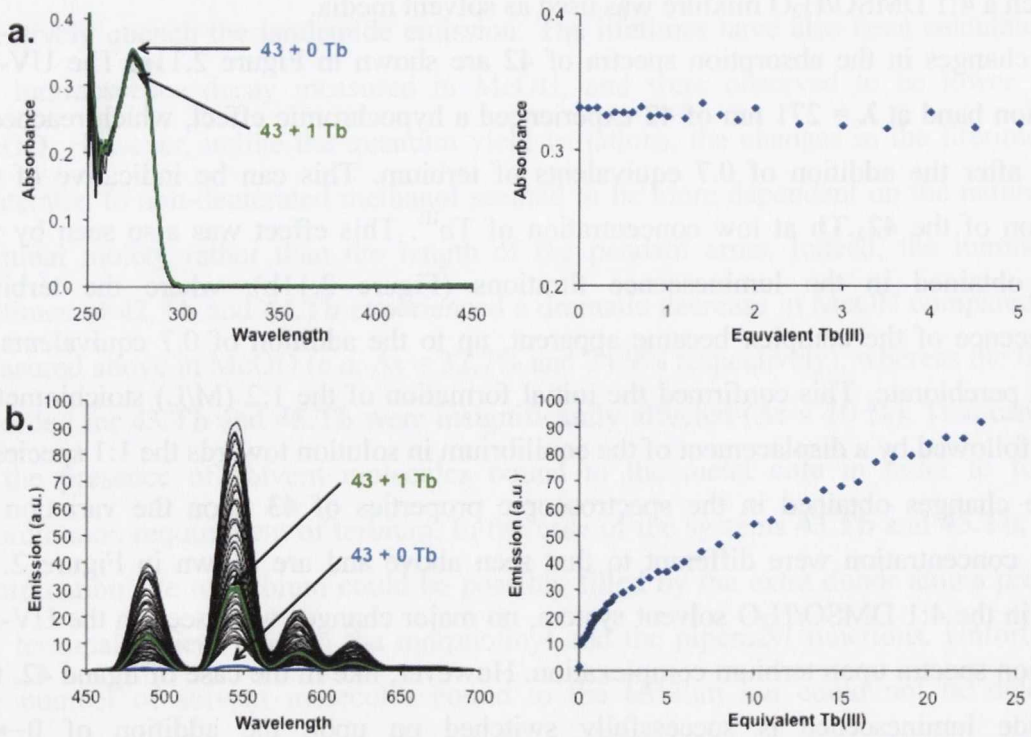


**Figure 2.12:** *a) Changes observed in UV-vis spectum (a) and in the emission (b) titrating* ***43*** *with* $Tb(ClO_4)_3$ *in 4:1 DMSO/*$H_2O$ $C = 2\times10^{-4}M$

addition of $Tb^{III}$ ranging from 1 to 2 equivalents and where the luminescence evolution adopted a linear increase proportional to the quantity of $Tb^{III}$ added, which can be due to the luminescence of $Tb^{III}$ perchlorate in DMSO. This indicated the formation of the bimetallic species **43.Tb$_2$** at higher lanthanide concentration. The formation of the 2:1 M/L species, which was not observed in the case of ligand **42**, can occur due to the presence of the four extra oxygen atoms provided by the morpholine terminal moieties, which can

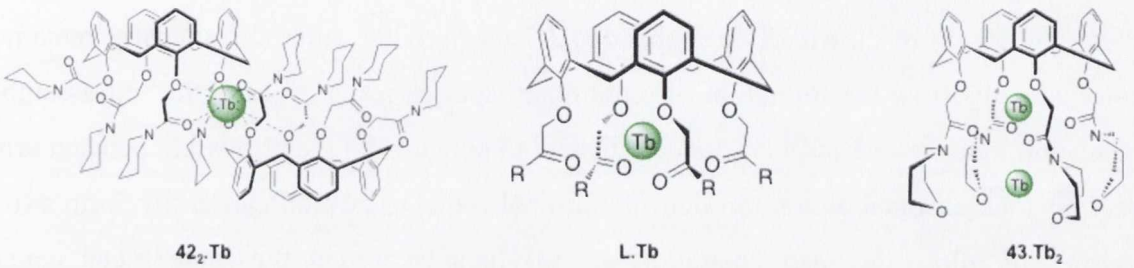


**Figure 2.13:** *Proposed binding mode for the 1:2, 2:1 and 1:1 stoichiometric complexes, illustrated by the examples of* ***42*** *and* ***43***

form a secondary cavity capable of hosting another terbium ion as shown on the proposed binding mode in Figure 2.13. The complexation studies of **43** against terbium triflate have also been performed in a mixture 9:1 MeOH/DMSO and resulted in the same pattern.

### 2.2.3.2 Study of the formation of the complexes L.Tb (L= 44-45) *in situ*

The complexation of $Tb^{III}$ by ligand **44-45** has also been investigated in MeOH varying the quantity of $Tb(ClO_4)_3$ in solution from 0 to 20 equivalents. In each case the UV-vis absorption spectrum of the ligand remained unchanged, as already observed during the last section and shown in appendix 2.2. Also, the $Tb^{III}$ luminescence was switched *on* in the presence of lanthanide ion, indicative of the $Tb^{III}$ complexation. In the case of compound **44** (Figure 2.14), the emission intensity increases upon the addition of terbium salt and

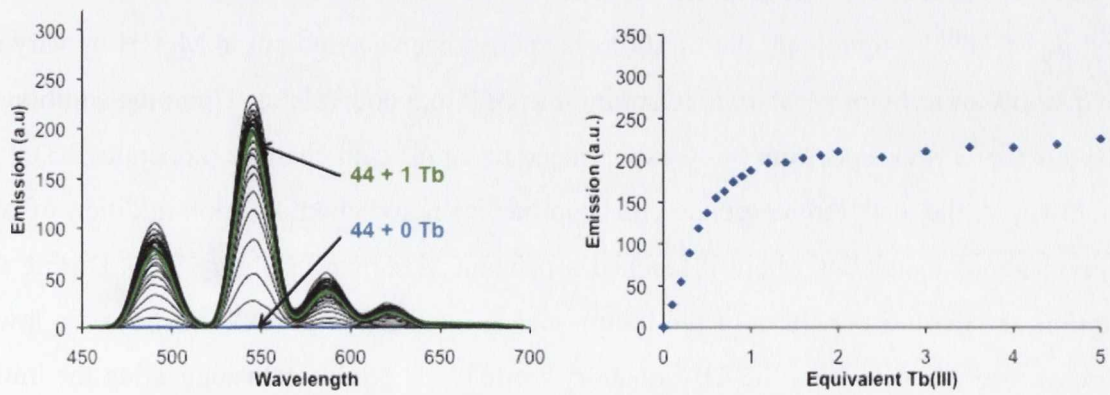


**Figure 2.14:** *Changes in the $Tb^{III}$ emission furing the titration of* ***44*** *versus $Tb(ClO_4)_3$ in MeOH C = $2\times10^{-4}$M*

reaches a plateau in the presence of one equivalent of metal suggesting the main formation of the 1:1 species **44.Tb**, in solution. At high concentrations of terbium, the emission intensity was weakly enhanced in proportion to the quantity of metal added, which is due to the luminescence of terbium directly excited on its UV-vis absorption band at 271 nm.

While varying the equivalents of terbium from 0 to 20, the behaviour of the luminescence of **45** followed a different pattern than the other complexes as demonstrated in Figure 2.15. Firstly, no significant changes were observed in the UV-vis absorption spectrum of **45** as shown in the appendix 2.3 the terbium emission intensity remained constant suggesting the formation of preliminary species resulting from the self-assembly of several ligands with terbium. Indeed, ligand **45** contains long and flexible pendant arms bearing four nitrogen atoms through its terminal moieties, which can easily form extra-cavities or allow the interpenetration of two ligands around the same metal centre. However, upon further addition of $Tb^{III}$ the displacement of the complexation equilibrium

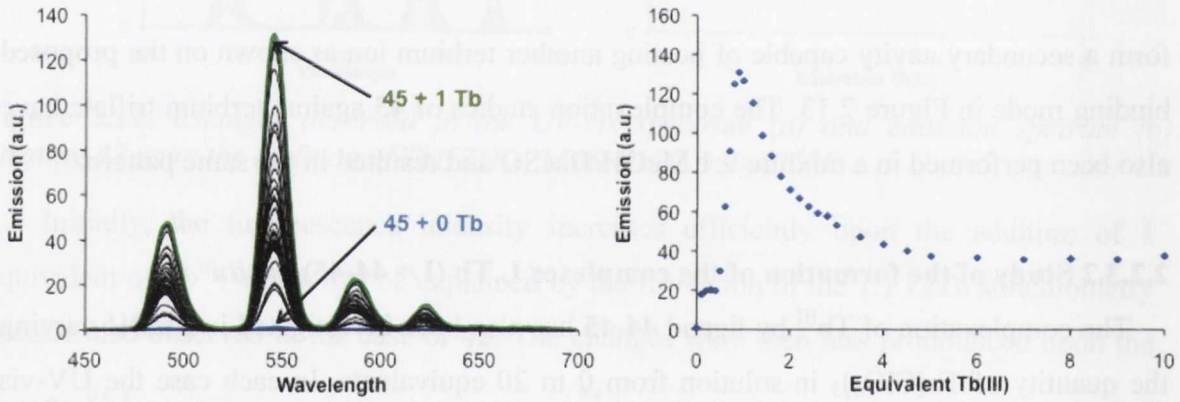


**Figure 2.15:** *Changes observed in the $Tb^{III}$ luminescence for the titration of **45** with $Tb(ClO_4)_3$ in MeOH $C = 2\times10^{-4}M$*

towards the stable formation of the host-guest system **45.Tb** was observed by the large increase in the terbium emission.

In order to further investigate the influence of the diethylamine terminal moieties on the binding of $Tb^{III}$ by ligand **46**, the titrations have also been carried out in MeOH by varying the quantity of terbium perchorate in solution from 0 to 5 equivalents. Upon the addition of terbium, the UV-vis spectrum of **46** experienced no significant changes (appendix 2.3).

However, the $Tb^{III}$ luminescence emission has been switched on upon addition of two equivalents of metal salt where it reached a plateau, as shown in Figure 2.16. During the titration, the evolution pattern of the luminescence intensity (Figure 2.16) showed a lower increase rate when varying the $Tb^{III}$ quantity from 1 to 2 equivalents suggesting the initial formation of the **46.Tb** and the displacement of the speciation equilibrium towards the dimetallic species **46.$Tb_2$**.

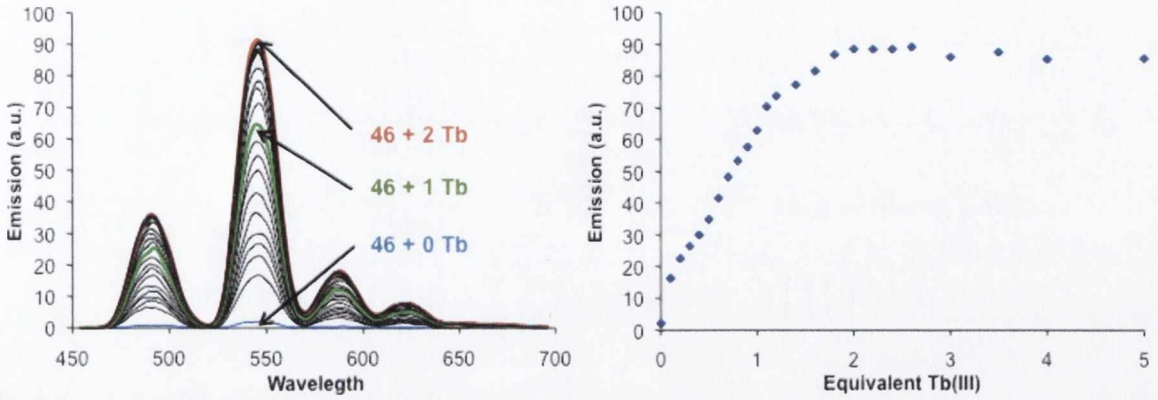


**Figure 2.16:** *Changes in the $Tb^{III}$ emission for the titration of* ***46*** *with $Tb(ClO_4)_3$ in MeOH $C = 2\times10^{-4}M$*

Despite the minor influence that the terminal moiety seemed to have on the photophysical properties of the complexes **L.Tb** (L = **42-46**), the binding process was highly affected by the nature of the four pendant arms. The preliminary spectroscopic studies have demonstrated the presence of the species **L.Tb** in solution and the potential formation of other different topologies.

### 2.2.3.3 Calculation of the binding constants of the complexes L.Tb

With the purpose of highlighting the complexation process, the above titrations were fitted. The speciation plots and the binding constants relative to the formation of each species have been determined using SPECFIT® from the definition of the global complexation process, which corresponds to the general equation (eq.1 with M representing the Ln and L the ligand).

$$nL + mM \xrightarrow{\beta_{mn}} L_nM_m \qquad \beta_{mn} = \frac{[L_nM_m]}{[L]^n[M]^m} \qquad \textbf{Eq. 1}$$

However, the factor analysis usually shows the presence of several different luminescent species. In most cases discussed during this section, the model utilised takes into account two or three different luminescent species namely the metal/ligand, 1:1, 2:1 or 1:2 species. Consequently, the data was fitted following the non-linear least squares method utilizing the set of equations (Eq. 2-4), which allows the estimation of the step-by-step binding constant $K_{mn}$ for each different species. Thus, the relation (Eq.5) linking the global constant $\beta_{nm}$ with the step-by-step constant $K_{nm}$ of each species can be deduced from the correlation between the equations Eq. 1-4 as shown below:

$$L + M \xrightarrow{K_{11}} LM \qquad K_{11} = \frac{[LM]}{[L][M]} \qquad \textbf{Eq. 2}$$

$$LM + M \xrightarrow{K_{12}} LM_2 \qquad K_{12} = \frac{[LM_2]}{[LM][M]} \qquad \textbf{Eq. 3}$$

$$LM + L \xrightarrow{K_{21}} L_2M \qquad K_{21} = \frac{[L_2M]}{[LM][L]} \qquad \textbf{Eq.4}$$

$$\beta_{mn} = \prod_{i=1}^{m}\prod_{j=1}^{n} K_{ij} \Rightarrow Log(\beta_{mn}) = \sum_{i=1}^{m}\sum_{j=1}^{n} Log(K_{ij}) \qquad \textbf{Eq.5}$$

In this thesis, all the binding constants are reported as their logarithmic values, for which the expression of the global binding constant ($Log\beta_{nm}$) correspond to the sum of the step-by-step values ($LogK_{ij}$). In each case, the luminescence data were fitted successfully with good convergence factors and the binding constants resulting from the fits are summarized in Table 2.4. It can be concluded from these results that in each case the formation of the 1:1 stoichiometric species occurs. However, the speciation and the stability of the complexes formed seem to be influenced significantly by the nature of the pendant arms. For example, the fitting of the data obtained from the titrations of **42** and **43** with $Tb^{III}$ showed in both cases the major formation of the 1:1 stoichiometric species with $LogK_{11}$ = 8.2 ± 0.8 and 5.5 ± 0.2, respectively. However, the stable formation of the species **$42_2$.Tb** also being detected with $LogK_{12}$=5.2, which indicates that the complex **42.Tb** is the most stable species present in solution. The speciation distribution plot derived from these calculations (Figure 2.17) showed that the formation of the species **$42_2$.Tb** is maximal in the presence of 0.5 equivalents of terbium in solution (66.4%) and that the equilibrium was displaced to the exclusive formation of **42.Tb** (89.5%) upon the addition of an equimolar ratio of lanthanide salt. In the case of **43**, the convergence of the mathematical model could be reached only with the introduction of the 2:1 M/L species, for which the formation at

**Table 2.4:** *Binding constant calculated form the fitting of the changes observed during the $Tb^{III}$ emission titrations of the calixarenes derivatives*

| $Log\ \beta_{ML}$ | 42 | 43 | 44 | 45 | 46 |
|---|---|---|---|---|---|
| $Log\ \beta_{11}$ | 8.2 ± 0.8 | 5.5 ± 0.2 | 7.8 ± 0.3 | 5.3 ± 0.1 | 4.5 ± 0.2 |
| $Log\ \beta_{21}$ | - | 6.8 ± 0.3 | - | - | - |
| $Log\ \beta_{12}$ | 13.4 ± 0.9 | - | 13.5 ± 0.5 | - | - |
| $Log\ \beta_{23}$ | - | - | - | 18.4 ± 0.1 | - |

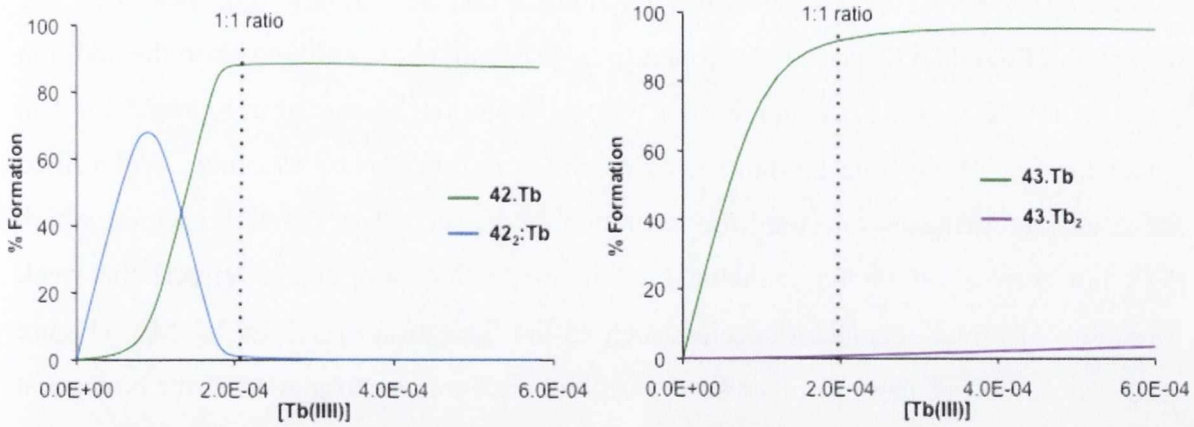


**Figure 2.17:** *Speciation distribution diagrams calculated from the fitting of the changes obtained from the luminescence emission titration for ligand* ***42*** *(left) and* ***43*** *(right) with* $Tb^{III}$

high terbium concentration ($[Tb^{III}] > 2\times10^{-4}$ M) was calculated to be low with $LogK_{21}$=1.4. The speciation distribution plot describing the binding process of **43** with $Tb^{III}$ (Figure 2.17) confirmed the expected behaviour, showing the unique formation of **43.Tb** in the presence of 1 equivalent of $Tb^{III}$, which is followed by the slow formation of the second less stable species **43.Tb$_2$**. The difference in behaviour between **42** and **43** can be explained by the nature of the terminal amine moieties: The self-assembly of two ligands of **42** around the same terbium ion can potentially occur *via* tail to tail arrangement after rotation of one or several pendant arms, as depicted in Figure 2.13. Nevertheless, the formation of the 1:2 M/L has not been observed in the case of **43,** which can be due to the configuration of the morpholinyl group, shielding the access to the metal centre and preventing the formation of multi-ligand species. The weak formation of the dimetallic species can also potentially occur through the complexation of a second terbium ion with the terminal oxygen atoms present on the morpholinyl of **45**, as proposed in the binding mode in Figure 2.13.

The influence of the nature of the pendant arms on the binding process has also been studied using the results obtained from the titration of the longer armed ligands **44-45**, which despite their structural similarities, showed three different behaviours. The results obtained from the luminescent titration of compound **44**, were similar to those obtained for ligand **42**, which bears the same terminal moieties. The fitting of the luminescence titration data suggested the formation of the two species **44$_2$.Tb** and **44.Tb.** In the case of **44**, the 1:2 M/L stoichiometric complexes were observed to be more favoured ($LogK_{12}$ = 5.60) than in the case of **42** and reached a maximum formation of *c.a.* 85.4% in the presence of 0.5 equivalents of terbium salt. As previously discussed, this can be due to the higher flexibility of the pendant arms, which can stabilize the self-assembly

of ligands to fulfil the coordination requirement of the terbium ion. However, the formation of the **44.Tb** species was found to be predominant in solution upon the addition of an equimolar ratio of lanthanide ion ( > 95% formation) as shown in Figure 2.13. The calculations resulting from the luminescence emission titrations of **45** could also be fitted accurately by taking into account the formation of the secondary 2:3 M/L species, which does not correspond to the probable binding mode but more likely reflects the weak formation of minor secondary species, such as the formation of 1:2 or 3:2 M/L (Figure 2.18). Nevertheless, these results also showed the predominant formation of the host-guest system **45.Tb** during the titration, with a binding constant of $LogK_{11}$ = 5.3, which was in the same range as the one obtained for the formation of **45.Tb**.

Finally, the evolution of the lanthanide luminescence emission of **45** during the complexation of terbium could be successfully fitted with good factors of convergence and the results from the calculation are shown in Figure 2.18. The non-linear regression analyses of the terbium titration of **45** demonstrated formation of the **45.Tb** complex with a lower binding constant ($LogK_{11}$ = 4.5) than for the other analogues. This can possibly be due to the bulkier diethylamine moieties, which can shield the access to the binding site introducing a kinetic aspect to the binding process.

For example, compounds **42** and **44** experienced the same complexation profile with binding constants in the same range while **43**, **45** and **46** presented similar lower binding constants showing the weak formation of diverse dimetallic species demonstrating that the

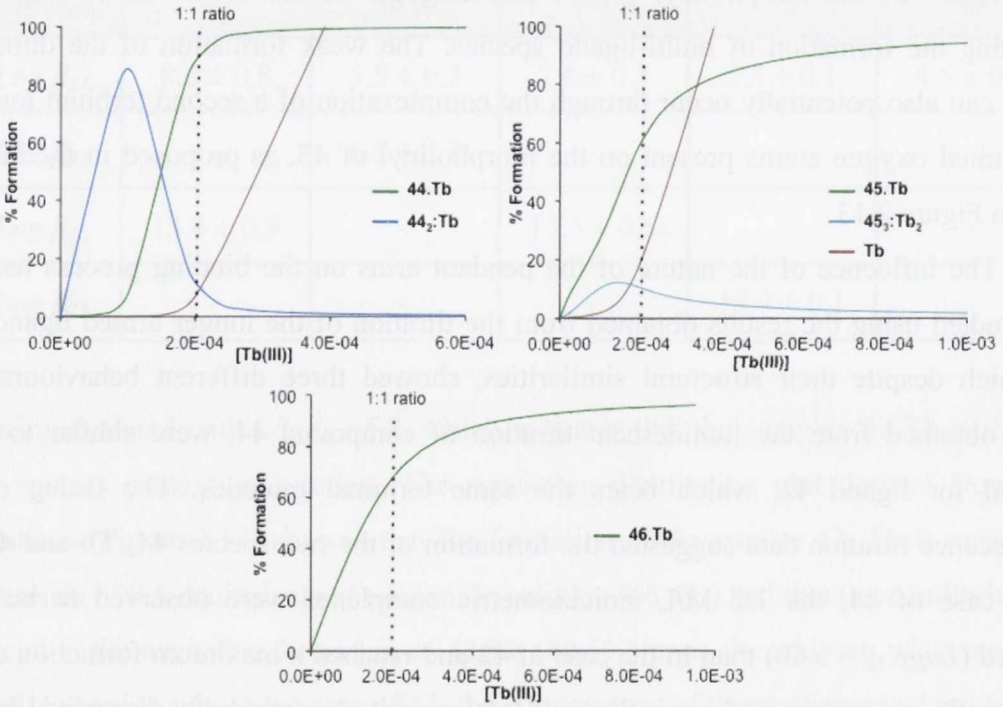


**Figure 2.18:** *Speciation plots calculated from the luminescence titration for ligand **44** (left), **45** (right) and **46** (bottom)*

coordination and the photophysical properties of the calix-[4]-arene analogues can be tuned by the nature of the pendant arms.

### 2.3 Conclusion

The work of Quinlan *et al.* has shown that the alkylation of calix-[4]-arene on the lower rim provides an interesting strategy to produce ligands suitable to complex lanthanide ions such as $Tb^{III}$. The study of such complex formation and the investigation of the photophysical properties of these complexes has been the purpose of this chapter. From these results it can be concluded that the nature of the pendant arms can have a dramatic effect on the formation and the photophysical properties of the resulting molecular architectures. First of all, we have shown that the analogues with shorter pendant arms gave rise to longer-lived luminescence and higher quantum yields, which can be due to the shorter arm distance and a more efficient deactivation of the excited state of the lanthanide provoked by the presence of the amide protons. It has been clearly observed that the intrinsic photophysical properties of the complexes **42-46.Tb**, such as lifetimes, quantum yields, absorption coefficients, were only weakly affected suggesting the poor influence of the terminal moiety on the properties of the adducts.

The $Tb^{III}$ complexation studies performed on each ligand have shown the predominant presence of the **L.Tb** complex and also the secondary formation of minor species such as the 1:2, 2:1 M/L stoichiometric species. Moreover, it can be clearly deduced from the titrations and their resulting fitting that the binding process can be tuned by the nature of the terminal moiety: For example, the ligands **42** and **44**, which possess the same piperidine function, self-assemble around terbium to form predominantly the **$L_2$.Tb** complex in the presence of 0.5 equivalents of metal (up to 86% formation) prior to the total formation of the **L.Tb** complex with high binding constant ($Log\beta \approx 8$), whereas the studies of the other analogues have resulted in a different speciation with a lower binding constant for the 1:1 species ($Log\beta \approx 5$). This can be due to the different configurations adopted by the terminal moiety, which can shield more or less the access of the cavity. However, in order to fully understand the role played by the terminal moieties, further studies such as low temperature high-resolution fluorescence spectroscopy in order to quantify the potential back energy transfer, are needed. The synthesis and the studies of other analogues bearing morpholinyl, pyridinyl are currently in progress.

# Chapter 3:

# Chiral lanthanide luminescent monometallic self-assemblies

## Chapter 3: Chiral lanthanide luminescent monometallic self-assemblies

### 3.1 Introduction

The use of self-assemblies provides an effective route for the development of highly luminescent and stable architectures.[9,11,22] It has also been well established that the design of the ligands is essential for the control of the geometry and the chemical and photophysical properties of the resulting structures, as described in Chapter 1.[1,84] Recently, the synthesis and the study of chiral luminescent self-assembly lanthanide complexes attracted a great interest particularly for the development of novel chiral luminescent responsive probes for potential *in vivo* applications.[120-122]

With the aim of generating the chiral emission of such systems, the incorporation of a chiral antenna into various ligands has been undertaken. This resulted in the chiral emission of the complexes, where the chirality of the ligand was transferred to the excited states of the lanthanide ion.[90,123] Alternatively, the optical activity can also be induced by the final geometry of the resulting self-assemblies, such as in the case of molecular knots and helicates. This is called topological chirality,[124] where the three-dimensional arrangement of the resulting structure generates crossing points (knots). Each knot can adopt two different configurations, depending on which strand crosses the other from above, as shown in Figure 3.1. This can result in the topology possessing a non-superimposable mirror image (Figure 3.1). The topological chirality depends then on the ability of the molecule to be transformed into its mirror image as shown in Figure 3.1. **a** possesses a mirror image **b** but the conversion between the two forms can easily happen, this results in the absence of chirality, in solution. Conversely, the conversion of **c** into its mirror image **d** cannot occur due to their "locked" conformation generating topological chirality.[124] In the case of ternary metal templated self-assemblies, such as triple stranded helicates or molecular bundles, the conformations of the self-assemblies are locked due the geometry of the coordination sphere of the metal. Consequently, the arrangement of three

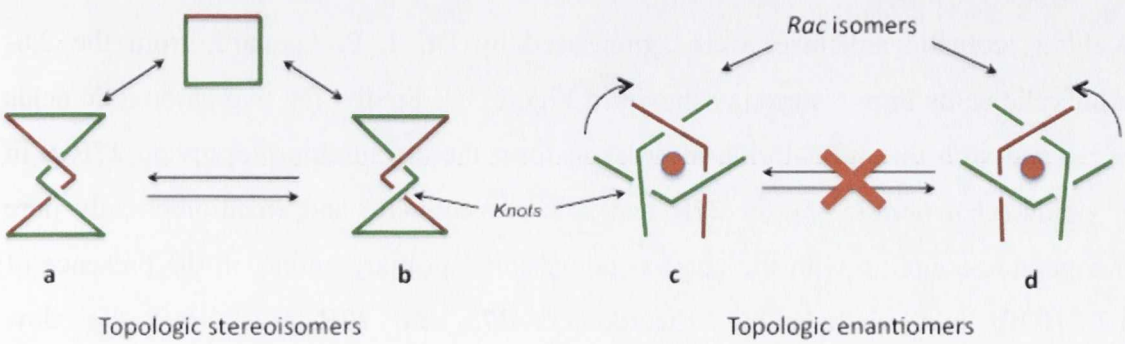


**Figure 3.1:** *Schematic representation of the topological isomers* ***a*** *and* ***b****, and enantiomers* ***c*** *and* ***d****.*

ligands around the metal ion can occur with different helical directions giving rise to two different *rac* isomers as illustrated in Figure 3.1. The induction of chirality *via* self-assembly has been well established in the literature particularly by the pioneering work of Piguet and coworkers who have developed various examples of triple stranded helicates[100,105]

### 3.1.1 Previous work preformed in the Gunnlaugsson group

With the view of developing novel enantiomerically pure chiral luminescent mono- and bi-metallic lanthanide complexes, our research group has focused on the incorporation of chiral antennae into acyclic structures, which can be used to give chiral luminescent self-assembled architectures. In addition, the self-assembly of three asymmetric ligands can tune the overall chirality of the supramolecular structure by inducing a left or right handed helicity as shown in Figure 3.1. Each of the ligands was designed from the

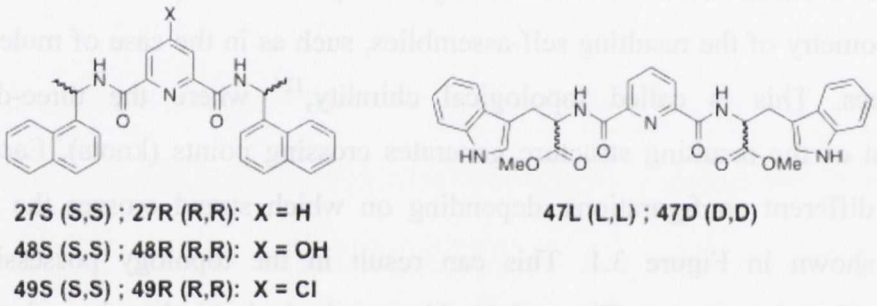


**Figure 3.2:** *Ligands designed in our group for the development of mono-metallic lanthanide chiral luminescent probes.*

tridentate 2,6-diamidopyridine moiety (**dpa**), which forms a stable 1:3 complex with lanthanide ions such as $Tb^{III}$ and $Eu^{III}$ in a helical geometry as previously discussed in Chapter 1. The pairs of ligands **27** and **47-49**, shown in Figure 3.2 were designed for the formation of mono-metallic complexes, These latter examples were analysed using UV-vis absorption and luminescence emission spectrophotometric methods.

The compounds **27R-S** and **47R-S**, which consist of a simple **dpa** unit flanked with two chiral aromatic antennae, were synthesised by Dr. J. P. Leonard, from the 2,6-dicarbolxylic acids in two steps, as shown in Figure 3.3. Firstly, the two carboxylic acids were reacted with thionyl chloride in order to form the diacid chloride, giving **27R-S** in high yields (66.4 and 75.5% for **27R** and **27S**, respectively) and enantiomerically pure after a peptide coupling with the corresponding chiral primary amine, in the presence of EDCI, HOBt and triethylamine. Enantiomers **27S** and **27R** crystallised *via* slow evaporation from methanol and the crystals were suitable for X-ray diffraction, which

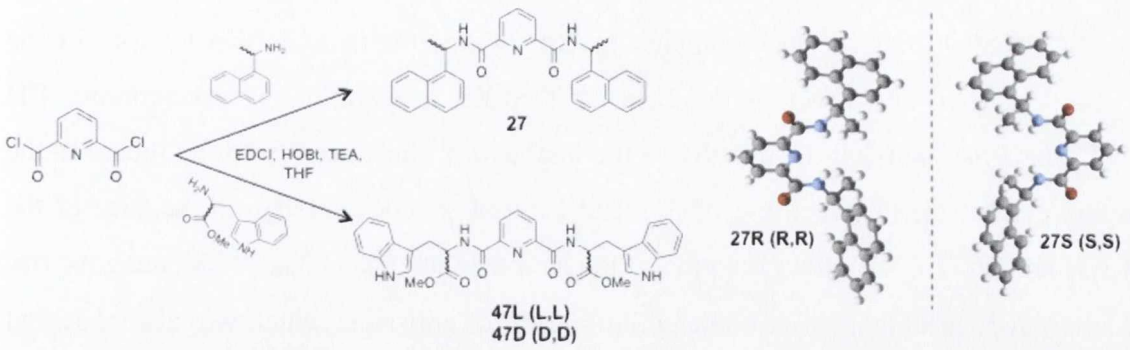


**Figure 3.3:** *One step synthetic route for the formation of the pairs of ligands 27 and 47 and the crystal structure of enanthiomers 27R and 27S.*

correlated with the CD (circular dichroism) analysis, and confirmed the enantioselective formation of these products. Based on this work, the enantiomers **47L** and **47D** were also designed with two tryptophan moieties, which are more suitable to sensitise $Tb^{III}$ following the same route as for the synthesis of **27**.[102] The formation and the study of the complexes of **47** with $Tb^{III}$ and $Eu^{III}$, is the subpart of this chapter.

The *Trinity Sliotars* (**27S-27S$_3$.Ln**) were synthesised by reacting **27S** or **27R** with $Ln(CF_3SO_3)_3$ (Ln = Tb, Sm, Eu, Nd, and Yb) in a 3:1 stoichiometry in dry $CH_3CN$ (Figure 3.4). The resulting molecular bundles were isolated as an off white solid in high yields after precipitation from diethyl ether. The $^1$H-NMR analysis showed the typical paramagnetic effect due to the lanthanide ion and exhibited, in each case, the high degree of symmetry of the resulting complexes in solution. As shown in Figure 3.4, the successful

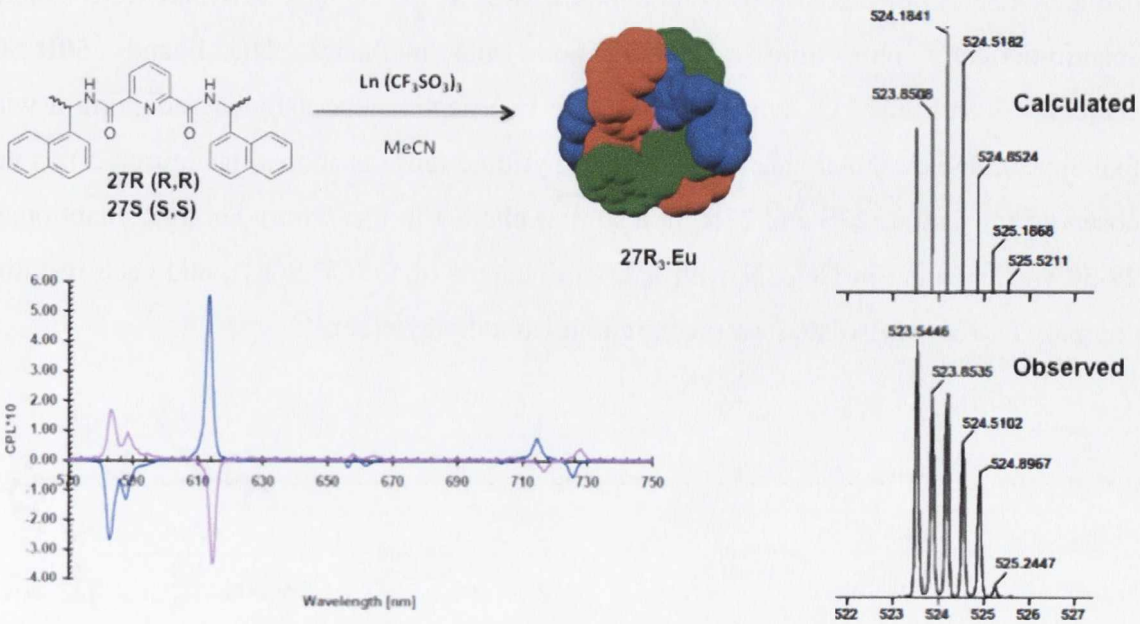


**Figure 3.4:** *General procedure for the synthesis of the trinity sliotars (Top). CPL emission (bottom) and mass spectrometry analyses of the Eu complex analogues (right).*

formation of the **$L_3$.Ln** (L = **27S-27R** Ln = Tb, Sm, Eu, Nd, and Yb) was also confirmed by HRMS studies. Indeed, each complex **$L_3$.Ln** showed the isotopic distribution for the calculated pattern, as shown in the case of **$27S_3$.Eu** in Figure 3.4. Furthermore, CD analysis demonstrated that the chiralty of the ligand was transferred from the ligand to the complex giving rise to either a Δ or Λ metal centred stereochemistry. In the case of the **$L_3$.Ln** (Ln = Eu, Tb, Sm), the excitation of the naphthyl antenna at $\lambda_{max}$ = 281 nm gave rise to a long lived chiral lanthanide centered luminescence emission, which was also observed in the CPL emission spectra of **27S-$27R_3$.Eu**, Figure 3.4.

This demonstrated that the chirality was transferred to the excited states of the lanthanide ion and that each molecular bundle was stereoselectively isolated. Finally the chiral nature of the molecular bundles was also confirmed by X-ray analysis. The complexes **$L_3$.Ln** (Ln = Eu, Sm, Nd, Tb) were crystallised from methanol and the resolution of the single crystal diffraction (see example **$27S_3$.Eu** in Figure 3.4) demonstrated clearly that **27R** (*R,R*) induces Λ chirality, whereas **27S** (*S,S*) induces Δ chirality.[37]

The formation of molecular bundles was also carried out by Dr. N. S. Murray and Dr E. Pazos, using the two pairs of enantiomers, **49** and **50**, which have a -OH or –Cl function at position 4 of the pyridyl ring. Firstly, the ligands **49R-49S** were synthesised in one step from the chelidamic acid **48** in high yields (62% and 65%, respectively), following the same synthetic route as for **27S** and **27R**. The ligands **50R** and **50S** were obtained after a simple chlorination of the alcohol moiety at the 4 position of the pyridine, using $SOCl_2$. As in the case of compounds **27S-27R**, the ligands **50R-50S** were isolated enantiomerically pure after recrystallisation from methanol. The ligands **50R-50S** crystallized with local $C_2$ symmetry with the two naphthalene antennae adopting a wing like appearance on either side of the central pyridine unit (as shown in Figure 3.5) as was observed for ligands **27S** and **27R**. In a similar manner to the *Trinity Sliotars,* enantiomers **49-50** were reacted in $CH_3CN$ with 0.33 equivalents of $Eu(CF_3SO_3)_3$, and each resulting complex **$L_3$.Eu** was isolated *via* precipitation from diethylether.[125]

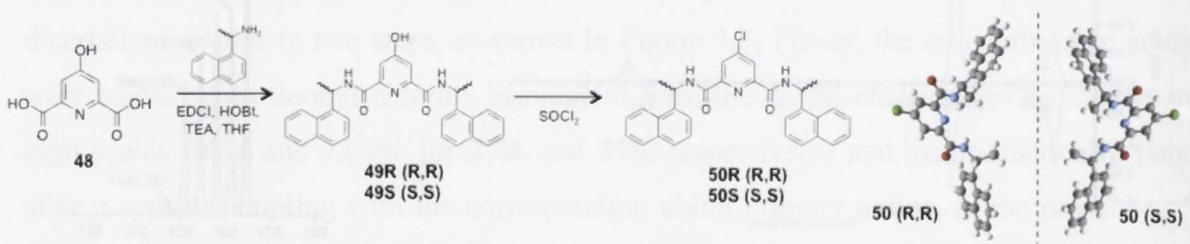


**Figure 3.5:** *Synthetic route for the formation of the enantiomers **49R**, **49R**, **50R** and **50S**. Crystal structures obtained for **50R** and **50S**.*

The successful complexation of $Eu^{III}$ was confirmed by mass-spectrometry and $^1$H-NMR spectroscopy, which gave similar results as for the molecular bundles **27S-R$_3$.Ln**. The $^1$H-NMR spectra of the complexes experienced the typical broadening and shifting effect due to the presence of the europium ion and showed a high symmetry level indicative of the $C_3$ geometry of the final structures. Moreover, the Δ and Λ chirality was also observed in the CD spectra of the complexes, Figure 3.6, where each pair of enantiomers gave rise to exciton couplings that were of equal magnitude and of opposite signs. Upon complexation of these ligands with $Eu^{III}$, the CD spectra experienced dramatic changes where the $S_0 \rightarrow \pi\pi^*$ transitions of the naphtyl antenna ($\lambda_{max}$ = 281 nm) were red shifted and changed signs. The changes in the optical activity between the ligands and their resulting europium complexes can be due to the induction of further topological chirality

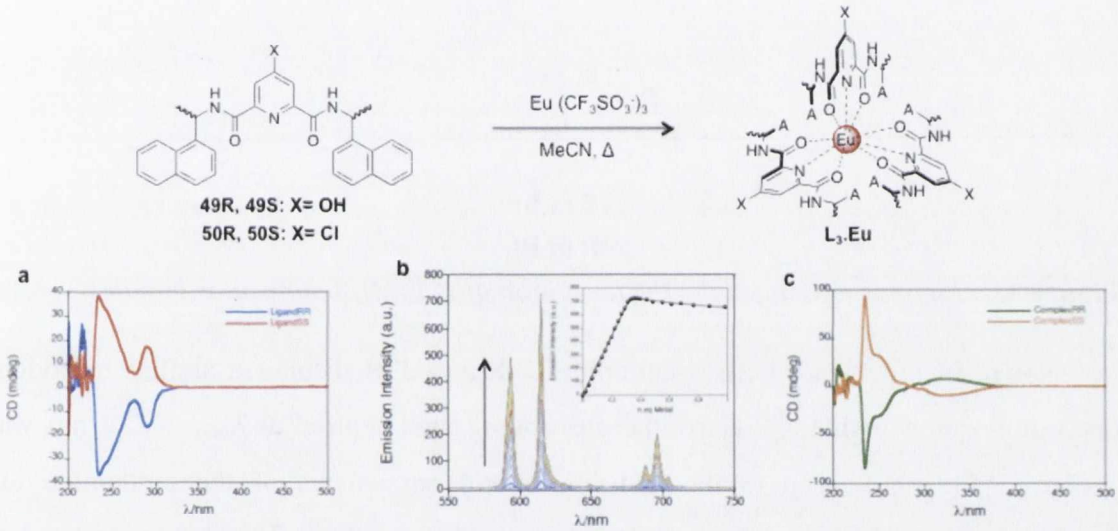


**Figure 3.6:** *General procedure for the formation of the molecular bundles* ***L$_3$.Eu.*** *(a) CD spectrum of ligands* ***49R*** *and* ***49S****. (b)Luminescence Titration of* ***49R*** *upon the addition of Eu(CF$_3$SO$_3$)$_3$.. (C) CD spectrum of* ***49R$_3$.Eu****.*

during the self-assembly process. The formation of the complexes was also investigated *in situ* using different spectroscopic methods, such as UV-vis absorption, fluorescence and time delayed emission spectroscopy. Here, the $Eu^{III}$ luminescence was "switched on" up to the addition of 0.33 equivalents of $Eu(CF_3SO_3)_3$ confirming the formation the desired 1:3 (M/L) complexes, as shown for **50R** *vs* $Eu^{III}$ in Figure 3.5. This stoichiometry was confirmed by fitting of the spectroscopic data using the non-linear regression analysis software SPECFIT®, which has calculated the quasi-exclusive formation of the **L$_3$.Eu** complexes in solution.[125]

This previous work performed in our group has illustrated that the lanthanide directed self-assembly of small chiral ligands offers an efficient route towards the formation of chiral luminescent structures. With the aim of enhancing our understanding of the

formation of chiral luminescent complexes, such as mono-metallic molecular burdles and triple stranded bimetallic helicates, this next chapter focuses on the study of the formation of $Eu^{III}$ 1:3 (M/L) complexes based on the ligands **27S-R** and **51S-R** *in situ* and their resulting photophysical properties in solution will be investigated.

### 3.2 Formation of the Trinity Sliotar 27S-27R$_3$.Eu *in situ*

#### 3.2.1 UV-vis absorption and luminescence emission investigations

Having demonstrated the presence of the molecular bundles **$L_3$.Eu (L = 27S** and **27R)** in solid states and in solution, the next step was to investigate and quantify their formation *in situ*. Firstly, the complexation of $Eu^{III}$ by **27S** and **27R** was studied using UV-vis absorption, fluorescence and time delayed emission spectrophotometric titrations in $CH_3CN$ ($C_L = 1\times10^{-5}$M).

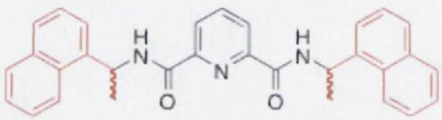

**27S (S,S)**
**27R (R,R)**

**Figure 3.7:** *Ligands envisaged for the formation of 1:3 (M;L) molecular bundles.*

As shown, in Figure 3.8 both enantiomers **27S** and **27R** displayed similar behaviour upon complexation with $Eu^{III}$. Here, the absorption band centred at $\lambda_{max}$ = 222 nm was hypochromically shifted up to the addition of 0.4 equivalents of the lanthanide ion followed by a hyperchromic shift upon the addition of further $Eu^{III}$. The absorption band of the naphthyl antenna also experienced a broadening effect up to the addition of 0.33 equivalents of lanthanide. These results are indicative of the formation of the 1:3 M/L stoichiometric species in solution.

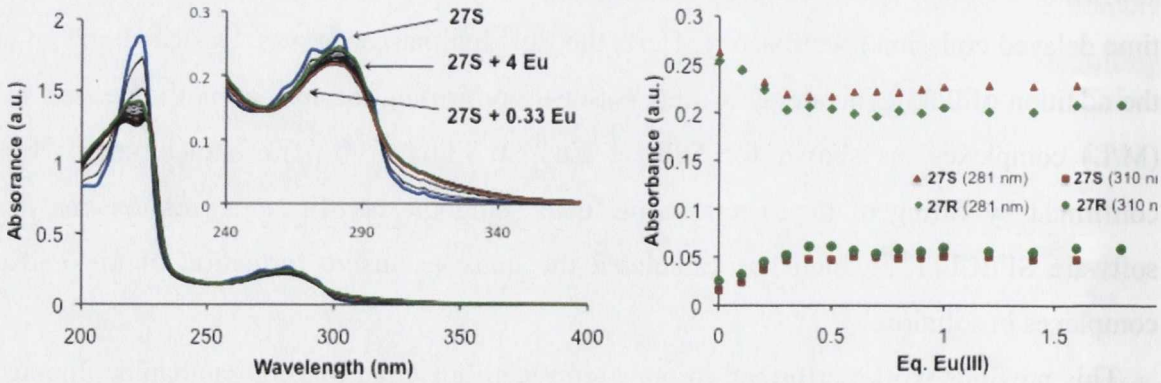


**Figure 3.8:** *UV-Vis absorption titration of **27S** in $CH_3CN$ (left) and isotherm of complexation of **27S** and **27R** at 281 nm and 310 nm (right).*

Similar results were observed for the absorption at 310 nm. These results suggested that the equilibrium is only weakly displaced towards the 1:2 and 1:1 (M/L) species, indicating the high stability of the **$L_3$.Eu** species. This has also been confirmed by carrying out luminescence titrations, the results of which are shown in Figure 3.9. Indeed, in both cases, the $Eu^{III}$ emission was "switched on" upon the addition of 0-0.33 equivalents of

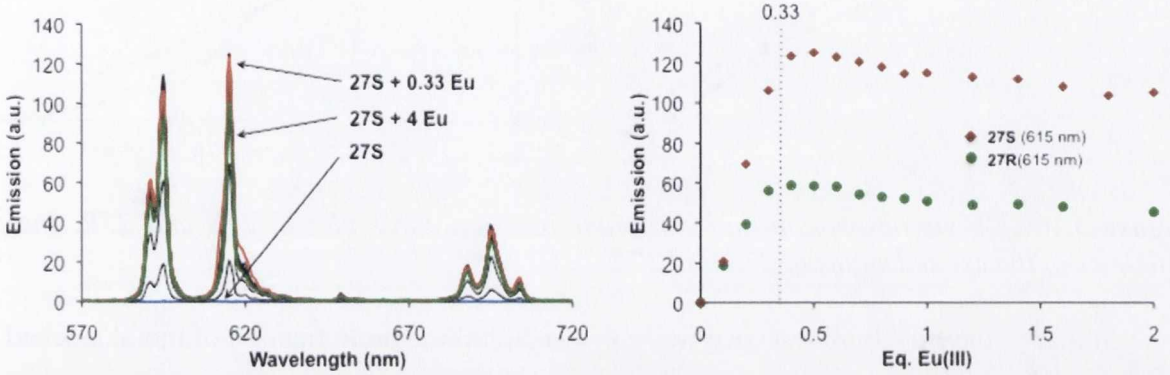


**Figure 3.9:** *Europium emission titration of **27S** (left) and isotherms of complexation of **27S** and **27R** at 615 nm (right)*

lanthanide by excitation of the naphthyl antenna, again demonstrating the formation of the desired 1:3 stoichoimetric species. Again, at higher $Eu^{III}$ concentration, a gradual decrease of the emission was also observed, indicative of the formation of minor species in solution as observed in the UV-vis absorption experiments.

To further analyse the complexation process, Job's plot (continuous variation experiments) were performed, where the molar fraction of the lanthanide ion was varied from 0 to 1, keeping the sum of concentration of metal ion and ligand constant as illustrated by the equation 1.

$$\chi_{Eu} = \frac{C_{Eu}}{C_{Eu} + C_L} \quad \text{with } C_{Eu} + C_L = constant \qquad \textbf{Eq 1}$$

Here, the UV-vis absorption and emission spectra were recorded after stirring for five minutes fresh solutions containing the appropriate ratio of ligand and lanthanide ion. The lifetimes of the $Eu^{III}$ centred emission were also recorded from the same solutions.

Firstly, the changes in the UV-vis absorption spectrum of the naphthyl antenna showed a large decrease due to the hypochromic effect upon the addition of $Eu^{III}$. However, these changes followed three different trends, suggesting the formation of two different stoichiometric species in solution, as shown in Figure 3.10. Initially, the UV-vis absorption spectrum experienced a decrease up to the formation of the 1:3 M/L **$L_3$.Eu** species, followed by a second decrease, which was observed (in both cases) between $\chi_{Eu}$ =

*0.25* and $\chi_{Eu}$ = *0.5*. This is most likely due to the weak displacement of the 1:3 equilibrium toward the formation of a 1:1 stoichiometric species.

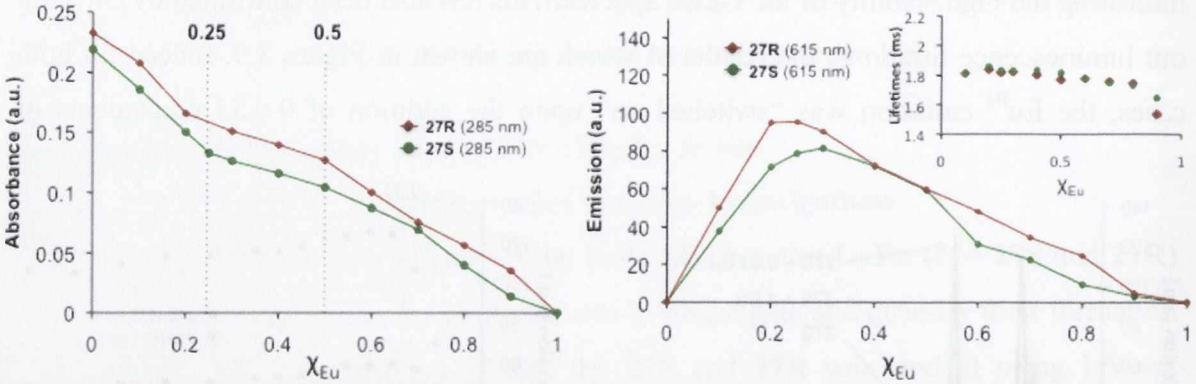


**Figure 3.10:** *UV-vis absorption and europium emission Job's plot of* ***27S*** *and* ***27R****. Inset: Lifetimes of the excited states of* ***27S*** *and* ***27R***

Similarly, the $Eu^{III}$ luminescence was enhanced until the mole fraction of metal reached 0.25, before experiencing a quenching effect. This confirmed that the 1:3 M/L stoichiometry was formed as the major species formed. In comparison to that seen above, the formation of the minor 1:2 and 1:1 M/L species was not detected in the luminescence experiment. Similarly, the lifetimes of the self-assembled species were all fitted to mono-exponential decays and remained similar at each metal to ligand ratio ($\tau_{MeCN} \approx$ 1.80 ms). This suggested that the same species **$L_3$.Eu** was formed throughout the experiment, as a change in the stoichiometry would cause a dramatic decrease in the lifetime values due to the presence of solvent molecules within the coordination sphere of $Eu^{III}$.

### 3.2.2 Determination of the binding constants and the speciation distribution of the complexation process

The previous titrations and Job's plot experiments have showed the successful formation of the **$L_3$.Eu** bundles in solution and these measurement have also shown that both *R,R* and *S,S* enantiomers gave rise to similar changes in the presence of $Eu^{III}$. Consequently, the next step was to quantify the complexation process, by analysing by means of the non-linear regressions analysis (using the equilibrium equations described previously in section 2.2.3.2). The fitting of the results obtained from the UV-*vis* titrations using SPECFIT® have shown, for both enantiomers, the presence of two major species in solution (speciation distribution diagrams in Figure 3.11). In the case of ligands **27R** and **27S** (see Appendix 3.1), **$L_3$.Eu** (L = **27S** and **27R**) stoichiometry was found to be the predominant species formed with the addition of 0-4 equivalents of $Eu^{III}$, reaching a maximum formation of 93% in the presence of 0.33 equivalents of lanthanide for both **$27S_3$.Eu** and **$27R_3$.Eu**. The formation of the second 1:1 species was also observed in the

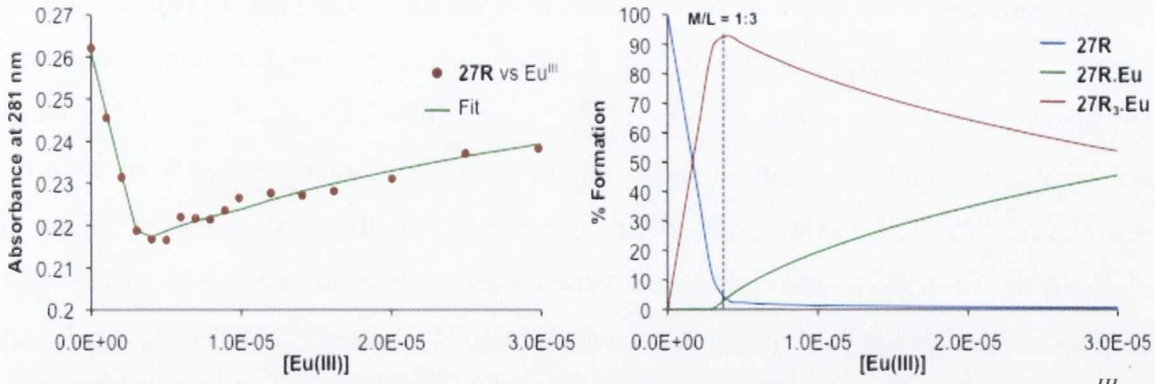


**Figure 3.11:** *Changes obtained in the UV-vis spectrum for **27R** upon the addition of $Eu^{III}$ at 281 nm (left). Speciation distribution diagram resulting from the fits (right)*

presence of higher quantities of $Eu^{III}$ (from 0.4 to 6 equivalents of metal) in solution. From these results, the binding constants were determined for the formation of complexes **$L_3$.Eu** and **L.Eu** (L= **27S, 27R**), using SPECFIT® and these are summarised in Table 3.1. In both cases, the molecular bundles **$L_3$.Eu** were formed with high binding constants of *log* $\beta_{1:3}$ = 20.3 and 21.5 for **27S** and **27R**, respectively. These are of the same magnitude as those reported by Chauvin *et al.* for several **(dpa)$_3$.Eu** derivatives,[126] while the second 1:1 stoichiometric species was formed with binding constants of *ca. log* $\beta_{1:1}$= 6.4 and 6.9, for **27S.Eu** and **27R.Eu**, respectively.

The analyses of the $Eu^{III}$ luminescence titrations yielded similar results for **27S**. A 1:1 and 1:3 species were calculated to be formed with binding constants that were *ca.* one log unit greater in magnitude than that determined from the UV-vis absorption titrations (*log* $\beta_{1:1}$ = *7.5* and *log* $\beta_{1:3}$ = 21.5). The calculated speciation distribution diagram, in Figure 3.12, shows the predominant formation of the "molecular bundle" **27S$_3$.Eu**, between 0 and 1 equivalents of $Eu^{III}$, with a maximum of formation of 88 % upon the addition of 0.33 equivalents of $Eu^{III}$. However, while the formation of the 1:1 species can be considered as negligible at low lanthanide ion concentration (0.7 % at M/L = 1:3), its formation became

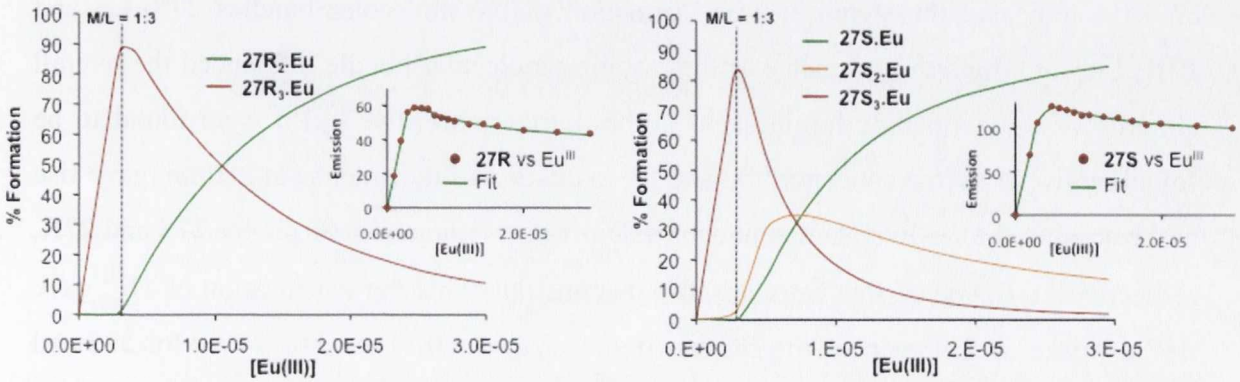


**Figure 3.12:** *Speciation distribution diagram calculated from the fitting of the europium emission titrations of **27R** (left) and **27S** (right). Insets: Convergent fit obtained from the calculations*

predominant upon the addition of 1.1 equivalent of $Eu^{III}$. The data obtained from the luminescence titration performed on ligand **27S** could not be fitted accurately following the binding model discussed above, and the introduction of a third 1:2 stoichiometric species was needed to be taken into account. However, the results obtained from these fits, see Figure 3.12 and Table 3.1, were in agreement with those obtained by fitting the changes in the UV-vis absorption and luminescence emission previously discussed in section 3.2.1, with similar binding constants to those observed for **27S** ($log\ \beta_{1:1}$ = 7.7 and $log\ \beta_{1:3}$ = 21.8), where the formation of the complex **27R$_3$.Eu** was achieved in 84 % at M/L = 1:3. This has confirmed the selective formation of the supramoleclar monometallic architectures **L$_3$.Tb** occurring in solution with high binding constants. Indeed, the results

**Table 3.1:** *Summary of the results obtained from the fitting of the titration data of 27S and 27R.*

| L vs $Eu^{III}$ | UV-vis | | | | Luminescence | | | | | |
|---|---|---|---|---|---|---|---|---|---|---|
| | $log\ \beta_{1:1}$ | $log\ \beta_{1:3}$ | % Species at M/L =1:3 | | $log\ \beta_{1:1}$ | $log\ \beta_{1:2}$ | $log\ \beta_{1:3}$ | % Species at M/L =1:3 | | |
| **27S** | 6.4 ± 0.3 | 20.3 ± 0.5 | 0.2 | 92.5 | 7.5 ± 0.2 | -- | 21.5 ± 0.4 | 0.7 | -- | 87.8 |
| **27R** | 6.9 ± 0.7 | 21.5 ± 0.9 | 0.4 | 92.6 | 7.7 ± 0.2 | 14.7 (fix) | 21.8 ± 0.3 | 0.2 | 3.8 | 83.6 |

obtained here, showed that the self-assembly of the three ligands provides the nine donor atoms needed to fulfill the coordination requirement of the europium ion and the six naphtyl chiral antennae capable of sensitising the circular polarised europium luminescence of the complexes.

Also, the correlation of these results with the investigation performed by Leonard *et al.* have indicated the stereoselective formation of the molecular bundles **27S$_3$.Ln** and **27R$_3$.Ln**, for which the geometry of the resulting molecular bundle influenced the overall chirality of the lanthanide luminescent probe. Furthermore, the **L$_3$.Ln** were found to be soluble in water at low concentration and the excitation of the antenna at 280 nm gave rise to the sensitised long-lived lanthanide emission ($\tau_{H2O}$ = 1.66 and 1.67 ms for **27S** and **27R**, respectively). However, this work has also demonstrated that the sensitisation of $Tb^{III}$ gave rise to weaker luminescence with shorter lifetimes ($\tau_{H2O}$ = 0.116 and 0.114 ms for **27S** and **27R**, respectively).[102] In addition, it can be concluded from comparing these results with those obtained by Dr. N. S Murray that the functionalisation of the central pyridine moiety

at position 4 can have a dramatic influence on the photophysical properties of the resulting molecular bundles. Indeed, the CD analyses have shown identical spectra for ligands **27S-R** and **49S-R** while upon complexation with $Eu^{III}$, the CD band located between 300 and 320 nm was found to be of opposite sign in the case of **49R-$S_3$.Eu,** to that observed for **27S-$R_3$.Eu**. This suggested that the complexes **49S-$R_3$.Eu** and **50S-$R_3$.Eu** resulted in different helicity than **27S-$R_3$.Eu**. This effect was also observed in the circularly polarised luminescence analyses (CPL), previously published in the PhD thesis of N. S. Murray. This confirmed that the chirality and consequently the geometry of the molecular architecture can be also modified *via* functionalisation of the 4 position of the tridentate diaminopyridinyl central moiety.[125]

The overall solution studies of the complexation process, showed the predominant formation of the 1:3 species with a binding constant of $log\ \beta_{1:3} \approx 17.4$.[125] This is somewhat lower than those found for **27S** and **27R**. Thus, further functionalisation of the ligand can allow for the tuning of the stoichiometry and the overall properties of the architecture and can demonstrate that the choice of the functional group added onto the ligand is essential for the formation of the supramolecular structures, work which is currently being undertaken in our research group.

### 3.3 Ln-directed formation *in situ* of molecular bundles containing tryptophan antennae

With the purpose of investigating the potential functionalisation of the aforementioned molecular bundles for the development of other novel and responsive chiral luminescent probes, ligands **47L** and **47D** were synthesised by J. P. Leonard using the same synthetic strategy as used before for **27S** and **27R**. As shown above, the two enantiomers consist of a

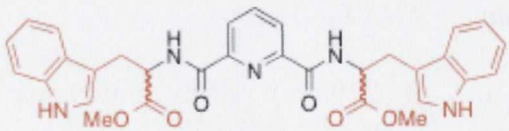


**47L (L,L)**
**47D (D,D)**

central tridentate diamidopyridinyl moiety flanked with two tryptophan antennae, which have been established to sensitise efficiently the luminescence emission of terbium. The ester functionalities of the tryptophans deliver two extra oxygen donor atoms, which can possibly provide a 1:2 (M/L) stoichoimetry to the molecular bundles. Furthermore, the methoxy moieties offer two bulky arrays that can strongly influence the geometry of the

overall architecture due to steric effects. As mentioned previously, each ligand was isolated enantiomerically pure and fully characterised by conventional methods.

The aim of this section was to investigate the self-assembly in solution of **47L** and **47D** with lanthanide ions, such as $Eu^{III}$ and $Tb^{III}$.

### 3.3.1 Photophysical properties of the 47L-$6_2$.Eu complexes in solution

In the case of **47L,** the UV-vis absorption spectrum, shown in Figure 3.13, showed two major absorption bands at $\lambda_{max}$ = 220 nm ($\varepsilon$ = 62170 $M^{-1}$ $cm^{-1}$) and at $\lambda_{max}$ =281 nm ($\varepsilon$ = 13614 $M^{-1}$ $cm^{-1}$), assigned to the $S_0 \rightarrow {}^1\pi\pi^*$ transitions of the pyridine and the tryptophan moieties. Upon excitation at $\lambda_{max}$ = 270 nm, each ligand gave rise to the typical tryptophan fluorescence emission, Figure 3.13, as an intense broad band centred at $\lambda_{max}$ = 423 nm. Firstly, the photophysical properties of the $Eu^{III}$ complexes of these ligand were investigated *in situ,* stirring ligands **47L** or **47D** ($1\times10^{-5}$ M) with 0.5 equivalent of $Eu(CF_3SO_3)_3$ in $CH_3CN$ over five minutes. Upon complexation with $Eu^{III}$, the $S_0 \rightarrow {}^1\pi\pi^*$ transition experienced a hyperchromic effect of *ca.* 62% (at $\lambda$ = 281 nm) and a 9 nm red

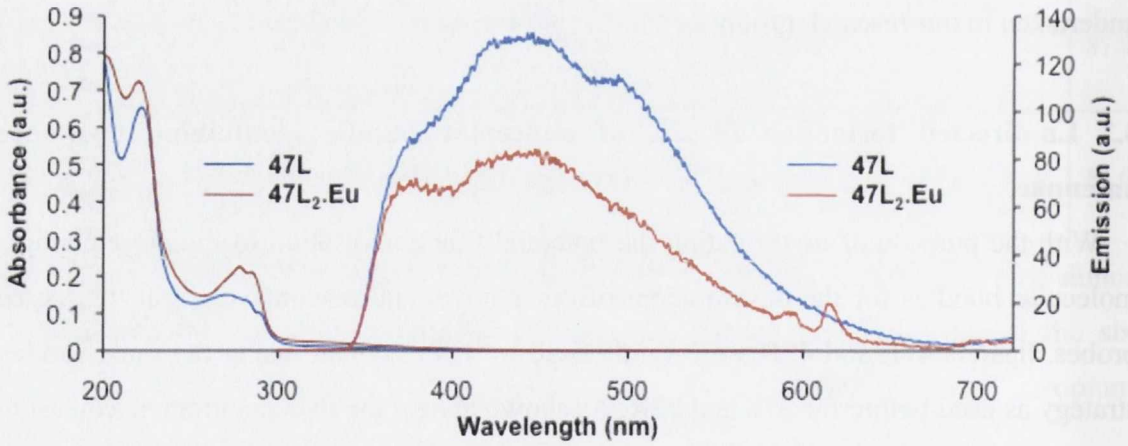


**Figure 3.13:** *UV-vis absorption and fluorescence emission spectra of* ***47L*** *($1\times10^{-5}$M) (blue) and its resulting complex* ***47L$_2$.Eu*** *(red).*

shift (from $\lambda_{max}$ = 270 nm to $\lambda_{max}$ = 279 nm), as shown in Figure 3.13 (and in appendix 3.2 for **47D**). Moreover, the ligand centred fluorescence emission was quenched by 36% in the presence $Eu^{III}$ ($\lambda_{max}$ = 420 nm), while the emission of $Eu^{III}$ was observed indicating that the population of the $^5D_0$ excited states occurred *via* energy transfer from the excited states of the ligand.

This was further confirmed by observing the time delayed lanthanide emission as well as the excitation spectra, in Figure 3.14. The resulting excitation spectrum from the time delayed $Eu^{III}$ emission, also shown in Figure 3.14, displayed two excitation bands at 225 nm and 275 nm, which matched the bands observed in the UV-vis absorption spectrum of

the ligands, confirming that the luminescence emission resulted from the energy absorbed by the indole chromophore. However, the resulting europium luminescence intensity was found to be weak, with a quantum yield of $\Phi_{281} = 0.15\%$.

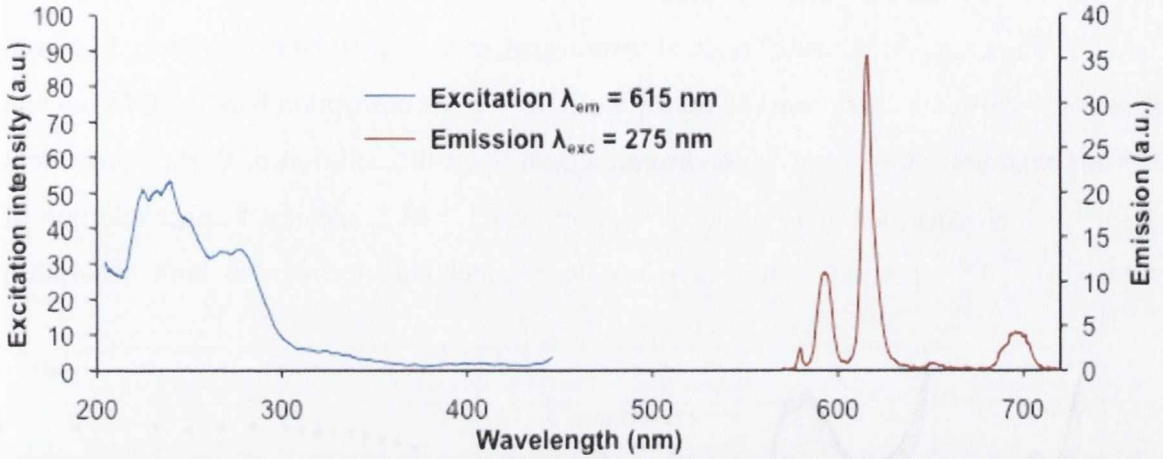


**Figure 3.14:** *Time delayed emission spectra ($\tau$ = 0.1 ms) of **47L$_2$.Eu** (red) and excitation spectra resulting from the europium emission at $\lambda$ =615 nm (blue).*

The lifetimes of the excited states of the europium centre have been calculated from the luminescence emission decays, shown in Figure 3.15, which was fitted following a mono-exponential decay giving $\tau$ = 0.368 ms and $\tau$ = 0.276 ms for **47L$_2$.Eu** and **47D$_2$.Eu**, respectively. These relatively short lifetimes may be due to the energy of the excited triplet state of the tryptophan (E ≈ 24830 cm$^{-1}$), which is lying far from the $^5D_n$ levels of $Eu^{III}$ (E ≈ 17500 cm$^{-1}$). This can favour the non-radiative deactivation processes, competing with the population of the $Eu^{III}$ excited states *via* energy transfer. Additionally, the $^3\pi\pi^*$ is relatively close in energy to the Eu-C=O CT (previously mentioned in section 2.1), which can also be populated causing non-emissive deactivation of the excited states of $Eu^{III}$ [71]

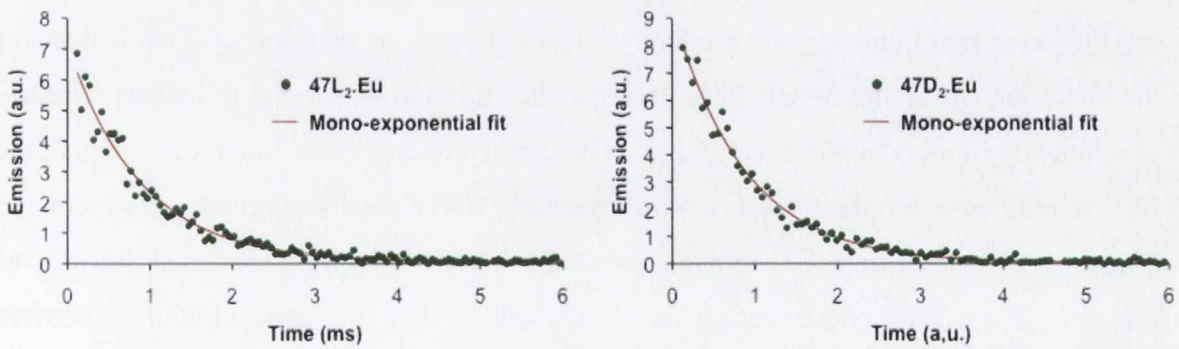


**Figure 3.15:** *Luminescence decays of **47L$_2$.Eu** (left) and **47D$_2$.Eu** (right) and their resulting mono-exponantal fits*

### 3.3.2 Solution studies of the complexation of $Eu^{III}$ by 47L and 47D

The self-assembly process was also investigated by monitoring the changes in the UV-vis absorption and lanthanide centred emission by titrating a solution **47L** and **47D** ($C_L = 2\times10^{-5}$ M and $1.5\times10^{-5}$ M, respectively) from 0→5 equivalents of $Eu(CF_3SO_3)_3$ in $CH_3CN$. The changes in the UV-vis absorption spectrum are shown in Figure 3.16, and these were similar to that observed for **$L_2$.Eu**. The UV-vis absorption bands at 275 nm and 225 nm experienced a strong hyperchromic effect upon the addition of 0→0.5 equivalent of $Eu^{III}$, which was indicative of the formation of a 1:2 M/L species. Further addition of metal (from 0.5→1 equivalents) gave rise to a small enhancement in both absorption

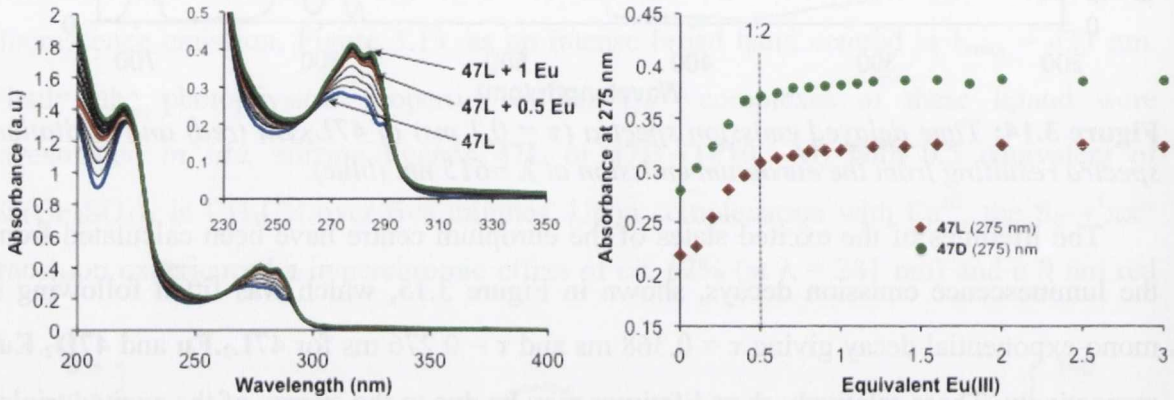


**Figure 3.16:** *UV-vis absorption $Tb^{III}$ titration of **47L** (left) and isotherms of complexation at $\lambda$ = 275 nm of **47L** and **47D** (at C =$2\times10^{-5}$M and $1.5\times10^{-5}$M respectively in $CH_3CN$)*

bands, before reaching a plateau upon the addition of 1 equivalent of $Eu^{III}$ ion. However, in contrary to the results observed for **27S** and **27R**, the formation of the 1:3 M/L stoichiometric species was not observed in the UV-vis absorption or luminescence emission titrations.

The luminescence emission titrations are shown in Figure 3.17. In the case of **47L** the $Eu^{III}$ emission intensity was gradually increased upon the addition of 2 equivalents of the metal ion. At higher metal concentrations, the emission was found to increase linearly as a function of metal ion concentration, without reaching a plateau. In the case of **47D**, the $Eu^{III}$ centred emission was found to follow a similar trend: the emission intensity increased gradually until reaching 1.5 equivalents of $Eu^{III}$, after which it increased linearly as function of the $Eu^{III}$ concentration. It is most likely that this concentration dependent enhancement above 1.5 equivalents may be due to the previously mentioned non-radiative deactivation of the excited states of the lanthanide, which is enhanced in the case of ligands **47L** and **47D** in comparison to that observed for ligands **27S** and **27R**.

Unfortunately, the contribution of the non-radiative processes could not be quantified successfully due to the poor photophysical properties of the resulting complexes.

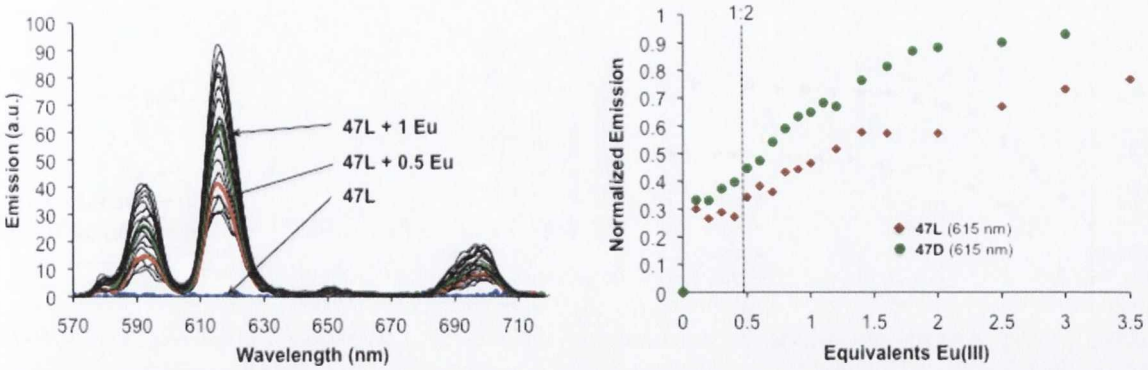


**Figure 3.17:** *Europium luminescence emission titration of **47L** (left) and isotherm of complexation of **47L** and **47D** at 615 nm (right).*

Consequently, the interpretation of the luminescence emission titrations was challenging and did not allow for any accurate determination of the complexation process. In order, to highlight the self-assembly process the lifetimes were calculated from the $Eu^{III}$ emission decays (at $\lambda_{em}$ = 615 nm) for a solution containing a 1:2, 1:1, 3:2 and 2:1 Eu:L ratio and these results are summarised in Table 3.2. In each case, the luminescence decays fitted a mono-exponential decay. These results were indicative of the formation of a predominant $Eu^{III}$ luminescent species in solution at each stage of the titration. Furthermore, the lifetime values remained *quasi*-constant upon the addition of 1 equivalent of europium, which

**Table 3.2:** *Lifetimes in $CH_3CN$ calculated from the luminescence decays at different M:L ratios in solution*

| M:L | $\tau_{1:4}$ | $\tau_{1:2}$ | $\tau_{1:1}$ | $\tau_{3:2}$ | $\tau_{2:1}$ |
|---|---|---|---|---|---|
| **47L** | 0.380 | 0.378 | 0.361 | 0.325 | 0.318 |
| **47D** | 0.282 | 0.276 | 0.262 | 0.248 | 0.223 |

suggests the formation of the desired **$47L_2$.Eu** species. However, at higher $Eu^{III}$ concentration, the lifetime values experience a decrease of 25% and 21% for **47L** and **47D**, respectively, which can be attributed to the previously mentioned formation of the 1:1 stoichiometric (M/L) complexes.

The self-assembly was further investigated using the non-linear regression analysis software SPECFIT®. In both cases, the serial fitting of the results obtained from different UV-vis titrations of **47L** and **47D** have all concluded the formation of two different species during the course of these titrations as shown by the resulting fits and calculated speciation distribution diagrams, in Figure 3.18 (and appendix 3.4 for **47D**). These results confirmed what was observed above, that in each case the predominant formation of the 1:2 species was detected, reaching a maximum of formation of 75% and 97% (at $[Eu^{III}] = 2\times10^{-5}$ M)

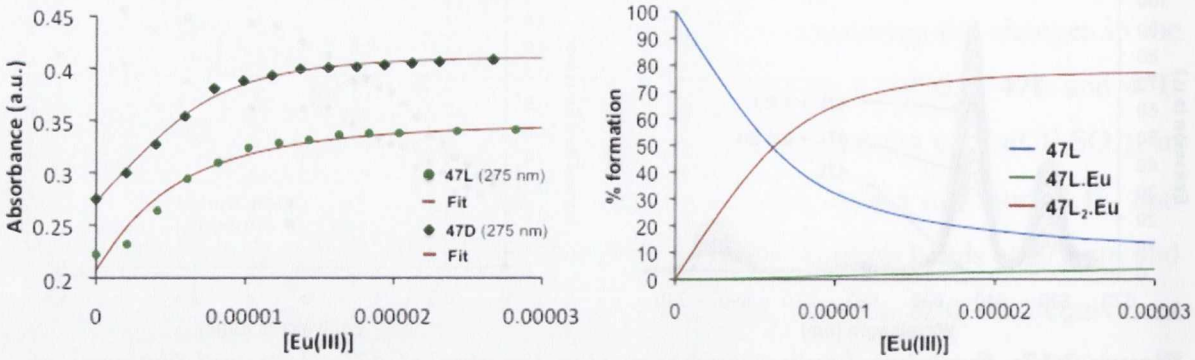


**Figure 3.18:** *Convergent fits obtained from the $Eu^{III}$ UV-vis absorption titration of **47L** and **47D** and the speciation distribution diagram obtained in the case of **47L**.*

for **47L$_2$.Eu** and **47D$_2$.Eu**, respectively. The presence of the 1:1 M/L complexes has also been detected after the addition of 1 equivalent of $Eu^{III}$. However, the formation of the **L.Eu** species, was calculated to be minor with a formation of less than 10% throughout the whole titration. The stepwise binding constants of the formation of each species (calculated from the overall binding constant *log* $\beta$) is summarised in Table 3.3 and these results confirmed that the 1:2 species was the most stable species formed with *log* $K_{1:2}$ = 5.4 and 6.8, for **47L** and **47D,** respectively. Unfortunately, the resulting lanthanide luminescence titrations could not be fitted accurately.

**Table 3.3:** *Binding constant and % formation of species obtained for **47L** and **47D** vs $Eu^{III}$ from the UV-vis titration.*

| M:L | *Log* $\beta_{1:1}$ | *Log* $\beta_{1:2}$ | *Log* $K_{1:2}$ | *% Formation at 1:2 M/L* | |
|---|---|---|---|---|---|
| **47L** | 4.7 ± 0.2 | 10.1 ± 0.3 | 5.4 | 1.3 | 71.1 |
| **47D** | 4.1 ± 0.6 | 10.9 ± 0.3 | 6.8 | 0.8 | 85.9 |

### 3.3.3 Photophysical properties of the 47L-47D$_2$.Tb complexes in solution

As previously mentioned, the triplet-excited states of tryptophan are lying at higher energy levels than the ones of the naphtyl chromophore making ligands **47L** and **47D** more suitable to sensitise the excited states of the $Tb^{III}$ ion than those of $Eu^{III}$. Consequently, the photophysical properties of the resulting terbium directed self-assemblies were also studied. The **L$_2$.Tb** molecular bundles were prepared *in situ* in a similar manner as the $Eu^{III}$ analogues, stirring ligands **47L** and **47D** ($C_L = 2\times10^{-5}$ M) over 5 minutes in the presence of 0.5 equivalents of $Tb(CF_3SO_3)_3$. As was observed in the case of **L$_2$.Eu**, the UV-vis absorption band centred at 275 nm experienced a strong hyperchromic effect of *ca.* 40%,

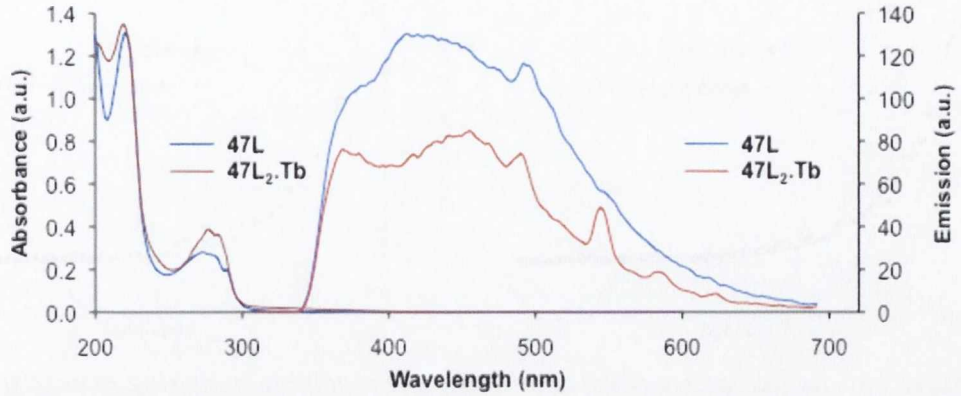


**Figure 3.19:** *UV-vis absorption and fluorescence emission spectra of* ***47L*** *($C=1\times10^{-5}M$) (blue) and its resulting complexes* ***47L$_2$.Tb*** *(red).*

which was accompanied by a red shift of 6 nm, as shown in Figure 3.19. Furthermore, the excitation of the tryptophan moiety gave rise to the metal centred $Tb^{III}$ luminescence of the complexes.

The excitation spectra of both enantiomers, which are shown in Figure 3.20 for **47L$_2$.Tb** (and in appendix 3.5 for **47D**), were also recorded and showed two major bands at 220 nm and 281 nm, matching the bands observed in the UV-vis absorption spectra of the ligands **47L** and **47D**, confirming that the $Tb^{III}$ emission was generated by an energy transfer from the $T^1$ excited states of the tryptophan antenna. The luminescence emission lifetimes were also recorded in $CH_3CN$, and were found to be longer than those seen for the $Eu^{III}$ complexes, fitting them to a mono-exponential decay (Figure 3.21), indicative of the presence of single luminescence species in solution. Furthermore, the lifetimes of the **L$_2$.Tb** excited states, $\tau$ = 0.860 and 0.910 ms for L = **47L** and **47D**, respectively.

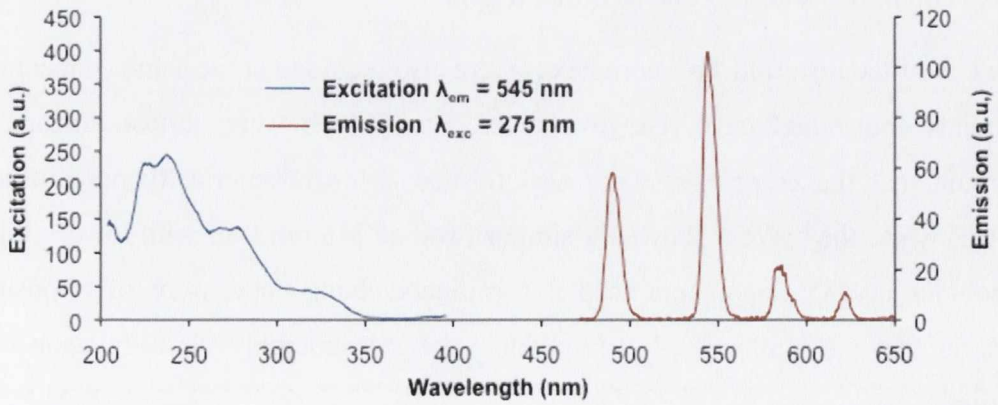


**Figure 3.20:** *Time delayed emission spectra ($\tau$ = 0.1 ms) of* ***47L$_2$.Eu*** *(red) and excitation spectra resulting from the $Tb^{III}$ emission at $\lambda$ =545 nm (blue).*

In order to further elucidate the influence the overall geometry of the complexes has on the optical activity of the molecular bundles **L$_2$.Tb** (L = **47L** and **47D**), the CD spectra of ligands **47L** and **47D,** and their resulting terbium complexes, were recorded in MeOH,

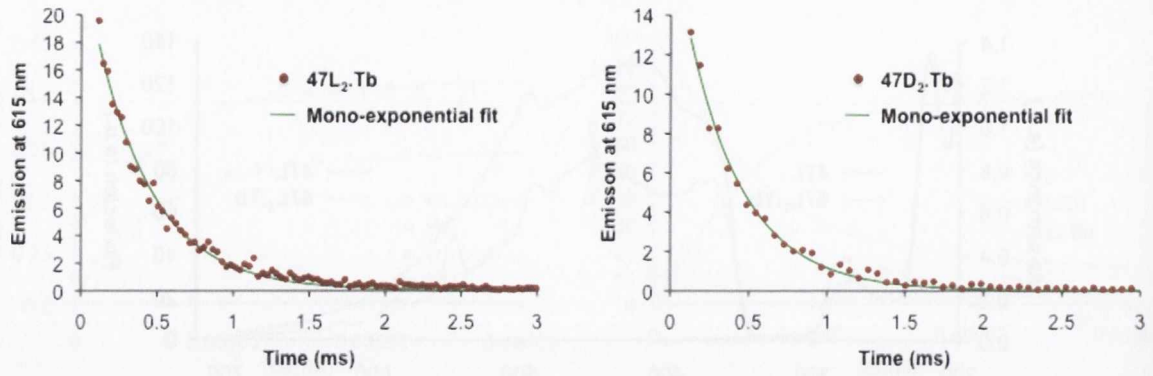


**Figure 3.21:** *$Tb^{III}$ luminescence emission decays at 545 nm and resulting mono-exponental fits of **47L$_2$.Tb** (left) and **47D$_2$.Tb** (right).*

Figure 3.22. The CD spectrum of **47L** displayed a major negative band centred at 249 nm with a shoulder at 285 nm, whereas the CD analyses of its isomer **47D** showed positive bands centred at the same wavelength, with the same intensity magnitude, confirming that each ligand was isolated enantiomerically pure.

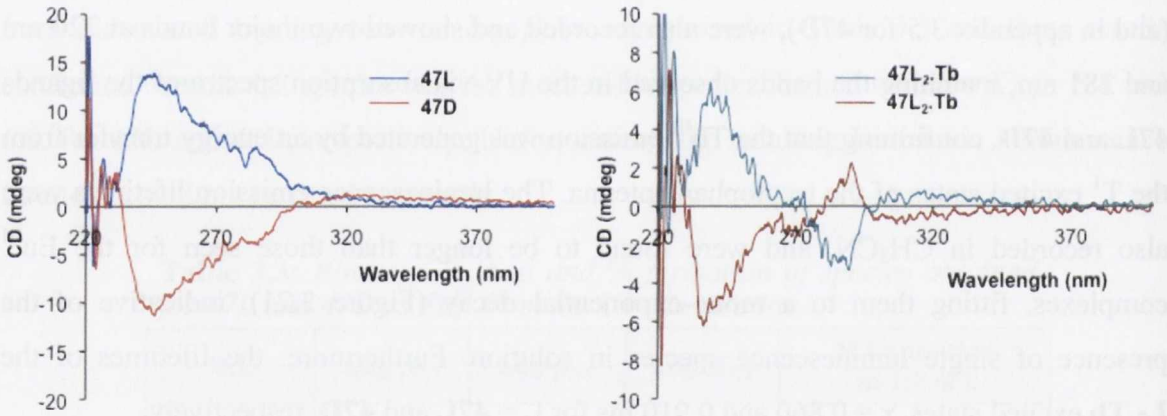


**Figure 3.22:** *CD absorption spectra of ligands **47L** and **47D** in $CH_3CN$ (left) and their resulting complexes **47L$_2$.Tb** and **47D$_2$.Tb** (right)*

The CD of the resulting $Tb^{III}$ complexes were also recorded at the same concentration as the ligands above and gave rise to two excitons, which were almost mirrors images confirming that the complexes were also formed as enantiomerically pure in solution. However, while the spectra showed a similar band at 245 nm (but with lower ellipticity), the shoulder at 285 nm experienced a significant change and were of opposite sign, suggesting that the lanthanide ion modulated the self-assembly chirality upon complex formation.

### 3.3.4 Solution studies of the complexation of $Tb^{III}$ by 47L and 47D

The formation of the $Tb^{III}$ complexes *in situ* was also studied by recording the UV-vis absorption and the luminescence emission spectra of the self-assemblies as a function of

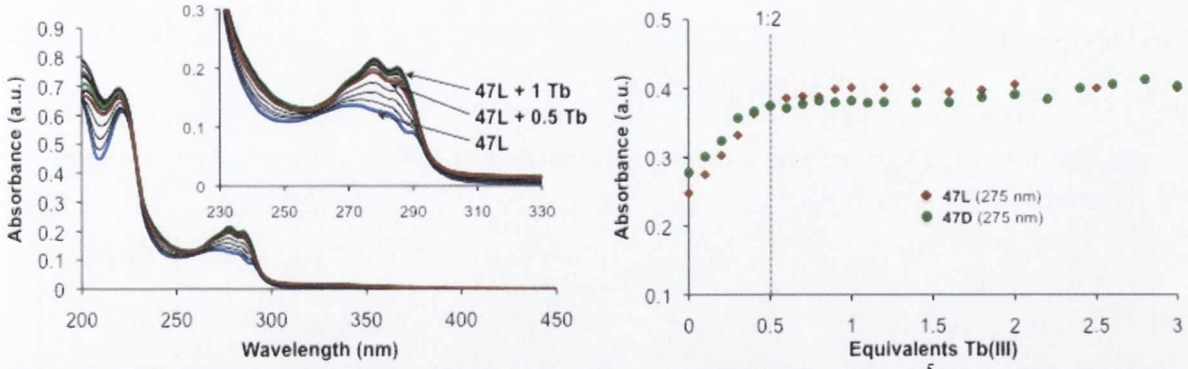


**Figure 3.23:** *UV-vis absorption terbium titration of* ***47L*** *at* $C_L = 2\times10^{-5}M$ *in* $CH_3CN$ *(left) and isotherms of complexation at* $\lambda = 275$ *nm.*

the quantity of terbium triflate in solution varying from 0→5 equivalents (**47L** and **47D** at $2\times10^{-5}$ M). The changes observed in the UV-Vis absorption spectrum are shown in Figure 3.23, and similar patterns to that previously obtained for the $Eu^{III}$ titrations were seen. The analyses of the changes in the UV-vis absorption titration showed that the formation of the 1:2 species occurred up to the addition of 0.5 equivalents. Therefore, the evolution of the UV-Vis absorption spectrum experienced only small changes at higher concentrations of $Tb^{III}$ ions.

The $Tb^{III}$ emission was also recorded and these changes are shown in Figure 3.24. In a similar manner to that seen for the complexation of $Eu^{III}$ by the ligands **47L** and **47D**, the terbium emission was "switched on" from 0→1 equivalents. However, at higher equivalents of metal ion in solution (1→2 equivalents), the evolution of the luminescence intensity enhanced slightly, beginning to reach a plateau upon the addition of 2 equivalents of $Tb^{III}$. These results might be due to either a kinetic effect for the formation of the desired 1:2 self-assembly, or even due to the formation of other minor species at high $Tb^{III}$ concentration. In order to investigate the behaviour of the self-assemblies in solution, the $Tb^{III}$ excited states lifetimes were recorded and these are summarised in Table 3.4. In each case, the luminescence decays were best fitted to a mono-exponential decay, indicative of

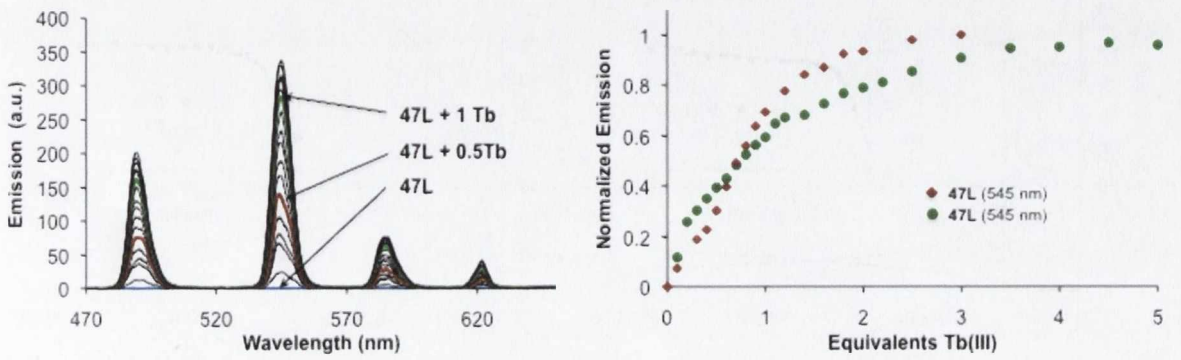


**Figure 3.24:** *$Tb^{III}$ luminescence emission titration of* ***47L*** *in* $CH_3CN$ *at C = 2×10-5M (left) and isotherm of complexation at 545 nm of* ***47L*** *and* ***47D****.*

the formation of a unique luminescent species in solution. Furthermore, the values of the lifetimes were found to remain constant throughout the titration, suggesting that the same species was formed at each molecular ratio.

**Table 3.4:** *Lifetimes of the terbium excited in $CH_3CN$ at different M:L ratio in solution*

| M:L | $\tau_{1:4}$ | $\tau_{1:2}$ | $\tau_{1:1}$ | $\tau_{3:2}$ | $\tau_{2:1}$ |
|---|---|---|---|---|---|
| L = 47L | 0.917 | 0.895 | 0.954 | 0.961 | 0.929 |
| L = 47D | 0.892 | 0.874 | 0.907 | 0.936 | 0.937 |

The formation of the self-assembly of ligands **47L** and **47D** with $Tb^{III}$ was further studied *via* non-linear regression analysis using the software SPECFIT®. The fitting of the absorption titration data, shown in Figure 3.23, gave rise to similar results to those calculated previously for the $Eu^{III}$ titrations previously studied. In the case of ligand **47L**, the formation of two species was observed and their overall speciation distribution determined, where a stable 1:2 stoichiometric species was formed after the first addition, reaching a maximum formation of 83.6% in the presence of 2 equivalents of $Tb^{III}$, indicative of the formation of the **$47L_2$.Tb,** with an average binding constant of $log\ \beta_{1:2}$ of 11.1. However, the convergence of the fits could not be obtained without taking into account the presence of a minor **47L.Tb** species, which was shown to be formed at $[Eu^{III}] > 0.5\times10^{-5}$M with a low binding constant ($log\ \beta_{1:1} = 4.6$). From these results the calculated speciation distribution plot (Figure 3.25), showed that the formation of the **47L.Tb** was detected to be less than 20% in the presence of an excess of $Tb^{III}$ in solution. This confirmed the formation of the complexes **$47L_2$.Tb,** the presence of which had been predicted by the lifetime experiments above.

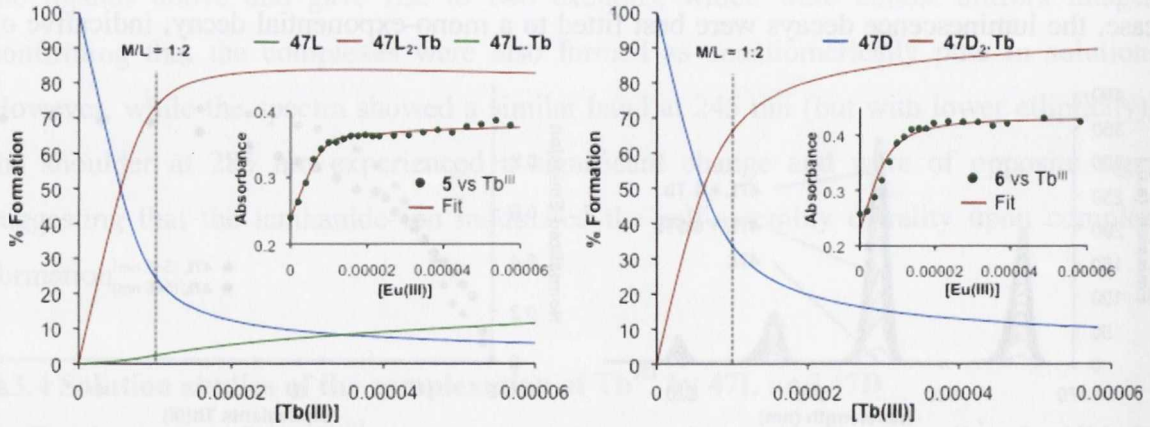


**Figure 3.25:** *Speciation diagrams obtained from the fits (insets) of the UV-vis absorption titrations of **47L** (left) and **47D** (right) with $Tb^{III}$*

The fitting of the data obtained for the UV-vis absorption titration of ligand **47D** with $Tb^{III}$, is shown in Figure 3.25, again showing the formation of the 1:2 stoichiometric species in the same concentration range as observed for **47L** (72.7% at 1:2 M/L ratio). From this analysis the binding constant log $\beta_{1:2}$ was detected as 11.3. However, unlike that seen above the formation of the **47D.Tb** species at higher $Tb^{III}$ concentrations was not observed. The binding constants determined for **47L** and **47D** summarised in Table 3.5 were calculated to be an average of two log units smaller than that obtained for the **27S-27R** analogues. This can be explained by the presence of the methoxy ester moieties, which can destabilise the supramolecular adducts due to their bulk.

**Table 3.5:** *Binding constant and % formation of species obtained for **47L** and **47D** vs $Tb^{III}$ from the UV-vis titration.*

| M:L | Log $\beta_{1:1}$ | Log $\beta_{1:2}$ | Log $K_{1:2}$ | % Formation at 1:2 M/L | |
|---|---|---|---|---|---|
| **47L** | 4.6 ± 0.3 | 11.1 ± 0.5 | 5.4 | 1.3 | 72.7 |
| **47D** | -- | 11.3 ± 0.3 | 5.6 | -- | 83.6 |

It can be concluded, from this study that ligands **47L** and **47D** gave rise to metal directed self-assemblies formation with $Eu^{III}$ and $Tb^{III}$, forming selectively the 1:2 stoichiometric complexes in solution. Indeed, each ligand can provide up to five donors atoms, forming a decadentate cavity, capable of fulfilling the coordination requirement of these lanthanide ions. It has also been established that the presence of the tryptophan moieties was more suitable for sensitising the $^5D_4$ excited state of $Tb^{III}$ than the $^5D_0$ of $Eu^{III}$. The correlation of the results displayed within the two last sections illustrated that the use of small chiral ligands was suitable for the stereoselective synthesis of chiral molecular bundles. Moreover, the synthetic strategy proposed for the pairs **27** and **47** offered a straightforward pathway for the synthesis of functional $C_2$ symmetric ligands, which allow for the modification of the overall chirality of the complexes by tuning the geometry and the stoichoimetry of the supramolecular architectures. Having illustrated that the utilisation of symmetric ligand containing two chiral antennae gave rise to enantiomerically pure molecular bundles, the formation of chiral luminescent self-assemblies was further investigated using asymmetric ligands containing a unique antenna.

### 3.4 Formation of molecular bundles based on linear asymmetric ligands

The next step in our research plan for the development of stereoselective lanthanide directed self-assemblies was to focus our study on non-symmetric ligands. The ligands **51R** and **51S** are like "half" structures of **27S** and **27R** and will be discussed in section 4.2.1 and are shown in Figure 3.26. These were synthesised, in collaboration with C. Destribats, in three steps from the dipicolic acid, following the procedure described in the

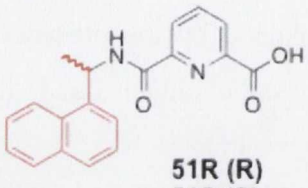


**51R (R)**
**51S (S)**

**Figure 3.26:** *Asymmetric ligands envisaged for the synthesis of chiral supramolecular bundles.*

thesis of Dr. F. Stomeo.[127] The ligands **51R** and **51S**, were originally developed for the synthesis of ditopic ligands, where it was foreseen that the asymmetric aspect of these compounds could induce a different geometry of the complexes formed to that observed for ligands **27S-R**. This could tune the helicity and consequently the overall chirality of the resulting self-assembly. The central pyridinyl moiety was functionalised with a carboxylic acid group, which would further allow for the functionalisation towards the development of larger non-symmetrical ligands.

#### 3.4.1 Photophysical properties of the 51R-51S$_3$.Eu complexes in solution

The complexes **L$_3$.Tb** were synthesised *in situ* in a similar manner to that previously described for **27**, where a solution of ligand **L (L=51R and 51S)** in $CH_3CN$ was stirred for 5 minutes with 0.33 equivalents of $Eu(CF_3SO_3)_3$. The UV-vis absorption and fluorescence

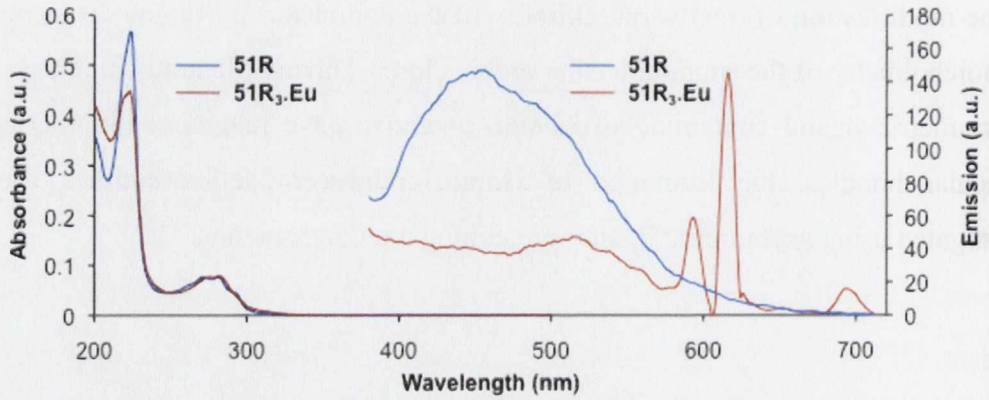


**Figure 3.27:** *UV-vis absorption and fluorescence emission spectra ($\lambda exc$ = 281nm) of **51R** (blue) and its resulting complex **51R$_3$.Eu** (red) in $CH_3CN$ $C_L = 1\times10^{-5}M$*

emission spectra were recorded in $CH_3CN$ (at $1\times10^{-5}$ M) and are shown in Figure 3.27 for **51R** and in appendix 3.6 for **51S**. In the presence of $Eu^{III}$, the absorption band centred at $\lambda_{max}$ = 224 nm experienced a significant hypochromic effect upon the complexation to $Eu^{III}$ of 22%, whereas a hyperchromic of the same magnitude (22%) was observed at 210 nm. In addition, the $^1\pi\pi^*$ transitions centred at 281 nm experienced a broadening effect upon complexation.

The excitation of the naphtyl chormophore gave rise to fluorescence emission caused by the radiative deactivation of the $^1\pi\pi^*$ excited states of the ligand with a $\lambda_{max}$ at 448 nm. Upon binding to $Eu^{III}$ this emission band was significantly quenched while the presence of the $Eu^{III}$ emission was observed, as shown in Figure 3.28, which indicates the successful double energy transfer from the excited states of the ligand to the $^5D_0$ level of $Eu^{III}$. The excitation spectrum of the lanthanide centred emission, is also shown in Figure 3.28,

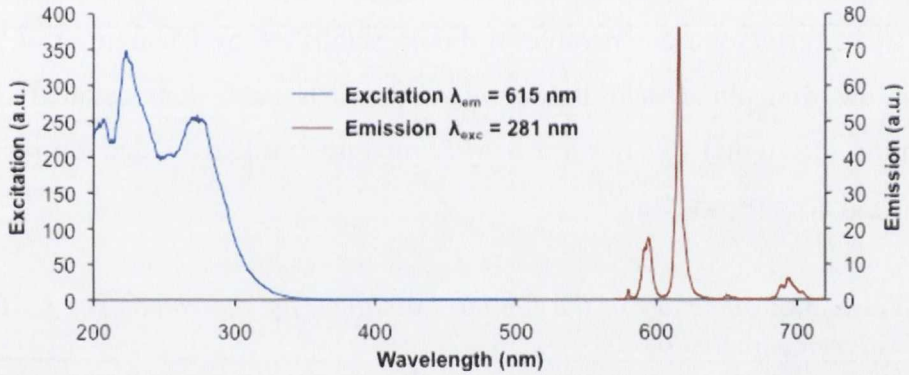


**Figure 3.28:** *Time delayed emission spectra ($\tau$ = 0.1 ms) of **51R$_2$.Eu** (red) and excitation spectra resulting from the $Eu^{III}$ emission at $\lambda$ =615 nm (blue).*

exhibited two major bands at 220 nm and 275 nm, which matched the transitions observed in the absorption spectrum of the ligands, confirming that the excited states of the europium ions are mainly sensitised *via* energy transfer from the ligand excited state.

The lifetime of the $^5D_0$ excited state of $Eu^{III}$ was also calculated form the luminescence emission decays, when recorded in $CH_3CN$, $H_2O$ and $D_2O$ and these are summarised in Table 3.6. These when recorded in $CH_3CN$ and $D_2O$ were fitted best to a mono-exponential decay, which suggests the presence of a single luminescent species in solution (Figure 3.29). However, the decay in $H_2O$ was fitted best to a bi-exponential function indicating the presence of several luminescent species in solution. The first species exhibited a long lifetime in the range of $\tau_1$ = 1.7 ms for both isomers and has been calculated to be the predominant species with a population of *ca.* 57% and 64% for **51R** and **51S**, respectively.

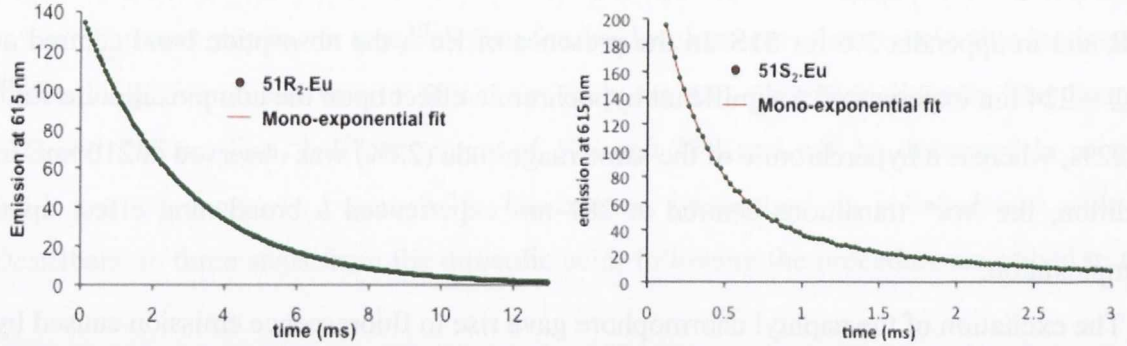


**Figure 3.29:** *Luminescence emission decays recorded in $CH_3CN$ for 51R3.Eu (left) and 51S3.Eu (right) and their resulting mono-exponential fits.*

The hydration state of this species was determined by the formula derived by Horrocks and co-workers,[18] and was found to be 0 suggesting that the major luminescent species present in water was the **L3.Eu** complexes. The second species, which was formed in *ca.* 35% yield, was determined to contain three water molecules in the inner coordination sphere of $Eu^{III}$ indicating the secondary formation of the 1:2 stoichiometric self-assembly in $H_2O$. These results are comparable to those established by Chauvin *et al.*[126] who has developed the dipicolinic acid based ligands, which have demonstrated that at low concentration ($1\times10^{-5}$M) in $H_2O$ a 1:3 M/L mixture resulted in the formation of 60% **(dpa)3.Eu** and 40% **(dpa)2.Eu**.

**Table 3.6:** *Summary of the lifetimes obtained for the complexes L3..Eu and hydration factors q*

| M:L | $\tau_{(CH_3CN)}$ | $\tau_{(D_2O)}$ | $\tau_{(H_2O)}$ % Pop | | q | |
|---|---|---|---|---|---|---|
| L = 51R | 0.917 | 2.760 | 1.683 | 0.304 | 0 | 3.21 |
| | | | 57% | 33% | | |
| L = 51S | 0.892 | 3.395 | 1.665 | 0.306 | 0.11 | 3.27 |
| | | | 64% | 36% | | |

### 3.4.2 CD and CPL invstigations of the 51R-S3.Eu complexes in solution

The dissymmetry of the excited state was also investigated by carrying out the CD analyses of the ligand and their resulting 1:3 complexes in $CH_3CN$. These results are shown in Figure 3.30. In both cases, the ligands and their resulting $Eu^{III}$ complexes, gave rise to two excitons of equal intensity but with opposite signs, indicating that each ligand and the corresponding 1:3 (M/L) complexes were obtained in enantiomerically pure form. The CD spectrum of both enantiomers gave two absorption bands centered at 234 nm and 287 nm, which were negative and positive in the case of the R and S isomer respectively. Moreover, these had higher ellipsity than their symmetric analogues **27S** and **27R**, which

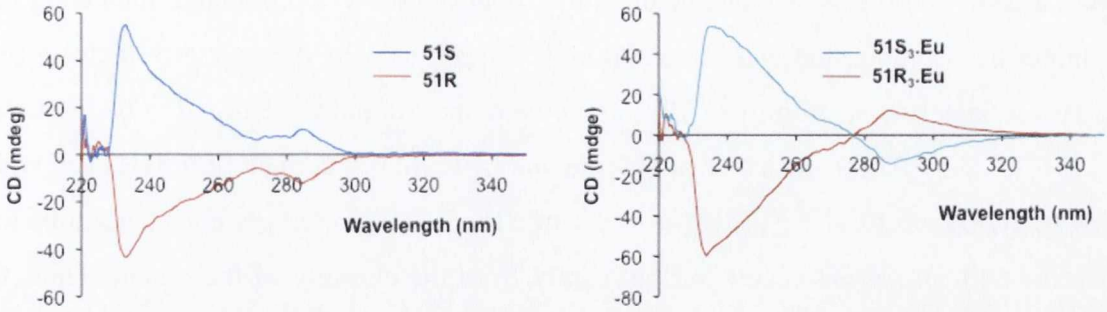


**Figure 3.30:** *CD spectra of ligands **51R** and **51S** in $CH_3CN$ (left) and their resulting complexes **51S$_3$.Eu** and **51R$_3$.Eu** (right).*

could suggest an enhanced chirality due to the asymmetric aspect of the ligands **51R** and **51S**. However, the self-assembly of the three ligands around the lanthanide ion resulted in significant changes in the optical activity of the resulting complexes. Hence, the band at 235 nm of **L$_3$.Eu** (L= **51R** and **51S**) showed similar intensities, the band typical of the $S_0 \rightarrow {}^1\pi\pi^*$ transitions of the ligand experienced a reversal of its sign, upon complexation with $Eu^{III}$, which was not observed for **27S-R$_3$.Eu**. This may be indicative of a different topologic chirality induced by the helical shape of the complexes **L$_3$.Eu**.

This was further confirmed by the CPL experiment, carried out by Dr. R. Peacock in Glasgow University, the results of which are shown in Figure 3.31. The CPL spectrum of **51R$_3$.Eu** displayed a negative band at 595 nm corresponding to the $^5D_0 \rightarrow {}^7F_1$ transition and a positive band at 617 nm for the $^5D_0 \rightarrow {}^7F_2$ transition with a weak negative shoulder at 620 nm. The emission band at 693 nm ($^5D_0 \rightarrow {}^7F_4$ transitions) showed a positive contribution at 692 nm followed by a negative one at 702 nm. Conversely, the complex

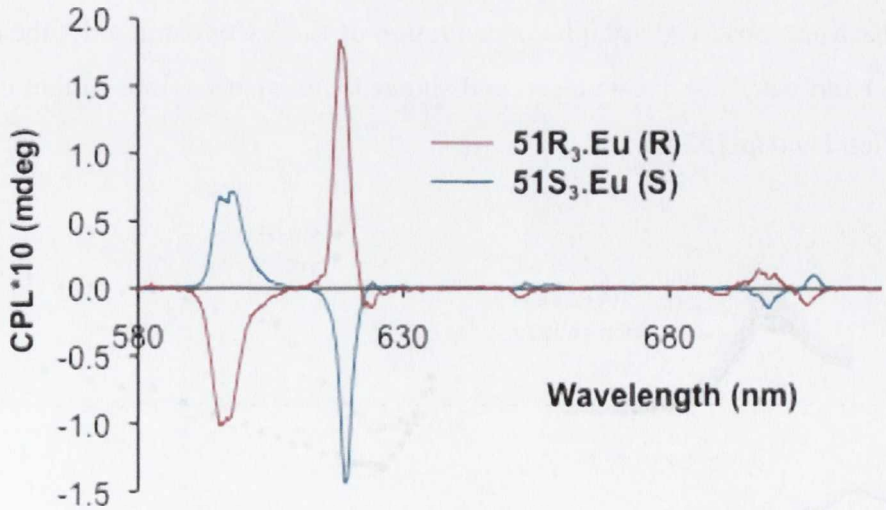


**Figure 3.31:** *CPL spectra of the complexes **51R$_3$.Eu** (red) and **51S$_3$.Eu** (blue) in $CH_3OH$ $\lambda_{ex}$ = 281 nm.*

**51S$_3$.Eu** exhibited the same bands with similar intensities but opposite sign indicating that the luminescence emission was chiral for both complexes. The dissymmetry factor $g$ ($g$ = 2ΔI/I) were determined from the CPL luminescent spectra and were found to be high with $g_{em}$ = -0.15 and 0.06 for the bands at 600 nm and 619 nm, respectively, for **51R$_3$.Eu**, while being $g_{em}(600)$ = 0.13 and $g_{em}(619)$ = -0.05 for **51S$_3$.Eu**. Reported $g$ values tend to be low when the CPL properties result predominantly from the chirality of the ligand. Thus, the relatively high values obtained here suggested that each helical isomer **L$_3$.Eu** was formed as enantiomerically pure and remained homochiral in solution. The comparison of these results with those previously obtained for **27S$_3$.Eu** and **27R$_3$.Eu,** for which the absolute configuration has been solved using X-ray crystallography allowed for the handedness of the mono-metallic helical complexes being Λ and Δ for **51R$_3$.Eu** (R) and **51S$_3$.Eu** (S), respectively, to be determined.

### 3.4.3 Solution studies of the complexation of $Eu^{III}$ with 51R-51S

The formation of the chiral supramolecular bundles **51R$_3$.Eu** and **51S$_3$.Eu** were investigated *in situ*. The spectrophotomeric titrations were performed in $CH_3CN$ ($1\times10^{-5}$ M) in a similar manner as described previously, using $Eu(CF_3SO_3)_3$ salt. The changes obtained in the UV-vis absorption spectrum are illustrated in Figure 3.32. Here, the major changes in the absorption spectra were observed for the high-energy transitions, the absorption bands centred at λ = 222 nm experiencing a large decrease in absorbance up to the addition of 0.33 equivalents of $Eu^{III}$, indicative of the formation of the 1:3 stoichiometric species. The displacement of the equilibrium towards other stoichiometry, such as the 1:2 or 1:1 M/L species could also be clearly observed by the hyperchromic effect in the spectrum, observed at high concentration of $Eu^{III}$. Concomitantly, the changes observed at 281 nm were less pronounced and showed similar behaviour to that observed for the absorption band at 222 nm.

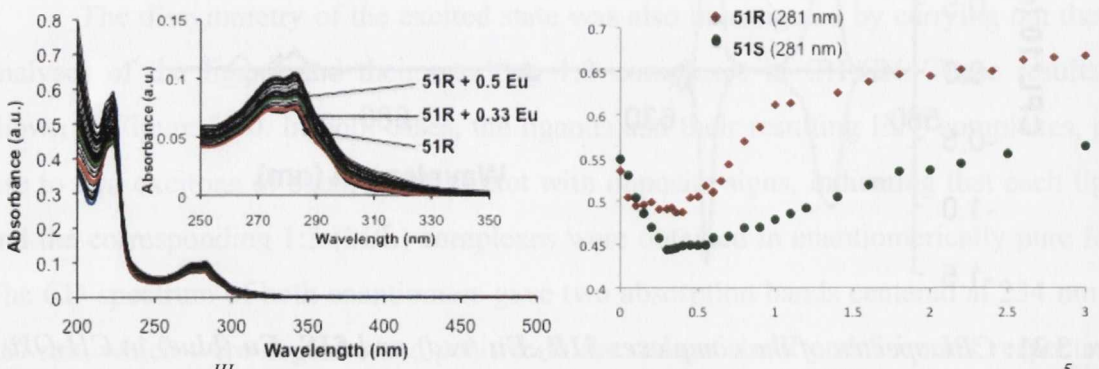


**Figure 3.32:** *$Eu^{III}$ UV-vis absorption titration of **51R** in $CH_3CN$ at CL =$1\times10^{-5}$M and isotherms of complexation at 222 nm for **51R** (red) and **51S** (green)*

The solution profiles obtained from the luminescence emission titrations (recorded from the same solutions) are shown in Figure 3.33. Here, the addition of $Eu(CF_3SO_3)_3$ to both enantiomers gave rise to typical europium emission. Here, the changes observed in the emission intensity experienced a significant increase upon the addition of 0→0.33 equivalents of $Eu^{III}$ (0.35 in the case of **51S**), where it reached a maximum intensity. These results suggested the stable formation of the 1:3 M/L complexes, as previously observed in the above UV-vis absorption titration. However, a large decrease in the emission intensity was observed in both cases upon the addition of 0.33→1 equivalents of $Eu^{III}$. This is significant of the aforementioned displacement of the complexation equilibrium towards the 1:2 species, which are less luminescent due to the higher hydration states of $Eu^{III}$. This decrease of the emission intensity of **51R** reached a plateau upon the addition of 1.5 equivalent (1.8 eq for **51S**) of metal ions, which can be attributed to either slow equilibration of the formation of the 1:1 M/L stoichiometric species.

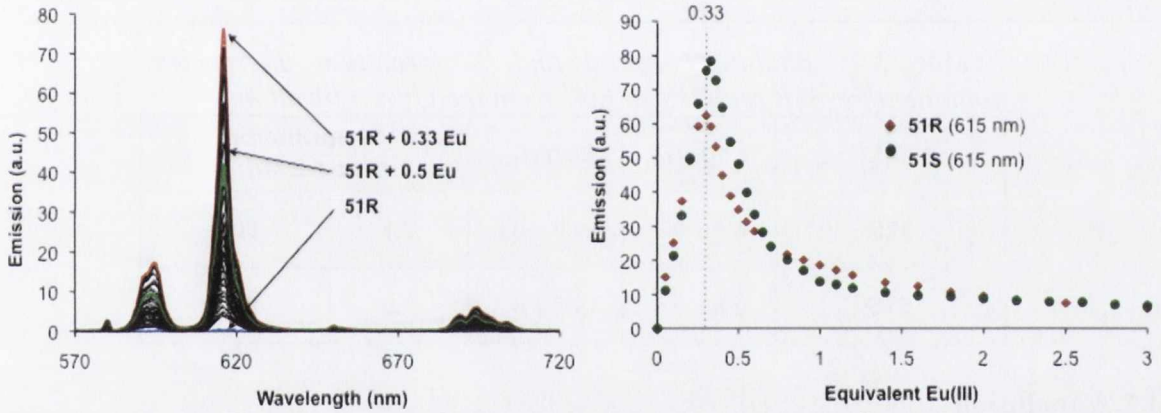


**Figure 3.33:** *$Eu^{III}$ luminescence emission titration ($C_L$ = 1×10$^{-5}$M; $\lambda_{ex}$ = 281 nm) in $CH_3CN$ of **51R** (left) and isotherms of complexation (right) of **51R** (red) and **51S** (green).*

The changes observed in the UV-vis titrations were analysed by fitting several different data sets using the non-linear regression analysis. This allowed for the calculation of the speciation distribution diagrams shown in Figure 3.34 (and in appendix 3.7 for **51S**). The binding constant for the formation of each of the species are summarised in Table 3.7. In the case of both isomers, the formation of two main species was observed. As anticipated, the 1:3 M/L stoichiometric species was solely formed at low $Eu^{III}$ concentration ($[Eu^{III}]$ < $3.3\times10^{-6}$ M for both isomers) with high binding constant of log $\beta_{13}$ = 19.8 and 19.7, for **51R$_3$.Eu** and **51S$_3$.Eu**, respectively, being formed in *ca.* 86.5 % and 90.5 % yields up to the addition of 0.33 equivalents of $Eu^{III}$ ion in solution. This confirmed the selective formation of the **L$_3$.Eu** complexes in solution, for which the nine coordination sites of the europium ion are fulfilled by the self-assembly of three ligands. However, the formation of the 1:1 species was also visible after the addition of 0.3 equivalents of europium, and

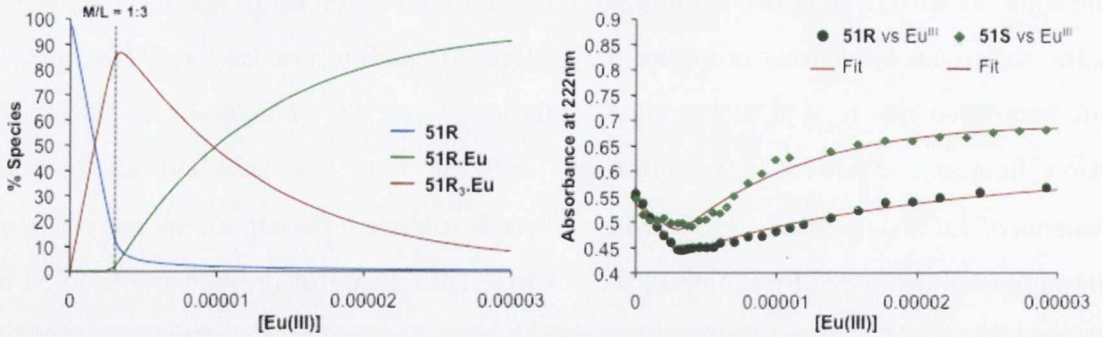


**Figure 3.34:** *Typical speciation diagram (left) obtained from the fits (right for **51S** and **51R**) of the $Eu^{III}$ UV-vis titration of **51R-S**.*

becoming the predominant species formed at equimolar metal-ligand ratio in solution with binding constants in the range of log $\beta_{11} \approx 6.5$-7. Even if the binding mode relative to the 1:1 stoichiometric species could not be solved accurately, it has been illustrated that the ligands **51R** and **51S** are suitable to form enantiomerically pure chiral supramolecular bundles.

**Table 3.7:** *Binding constant and % formation of species obtained for **51R** and **51S** vs $Eu^{III}$ from the UV-vis titration.*

| M:L | Log $\beta_{1:1}$ | Log $\beta_{1:3}$ | % Formation at 1:2 M/L | |
|---|---|---|---|---|
| **51R** | 6.5 ± 0.3 | 19.9 ± 0.6 | 2.1 | 90.5 |
| **51S** | 6.8 ± 0.4 | 19.7 ± 0.5 | 3.9 | 86.5 |

### 3.5. Conclusion

The previous work performed by Drs. J. Leonard and N.S. Murray, illustrated that the functionalisation of **dpa** units with chiral centres provided an efficient strategy for the formation of homochiral luminescent probes and have also shown that three ligands self-assemble around a $Ln^{III}$ ion in the form of a triple stranded helicate.

The work described within this chapter has shown the predominant formation of the desired complexes *in situ* with high binding constants. However, it was also shown that the design of the ligand could potentially allow tuning the geometry and therefore the photophysical properties of the complexes. The functionalisation of the **dpa** units with simple napthyl based chiral antennae, such as in the case of **27S-27R** and **51R-51S**, gave rise to 1:3 molecular bundles with a $C_3$ geometry, which showed large dissymmetry factors due to the induction of further topological chirality through self-assembly. However, the spectrophotometric $Ln^{III}$ titrations have shown that the tryptophan-based self-assemblies have been formed predominantly with a 1:2 (M/L) stoichoimetry. Furthermore, the CD of the ligand experienced dramatic changes upon complexation, which were more

pronounced than that of the naphtyl-based analogue, **27S-4$_3$.Eu** illustrating that the complexation influenced greatly the overall chirality of the resulting complexes. The formation of molecular bundles was also studied with asymmetric ligands containing only one naphthyl antenna and the complexation process was found to occur in a similar manner to that of the sliotar analogues. However, the CD and the CPL experiments gave rise to dissymmetry factors lower by *ca.* 50% in the emission, demonstrating the importance of both the overall geometry and the chiral antenna in the chirality of the complexes.

# Chapter 4:

# Synthesis and photophysical studies of dimetallic chiral luminescent triple stranded helicates

**Chapter 4: Synthesis and photophysical studies of dimetallic chiral luminescent triple stranded helicates.**

## 4.1 Introduction

It has been well established in the literature and previously discussed in the introduction, that the metal templated formation of self-assemblies offers an interesting strategy for the introduction of chirality within the resulting supramolecular structures.[128,129] With the aim of enhancing the dissymmetry of the lanthanide, the research in our group has more recently focused on the formation of chiral luminescent bimetallic triple stranded helicates. These systems give rise to elegant systems yielding highly stable chiral luminescent systems (described in the next section), the precursors of which (**51R-51S**) were studied in the previous chapter. We have also demonstrated that the design of the ligand could have a dramatic influence on the properties of the supramolecular architecture. [41,112,127]

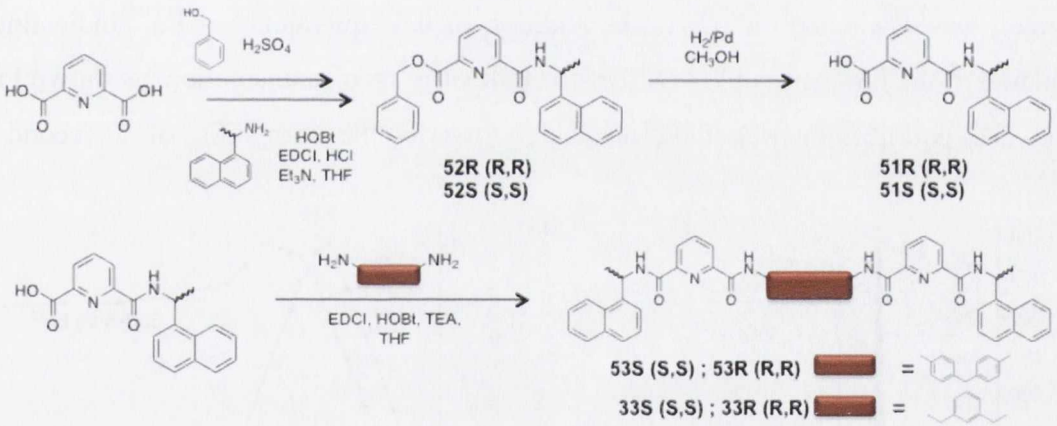


**Figure 4.0:** *Synthesis route for the development of the two pairs of enantiomers 53 and 33.*

The two pairs of ligands **53R-S** and **33R-S** were designed with two chiral naphthalene moieties connected to two pyridine-2,6-dicarboxamide tridentate moieties linked by a rigid aromatic spacer, such as 1,3-xylene (**33R-33S**) or 4,4'-diaminophenylmethane (**53S-53R**). Each of these ligands was synthesised from the pyridine-2,6-dicarboxylic acid in four steps, as shown in Figure 4.0. The starting di-carboxylic acid was first monoprotected to give the mono-benzyl ester, followed by peptide coupling of the chiral naphthalene antenna to the free carboxylic acid function of the resulting mono-benzyl ester in 81% yield. The deprotection of the benzyl group was achieved by hydrolysis in the presence of palladium catalyst, yielding the half-ligands **51R** and **51S**, which were isolated enantiomerically pure in 92% yield after filtration through

celite. The final peptide coupling with the corresponding diamine was achieved in the presence of EDCI and HOBt giving rise to the ditopic ligands **53S-33S** in 30-60% yields, respectively. The high-resolution mass spectrometry analysis showed, in each case, the presence of a mono-charged species $(M+Na)^+$, which matched the calculated isotopic distribution pattern, while the $^1$H-NMR spectra clearly demonstrated the presence of a single species with $C_2$-symmetry. Moreover, CD analysis confirmed that each of these ligands were isolated enantiomerically pure.[41,112,127]

The self-assembly of the ditopic ligands **53S-33S** was investigated in $CH_3CN$ solution, in order to establish the influence of the central spacer on the complexation process and on the resulting geometry. This was undertaken using UV-vis absorption spectroscopy, which showed that for ligands **53S** and **53R**, the band centred at $\lambda_{max}$ = 281 nm experienced a hypochromic effect upon complexation of the lanthanide. This suggested the stable formation of the $\mathbf{L_3.Ln_2}$ species (Ln = Eu for L= **53S-53R** and Ln = Eu, Tb, Sm, Lu for L=**33R-33S**), which was also shown to form during the luminescence titrations of **53R,** as demonstrated in Figure 4.1. Indeed, in each case, the lanthanide luminescence emission was "switched on" up to the addition of 0.6 equivalents of $Eu^{III}$ indicating the formation of the luminescent 2:3 (M/L) stoichiometric species in solution, as shown Figure 4.1b. The equilibrium was then displaced towards the formation of a second less

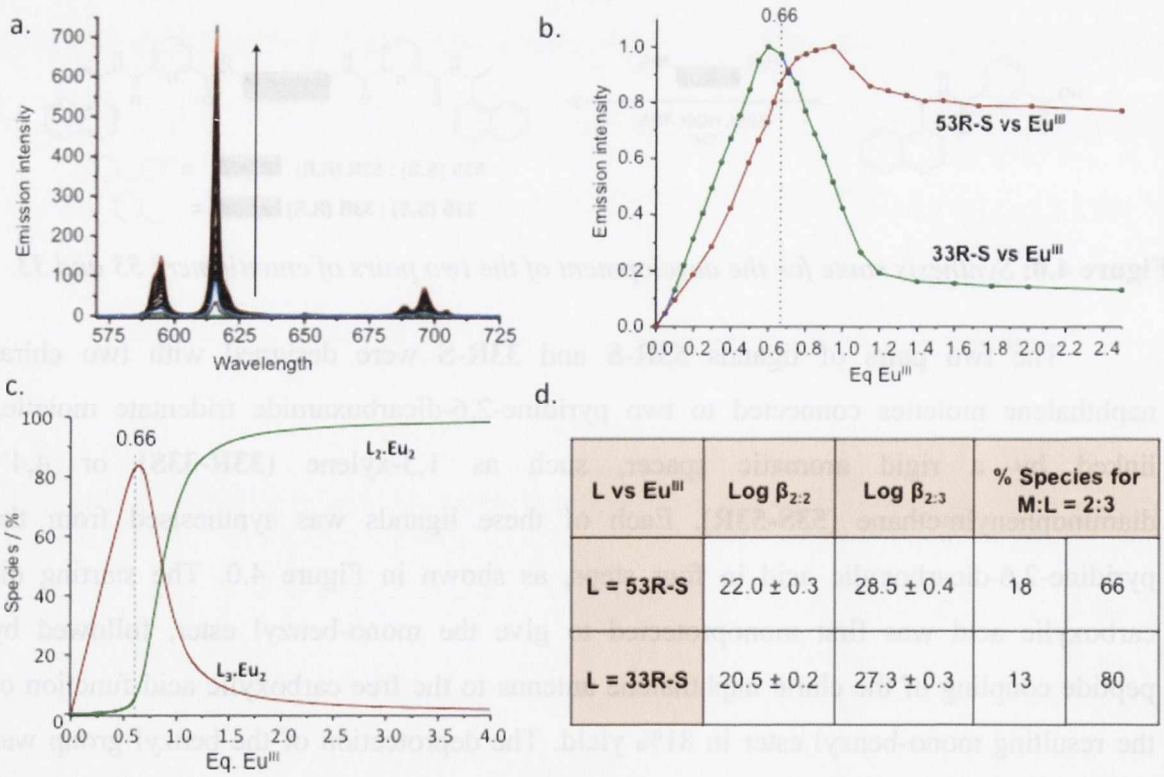


d.

| L vs $Eu^{III}$ | Log $\beta_{2:2}$ | Log $\beta_{2:3}$ | % Species for M:L = 2:3 | |
|---|---|---|---|---|
| L = 53R-S | 22.0 ± 0.3 | 28.5 ± 0.4 | 18 | 66 |
| L = 33R-S | 20.5 ± 0.2 | 27.3 ± 0.3 | 13 | 80 |

**Figure 4.1:** *Studies of the formation of the triple stranded helicates* $\mathbf{L_3.Eu_2}$ *in situ performing the luminescence titration in* $CH_3CN$ *(top) and the obtained from their fitting (bottom)*[41,112]

luminescent species, complexes $\mathbf{L_2.Eu_2}$, up to the addition of 1-1.2 equivalents of metal ion. In each case, the binding constants and the speciation distribution plots were calculated and the results are summarised in Figure 4.1d and also illustrated by the example of **53R** in Figure 4.1c. For each ligand, the $\mathbf{L_3.Eu_2}$ complex was calculated to form with similar binding constants of Log $\beta_{23} \approx 28$. The triple stranded helicates were more favourably formed for ligands **33R-33S** than for ligands **53S-53R**, 80% and 66% formation at a 2:3 M/L ratio, respectively. This may be due to the flexibility of the 1,3-xylene bridge, which could ease the self-assembly process of three ligands with the two lanthanide ions. However, the difference in behaviour between the two sets of enantiomers **53S-53R** and **33R-33S** remained small (2 log units of magnitude), with the predominant formation of the $\mathbf{L_3.Ln_2}$ being demonstrated in each case.[41,112]

### 4.2 Design of the ligands

Here, we aim to develop chiral ligands, building on the work described in the previous section, and study their interaction with lanthanide ions with the view of forming chiral luminescent self-assemblies. Thus, the ligands **53S-53R** and their structural isomers **54S-54R** (Figure 4.2) were designed to enable the coordination of two lanthanide ions *via* two subunits **51R** or **51S,** which consist of one naphthylethylaminepyridinyl capable of fulfilling three of the nine coordination sites of the lanthanide and allowing the sensitisation of its excited states. These subunits were separated by a methylene-diphenyl spacer, which can allow the tuning the geometry and the chirality of the resulting helicates. The enantiomers, **53S-53R**, contained a 4,4'-diaminodiphenylmethane bridge, offering an inherent preorganisation to the ditopic ligand, which could potentially stabilise the resulting helicates *via* weak interactions such as π-π stacking.

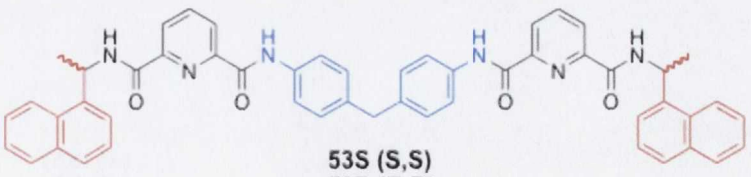

**53S (S,S)**
**53R (R,R)**

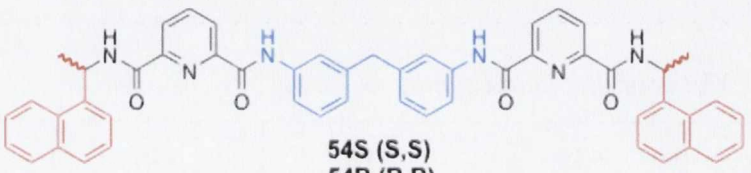

**54S (S,S)**
**54R (R,R)**

**Figure 4.2:** *Ditopic ligand envisaged for the synthesis of chiral luminescent triple stranded helicates.*

In order to investigate the relationship between the ligand conformation and the geometry of the resulting helicates, a second pair of isomers, **54S** and **54R,** were designed with a 3,3'-diaminodiphenylmethane bridge, which could potentially cause the phenyl ring to point outside the plane of the helicates, inferring different helicity and varied Ln-Ln distances to the helicates, as has been shown by Piguet *et al.*[83] The next section deals with the synthesis and the characterisation of these ligands.

### 4.3 Synthesis and characterisation of ligands 53S-53R and 54S-54R

The ligands **53S-53R** and **54S-54R** were synthesised in a one-step synthesis from the subunits **51R** and **51S** (studied in Chapter.3), following the synthetic procedure developed by Dr. F. Stomeo (PhD thesis) and shown in Figure 4.3.[127] The two half-helicates were joined with the corresponding diamino spacer *via* a peptide coupling reaction, using EDCI.HCl and HOBt. Each ligand was isolated in average yields (~ 40-60% summarised in Table 4.1) enantiomerically pure after a simple washing with a solution of sodium carbonate. Characterisation was carried out using conventional spectroscopic methods, such as $^{1}$H- and $^{13}$C-NMR, IR spectroscopy and mass spectrometry, as well as elemental analyses.

The $^{1}$H-NMR analyses ($CDCl_3$, 400 MHz) demonstrated that in each case the ligands possessed a $C_2$ symmetry. The methylene bridge was visible as doublets occurring at 3.95, 3.40 and 3.46 ppm, for **53S-53R**, **54S** and **54R,** respectively, whereas the proton of the chiral centre resonated at 6.1 and 6.0 ppm for the pairs **53S-53R** and **54S-54R**,

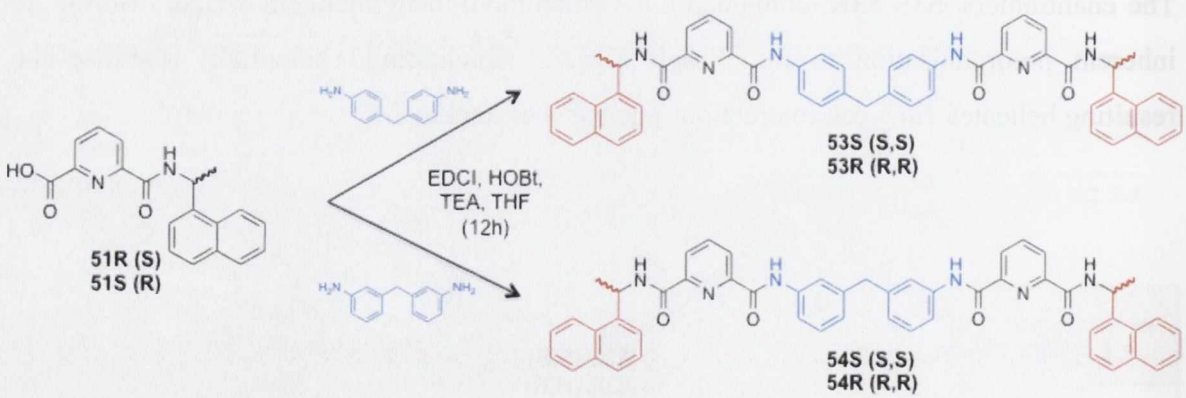


**Figure 4.3:** *One-step synthesis of ligands **53S-53R** and **54S-54R** from the half-ligands **51S-51R**.*

**Table 4.1:** *Yields of the ligand synthesis*

| L | 53S | 53R | 54S | 54R |
|---|---|---|---|---|
| **% yield** | 60 % | 44 % | 60 % | 62 % |

respectively. The methyl group resonated as a doublet, due to the scalar coupling with the previously mentioned, chiral centre, at 1.85 ppm, in the case of **53S** and **53R** and at 1.75 ppm for **54S-54R**. The HRMS experiments performed on **54S** and **54R** confirmed the successful synthesis of the ligands, which were detected as a mono charged fragment for $M+Na^+$ at m/z = 825.3137 and 825.3128, respectively (calculated at m/z = 825.3165). However, neither compound **53S** nor **53R** could be detected by ESI mass spectrometry and no evidence of the starting material was seen. Further analyses using MALDI-ToF MS and the use of different solvents did not identify the desired products.

### 4.4 Synthesis and characterisation of the triple stranded helicates $L_3.Eu_2$

The triple stranded helicates $\mathbf{L_3.Eu_2}$ ($\mathbf{53S_3.Eu_2}$ and $\mathbf{53R_3.Eu_2}$ published in the PhD thesis of Dr. F. Stomeo) were synthesised according to the general procedure previously published and shown in Figure 4.4.[127] In summary, the appropriate ligand was dissolved in acetonitrile and was refluxed for 12 hours with a 2:3 M/L ratio of $Eu(CF_3SO_3)_3$. The resulting complexes were isolated as off-white powders after precipitation from the

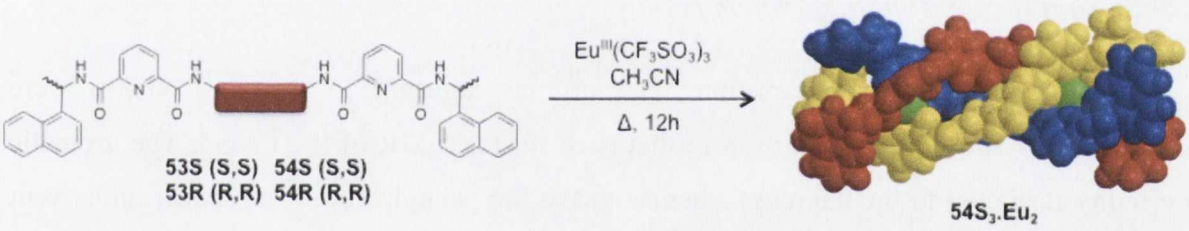


**Figure 4.4:** *One-step synthesis of ligands **53S-53R** and **54S-54R** from the half-ligands **51S-51R**.*

reaction mixture, upon the addition of diethyl ether in average yields (Table 4.2). In each case, the $^1$H-NMR analyses was carried out in $CD_3OD$ and $CD_3CN$ and the spectra obtained for the helicates $\mathbf{53S_3.Eu_2}$ and $\mathbf{53R_3.Eu_2}$, shown in Figure 4.5, matched the results previously obtained by Dr. Stomeo. The analyses of both enantiomers, $\mathbf{54S_3.Eu_2}$ and $\mathbf{54R_3.Eu_2}$, shown in Figure 4.5 (and in appendix 4.1) gave rise to similar results

**Table 4.2:** *Yields of the helicates synthesis*

| | $\mathbf{53S_3.Eu_2}$ | $\mathbf{53R_3.Eu_2}$ | $\mathbf{54S_3.Eu_2}$ | $\mathbf{54R.Eu_2}$ |
|---|---|---|---|---|
| **% yield** | 48 % | 90 % | 49 % | 75 % |

First, the characteristic broadening and shifting of the spectra of **54S** and **54R**, due to the paramagnetic nature of the $Eu^{III}$ ion, were clearly observed, which was indicative of the

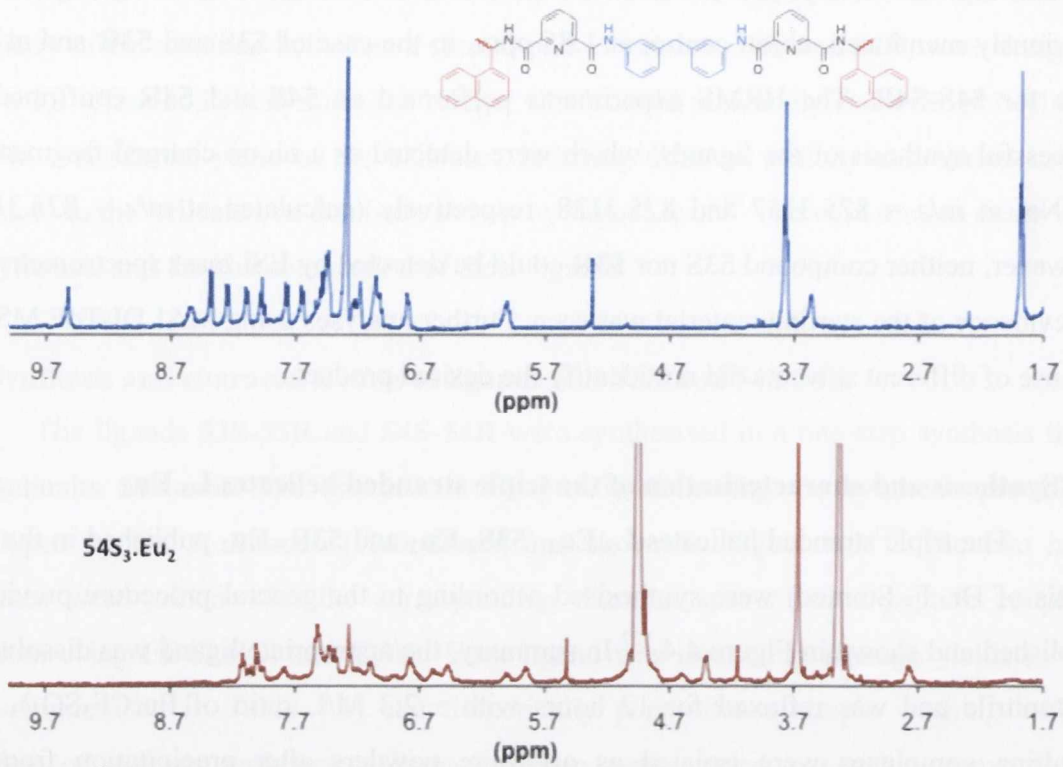


**Figure 4.5:** *$^1$H-NMR ($CDCl_3$; 400MHz) spectrum of **54S** (top) and of its resulting complex **$54S_3.Eu_2$** (MeOD; 400MHz) (bottom)*

successful lanthanide complexation. The protons adjacent to the $Eu^{III}$ centre were significantly shifted in comparison to that seen for the NMR of the ligand. The aromatic protons attributed to the naphthyl antenna and to the phenyl ring of the spacer underwent only minor shifts, as they are located further from the metal ion centre, which confirmed that the nine coordination sites required by the europium ion are provided by the cooperation of three ligands through their tridentate diaminopyridine moieties. Moreover, the $^1$H-NMR spectra also showed the high symmetry level of the complexes, suggesting that $D_3$ symmetry is predominant on the NMR time scale.[1] Furthermore, in each case, the formation of a helical isomer (*rac*) was suggested by the methylene bridge protons, which resonated as a singlet at 4.13 ppm and 3.90 ppm, for **$54S_3.Eu_2$** and **$54R_3.Eu_2$**, respectively. Characterisation *via* mass-spectroscopy analyses was attempted but neither the free ligand nor any of the possible lanthanide complexes were detected using ESI and MALDI MS.

### 4.5 Photophysical studies of the helicates $L_3.Eu_2$ (L= 53S-53R and 54S-54R)

The photophysical properties of ligands **L** (L= **53S-53R** and **54S-54R**) and their resulting complexes were investigated in MeOH, MeCN, $H_2O$ and $D_2O$ solution. The typical UV-vis spectra of **53S** and **54S**, Figure 4.6 (see appendix 4.2 for the R isomers), displayed a major UV-vis band centred at $\lambda$ =281 nm ($\varepsilon$ = 25090 $M^{-1}\cdot cm^{-1}$) and a

significant shoulder at 320 nm. In the case of the ligands **54S-54R**, Figure 4.6b, the same band indicative of the $^1\pi\pi^*$ transition of the naphthyl and the pyridinyl chromophores was observed with a similar shape presenting three narrow transitions at $\lambda$ = 281, 285 and 290 nm. However, for ligands **54S** and **54R** the shoulder at 320 nm was less pronounced and the presence of a transition centred at 222 nm was also observed. The formation of the $Eu^{III}$ complexes was clearly observed *via* two effects: The transition centred at 281 nm experienced a hypochromic effect of 20% and 16% in comparison to the ligands, for **53S-53R$_3$.Eu$_2$** and **54S-54R$_3$.Eu$_2$**, respectively.

**a.**

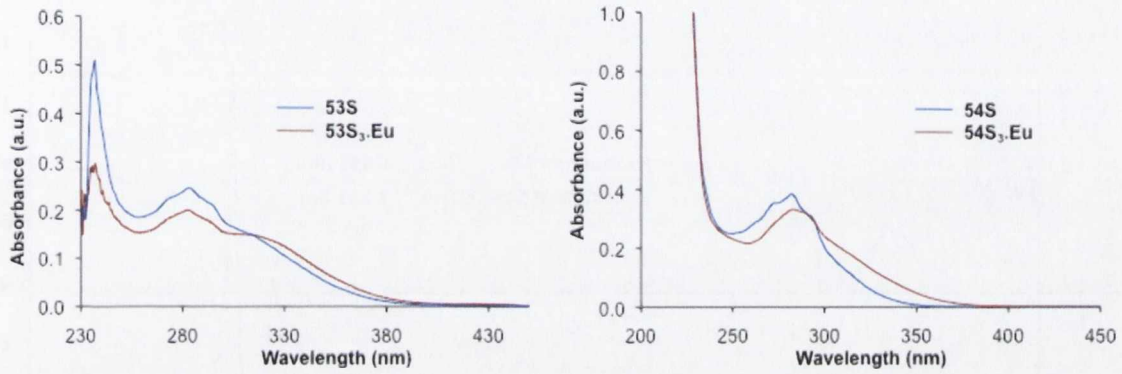


**Figure 4.6: a)** *UV-vis absorption spectra of **53S** (blue) and the resulting complexes **53S$_3$.Eu$_2$** (red) b) UV-vis absorption spectra of **54S** (blue) and **54S$_3$.Eu$_2$** (red).*

Similarly, in the case of **53S-53R**, this was accompanied by a hyperchromic effect of the shoulder at 320 nm, with the formation of an isobestic point at 316 nm. In the case of **54S** and **54R**, the absorption spectra of the ligands experienced a hypsochromic effect of 5 nm accompanied by the appearance of a shoulder at 320 nm, also confirming the complexation of the $Eu^{III}$ ion by these ligands.

In each case, excitation of the naphtyl antenna, gave rise to the typical luminescence of europium complexes occurring at 580, 595, 616, 655, and 701 nm for the

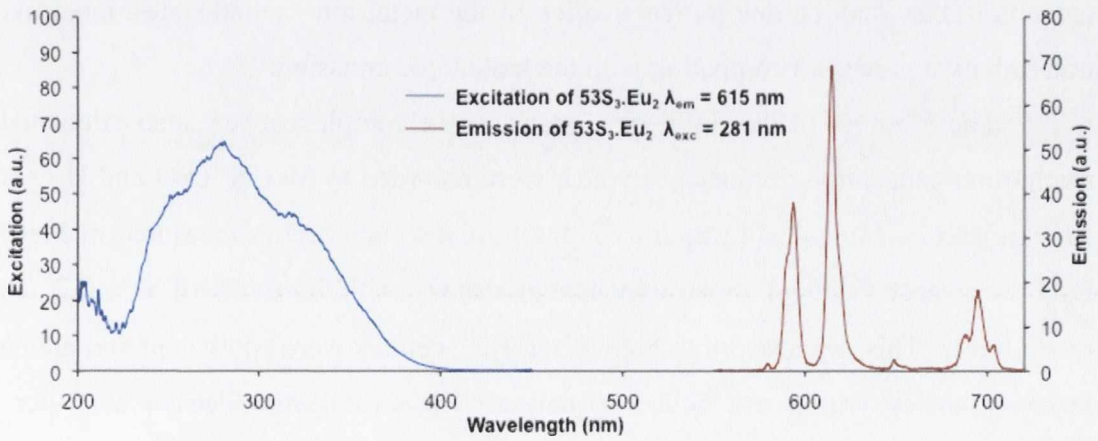


**Figure 4.7:** *Europium luminescence emission spectrum ($\lambda$ex =281nm) of **53S$_3$.Eu$_2$** (red) and resulting excitation spectrum ($\lambda$em = 615 nm) of the complex (blue).*

deactivation of the $^5D_0$ to $^7F_n$ (n = 0-4) transition, demonstrating the successful sensitization of the excited states of the europium ion, as shown in Figures 4.7 and 4.8 (and in appendix 4.3).

The excitation spectra resulting from the lanthanide emission of the helicates **53S-53R$_3$.Eu$_2$** displayed a maximum intensity at $\lambda$ = 281 nm and shoulder centred at 315 nm, which confirmed the sensitisation of the $^5D_0$ excited states of the europium ion *via* the antenna effect. Similar conclusions could be deduced from the excitation spectra obtained for **54S-54R$_3$.Eu$_2$,** which exhibited two major bands at 222 nm and 275 nm, similar to the

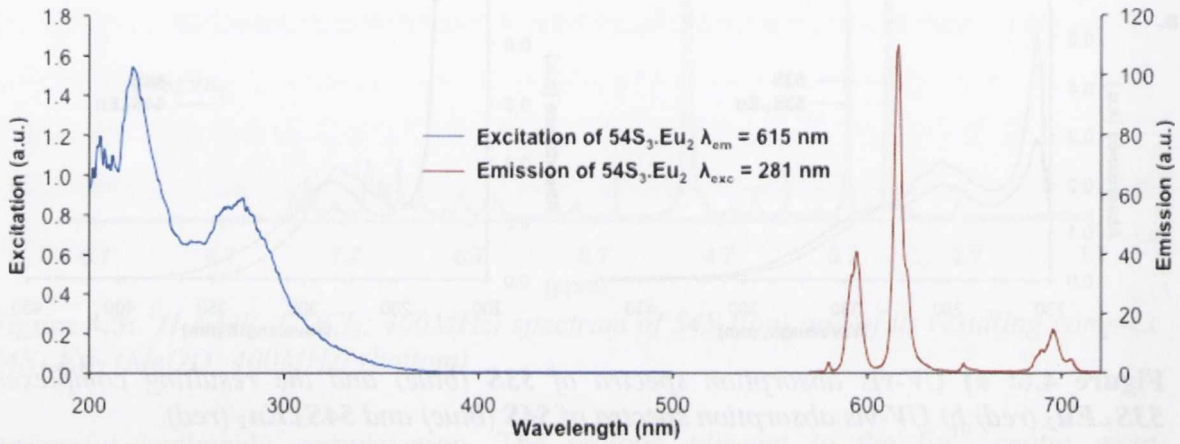


**Figure 4.8:** *Europium luminescence emission spectrum (λex =281nm) of* ***54S$_3$.Eu$_2$*** *(red)*

UV-vis spectra of the ligand.

The quantum yields for the europium emission were also measured for each of the helicates in water and are summarized in Table 4.3. They were measured as *c.a.* 0.5% and 0.6 % for **53S-53R$_3$.Eu$_2$** and **54S-54R$_3$.Eu$_2$** respectively, which was less than the values obtained for the monometallic analogues previously studied, **27S$_3$.Eu** and **27R$_3$.Eu,** and for the chiral luminescent complexes reported by Parker *et al.* using the same chiral antenna.[61] This may be due to deactivation of the metal ion excited states, most likely by non-radiative processes competing with the lanthanide emission.

The lifetimes of the $^5D_0$ excited states of the complexes were also calculated from the luminescence emission decays, which were recorded in MeCN, $D_2O$ and $H_2O$ and are summarized in Table 4.3. In each case, the luminescence decays measured in MeCN and $D_2O$ were best fitted to mono-exponential decays with lifetimes of $\tau$ = 2.2 and 3.1, respectively. This suggested that both of the $Eu^{III}$ centres were equivalent and adopted the same geometry within the helical structure. The exponential decays in water were, however, fitted to a bi-exponential decay with a long lifetime of $\tau$ = 1.6 ms and a short lifetime of *c.a.* $\tau$ = 0.32 ms. These are similar to the values obtained for the **dpa$_3$.Eu**

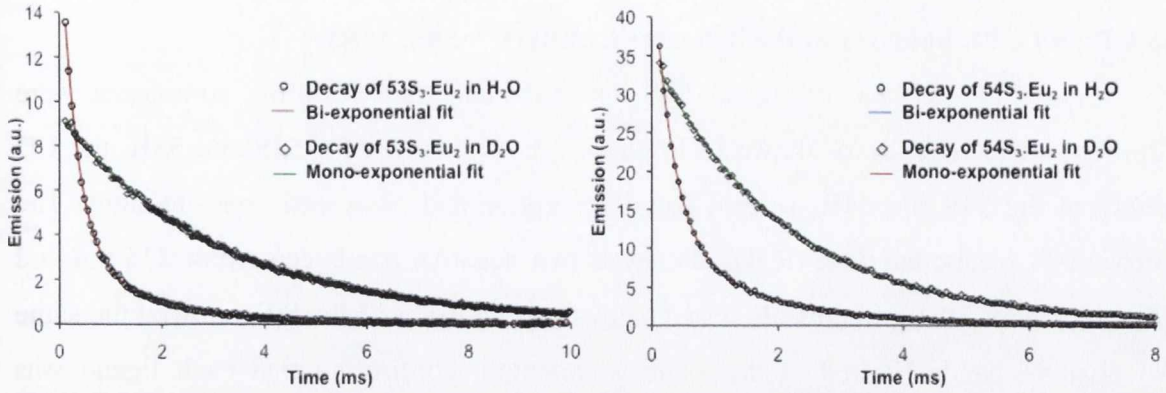


**Figure 4.9:** *Lumimescence emission decays and their resulting fits obtained in $D_2O$ and $H_2O$ for the helicates* ***53S$_3$.Eu$_2$*** *(left) and* ***54S$_3$.Eu$_2$*** *(right).*

derivatives previously discussed for the formation of 1:3 and 1:2 complexes in water at $C_{Eu} \approx 10^{-5}$ M.[126] The lifetimes calculated from the decays in $D_2O$ and $H_2O$ also allowed for the calculation of the hydration states of the helicates, and these are summarised in Table 4.3. These results showed that all the helicates have $q \approx 0$ for the long-lived species, confirming that the nine coordination sites of both $Eu^{III}$ ions are provided by the self-assembly of three ligands. However, the hydration state of the short-lived species was calculated to be $q \approx 3$, which confirmed the destabilisation of the 2:3 M/L complexes and the presence of the **L$_2$.Eu$_2$** species.

**Table 4.3:** *Photophysical properties of the* ***L$_3$Eu$_2$*** *(L = **53S**, **53R**, **54S**, **54R**) helicates in $CH_3CN$ and $H_2O$.*

| $L_3.Eu_2$ | $\tau_{(CH_3CN)}$ | $\tau_{(D_2O)}$ | $\tau_{(H_2O)}$ % Pop | | q | | $\Phi_{(H_2O)}$ |
|---|---|---|---|---|---|---|---|
| **L= 53S** | 2.25 | 3.125 | 1.622 | 0.353S | 0 | 3.11 | 0.6 % |
| | | | *55.3* | *44.7* | | | |
| **L= 53R** | 2.14 | 3.453 | 1.512 | 0.302 | 0 | 3.27 | 0.5 % |
| | | | *51.3* | *48.7* | | | |
| **L =54S** | 2.182 | 2.96 | 1.62 | 0.318 | 0.04 | 3.06 | 0.6 % |
| | | | *57.2* | *32.8* | | | |
| **L = 54R** | 1.990 | 3.30 | 1.45 | 0.314 | 0.11 | 3.15 | 0.7 % |
| | | | *52.1* | *47.9* | | | |

Furthermore, the emission spectra of the helicates **54S-54R$_3$.Eu$_2$** possess different band ratio (0.31 between the $^7F_1$ and $^7F_2$) than its structural isomer **53S-53R$_3$.Eu$_2$** (0.51), which showed that they adopted different geometries in solution. The geometry of the helicates and their chirality were also studied using CD and CPL spectroscopy. As the studies performed on the both of enantiomers **53S-53R$_3$.Eu$_2$** had already been performed by Dr. F. Stomeo, this discussion will be focused on the helicates **54S-54R$_3$.Eu$_2$** and the results obtained will be then studied in comparison to those published in her PhD Thesis.

### 4.6 CD and CPL analyses of the helicates $L_3.Eu_2$ (L = 54S, 54R)

The CD spectrum of ligand **54S** and **54R** and their resulting complexes were recorded in MeOH and are shown in Figure 4.10. As reported for **53S** and **53R**, the CD spectra of the **54S** and **54R** were of equal absorption and possessed opposite signs. The spectrum of compound **54R** (R,R), displayed two negative bands centred at 235 nm and 299 nm, whereas the ground state-based analysis of its isomer **54S** (S,S) showed the same two positive bands centred at the same wavelength, confirming that each ligand was isolated enantiomerically pure.

The CD spectra of the resulting complexes were recorded at the same concentration and gave rise to two spectral mirror images, which suggested that the helicates were also formed as a single helical isomer in solution. It was clear from the two CD spectra that the band at 235 nm remained similar in appearance to those of the ligands with a higher

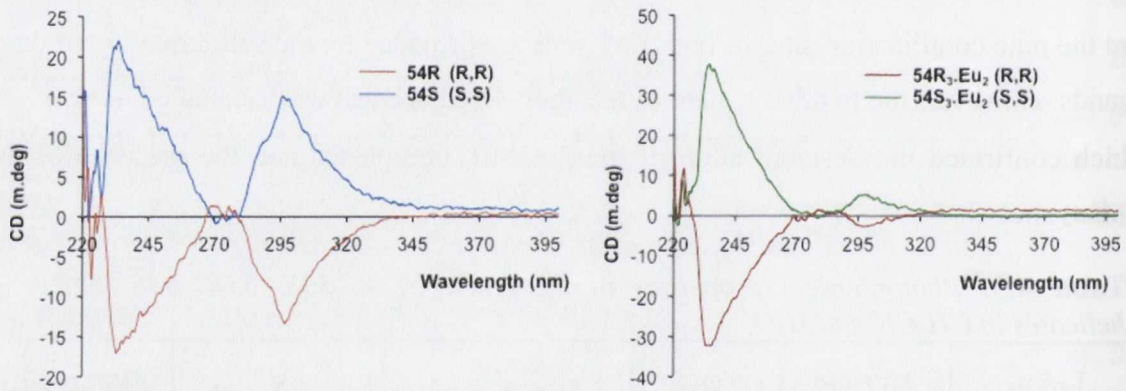


**Figure 4.10:** *CD absorption spectra of ligands **54R** and **54S** (left) and their resulting complexes **54S$_3$.Eu$_2$** and **54R$_3$.Eu$_2$** (right) in $CH_3CN$.*

ellipticity (± 40 m.deg for the complexes instead of ± 20 mdeg for the ligand), whereas the long wavelength transition attributed to the naphthalene moiety, at 300 nm experienced a large decrease in intensity in comparison to that seen for **54S** and **54R**, respectively. Such dramatic changes were not observed in the case of the helicates **53S-53R$_3$.Eu$_2$**, developed by Dr Stomeo. This suggested that the ligand **54S** and **54R** undergo significant conformational changes upon complexation to $Eu^{III}$. These results clearly demonstrate the influence of the diphenylmethane spacer on the overall geometry of the supramolecular architecture and on its overall chirality. The dissymmetry of the dimetallic triple stranded helicates **54S-54R$_3$.Eu$_2$** were also investigated using CPL spectroscopy. The CPL spectra of both helicates **L$_3$.Eu$_2$** (L = **54S** and **54R**) were recorded in Glasgow University by Dr. R. Peacock, in MeOH and are shown in Figure 4.11. The excitation of the chiral antennae of the helicates **L$_3$.Eu$_2$** (L = **54S** and **54R**) gave rise in all occasions to a chiral emission

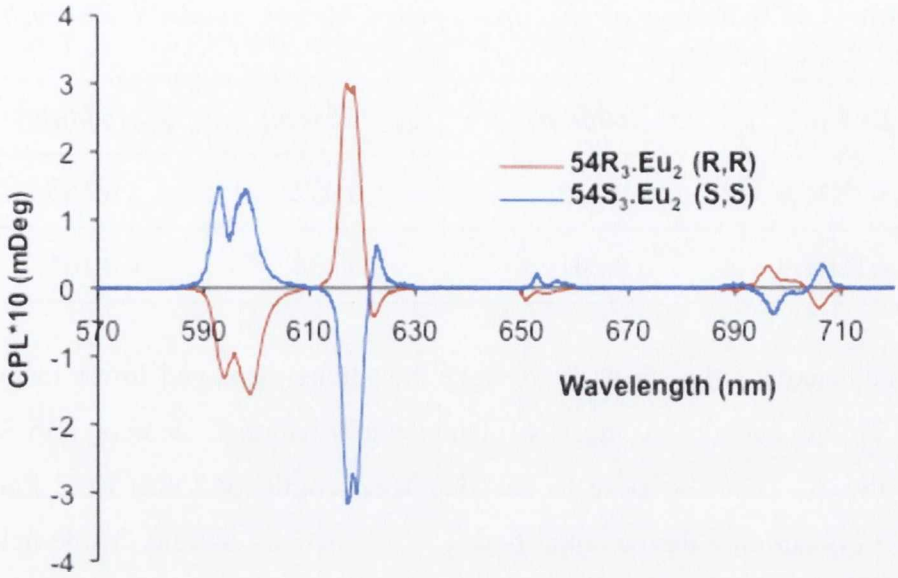


**Figure 4.11:** *CPL-luminescence spectra of* ***54S$_3$.Eu$_2$*** *and* ***54R$_3$.Eu$_2$*** *in $CH_3OH$.*

that were of opposite signs and of the same magnitude for both enanthiomers, confirming the enantiomeric nature of the supramolecular architectures.

The spectrum of **54S$_3$.Eu$_2$** exhibited two positive bands at $\lambda$ = 592 nm and 598 nm, which were attributed to the $^5D_0 \rightarrow {}^7F_1$ transitions and a negative band with a positive shoulder at $\lambda$ = 620 nm for the $^7F_2$ transitions, which were of almost the same intensity than the one obtained with total light. The $\Delta J = 4$ band centred at 701 nm was found to be split adopting a negative and a positive $\Delta I$ at 695 nm and 705 nm respectively. Conversely, the excitation of the complex **54R$_3$.Eu$_2$**, generated an exciton coupling of negative and positive intensity for the $^5D_0 \rightarrow {}^7F_J$ (J = 1,3) and $^5D_0 \rightarrow {}^7F_J$ (J = 2) transition respectively, which was the mirror image of the one obtained for its enantiomer **54S$_3$.Eu$_2$**.

This confirmed that the $Eu^{III}$ centres were lying in a chiral environment and that the chirality of the **54S** and **54R** was successfully transferred to the $^5D_0$ excited states of the lanthanide ion. These results were correlated with those obtained for the mono-metallic systems **27S-27R$_3$.Ln**, for which the absolute configuration has been determined *via* X-ray crystallography. This allowed the prediction of the handedness of the helicates **54R$_3$.Eu$_2$** and **54S$_3$.Eu$_2$** determined as being $\Lambda,\Lambda$ and $\Delta,\Delta$ respectively.

Furthermore, the dissymmetry factor $g_{em}$ relative to the circular polarized emission were calculated from these spectra for the transition centred at 600 nm ($\Delta J = 1$), at 615 nm ($\Delta J = 2$) and 654 nm ($\Delta J = 3$) and are summarized in Table 4.4. The dissymmetry factors were found to be larger at 600 nm than at 615 nm. The influence of the nature of the diaryl spacer was also illustrated by the $g_{em}$ values. Indeed, the dissymmetry factors of **54S-**

**Table 4.4:** *Summary of the dissymmetry factors obtained for each couple of enantiomers.*

| $L_3.Eu_2$ | $g_{em}$ (600nm) | $g_{em}$ (615nm) | $g_{em}$ (654nm) |
|---|---|---|---|
| **L = 53R-S** | ± 0.230 | ± 0.052 | ± 0.150 |
| **L = 54R-S** | ± 0.207 | ± 0.058 | ± 0.165 |

**$54R_3.Eu_2$** calculated for the short wavelength transitions displayed lower magnitude of 10% range in comparison to those of their conformational isomers **$53S\text{-}53R_3.Eu_2$**. Conversely, the $g_{em}$ factors relative to the long wavelength (615 nm) were found to be higher by 10% illustrating the potential tuning of the overall chirality of the helicates by the nature of the central spacer.

In order to further investigate the relationship between the nature of the diaryl bridge and the overall geometry of the resulting helical systems, molecular mechanics calculations were performed on the dimetallic complexes and the results of which be discussed in the next section.

## 4.7 Molecular Mechanics modelling studies of the helicates of the triple stranded helicates

The molecular mechanics studies were performed on **$53S_3.Eu_2$** an **$54S_3.Eu_2$** with Chem3D version 11 and the model of the complex **$54S_3.Eu_2$** was build guided by the $^1$H-NMR and elemental analyses, following two different approaches. The first method consisted of the optimization of the free ligand, which was used to create the resulting helicates *via* the introduction of two europium atoms. In the second approach, the $Eu^{III}$ centres were first optimized from the X-ray crystal structures obtained by Dr. J. Leonard, for the monometallic systems **$27S_3.Eu$** and the resulting helicates were built performing serial optimisations after linking the two complexes with the diaryl bridges.

The complexes **$53S_3.Eu_2$** were also modelled, as a control, following the same approaches and gave rise to similar results as those obtained by Dr. P. E. Kruger and already published in Dr. F. Stomeo PhD thesis.[127] In each case, both of the *meso*-(non-helical) and *rac*-(helical) isomers were simulated and the lowest energy structures were the *rac*-isomers, which are shown in Figure 4.12. It was clear from the molecular models that upon the complexation of two $Eu^{III}$ ions the ligands adopted a helical structure, where each metal ion is nona-coordinated by the self-assembly of three ligands.

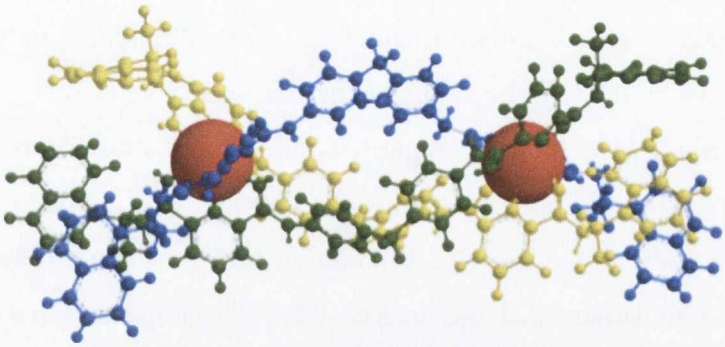

$53S_3.Eu_2$ (R,R)

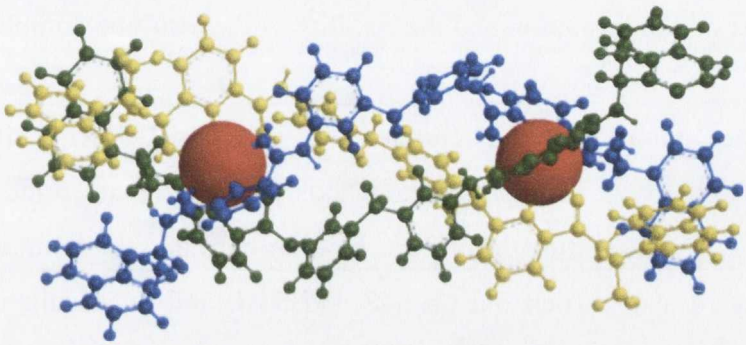

$54S_3.Eu_2$ (R,R)

**Figure 4.12:** *Molecular models obtained from the calculation performed in the MM2 force field for the optimisation of* ***53S3.Eu2*** *and* ***54S3.Eu2****.*

These simulations confirmed that both of the europium centres formed were equivalents and presented a $C_3$ local geometry while the overall geometry of the helicates was found to be $D_3$ as previously observed in the $^1$H-NMR analysis. Furthermore, in both cases the presence of central inter-strand cavity was observed. The shape and the size of these cavities, and consequently the geometry of the helicates, were directly related to the nature of the diaryl spacer. Indeed, in the case of **$53S_3.Eu_2$** the methylene protons of the bridge were found to be orientated outside of the structure generating a cavity of 9.0 Å (measured as an average of the C-C distances from the $CH_2$ of the methylene moieties of the bridge). On the other hand, in the case of **$54S_3.Eu_2$**, the methylene protons of the diaryl bridge pointed inside the helicate giving rise to a "squeezed" cavity of 4.5 Å. Moreover, π-

**Table 4.5:** *Size of inter-strand cavities and Eu-Eu distances obtained from the MM2 calculations.*

| $L_3.Eu_2$ | *Cavity* (Å) | $d_{Eu\text{-}Eu}$ (Å) |
|---|---|---|
| **L=53R** | 9.0 | 14.7 |
| **L =54R** | 4.5 | 14.3 |

π interactions between the phenyl ring of the spacer and the pyridinyl unit were also detected, which stabilised such a conformation and had a dramatical influence on the Eu-Eu distance as shown by the calculated values summarised in Table 4.5.

In this section the synthesis of homochiral triples stranded helicates has been illustrated, and it was also demonstrated that the chirality of the ligand was successfully transferred to the europium yielding chiral luminescence of the supramolecular complexes. It has also been demonstrated that the nature of the diaryl spacer separating the binding sites has a dramatic influence on the geometry and the chirality of the supramolecular structures. Therefore, the next step of our investigation was to determine the influence of the central spacer on the formation and the stability of the resulting complexes in solution.

### 4.8 Studies of the formation of the helicates $L_3.Eu_2$ (L= 54R-54R) in situ

As discussed above, titration of the ligands with $Ln^{III}$ enabled the determination of the stoichiometry and the estimation of the binding constants in solution. Consequently, such titrations were also carried out on **54S** and **54R**, and the results of which will be discussed in this section.

Firstly, the determination of the preferred stoichiometry was investigated performing the Job's plot experiment, where the molar fraction of metal ion was varied from 0 to 1 in $CH_3CN$, while keeping the overall concentration of the sample constant at C = $1\times10^{-5}$ M, in the same manner as assessed in Section II.2. Each point of the Job's plots, which are shown for both isomers in Figure 4.13, were measured by recording the europium emission from a fresh solutions made by stirring (during five minutes) the ligand with the corresponding quantity of $Eu(CF_3SO_3)_3$. In both cases, the maximum luminescence was reached when the molar fraction of metal in solution was $\chi_{Eu}$ = 0.4, indicative of the predominant formation of the desired 3:2 M/L dimetallic triple stranded helicates in solution.

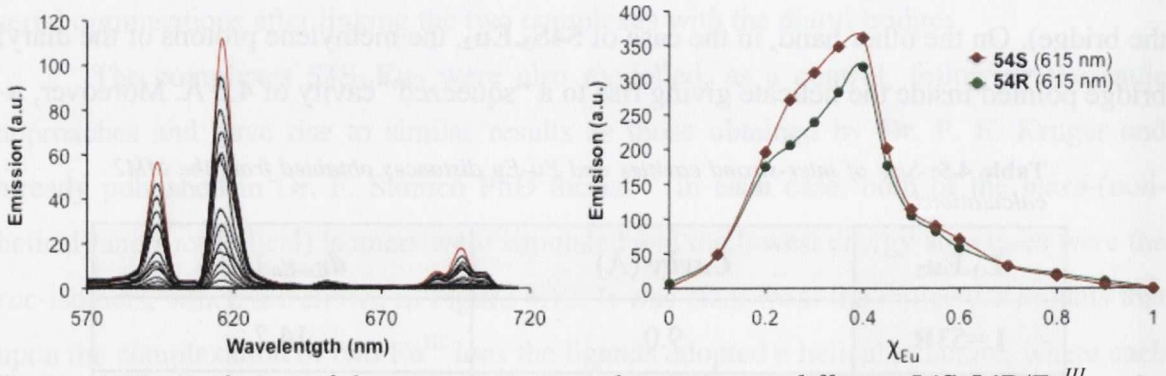


**Figure 4.13:** *Evolution of the europium centred emission at different* ***54S-54R****/Eu$^{III}$ ratio, and resulting Job's plot at 615nm.*

However, the continuous variation method allows only the estimation of the most stable species governed by molar thermodynamic control.

Consequently, further complexation studies were undertaken to enable the understanding of the binding process and titrations of the same manner as discussed for the bundles **$L_3$.Eu** (L=**27S-R**, **51S-R**) were carried out. These titrations were performed using **54S** and **54R** at $1\times10^{-5}$ M in $CH_3CN$, where the UV-vis absorption, the fluorescence and the time delayed europium emission ($\tau$ = 0.1 ms) were all measured.

The changes in the UV-vis absorption spectra are shown in the Figure 4.14 and the changes at larger wavelength are shown in inset. The experiments were performed three times and give rise to similar results each time. As it can be seen in Figure 4.14, the UV-vis absorption band centred at $\lambda$ = 281 nm experienced an hypochromic effect upon the

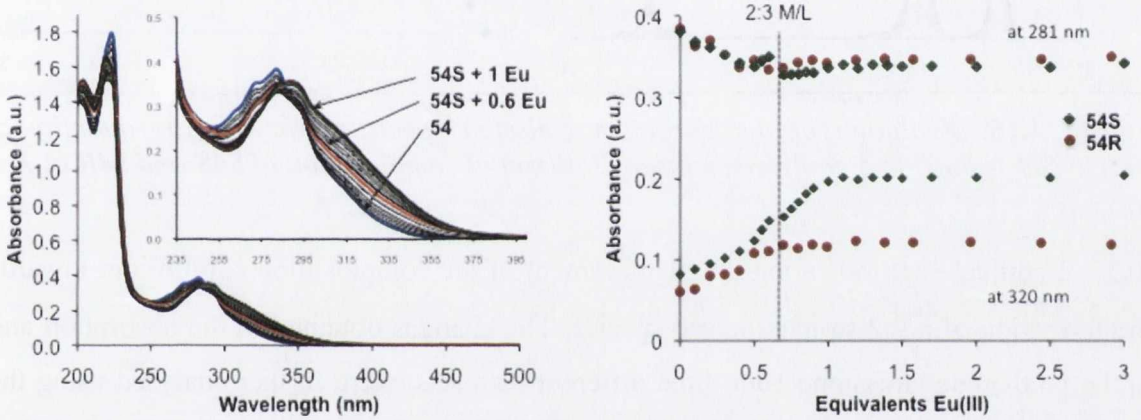


**Figure 4.14:** *Evolution of the UV-vis absorption spectrum during the europium titration of **54S** and isotherm of complexation at $\lambda$ =281 nm and $\lambda$ =310 nm.*

addition of 0→0.6 equivalents of $Eu(CF_3SO_3)_3$, suggesting the initial formation of the expected 3:2 stoichiometric self-assemblies. A concomitant hyperchromic effect was also observed in the shoulder occurring at 320 nm and reached a plateau after the addition of ~ 0.7 equivalents. However, some further changes were also observed upon addition of $Eu^{III}$, which suggested the formation of the species consisting in a 2:2 M/L stoichiometry such as **$L_2$.$Eu_2$**.

The changes in the fluorescence (appendix 4.4) were less pronounced but were in agreement with that observed in the absorption spectroscopy titrations. The weak emission band centred at 450 nm experienced a small quenching with the addition up to 0.7 equivalents of $Eu^{III}$ ion, and was seen to be totally quenched after the addition of 1 equivalent of metal ion. It was clear from the fluorescence evolution that the $Eu^{III}$ emission was "switched on" in parallel with the aforementioned quenching, signifying that the europium emission occurred after energy transfer from the ligand centred excited states.

Consequently, the formation of the helicates was also investigated following the changes in the $Eu^{III}$ luminescence, which was obtained from the same titrations and is shown in Figure 4.15.

The largest changes, here were observed within the addition of ~0.7 equivalents of $Eu^{III}$ suggesting the formation of the desired 2:3 M/L stoichoimetric species. This was followed by a weak luminescence quenching, occuring at higher $Eu^{III}$ concentration

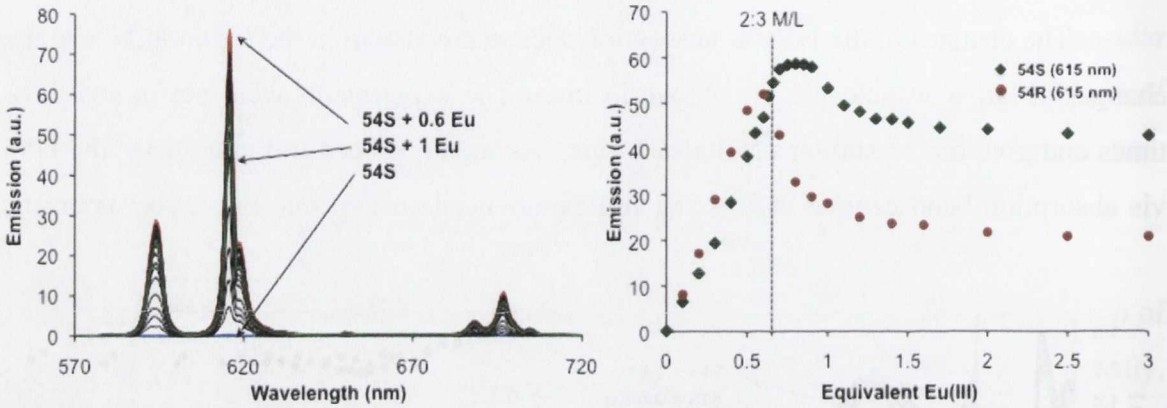


**Figure 4.15:** *Evolution of the europium emission spectrum varying the quantity of $Eu(CF_3SO_3)_3$ for 0 to 5 equivalents inset: Isotherm of complexation of **54S** and **54R** at $\lambda$ = 615 nm.*

(0.7→2 equivalents) indicating the displacement of the complexation equilibrium towards the formation of a 2:2 stoichoimetric species. The changes obtained in the absorption and in the lanthanide emission, from three different data sets, were further analysed using the non-linear regression analyses software SPECFIT®, in the same manner as previously discussed. The changes in the UV-vis absorption spectra were successfully fitted with satisfying convergence factors and give rise to similar results for both enathiomers **54S** and

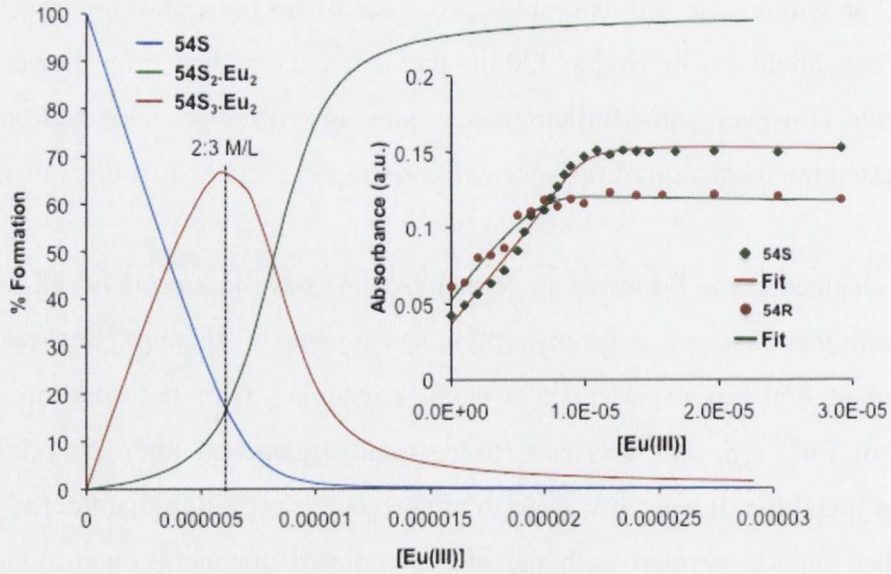


**Figure 4.16:** *Speciation diagram obtained from the fitting of the UV-vis absorption evolution of **54S**. Inset: Fits obtained for the non-linear regression analyses*

**54R**, the resulting fits and speciation diagram are shown in the Figure 4.16 and **54R**. From these results the predominant formation of the 3:2 stoichoimetric species was established in both case upon the addition of 0.67 equivalents with high binding constants of log $\beta$ = 26.7 and 25.8 for **54S** and **54R**, respectively, where these species were formed in 70% and 50% for $\mathbf{54S_3.Eu_2}$ and $\mathbf{54R_3.Eu_2}$ respectively. However, the displacement of the equilibrium towards the $\mathbf{L_2.Eu_2}$ was also observed and the presence of these species was found to become predominant after the addition of 0.8 equivalent of $Eu^{III}$ ion.

The fitting of the $Eu^{III}$ emission data was also performed and gave rise to similar results. In the case of both of the ligands the predominant formation of the 2:3 M/L was also detected with binding constants in similar range of log $\beta$ = 25 ± 0.3 and 27 ± 0.2 being formed in 80% and 60% for $\mathbf{54S_3.Eu_2}$ and $\mathbf{54R_3.Eu_2}$, respectively. The 2:2 species was also detected to become predominant after the addition of 0.9 equivalents of $Eu^{III}$ salt, as shown in the speciation distribution diagram in Figure 4.17 in the case of **54S**. It was clear

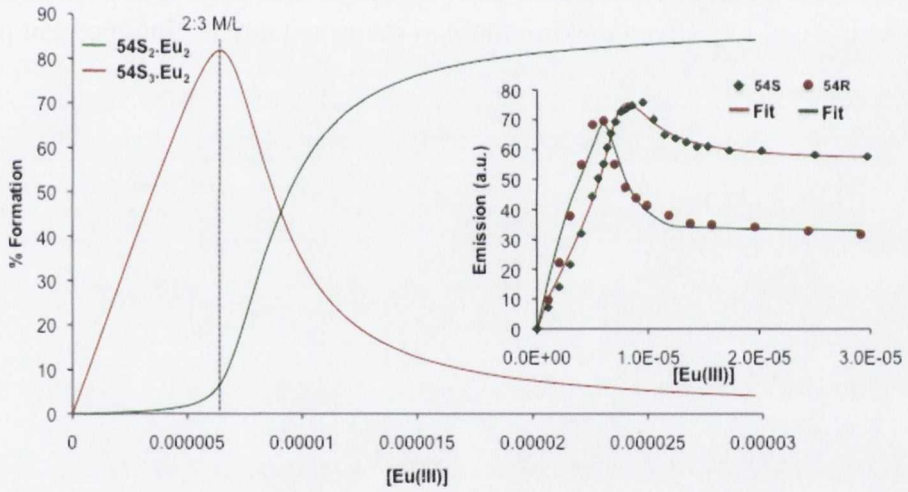


**Figure 4.17:** *Speciation diagram obtained from the fitting of the luminescence emission titrations of **54S** inset: Fits obtained for the non-linear regression analyses*

from the comparison of these results, that the nature of the diaryl linker also has a dramatical influence on the formation of the self-assemblies $\mathbf{54R\text{-}54R_3.Eu_2}$ which occurred with lower binding constants by two log unit of magnitude than their conformational analogues **53S** and **53R**.

### 4.9 Conclusion

The work performed by Dr. Stomeo and Dr. S. Comby demonstrated that the formation of ditopic ligand containing two binding sites derivated from the dpa unit, enabled the formation of bimetallic chiral triple stranded helicates and that the nature of

the central spacer was seen to dramatically influence the geometry and the photophysical properties of the complexes. This was further investigated with the ligand **54S** and **54R,** which possess a 3,3'-diaminodiphenyl spacer. The synthesis of these ligands was performed in high yields from the half-systems described in the previous chapter, and each ligand was isolated enantiomerically pure. The correlation of the results from $^{1}$H-NMR, UV-vis absorption, luminescence emission, and circular polarised light spectroscopy have allowed to predict the overall geometry of the dimetallic triple stranded helicates using MM2 molecular mechanices calculation. This has shown the presence of an inter-strand cavity, for which the sized could be tuned by the nature of the central diaryl spacer. The complexation of two europium ions by ligand **53S** or **53R** gave rise to a large cavity, whereas the helical wrapping of the ligand **54S-54R** was demonstrated to be 'tight fit' with the phenyl ring of the linker orientated towards the exterior of the 'squeezed' structure, giving an overall $D_3$ geometry in which the central cavity observed for **53S-53R$_3$.Eu$_2$** was almost removed. The emission of each self-assembly described during this chapter was highly chiral and long-lived making these systems suitable for luminescent probing.

# Chapter 5:

# Lanthanide templated synthesis of [3]-catenanes

## Chapter 5: Lanthanide templated synthesis of [3]-catenanes

### 5.1 Introduction

According to IUPAC classification, catenanes are defined as hydrocarbons formed from several interlocked molecules, which can be separated only by the cleavage of a covalent bond.[130] Although, the existence of the interlocked structure was envisaged from the beginning of the 20th century, [2]-catenane have only been observed in the nucleic DNA of several species of bacteria by Vinograd *et al.*[131] Even if the synthesis of such structures was predicted by Wasserman and Frish only in the late 1960's,[132] [2]-catenanes have been of a great interest over the past few decades and a numerous of examples have been developed in a wide ranged area of within the field of supramolecular chemistry.[133-137] It is also well established that the number of crossing points generated gives rise to different interlocked structures. The formation of a rotaxane, requires a unique crossing

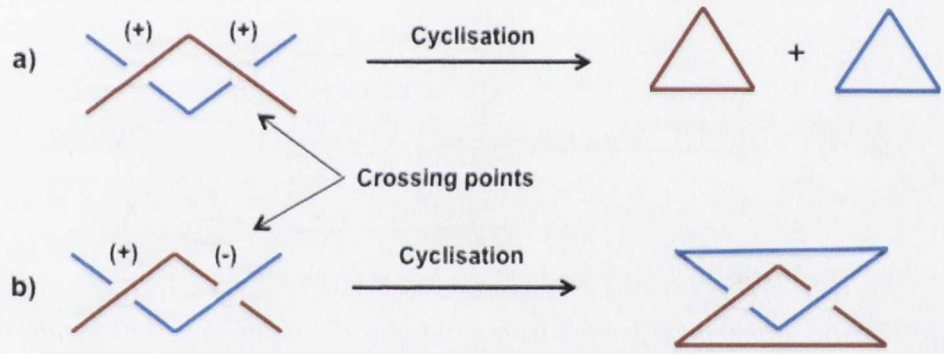


**Figure 5.1:** *Schematic representation of the isomers having different crossing points configuration a) two positive crossings points yielding to the formation of two macrocycles. b) a positive and a negative crossing points yielding to the formation of a [2]-catenane.*

point, whereas the formation of a [2]-catenane, or two interlocked rings, occurs through the formation of two crossing points, one of negative configuration (-) and one of a positive one (+)[124,138,139]. As shown schematically in Figure 5.1, for the synthesis of a [2]-catenane the succession of two positive crossing points (+) gave rise to two macrocycles (a), whereas that of a positive and a negative crossing point generated the expected connected rings (b) after the cyclisation.[139] Several strategies have been generated to create these crossing points and these can be classified into two different categories. 1) The Brownian approach is based on the probability of the ligands randomly reaching the ideal shape before closing. Two examples of this approach are discussed below. 2) The directed approach which consists of the templation of each crossing point at the ideal geometry in order to achieve the successful interlocking.

### 5.1.1 Synthesis of catenane using a Brownian approach

The first approach for the formation of catenanes consists of cyclisation of a linear bifunctional hydrocarbon **55** around the macrocycle **56** prepared beforehand. The catenane is formed successfully if the linear molecule is inside the macrocycle before the ring closing occurs, otherwise the formation of two independent macrocycles is observed, as shown in Figure 5.2. However, the authors have shown that the formation of the pseudo-rotaxane **57**, needed for the successful catenation, was minor and therefore the formation of the desired [2]-catenane was performed in low yield.[140]

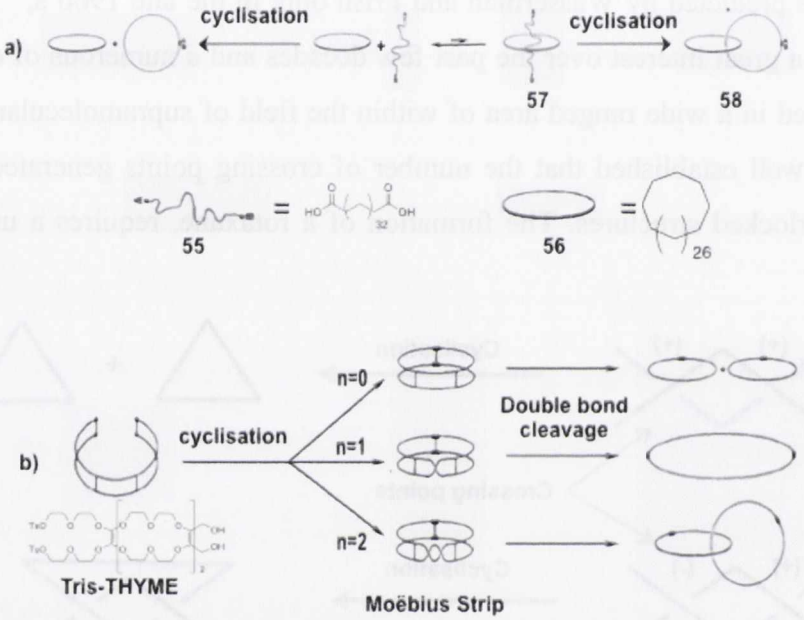


**Figure 5.2:** *a)Statistical approach for the fromation of a [2]-catenane.*[140] *b) Synthesis of a catenane through the formation of a Moëbius strip (when the precursor undergoes n = 2 twists.)*

The second approach was developed by Walba *et al.* and was based on the ability of a ladder shaped molecule (tris-THYME) to twist twice, forming a moëbius strip, prior to ring closing. The cleaving of the double bonds moieties of the precursor gave rise to the desired catenane in 22% as shown in Figure 5.2. However, there is a random aspect to this strategy, as the molecule can undergo several twists *(n)*, yielding different isomers. For example, if the tris-THYME experiences any twist the cleaving of the allylic moieties will result in the formation of two independent macrocycles, whereas the formation of the moëbius strip resulting from two twists gave the desired [2]-catenane (Figure 5.2)[141]. However, due to the disorder of these strategies, several different topologies can arise. These structures can be challenging to isolate and can also give rise to low yields for the desired product.

### 5.1.2 Synthesis of catenane *via* directed approach

The second method, or directed approach, consists in the templation of each crossing point, at the ideal geometry, in order to achieve successful interlocking of the molecules, as shown by the examples in Figure 5.3. It has been well illustrated in the literature that the preoganisation of two ligands, in order to form interlocked structures such as catenanes or molecular knots require a certain degree of orthogonality prior to the catenation.[138] This orthogonality can be provided by inherent preorganisation of the molecule itself, such as shown in Figure 5.3.a, in the example of Schill *et al.* Here two rings of the catenane are perpendicular to each other, one in the plane of the phenyl ring and the second one interlocked *via* covalent linking at each of the two crossing points, the trigonal nitrogen and the tetrahedral carbon, which are both in the perpendicular plan of the phenyl ring.[142]

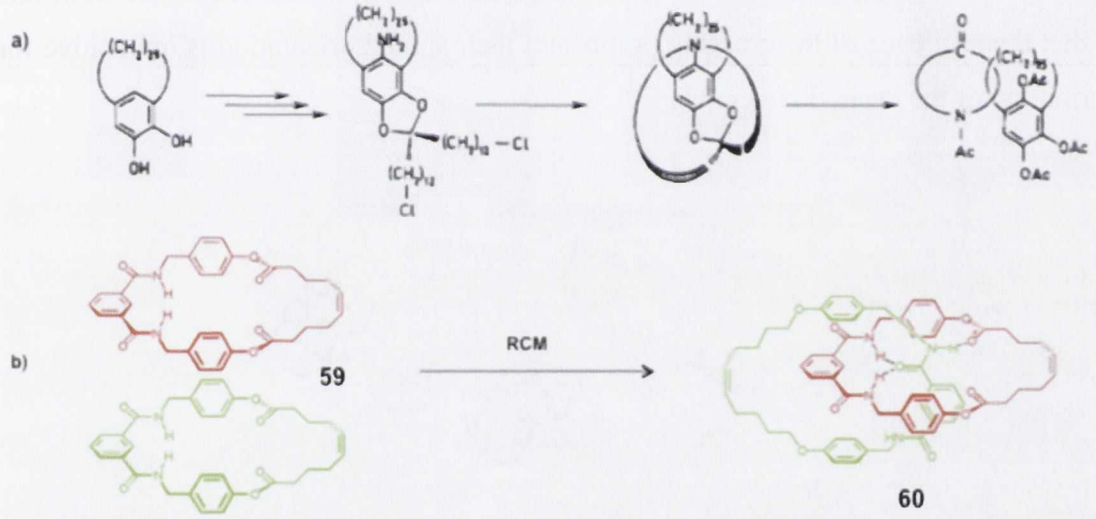


**Figure 5.3:** *Examples of the directed approach for the formation of [2]-catenanes a) using preorganisation induced by covalent bonds.*[142] *b) Using H-bonding as a template.*[133]

Weak interactions such as H-bonding[137,143] electrostatic or π-π interactions[135,138] have also been used to template the synthesis of interlocked structures such as [2]-catenanes, rotaxanes and molecular knots. As shown in the example developed by Leigh *et al.* (Figure 5.3), two self-complementary macrocycles **59** can dimerize by forming four hydrogen bonds from the amide hydrogen atoms and the ester carbonyls to give catenane **60** in 95% yields, under appropriate ring opening and ring closing metathesis conditions.[133]

However, the use of transition metals remains one of the most efficient strategies to achieve the synthesis of such structures, due the thermodynamic stability as well as the high level of geometry in their coordination sphere. The use of tetrahedral metal ions such as $Cu^{I}$ and $Zn^{II}$ to hold bidentate ligands in a suitable orientation prior to macrocyclisation,

has been intensively developed since the pioneering work of J.P. Sauvage and coworkers over the past two decades, following either the clipping or the double clipping strategies, shown in the Figure 5.4.a.[144,145] These approaches consist of the preorganisation of the two precursors around a $Cu^{I}$ ion, prior to the catenation using macrocyclisation *via* Williamson ether synthesis, resulting in the formation of the [2]-catenane in high yields.

The directed approach for the formation of interlocked molecules has also yielded the formation of more complicated systems, such as multi-catenanes, [3]-rotaxanes, other molecular knots and borromean rings. An example of the use of metal templation in the synthesis of more complex interlocked systems was demonstrated by Stoddart and coworkers and is shown in Figure 5.4.b. Here, six crossing points were first formed *via* the complexation of $Zn^{II}$ with dipyrinyl derivatives. These preformed complexes were linked to each other in order to form the borromean rings **61**, which consisted of three interpenetrated rings with no macrocycle interlocked with any other. It is clear from this work that the sequence of the crossing points and their spatial orientation is imperative for the formation of the desired molecules.[146]

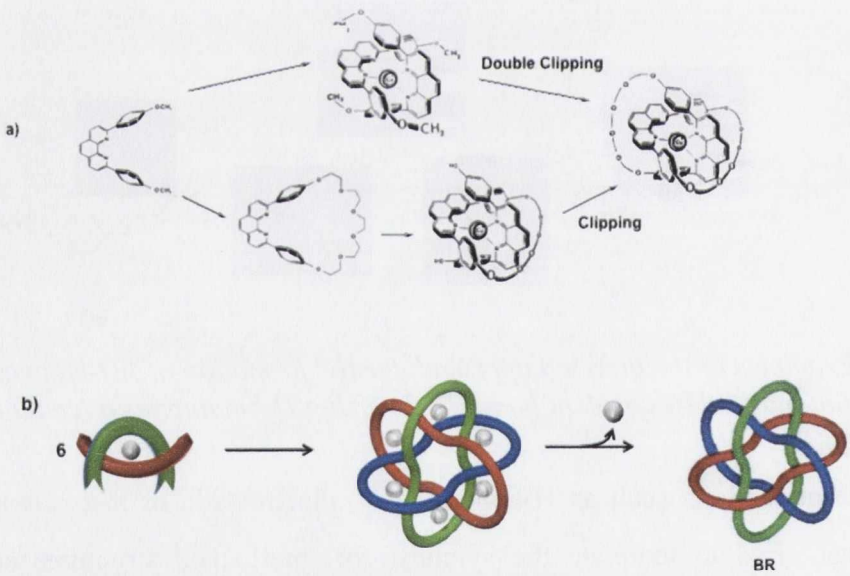


**Figure 5.4:** a) *Examples of transition metal templated synthesis of a [2]-catenane via clipping and double-clipping*[144,145] *b)* $Zn^{II}$ *directed synthesis of borromean ring.*[146]

As demonstrated in the previous chapter, the complexation of lanthanide ions with tridentate ligands gives rise to highly stable 1:3 stoichiometric supramolecular complexes, through a self-assembly process involving metal coordination and π-π structural interactions. This idea can also potentially provide the ideal geometry for templating the formation of ternary interlocked structures, such as [3]-catenanes and [3]-rotaxanes, as the lanthanide ion can bring together three ligands. With the aim of synthesising the first fully

interlocked [3]-catenane known to date, our strategy, shown schematically in Figure 5.5, was focused on using the lanthanide ion to direct the formation of a ternary self-assemblies, into **62**, followed by a triple clipping catenation yielding the [3]-catenane **63**.

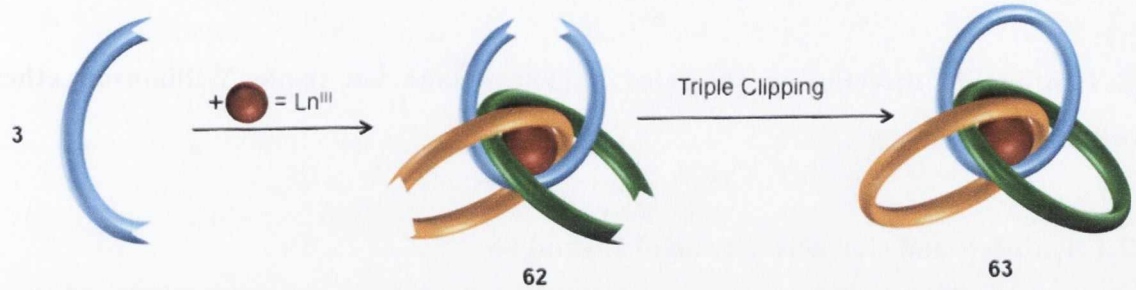


**Figure 5.5:** *Strategy envisaged for the synthesis of a [3]-catenane.*

### 5.1.3 Design of the ligands

As demonstrated in the previous chapters, the tridentate diaminopyridnyl derivative can self-assemble around lanthanide ions such as $Tb^{III}$ and $Eu^{III}$, giving rise to a local $C_3$ geometry. It was foreseen that this coordination could potentially organise the ligand into the required orientation for interlocking, which could then be followed by the formation of the [3]-catenane. Furthermore, the solution studies performed using various ligands (such as **27**, and **51**) demonstrated the stability of the resulting 1:3 (M/L) complexes, and also the retention of their geometry in solution. Hence, to form the aforementioned [3]-catenane, ligands **66** and **71** were designed. These consisted of a central pyridinyl moiety alkylated at positions 2 and 6, with flexible pendant arms made from two and three ethylene ether moieties, which could then undergo ring closing, as shown in Figure 5.6. The (ethoxy)ethyl arms were preferred to the aliphatic analogues, due to the poor rigidity of the latter, which would undergo less Brownian motion. Additionally, it was thought that the (ethoxy)ethyl arms would facilitate the preorganisation of the complexes *via* electrostatic interactions within the second sphere of the lanthanide ion. Ligand **66**, which bears (ethoxy-)ethanol pendant arms, contains terminal alcohol groups to facilitate closing by Williamson ether

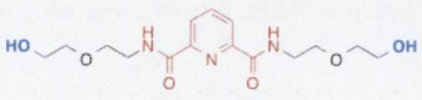


**66**

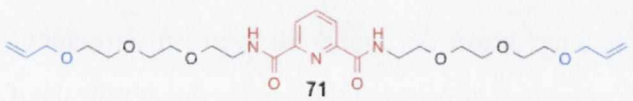

**71**

**Figure 5.6:** *Ligands designed for the synthesis of [3]-catenane.*

synthesis, with the appropriated linker for the formation of the final catenane. Ligand **71** was designed with longer arms terminated with allylic moieties, as this functionality can form a 29 membered ring *via* ring closing metathesis. Firstly, our study was focused on the templation process induced by **66** and this will be investigated in the following sections.

## 5.2 Lanthanide directed synthesis of a [3]-catenane *via* triple Williamson ether synthesis

### 5.2.1 Synthesis and characterisation of Ligand 66

The synthesis of compound **66,** which is shown in Scheme 5.7, was achieved in two steps, by first reacting pyridine-2,6-carboxylic acid under reflux with neat thionylchloride. Removing the excess $SOCl_2$ under reduced pressure gave the acid chloride **64** in 99% yield. A double acylation of **64** using 2-(2-aminoethoxy)ethanol **(64)** and triethylamine in dichloromethane gave ligand **66** as a pale pink oil in 78% yield, after stirring for 48 hours at room temperature and isolation by precipitation.

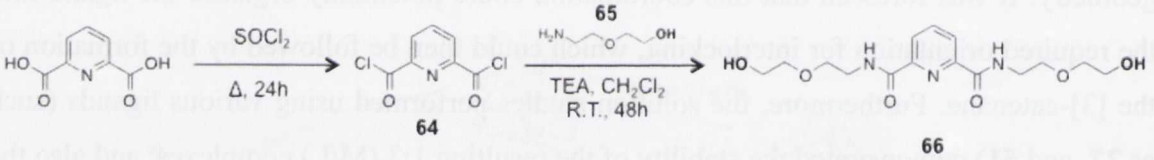


**Scheme 5.7:** *Synthesis in two steps of ligand* ***66*** *from the dipicolinic acid.*

The $^1$H-NMR (400MHz; MeOD-$d_4$) spectrum, shown in Figure 5.8 (Section 5.2.2), showed the characteristic chemical shifts of the pyridine proton as a doublet at 8.12 ppm and a triplet at 7.94 ppm, respectively. The scalar coupling and the integration of these resonances indicated that the central pyridinyl moiety was successfully alkylated at positions 2 and 6, giving the ligand an overall $C_2$ symmetry. Furthermore, the resonances of the alkyl chains were assigned using $^1$H-$^1$H COSY NMR analyses. The α-ether protons coalesced as a multiplet centred at 3.71 ppm and the -$CH_2$ protons next to the alcohol moieties resonated as a triplet at 3.59 ppm, due to the shielding effect induced by the terminal –OH moieties. The protons located α-to the amide moieties formed a well-defined triplet, centred at 3.15 ppm.

Ligand **66** was further characterised by electrospray mass spectrometry analysis in MeOH and was detected as a mono-charged fragment $M^+$+HCl at $m/z$ = 378.2. The results obtained for the characterisation of ligand **66** were in agreement with those previously published by Bañuls *et al.* and confirmed the successful synthesis of **66** in high yields.[147]

### 5.2.2 Synthesis and characterisation of the complexes $66_3$.Ln (Ln = $Eu^{III}$, $Tb^{III}$, $Lu^{III}$)

The synthesis of the various lanthanide complexes **$66_3$.Ln** was carried out following the general procedure discussed in the previous chapters and is shown in Figure 5.8, where ligand **66** was refluxed with 0.3 equivalents of $Ln(CF_3SO_4)_3$ (Ln = $Eu^{III}$, $Tb^{III}$,

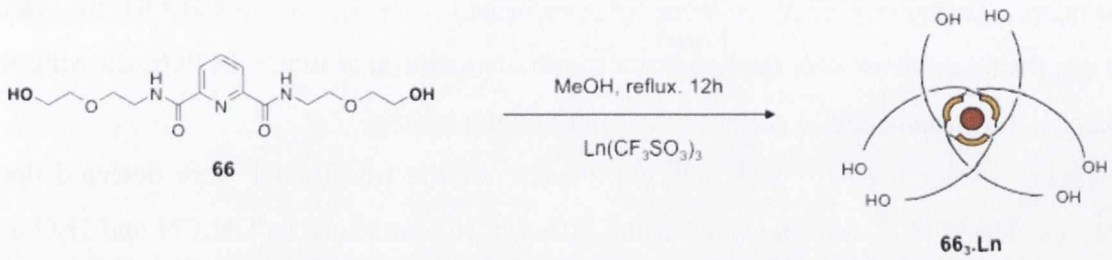


**Scheme 5.8:** *Synthesis of the complexes **$66_3$.Ln** (Ln = $Tb^{III}$, $Eu^{III}$, $Lu^{III}$).*

$Lu^{III}$) for 12 hours in $CH_3CN$. The reaction mixture was concentrated and the resulting complexes were precipitated from solution upon the addition of diethylether, which after filtration gave complexes **$66_3$.Tb** in 51%, **$66_3$.Eu** in 55.5%, and **$66_3$.Lu** in 67% yield.

The characterisation of each of these complexes was performed using conventional analytical methods, such as $^1$H-NMR spectroscopy, mass spectrometry, and elemental analysis. The $^1$H-NMR spectra (400 MHz, $CH_3OD$) of each complex are shown in Figure

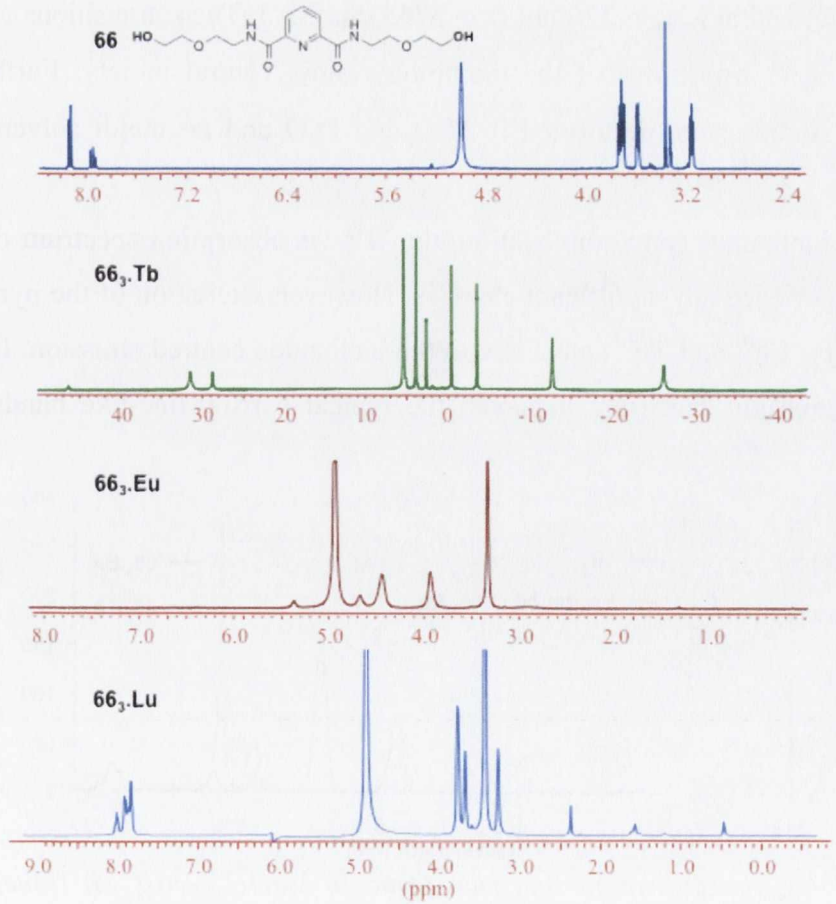


**Figure 5.9:** *$^1$H-NMR (400 MHz, $CD_3OD$) of the lanthanide complexes **66** (top), **$66_3$.Tb** (green), **$66_3$.Eu** (red) and **$66_3$.Lu** (blue).*

5.9 and confirmed the successful formation of single products with high levels of symmetry. Furthermore, in the case of $Tb^{III}$ and $Eu^{III}$, the paramagnetic nature of the lanthanide ions gave rise to shifted and broadened spectra, which indicated successful complexation of these ions to **66.**

The mass spectrometry analyses were first performed using ES/MS in $CH_3OH$, for which the **66$_3$.Eu** complexes were detected as a mono-charged ion at m/z = 1179.6, showing the typical isotopic distribution pattern of europium complexes.

However, neither the $Tb^{III}$ and $Lu^{III}$ complexes nor the free ligand were detected upon analyses. The studies were repeated using different solvents such as $CH_3CN$ and $H_2O$ and using MALDI-Tof MS. Unfortunately, these had no major effect on the results of the mass spectrometry experiments.

### 5.2.3 Investigation of the photophysical properties of the luminescent lanthanide complexes 66$_3$.Ln (Ln = $Eu^{III}$, $Tb^{III}$)

The photophysical properties of the complexes **66$_3$.Eu** and **66$_3$.Tb** were investigated in $CH_3OH$. The UV-vis absorption spectrum of ligand **66** recorded at $C_L$ = $2\times10^{-5}$ M is shown in Figure 5.10 and displayed major bands centred at $\lambda_{max}$ = 217 nm ($\varepsilon$ = 16590 $cm^{-1}M^{-1}$) and at $\lambda_{max}$ = 276 nm ($\varepsilon$ = 5745 $cm^{-1}M^{-1}$). These transitions are indicative of the $S_0 \rightarrow \pi$-$\pi^*$ transitions of the diaminopyridinyl central moiety. Furthermore, the ground state studies were performed in $H_2O$ and $D_2O$ and no major solvent effect was observed.

Upon lanthanide ion complexation, the UV-vis absorption spectrum of compound **66** did not experience any significant changes. However, excitation of the pyridine groups of **66$_3$.Ln** (Ln = $Eu^{III}$ and $Tb^{III}$) gave rise to the lanthanide centred emission. In the case of **66$_3$.Tb,** the emission spectrum displayed the typical narrow line-like bands of terbium

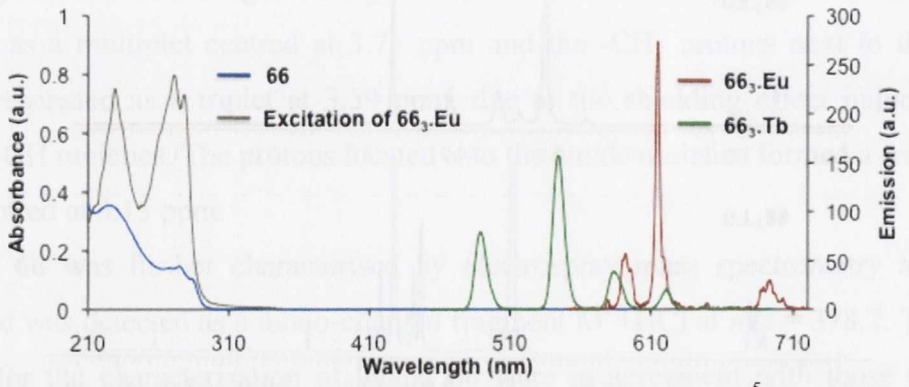


**Figure 5.10:** *UV-vis absorption spectrum of **66** in MeOH ($2\times10^{-5}$M) (blue), lanthanide emission of **66$_3$.Eu** (red) and **66$_3$.Tb** (green) ($\lambda ex$ = 275 nm) and excitation spectrum of the $Eu^{III}$ emission at 615 nm of **66$_3$.Eu** (brown)*

occurring at 487 nm, 545 nm, 581 nm and 613 nm, indicative of the $^5D_0 \rightarrow {}^7F_n$ (n = 4-1) deactivation, respectively. Similar results were obtained for **66$_3$.Eu**, for which the $Eu^{III}$ emission (Figure 5.10), showed the successful population of the $^5D_0$ excited states of the ion. The energy transfer process was also confirmed by carrying out fluorescence excitation spectra experiments, the results of which are shown in Figure 5.10 and in appendix 5.1 for **66$_3$.Eu** and **66$_3$.Tb**, respectively. These exhibited in each cases, two major bands centred at 217 nm and 271 nm, which matched the UV-vis absorption spectrum of ligand **66** in both cases. Furthermore, the emission spectrum of **66$_3$.Eu** showed the presence of the $^5D_0 \rightarrow {}^7F_0$ transition at 573 nm, which suggested that the europium centre was in a $C_3$ symmetrical environment.

The excited state lifetimes of the **66$_3$.Ln** complexes are summarised in Table 5.1 and were calculated from the luminescence emission decays recorded in $H_2O$, $D_2O$ and $CH_3OH$ (shown in Figure 5.11 and appendix 5.2). These were best fitted to a mono-exponential decay, which was indicative of the formation of a main luminescent species with excited states lifetimes of $\tau_{D2O}$ = 2.34 ms and $\tau_{D2O}$ = 2.94 ms for **66$_3$.Tb** and **66$_3$.Eu**, respectively. However, as observed in the case of the diaminopyridinyl derivatives **27R-S** and **51R-S** in Chapter 4, the luminescence decays recorded in $H_2O$ were best fitted to bi-exponential decays significant of the presence of more than one species in solution. The first luminescent species exhibited long lifetimes of $\tau$ = 1.52 and $\tau$ = 1.4 ms and were calculated to be the predominant species in solution with contributions of 81.2 and 83.6 % for the $Tb^{III}$ and $Eu^{III}$ complexes, respectively.

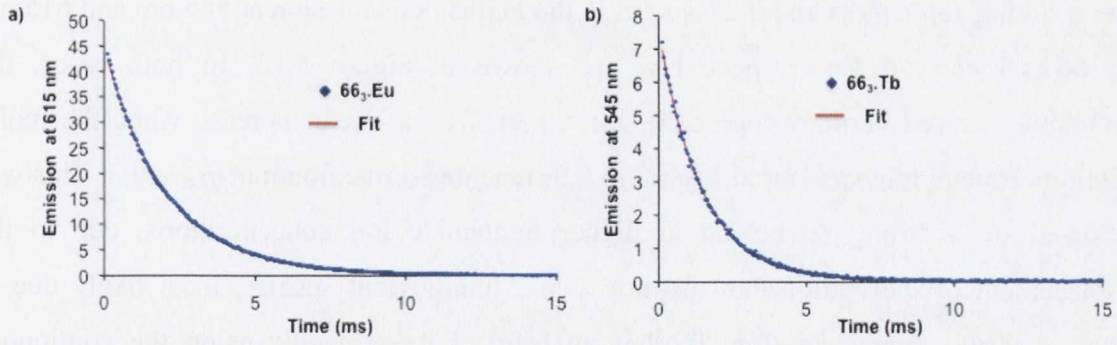


**Figure 5.11:** *Luminescence emission decays ($\lambda ex$ = 275 nm) of **66$_3$.Eu** (a) and **66$_3$.Tb** in MeOH (b) and resulting mono-exponential fits (red).*

The hydration states were calculated as $q \approx 0$ and $q \approx 0.8$ for **66$_3$.Eu** and **66$_3$.Tb**, respectively, suggested that the lanthanide ions were in a nonadentate coordination environment, where each of the pyridyl nitrogens and the two amides were coordinated to the metal ion. The second minor species, which possessed shorter lifetimes of $\tau$ = 0.87 ms

**Table 5.1:** *Lifetimes of $Ln^{III}$ excited states obtained from the emission decays of $66_3$.Ln and q values*

| $L_3$.Ln | $\tau(CH_3OH)$ | $\tau(D_2O)$ | $\tau(H_2O)$ % Pop | | q | |
|---|---|---|---|---|---|---|
| Ln = $Tb^{III}$ | 1.44 | 2.34 | 1.52<br>*81.2* | 0.870<br>*18.8* | 0.8 | 3.8 |
| Ln = $Eu^{III}$ | 2.02 | 2.94 | 1.42<br>*83.6* | 0.34<br>*16.4* | 0.1 | 2.8 |

(in the case of $Tb^{III}$) and $\tau$ = 0.34 ms (for the $Eu^{III}$), were calculated to contain three $H_2O$ molecules, suggesting the potential formation of **$66_2$.Eu** complexes.

The above results demonstrated the successful synthesis of the **$66_3$.Ln** complexes and suggested that they adopted the optimum $C_3$ symmetry necessary to potentially lead to the formation of a [3]-catenane. The next step in the investigation was the study of the formation and the stability of the complexes *in situ*.

### 5.2.4 Studies of the formation of the complexes $66_3$.Ln *in situ*.

Initially, the stoichiometries of the above complexes were investigated using Job's Plot experiments, in a similar manner to that discussed in the previous chapter. In each case, the experiment was performed in $CH_3OH$ at an overall concentration of $C = 2\times10^{-5}$ M, by varying the molar fraction of **$Ln(CF_3SO_3)_3$** from $\chi_{Ln} = 0$ to 1. Each luminescence spectrum was recorded from a freshly made solution, which was formed by stirring the appropriate quantities of **66** with the lanthanide salt at room temperature for five minutes. The resulting Job's plots and the changes in the lanthanide emission at 545 nm and 615 nm for **$66_3$.Tb** and **$66_3$.Eu**, respectively, are shown in Figure 5.12. In both cases, the lanthanide centred luminescence emission experienced a linear increase when the molar fraction of metal ion was varied from 0 to 0.3; reaching a maximum at $\chi_{Ln} = 0.3$. This was followed by a strong quenching at higher lanthanide ion concentrations, due to the displacement of the equilibrium towards a less luminescent species, most likely due to dilution of the ligand solution. Further analysis of these results using the continuous variation methods suggested that the overall stoichiometry of the **$66_n$.$Tb_m$** and **$66_n$.$Eu_m$** complexes, as a function of m/n, were 0.3 and 0.28, respectively, confirming that the most stable species in solution were the **$66_3$.Tb** and **$66_3$.Eu** complexes.

The formation of the complexes *in situ* was further investigated observing the changes in the UV-vis absorption and time delayed emission spectra by carrying out lanthanide titrations in $CH_3OH$ at $C_L = 3\times10^{-5}$ M. No major changes were observed in the UV-vis absorption spectrum of **66** upon the addition of $Ln(CF_3SO_3)_3$, as shown in

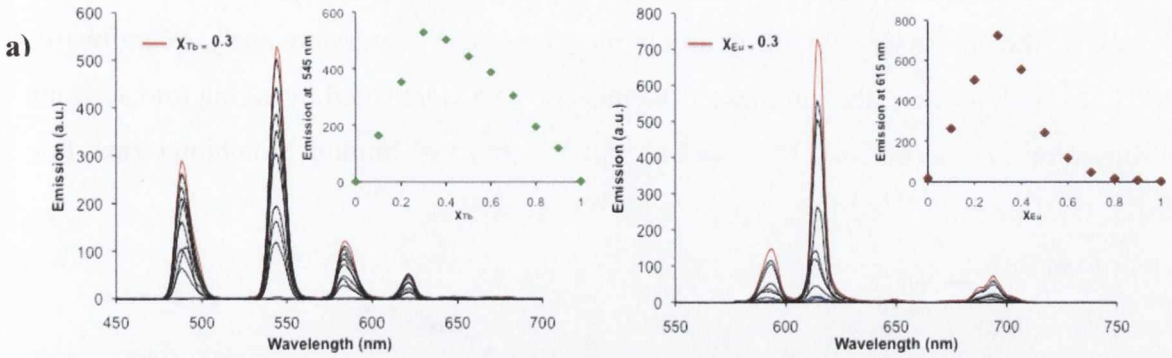


**Figure 5.12:** *Job's plot for the determination of the stoichiometry of the complexes* ***66₃.Ln*** *in $CH_3OH$ at C =2×10$^{-5}$M. a) when Ln =Tb$^{III}$, inset: changes at 545 nm. b) when Ln = Eu, inset: changes at 615 nm.*

appendix 5.3. However, the changes observed in the lanthanide emission, shown in Figure 5.12, demonstrated that in the case of $Tb^{III}$, the largest changes were recorded up to the addition of 0.4 equivalents, which suggested the formation of the desired 1:3 stoichiometric species.

Moreover, after the addition of 0.5 equivalents of $Tb^{III}$, the emission intensity showed a less pronounced increase, which reached a plateau upon the addition of 1 equivalent. These results suggested the displacement of the equilibrium towards the formation of a minor species in solution, such as the 1:2 or 1:1 (L/M) species. Similar conclusions were deduced from the $Eu^{III}$ titration, which is also shown in Figure 5.13. Here, the europium centred luminescence emission was initially "*switched on*" and reached

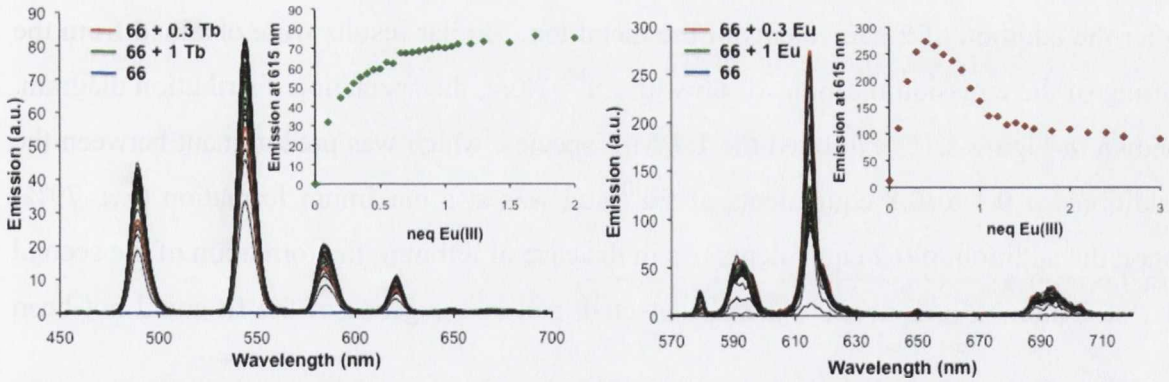


**Figure 5.13:** *Changes obtained in the emission spectrum of* ***66*** *during the Ln titration at $C_2$ =3×10$^{-5}$M in MeOH. a) Ln =Tb$^{III}$, inset: isotherm of complexation at 545 nm. b) Ln = Eu$^{III}$, inset: isotherm of complexation at 615 nm*

a maximum intensity upon the addition of 0.4 equivalents of lanthanide ion, indicating the formation of the **66₃.Eu** complexes (Figure 5.13). The equilibrium was then displaced, as a quenching of the emission intensity was observed. This was not observed for the $Tb^{III}$ ion, as it is less sensitive to the presence of solvent molecules in its coordination sphere, when compared with the europium ion. In both cases, the formation of the desired 1:3 stoichiometric species was detected, as shown in the insets of Figure 5.13.

The templation process was further investigated by fitting the spectroscopic changes in the lanthanide emission using the non-linear regression analyses software, SPECFIT®. In both case, the luminescence emission data were fitted by taking into account the formation of 1:1 (**66.Ln**), 1:2 (**66$_2$.Ln**) and 1:3 (**66$_3$.Ln**) binding stoichiometries. For

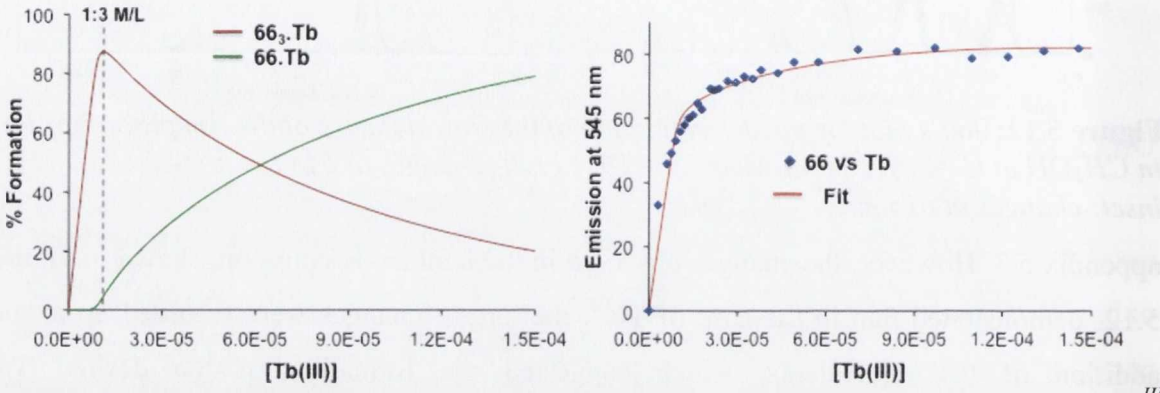


**Figure 5.14:** *Speciation distribution diagram of the species formed during the Tb$^{III}$ emission titration of* ***66*** *and fit resulting from the calculations.*

the complexation of Tb$^{III}$, the speciation distribution diagram resulting from the fit, which is shown in Figure 5.14, displayed the presence of two major species in solution. The **66$_3$.Tb** complex was the most predominant species formed upon the addition of 0.1 to 2 equivalents of terbium and was present in over 87% formation in the presence of 0.33 equivalents of $Tb(CF_3SO_3)_3$. However, a second 1:1 stoichiometric species was also formed at higher Tb$^{III}$ concentration and became the most predominant species in solution after the addition of 2 equivalents of the metal ion. Similar results were obtained from the fitting of the emission titrations of **66** with Eu$^{III}$. Here, the speciation distribution diagram, shown in Figure 5.15, exhibited the 1:3 M/L species, which was predominant between the additions of 0.1 to 0.8 equivalents of Eu$^{III}$ and was at a maximum formation (*c.a.* 79%) upon the addition of 0.3 equivalents. As in the case of terbium, the formation of the second 1:1 stoichiometric complex was also detected, and convergence of the fit could not been

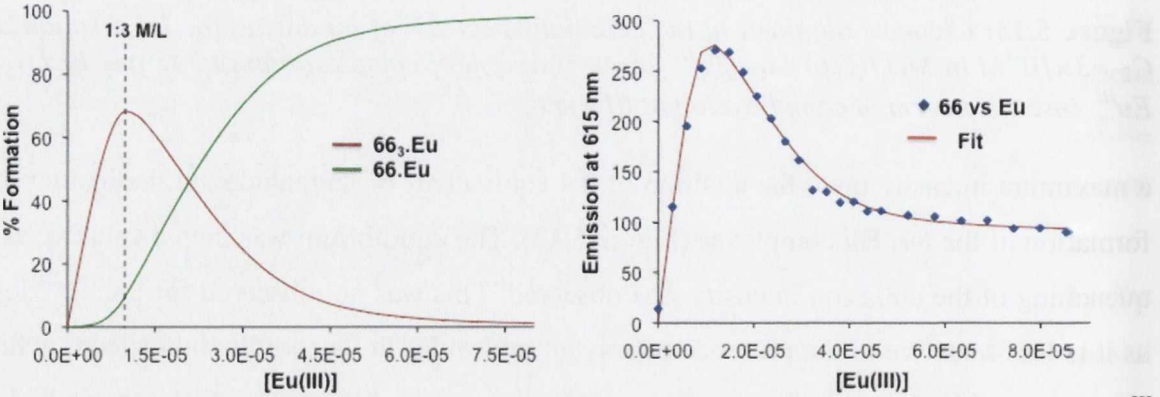


**Figure 5.15:** *Speciation distribution diagram of the species formed during the Eu$^{III}$ emission titration of* ***66*** *and fit resulting from the calculations.*

reached without the inclusion of this species. From these fits we were able to determine the stability constants associated with the formation of each species, and these are summarized in Table 5.2. In both cases, the **66$_3$.Ln** complexes were formed with high binding constants of $log\ \beta_{1:3}$ = 17.1 and 17.8 for **66$_3$.Eu** and **66$_3$.Tb**, respectively, which are of the same magnitude to those reported within the previous chapter for the other diaminopyridine derivatives.

**Table 5.2:** *Binding constants and % formation species at 1:3 M/L ratio obtained from fitting of the luminescence titirations of* **66** *with* $Tb^{III}$ *and* $Eu^{III}$

| **66$_3$.Ln** | $log\ \beta_{13}$ | $log\ \beta_{11}$ | **% formation at 1:3 M/L** | |
|---|---|---|---|---|
| **Ln=$Tb^{III}$** | 17.8 ± 0.8 | 5.77 ± 0.6 | 87.3 | 3.6 |
| **Ln=$Eu^{III}$** | 17.0 ± 0.5 | 6.3 ± 0.2 | 69.1 | 7.0 |

In summary, the results obtained within the last section demonstrated that the **66$_3$.Ln** complexes were successfully synthesised in high yield and, in general, showed high stability in solution. Furthermore, the $^1$H-NMR analyses and the results obtained from the photophysical studies of each complex were compared with those obtained for the monometallic molecular bundles **27S** and **27R** (Section 3.2) and showed that the **66$_3$.Ln** complexes adopted the desired $C_3$ symmetry and, therefore, should be suitable for attempting catenation *via* triple clipping using the Williamson ether synthesis.

### 5.2.5 Catenation *via* triple-Williamson ether synthesis of 66$_3$.Ln

As previously mentioned, the strategy envisaged for the synthesis of a Ln-templated [3]-catenane involves a triple clipping strategy using Williamson ether synthesis. This would involve the reaction of an appropriately sized diodo-(ethoxy)ethylene linker with the two alcohol moieties of the same ligand. The success of the catenation process resides in the balance between the bulk provided by the templation process and the Brownian motion caused by the triple clipping, which is directly linked to the size of the space employed in the clipping process. Consequently, the feasibility of the catenation was investigated by performing MM2 calculations on the **66$_3$.Tb** complex and the various catenates resulting from the use of diodo-(ethoxy)$_n$ ethylene as linkers, where n was varied from 0→2.

For these calculations, each model, shown in Figure 5.16, was built from the crystallographic data previously reported for the **27R$_3$.Tb** complexes (Chapter 3). It was clear from the molecular models that the formation of the catenane was dependant of the

size of the linker. Indeed, the longer the linker, the lower the steric energy associated with the system. This suggested that longer linkers gave rise to more stable catenane structures.

However, a longer linker could increase the freedom of the architecture and, therefore, reduce the selectivity of the ring closing, giving rise to a higher number of conformation isomers. The utilization of the iodo-(iodoethoxy) ethane linker appeared to be the best compromise between the steric energy and the Brownian motion of the triple ring closing. The calculations were also performed on the molecular knot (**K66$_3$.Eu**), which resulted from an interligand reaction and the resulting energy obtained was in the same range to that obtained for **Cat66.Eu.** This suggested that not one of the inter- or intra-ligand based topologies was specifically favoured over another.

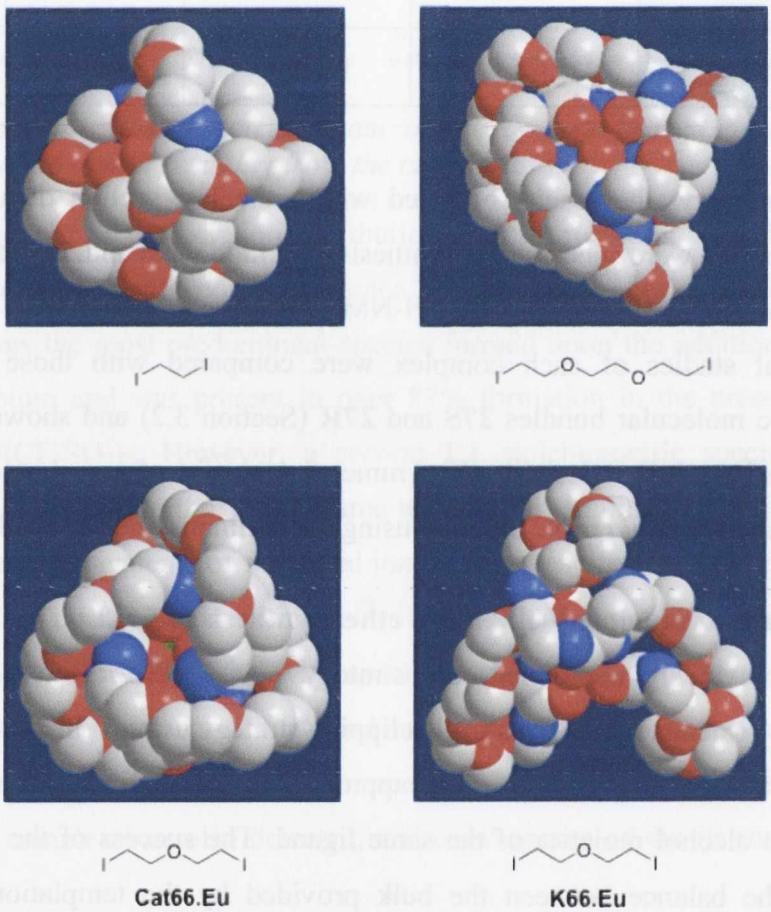


**Figure 5.16:** *Molecular models of the prospective catenanes obtained by the utilisation of various diodo-(ethoxy)$_n$ ethylene. a) when n = 0, b) n = 2 c) n =1 d) molecular knot obtained from the interligand ring closing when n =2.*

The catenation reactions were carried out at low concentration in order to avoid potential polymerisation due to intermolecular reactions. Following the procedure shown in Figure 5.17, the **66$_3$.Ln** complexes were stirred in DMF with $Cs_2CO_3$ in order to activate the hydroxyl moieties. To this solution, linker diodo-(ethoxy)$_2$ethylene was added dropwise and the resulting mixture was stirred at room temperature for 48 h. After,

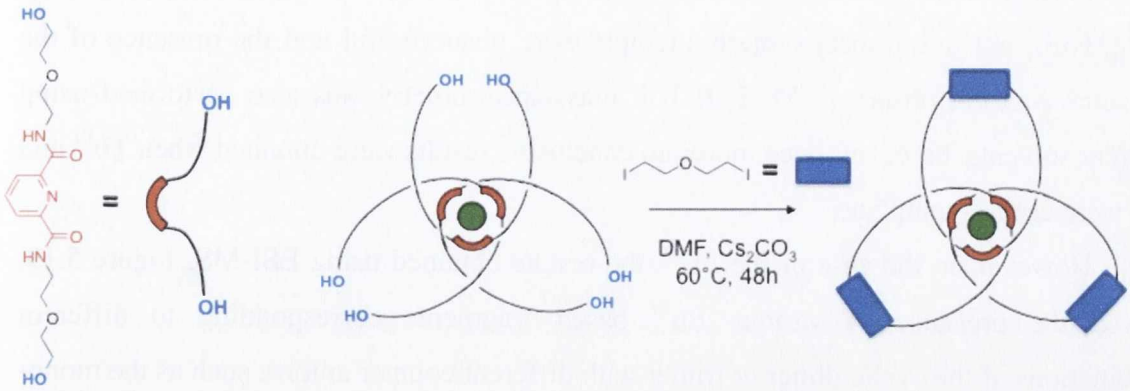


**Figure 5.17:** *Schematical representation of the general procedure used for the formation of the catenanes.*

removing the solvent under reduced pressure, the **Cat66.Ln** complexes were obtained as white solids after precipitation from a concentrated $CH_3OH$ solution using diethyl ether. The $^1$H-NMR analyses of the resulting oils (600MHz, MeOD), shown in Figure 5.18, gave rise to simple spectra, which suggested the presence of a predominant species with a high degree of symmetry. This also indicated that the symmetry of the **$66_3$.Ln** complexes was transferred to the resulting products, confirming the successful minimisation of the competitive intermolecular processes during the macrocyclisation. Indeed, intermolecular Williamson reactions would give rise to larger architectures containing several metal centres. This would give rise to more resonances in the NMR spectra of the adducts, in contrast to the spectra shown in Figure 5.18.

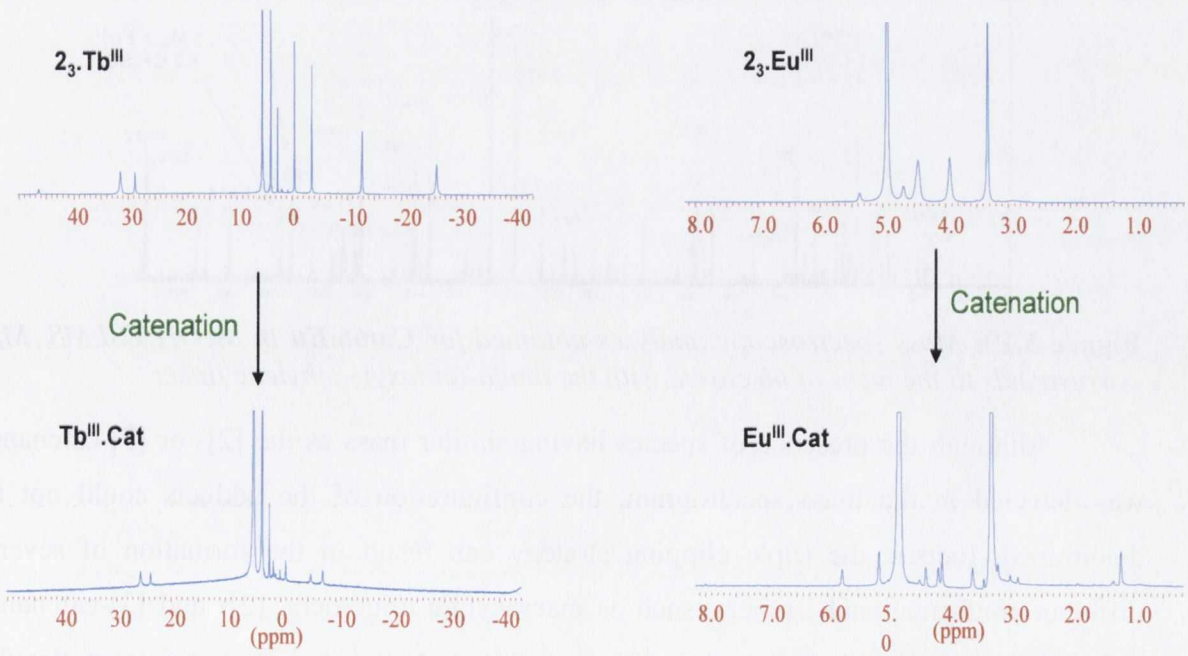


**Figure 5.18:** *$^1$H-NMR ($CD_3OD$) spectra of **$66_3$.Tb** and **$66_3$.Eu** and the resulting potential catenanes.*

Further characterisation of the catenates was performed using mass spectrometry (ESI-QToF), but unfortunately these attempts were unsuccessful and the presence of the catenanes was not observed. MALDI-ToF mass-spectrometry was also performed using different solvents, however, once more; no conclusive results were obtained when $Tb^{III}$ and $Lu^{III}$ were used as templates.

However, in the case of the $Eu^{III}$, the results obtained using ESI-MS, Figure 5.19, showed the presence of various $Eu^{III}$ based fragments corresponding to different combinations of the cyclic dimer or trimer with different counter anions, such as the mono-charged ions at m/z = 1119.8, 1662.5 and 1685.6 found for $[2M_m+Eu^{3+}+OH^-+I^-]$ (calculated at 1119.22), $[3M_m+Eu^{3+}+CF_3SO_3^-+I^-]$ (calculated at 1662.37), and $[3M_m+Eu^{3+}+2CF_3SO_3^-]$ (calculated at 1685.62), respectively (with $M_m$ = mass of the macrocycle resulting from the closing of **66** with the diodo-(ethoxy)$_2$-ethylene linker). However, the presence of the open complexes **66$_3$.Eu** was not detected, indicating the efficiency of Williamson ether synthesis process.

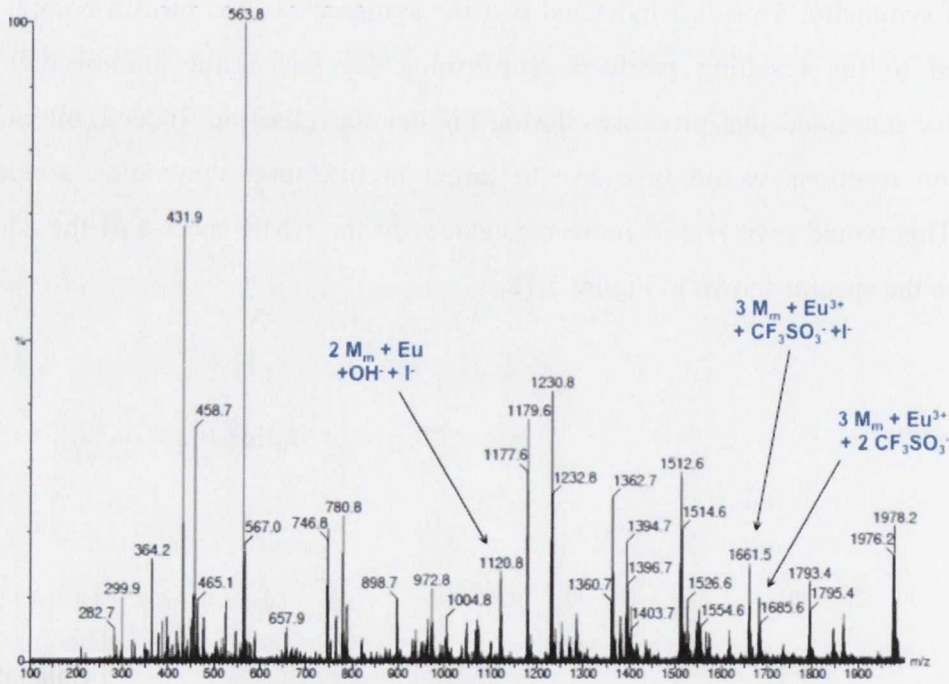


**Figure 5.19:** *Mass spectroscopy analyses obtained for* ***Cat66.Eu*** *in MeOH ESI.MS, $M_m$ corresponds to the mass of* ***66*** *closed with the diodo-(ethoxy)$_2$-ethylene linker*

Although the presence of species having similar mass as the [2]- or [3]-catenanes was detected in the mass spectrogram, the configuration of the adducts could not be determined. Indeed, the triple clipping strategy can result in the formation of several different conformational isomers, such as macrocyclic oligomers, [2]- and [3]-catenanes and other molecular knots, as the catenation occured *via* an inter- or intra-molecular pathway, some examples of which are shown schematically in Figure 5.20. Each of these

topologies adopts a different geometry upon catenation, which is usually governed by the various interactions taking place within the structures. The resulting supramoleculer architectures have different stabilities, which upon decomplexation can give rise to the formation of further compounds (Figure 5.20).

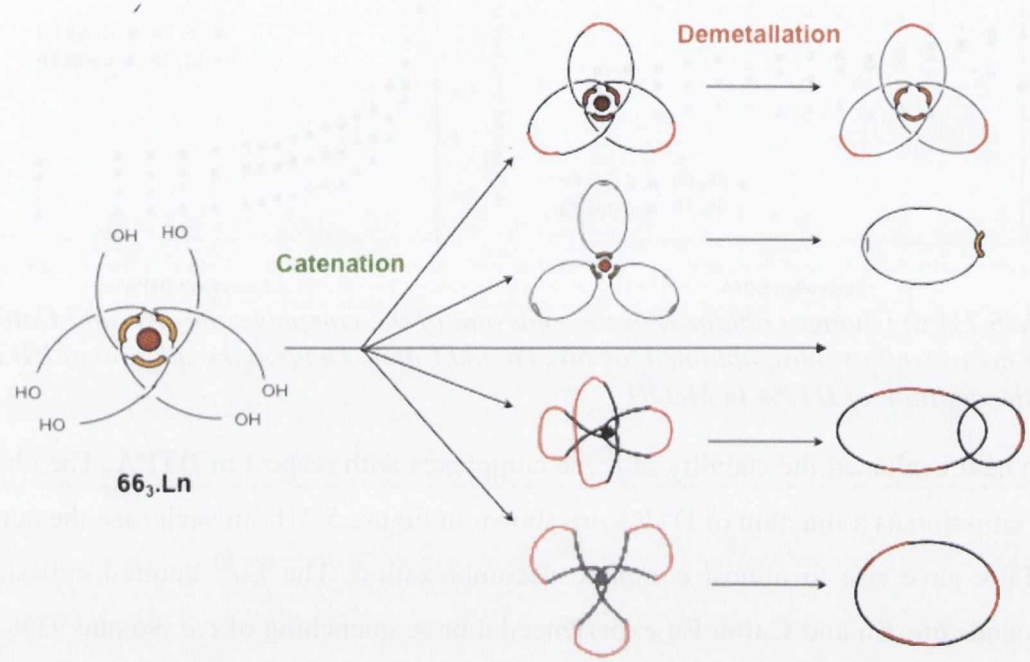


**Figure 5.20:** *Schematic representation of some of the different isomers which could be obtained from a triple clipping catenation strategy*

As the luminescent properties of the lanthanide are highly dependent on the coordination environment, the emission spectra of the resulting complexes would be different to that of **$66_3$.Tb** and **$66_3$.Eu**. Consequently, the stability of the compounds formed after the catenation reaction, were also investigated using a known $Ln^{III}$ competitor. These studies, referred to as demetallation studies, were performed on the **$66_3$.Tb** and **$66_3$.Eu** complexes and the corresponding **Cat66.Eu** and **Cat66.Tb** adducts using **EDTA** and **DTPA**, which are known to be competitive binders for lanthanide ions, forming 1:1 M/L stoichiometric complexes with high binding constants in the range of log $\beta_{11}$ = 17 and 22 respectively, along the lanthanide serie.[12] The demetallation was performed titrating a solution of the corresponding adduct in MeOH ($C_{Ln} = 2\times10^{-5}$ M) with **EDTA** and **DTPA**. The resulting solution was stirred for 5 minutes between each addition.

When the demetallation was undertaken with **EDTA** only minor quenching of the $Ln^{III}$ centred emission was observed, as is shown in Figure 5.21a. In the case of **$66_3$.Eu**, the luminescence emission experienced only minor changes upon the addition of **EDTA**, whereas a minor quenching of 10% was observed for the **Cat66.Eu** adduct, indicating the

stability of both structures with respect to **EDTA**. The demetallation process was more efficient in the case of the $Tb^{III}$. In both cases, a quenching of *c.a.* 40% of the $Tb^{III}$ emission was observed, with both profiles following similar patterns.

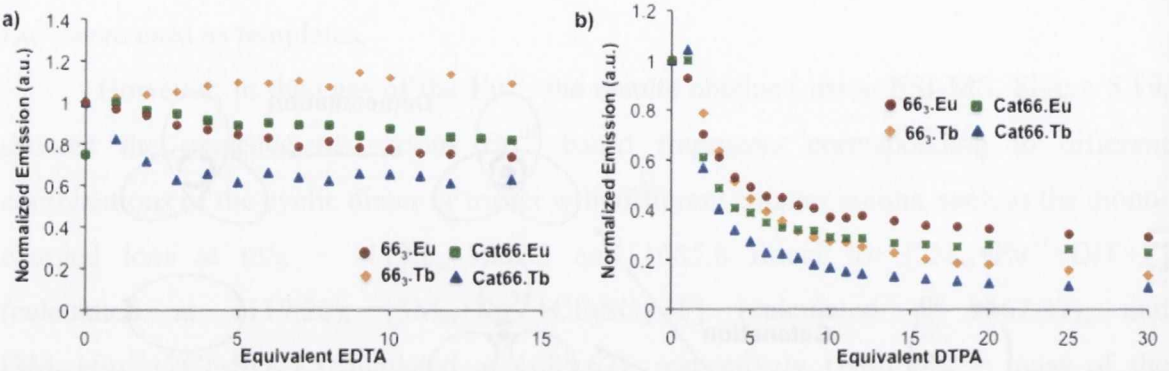


**Figure 5.21:** a) *Changes obtained in the emission of the complexes* ***66₃.Eu*** *and* ***Cat66.Eu*** *at 615 nm as well as those obtained for* ***66₃.Tb*** *and* ***Cat66.Tb*** *upon the addtion of* ***EDTA*** *b) upon the addition of* ***DTPA*** *in MeOH*

We next evaluated the stability of these complexes with respect to **DTPA**. The changes in the emission as a function of DTPA are shown in Figure 5.21b. In each case the addition of **DTPA** gave rise to almost complete decomplexation. The $Eu^{III}$ centred emission of compounds **66₃.Eu** and **Cat66.Eu** experienced a large quenching of *c.a.* 96 and 93% upon the addition of 20 equivalents of **DTPA**, indicating the successful demetallation of these two complexes. However, the profiles of the luminescence emission followed a similar trend suggesting that each of the four compounds possessed the same stability with respect to such a competitor. The same effect was observed for the $Tb^{III}$ based structures **66₃.Tb** and **Cat66.Tb**, which were demetallated upon the addition of 20 equivalents of **DTPA.** The luminescence emission of **66₃.Tb** and **Cat66.Tb** showed quenching of *c.a.* 77 and 80 %, respectively, following similar profiles. As previously mentioned, the interlocking of the **Cat66.Ln** structures upon catenation would be expected to give rise to highly symmetrical structures providing efficient shielding of the lanthanide ion. Therefore, these structures would benefit from a higher stability with respect to such a competitor, in comparison to their open form analogues. However, it was clear from these experiments that the macrocyclic ring closing did not give rise to the desired interlocked structures. For this reason, our investigation of the formation of [3]-catenanes will focus on the study of the systems based on ligand **71**, which will be the subject of the next sections.

## 5.3 Synthesis of [3]-catenane using triple-ring closing metathesis

### 5.3.1 Introduction to Ring-Closing metathesis using Grubbs catalyst

The olefin metathesis mechanism involves a metal-directed [2+2] cyclo-addition, which is symmetry forbidden and consequently possesses a high energy of activation. Thus, the metathesis pathway is usually thermodynamically driven and the distribution of the final products is determined by their energy levels.

The ring closing metathesis (RCM reaction), which consists of an intramolecular olefin metathesis, has been widely studied over the past century and, as such, has allowed the ring closing of cyclic alkenes of different size (from 5 up to 30 member ring), using catalysts based on transition metal such as $Ru^{II}$, $Re^{II}$ and $Os^{II}$.[148,149] The most versatile of these is the modern second generation Grubb's catalyst, which operates following the mechanism proposed by Chauvin (Figure 5.22).[150] The catalytic cycle is initiated by the formation of the metallacyclobutane, a key intermediate **a**, which can undergo cyclo-reversion towards metallo-alkene **b** or back to starting materials. Consequently, the driving of the catalytic cycle of the olefin metathesis is the removal of the resulting ethene from the reacting mixture. However, the success of the RCM resides in the reaction of the metallo-alkene terminal moiety of **b** with its second free allylic terminal to form the desired cycle and regenerate the catalyst.

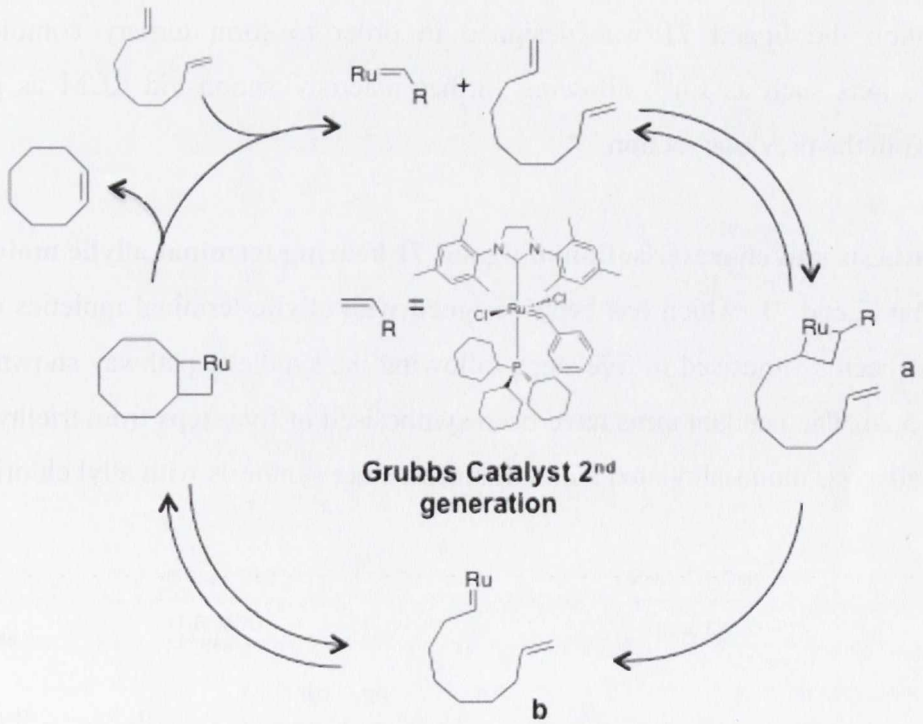


**Figure 5.22:** *Schematic representation of the mechanism of the ring closing metathesis enunciated by Chayvin et al.*[150]

It has been well established that the formation of smaller rings (from 5 to 8 member ring), which is energetically highly favorable, is usually thermodynamically driven, whereas the synthesis of larger macrocycles can be formed under kinetical control by carrying out the reaction at large dilution. It has also been proven that the rigidity and geometry of the acyclic ligand can have a significant influence on the rate of the reaction and on the control of the double-bond stereoisomerism; the ring closing of a long and flexible ligand can direct the selective formation of a macrocyle with *E-trans* configuration, while a smaller and more rigid ligand benefits from an inherent pre-organization, which allows the selective formation of the *Z-cis* conformation with higher rates.[151] However, the formation of the desired cyclic monomer is in competition with different cyclic and acyclic adducts *via* different intermolecular processes called oligomerization-backbiting. Consequently, the control of this oligomerization-backbiting pathway is essential for a selective RCM. It has been demonstrated by Grubbs and co-workers that the rate of the undesired reaction is highly dependent on the concentration and on the preorganization (or templation) of the linear starting material; In absence of preorganization, the reaction mixture has to be sufficiently dilute to shift the ring-chain equilibrium in favor of the RCM.[152] Thus, the design of linear ligands capable of RCM, for the use in the synthesis of interlocked systems can be quite challenging; the size of the linear precursor should be "ideal" in order to offer a perfect compromise between an effective threading and the control of all the reaction parameters. Taking these into consideration the ligand **71** was designed in order to form ternary complexes with lanthanide ions such as $Eu^{III}$, allowing further macrocylisation via RCM as previously mentioned in the previous section.

### 5.3.2 Synthesis and charaterisation of ligand 71 bearing terminal allylic moieties

The ligand **71**, which has been designed with allylic terminal moieties capable of RCM, has been synthesised in five steps following the synthetic pathway shown in Figure 5.23 and 5.24. The pendant arms have been synthesised in five steps from triethylenglycol, which firstly was mono-alkylated *via* Williamson ether synthesis with allyl chloride.

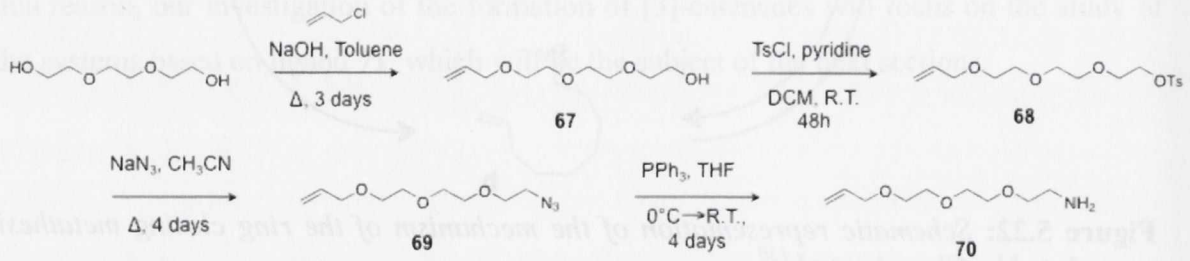


**Figure 5.23:** *Four steps synthesis of the compound **70** from the triethlyene glycol*

The triethyeneglycol was dissolved at low concentration in toluene and activated with an equimolar ratio of sodium hydroxide. A solution of allyl chloride was then added dropwise to the reaction mixture, which was allowed to stir for three days at room temperature. The compound **67** was isolated in 27 % yield after chromatographic purification over silica using a 7:3 EtOAc/hexane eluent system. The mono-allyl compound **67** was then reacted with TsCl in the presence pyridine in DCM leading to the mono-tosylated species **68** in 45% yield after chromatographic purification over silica gel.

The nucleophilic substitution of the tosyl leaving group of **68,** with an azide, was performed by refluxing **68** for four days in the presence of a large excess of $NaN_3$ in $CH_2Cl_2$. The mono-azide **69** was then isolated in high yields (80%) after removal of the solvent as a white powder, and characterisation of it showed that no further purification was needed. The reaction of the azide terminal moiety of **69** with triphenylphosphine in THF yielded **70** in high yield (>99%).

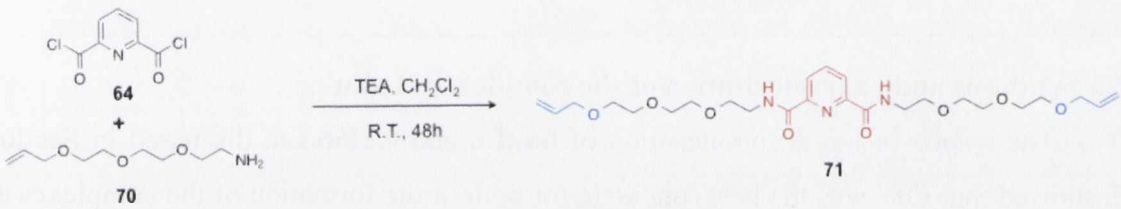


**Figure 5.24:** *Synthesis of 71 from the diacid chloride 64*

The ligand **71** was finally obtained reacting the acid chloride **64** with compound **70** in a similar manner than for the synthesis of ligand **66** (Section 5.2), as shown in Figure 5.24. Here, the two equivalents of compound **70**, were activated in the presence of 2 equivalents of triethylamine, and the resulting mixture was added dropwise to a solution composed of the acid chloride **64** and another 4 equivalents of triethylamine at 0 °C. The resulting mixture was then allowed to reach room temperature and was further reacted for two days. The ligand **71** was isolated after serial acid-base extractions and column chromatographic purification in 48% yields as yellow oil. The $^1$H-NMR analysis ($CDCl_3$, 400 MHz) of **71** showed the presence of a single compound with an overall $C_2$ symmetry (Figure 5.25). It displayed the typical resonances of the allylic protons observable as a multiplet at $\delta_H$ = 5.89 ppm in the case of the CH and a doublet-doublet between 5.14 and 5.29 ppm for the terminal protons of the allyl group, and the protons of α-position next to double bound were found to resonate as a doublet at 3.56 ppm due to the shielding effect caused by the neighbouring allylic group, whereas the protons $H_d$, which were unshielded due to the amide function were observed as a well defined triplet downfield of the alliphatic region at δ = 3.9 ppm.

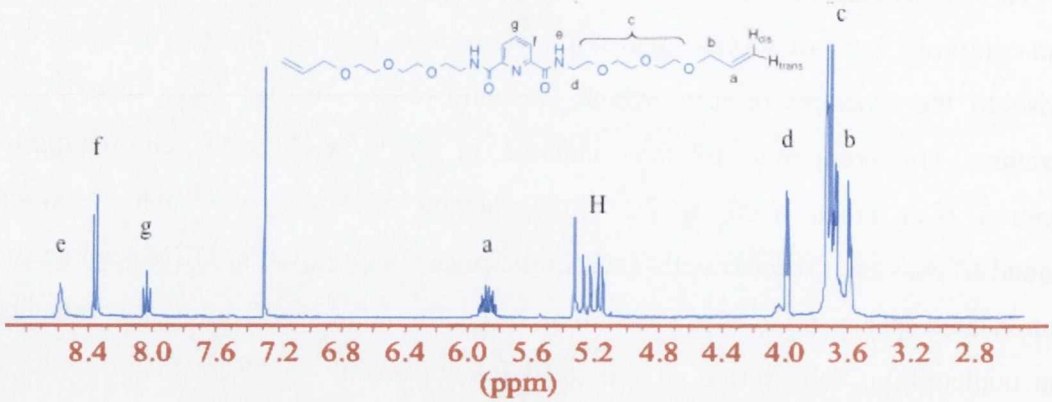


**Figure 5.25:** *$^1$H-NMR ($CDCl_3$, 400MHz) spectrum of 71*

The successful formation of ligand **71** was further confirmed *via* ESI mass spectrometry, in which compound **71** was detected as a mono-charged fragment at m/z = 472.28 corresponding of the $[M+Na^+]^+$ ion. The next step of our study was the investigation of the templation process prior to the catenation.

### 5.3.3 Synthesis and characterisation of the complexes $71_3$.Eu

The results of the decomplexation of **$66_3$.Ln** and **Cat66.Ln**, discussed in Section 5.2, showed that $Eu^{III}$ was the best candidate for both of the formation of the complexes as well as for the catenation. For these reasons our investigation will be focused on the study of the templation using $Eu^{III}$. The synthesis of **$71_3$.Eu** has been performed in $CH_3CN$ and in MeOH following the general procedure described bellow and shown in Figure 5.26.

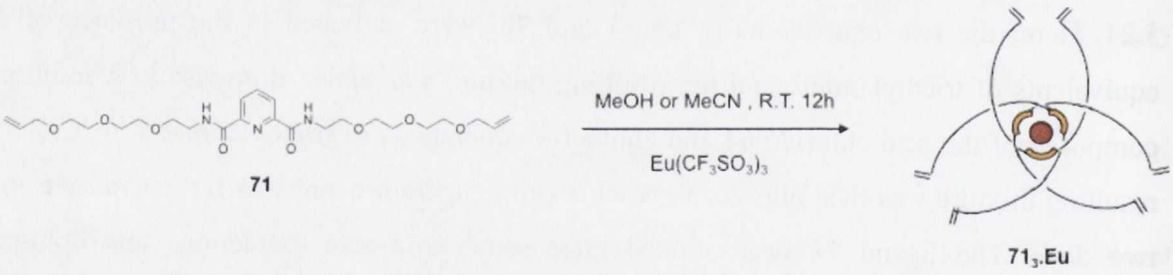


**Figure 5.26:** *General procedure for the synthesis of $71_3$.Eu*

The ligand **71** was mixed with 0.33 equivalent of $Eu(CF_3SO_3)_3$ in MeOH or MeCN. The resulting mixture was refluxed for 24h. Finally the complex **$71_3$.Eu** was isolated in 27% (from MeOH) and 32% (from MeCN), as a yellow oil after diethyl-ether diffusion in $CH_3OH$. Unfortunately, during the ESI mass spectrometry analyses, neither of the unreacted ligands or the complexes was detected. Further mass spectrometry studies were also performed in different solvent and using MALDI but these experiments remained unsuccessful in all cases.

The characterisation of the complex was also achieved using $^1$H–NMR and IR analyses. The $^1$H-NMR spectrum ($CDCl_3$; 400MHz) of **71$_3$.Eu**, shown in Figure 5.27, clearly indicated the presence of a single species in solution with $C_3$ symmetry. Furthermore, the significant broadening due to the paramagnetic effect of the europium ion was also observed confirming successful complexation. The shifting was found to be weak, as previously observed in the case of the analogues **66$_3$.Eu,** containing –OH terminal moieties.

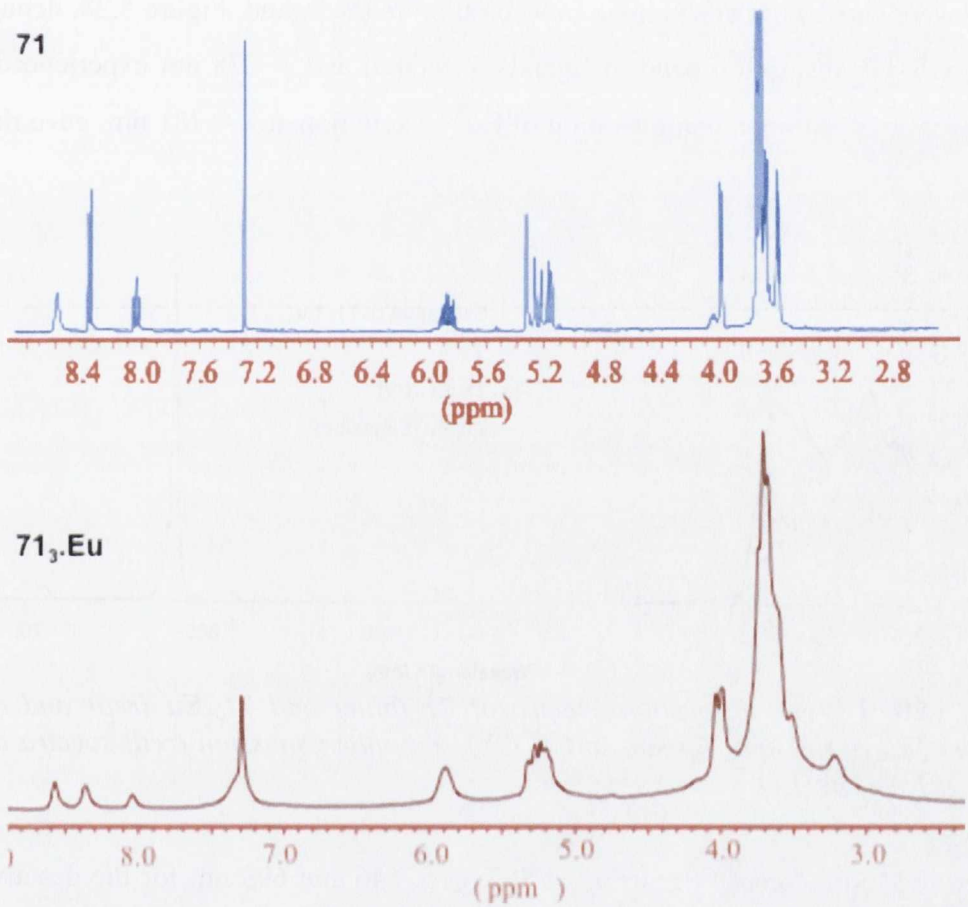


***Figure 5.27:*** *$^1$H NMR spectrum (400MHz in $CDCl_3$) of ligand **71** (top) and of the europium complex **71$_3$.Eu** (bottom).*

The resonances of the alkene protons at 5.3 and 5.9 ppm experienced a similar broadening as those of the pyridinyl at 8.0 and 8.3 ppm. This further preorganisation of the (ethoxy)$_2$-ethylenyl pendant arms, which was also suggested by the aforementioned high degree of symmetry, confirmed that the complexation of $Eu^{III}$ with compound **71** provides a suitable method for the templation of interlocked structures, arranging three ligands in a optimal position in order to favour the interlocking of the macrocycles upon catenation.

### 5.3.4 Photophysical studies of the complex $71_3$.Eu

The photophysical properties of **71** and its resulting $Eu^{III}$ complex **$71_3$.Eu** were investigated in $CH_3CN$, $H_2O$ and $D_2O$. The UV-vis absorption spectrum of the ligand **71**, shown in Figure 5.28, displayed two absorption bands centred at $\lambda$ = 227 nm ($\varepsilon$ = 9500 $M^{-1}$ $cm^{-1}$) and $\lambda$ = 278 nm ($\varepsilon$ = 4010 $M^{-1}\cdot cm^{-1}$) indicative of the $^1\pi$-$\pi^*$ transitions of the diamido-pyridine chromophore. The excitation of these transitions gave rise to only minor fluorescence emission, which indicated that the $S_1$ excited states of the ligand was deactivated *via* non-radiative processes. The UV-vis absorption analysis of the complex **$71_3$.Eu**, were carried out at a similar concentration to the ligand, Figure 5.28, demonstrates that the UV-vis absorption band of ligand **71** centred at $\lambda$ = 278 nm experienced a large hyperchromic effect upon complexation of $Eu^{III}$. Excitation at $\lambda$ = 281 nm, gave rise to the

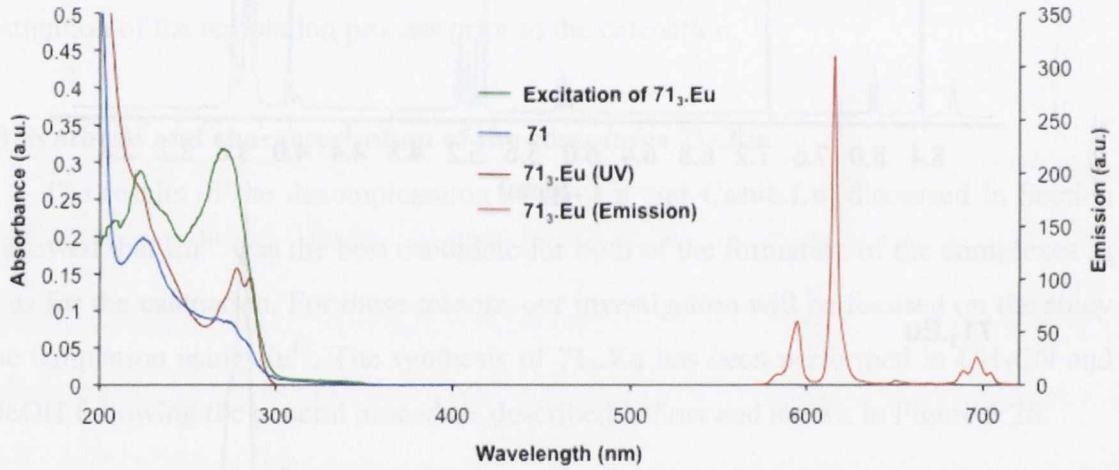


**Figure 5.28:** *UV-vis, absorption spectra of 71 (blue) and **$71_3$.Eu** (red) and excitation spectrum ($\lambda_{em}$ = 615 nm) (green) in $CH_3CN$). Europium emission (red) spectra of **$71_3$.Eu** ($\lambda_{exc}$ = 281 nm) in $H_2O$.*

$Eu^{III}$ centred luminescence occurring at 592, 615, 646 and 693 nm for the deactivation of the $^5D_0$ excited-states of the lanthanide to its $^7F_j$ ground states ($j$ = 1, 2, 3 and 4, respectively). Furthermore, the presence of the $\Delta J_0$ band 577 nm indicative of the $^5D_0 \rightarrow {}^7F_0$ suggested the $C_3$ symmetry for the complex. The excitation spectrum was also measured (Figure 5.28, $\lambda_{em}$ = 615 nm) and exhibited two major bands at 275 nm and 222 nm, which were structurally similar to the UV-vis absorption spectrum of **$71_3$.Eu**, indicating that the luminescence emission of the complex was sensitized by the antenna.

The decays of the $Eu^{III}$ emission intensity were measured in $CH_3CN$, $D_2O$ and $H_2O$. In $D_2O$ and $CH_3CN$ in (Figure 5.29 and appendix 5.4), the decays fitted best a mono-exponential decay, which indicated the presence of a single and long-lived luminescent species in solution possessing lifetimes of $\tau$ = 1.61 ms and $\tau$ = 1.67 ms, respectively.

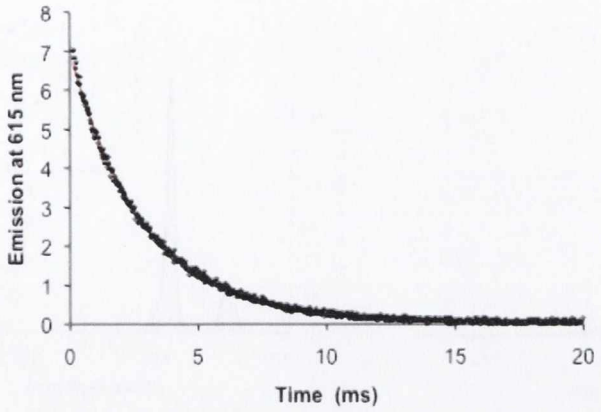


**Figure 5.29:** *Luminescence decay of* ***71$_3$.Eu*** *in $D_2O$ and mono-exponential fit (red)*

However, in $H_2O$ (appendix 5.4), the luminescence decays best fitted a bi-exponental decay indicative of the presence of two luminescent species in solution. A long-lived species with lifetimes of $\tau$ = 1.08 ms was detected to be predominant (>60% in solution). The hydration factors were calculated by to be 0, whereas the q values calculated for the second species were found to be $q \approx 3$, as the **dpa** derivative complexes were destabilised towards the formation of the 1:2 species in $H_2O$.[126] Therefore, the next step of our study was the investigation of the complexation process *in situ* and the stability of the template in solution.

### 5.3.5 Study of the formation of the complexes 71$_3$.Eu *in situ*

As in the case of **66$_3$.Eu** the stoichiometry of the binding of $Eu^{III}$ by **71** was investigated by using the Job's plot experiments in $CH_3CN$ at a sample concentration of C = $2\times10^{-5}$ M. The changes in the UV-vis absorption spectrum of ligand **71**, is shown in Figure 5.30 (left) and demonstrated the hyperchromic effect upon complexation of **71** to the $Eu^{III}$ ion, occurring while the molar fraction of metal ion in solution was varied from 0→0.3, where it reached a maximum intensity. This was followed by a strong decrease in the absorbance at higher molar fractions of metal, which confirmed the predominant formation of the 1:3 (M/L) stoichiometric species. The evolution of the europium centred luminescence, is shown in Figure 5.30 (right) and displayed similar results to those obtained in the UV-vis Job's plot. The $Eu^{III}$ emission was enhanced and reached a maximum when $\chi_{Eu(III)}$ = 0.25, confirming the major formation of the desired complex **71$_3$.Eu**. The displacement of the complexation equilibrium towards the formation of the 1:2 and 1:1 stoichiometric species was also detected as the decrease of the luminescence emission was more pronounced for the molar fraction ranging from 0.3 to 0.5 (inset Figure 5.30, right).

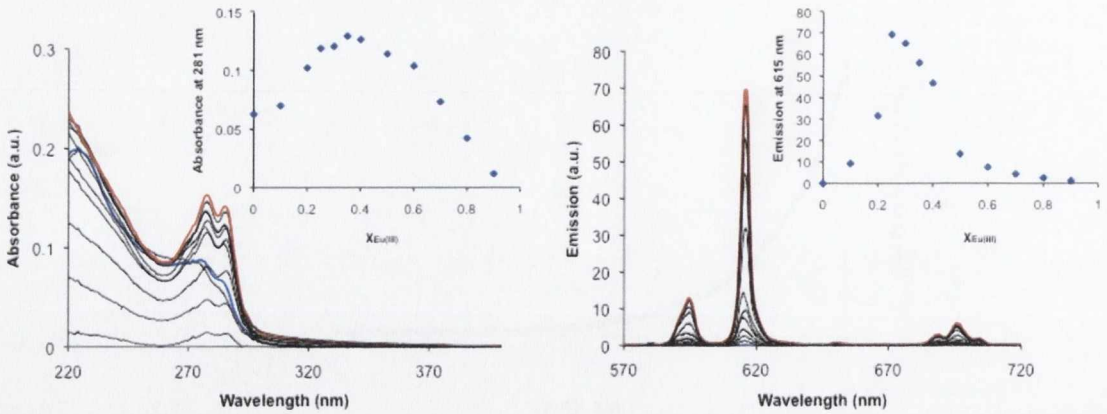


**Figure 5.30:** *Job's plot obtained in the UV-vis absorption (left) and in the lanthanide luminescence (right) in $CH_3CN$ at $C = 2\times10^{-5}$ M*

The formation of the complexes between **71** and $Eu^{III}$ was also investigated *in situ* using UV-vis and time delayed emission spectrophotometric titrations in $CH_3CN$ at $C_L = 2\times10^{-5}$ M. The results obtained for the UV-vis absorption, titrations are shown in Figure 5.31. Upon the addition of the $Eu^{III}$ ion, the π-π* transition of the pyridine chromophore centred at λ = 275 nm experienced hyperchromic effect reaching a plateau after the addition of 0.33 equivalents of europium, which was indicative of the aforementioned predominant formation of the complex **$71_3$.Eu**.

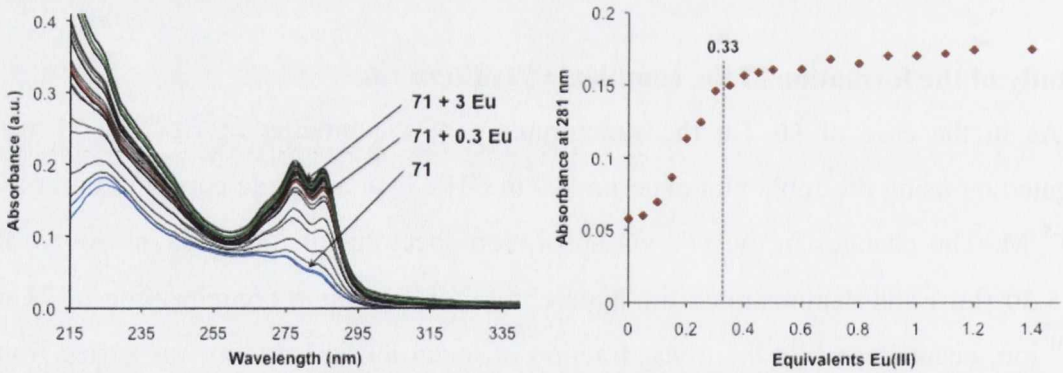


**Figure 5.31:** *UV-vis titration of **71** versus $Eu(CF_3SO_3)_3$ in $CH_3CN$ (right) Isotherm of complexation at λ = 281nm*

Here, as before, after the addition of 0.4 equivalents of $Eu^{III}$ the changes were less pronounced and the absorbance of the sample reached a plateau upon the addition of 0.6 equivalents of lanthanide ion. This suggested the weak formation of complexes possessing a different stoichiometry, such as possibly the 1:1 and 1:2 stoichiometric species. The changes obtained from the luminescence emission titrations, shown in Figure 5.32, allowed the same conclusions to be made; The europium centred luminescence was switched on and reached a maximum intensity upon the addition of 0.33 equivalents of lanthanide ion,

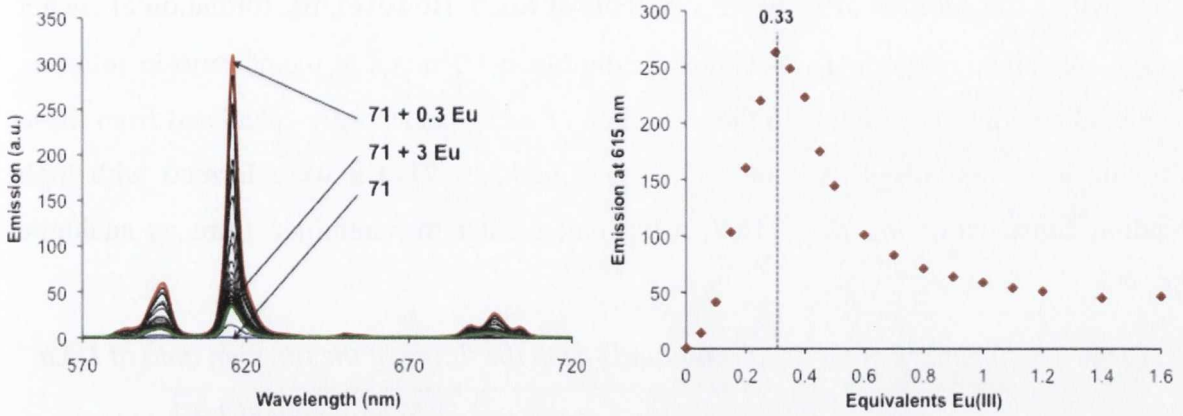


**Figure 5.32:** *Changes observed in the lanthanide emission spectrum during the titration in the of* ***71*** *versus* $Eu(CF_3SO_3)_3$ *in* $CH_3CN$ ($\lambda_{ex}$= *281 nm). (right) Isotherm of complexation at 615 nm.*

indicating the formation of the 1:3 (M/L) species. Further addition of metal ion resulted in a decrease of the luminescence intensity shown for the $\Delta J = 2$ transitions in Figure 5.32 (right), which reached a plateau upon the addition of 1 equivalent of $Eu^{III}$. This confirmed the displacement of the complexation equilibrium towards the formation of the 1:2 and 1:1 species.

Having shown the predominant formation of the **$71_3$.Eu** complex, the next step of our investigation was to quantify the formation of each luminescent species and deduce their stability. The changes obtained during the UV-vis titration were analysed using both non-linear regression analyses software SPECFIT®.

The fitting of several UV-vis data sets showed the presence of two major species in solution, as shown in the speciation distribution diagram in Figure 5.33. Here, the **$71_3$.Eu** was observed to be the most predominant species throughout the whole titration reaching a maximum formation of 82% upon the addition of 0.4 equivalents of $Eu^{III}$. The formation of the **$71_2$.Eu** species was also observed to be formed in the presence of higher quantities of

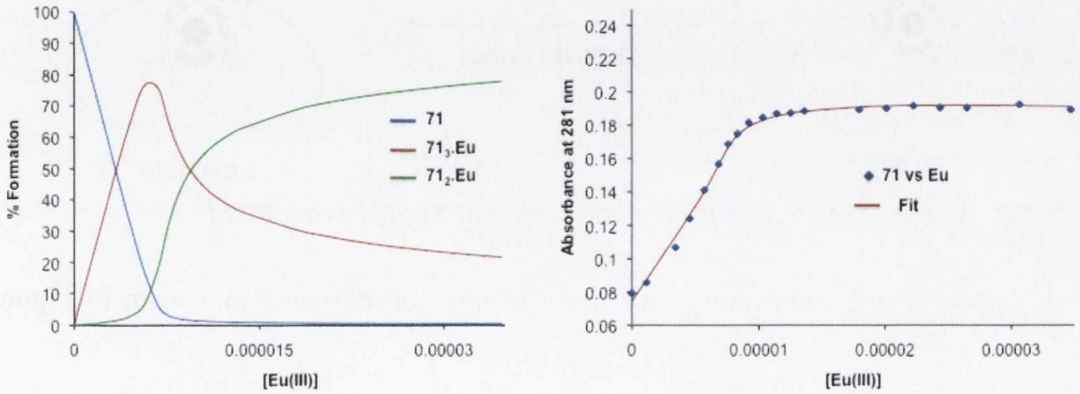


**Figure 5.33:** *Distribution speciation plot (left) calculated from the fit (right) resulting of the UV-vis titration of* ***71.***

$Eu^{III}$ (within the addition of 0.4→6 equivalents of $Eu^{III}$). However, the formation of such a species remained minor and was almost negligible at 1:3 metal to ligand ratio in solution. The binding constants relative to the formation of each species were calculated from those fits and are summarised in Table 5.3. The complexes **$71_3$.Eu** were formed with high binding constants of $log\ \beta_{13}$ = 18.7, a log unit greater in magnitude from its analogue **$66_3$.Eu.**

**Table 5.3.** *Summary of the results obtained from the fitting of the titration data of $L_3Ln$.*

| $71_3$.Ln | $log\ \beta_{13}$ | $log\ \beta_{12}$ | % formation at 1:3 M/L | |
|---|---|---|---|---|
| Ln = Eu | 18.7 ± 0.8 | 12.6 ± 0.6 | 76.5 | 6.5 |

Consequently, the results illustrated within the last section have shown the stable and quasi-selective formation of the complex **$71_3$.Eu**. Furthermore, the $^1$H-NMR analyses combined with the spectrophotometric studies of these complexes have shown that the molecular architectures adopted a $C_3$ symmetry in solution. The next step of our strategy was the formation of a [3]-catenane using a triple ring closing metathesis.

### 5.3.6 Catenation of $71_3$.Eu using a triple clipping using ring closing metathesis.

The ligand **71**, which was designed to form a 29 member-ring using RCM, benefits from high flexibility in order to allow a total kinetic control of the ring closing. However, the length and the flexibility of **71** could favour, in absence of templation, the oligomerisation-backbiting process, which consists in intramolecular metathesis reactions leading to the formation of various length of repeatable unit **71**. In order, to overcome this

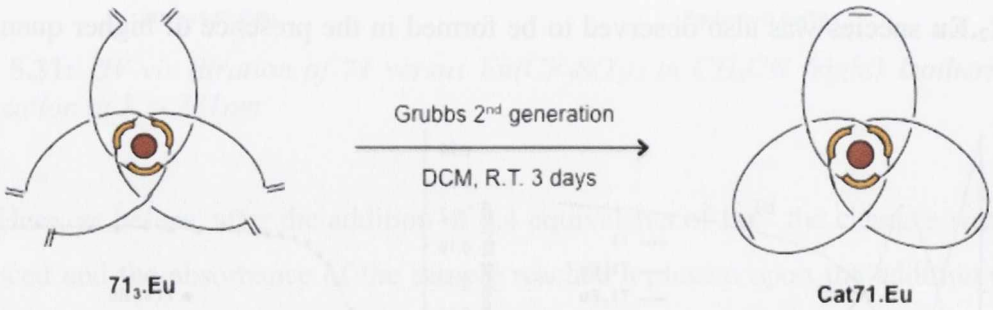


**Figure 5.34:** *Synthetic procedure for the catenation of **$71_3$.Eu** using RCM*

undesirable process, the catenation was carried at low concentration as shown in Figure 5.34.

The complex **$71_3$.Eu**, which was dried under high vacuum over $P_2O_5$ for several days, was dissolved in distilled DCM at low concentration ($10^{-4}$ M range). The second-

generation Grubbs catalyst (benzylidene [1,3- bis(2,4,6-trimethylphenyl)-2-imidazolidinylidene] dichloro(tricyclohexylphosphine)ruthenium) was then added slowly drop wise under an inert atmosphere, and the resulting mixture was stirred at room temperature for three days under flow of argon. The solvent was removed under reduce pressure and the resulting oil was dissolved in water. The Grubbs catalyst was then removed *via* simple washing with different organic solvents such as chloroform and the resulting adducts were obtained as a crude yellow oil after evaporation of the aqueous layer. Further purifications were attempted using column chromtagraphy and size exclusion separations but remained unsuccessful. However, after these attempts, the trituration of the yellow oil in DCM allowed the separation of two different compounds. The first one, **Cat71**, was soluble in DCM and showed no luminescence emission upon the excitation of the pyridinyl unit at $\lambda$ = 275 nm. The second compound, **Cat71.Eu** was isolated as a brown oil after precipitation out from a DCM/diethyether mixture, showing the typical luminescence of $Eu^{III}$ emission.

The $^1$H-NMR spectrum ($CD_3OD$, 400 MHz) of **Cat71**, is shown in Figure 5.35 and displayed the predominant formation of a highly symmetric compound. It was clear from the spectrum of **Cat71** that the RCM has occurred successfully giving rise to a macrocylic species as the resonances typical of a terminal double-bond were not observed. Furthermore, the broadening effect indicative of the $Eu^{III}$ complexes was not seen, suggesting that decomplexation occurred during the catenation process.

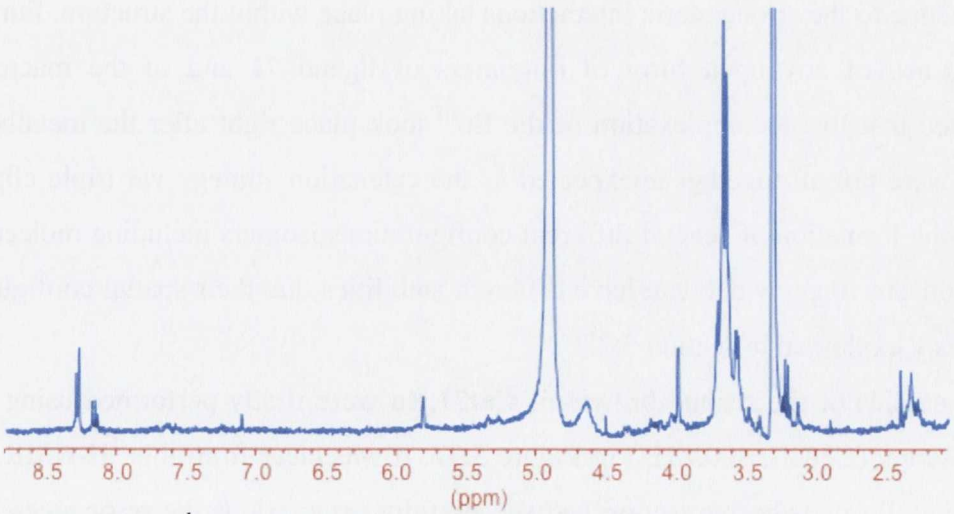


**Figure 5.35**: *$^1$H-NMR spectrum (MeOH, 400 MHz) of* ***Cat.71***

The mass spectrometry analyses were also performed on **Cat71** using MALDI-ToF mass-spectrometry, and are shown in Figure 5.36. These HRMS spectrum showed the presence of a single organic species, which was observed as two fragments at m/z = 1466.7150 and m/z = 1482.6909, calculated for $[3\times M_{72} + Na]^+$ = 1466.7170 and $[3\times M_{72} +$

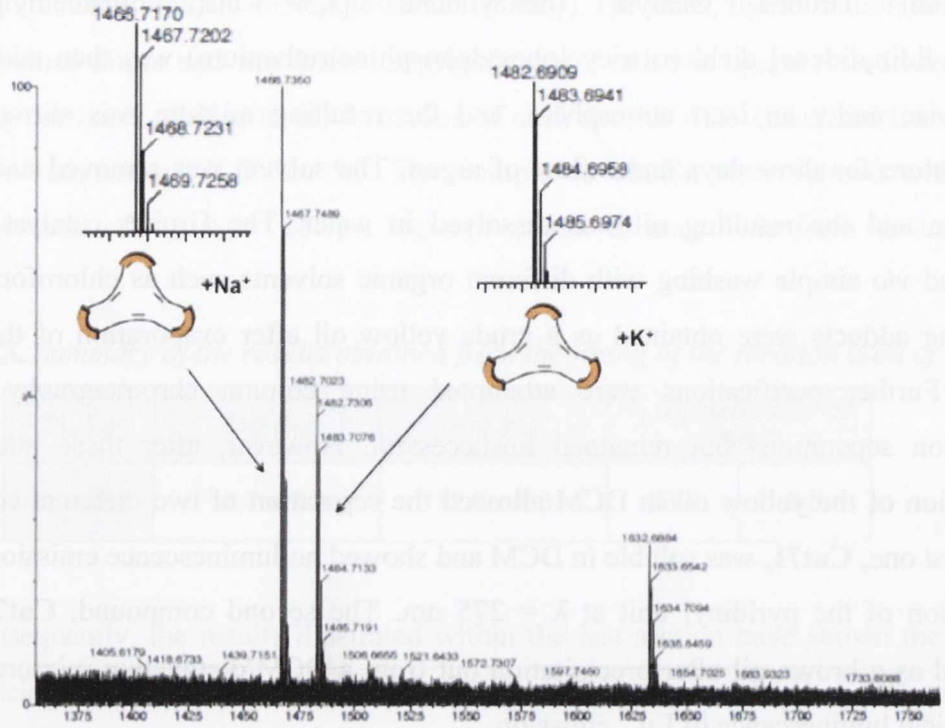


**Figure 5.36:** *MALDI-ToF mass spectrum of* ***Cat71****, showing the presence of a cyclic trimer. Inset calculated isotopical distribution patterns of each fragment*

$K]^+$ = 1482.6854, respectively, where $M_{72}$ corresponds to the mass of the macrocycle **72** resulting on the ring closing metathesis of **71**. These corresponded to a demetallated cyclic trimer resulting from the metathesis of **$71_3$.Eu**. This could be due to the inter-ligand metathesis resulting in the formation of a molecular knot, followed by the decomplexation of $Eu^{III}$, due to the strong steric interactions taking place within the structure. Furthermore, the absence of any open form of oligomers of ligand **71** and of the macrocycle **72** suggested that the decomplexation of the $Eu^{III}$ took place right after the metathesis. This results were not all together unexpected as the catenation strategy *via* triple clipping can lead to the formation of several different configurations isomers including molecular knots or borromean rings, which can have different stabilities due their spatial configuration, as previously explained in section 5.2.4.

The studies of the second brown oil **Cat71.Eu** were firstly performed using $^1$H-NMR spectroscopy ($CDCl_3$, 400MHz) in Figure 5.37. It was clear from this $^1$H-NMR spectrum that the olefin metathesis reaction had successfully occurred, as the resonances indicative of the terminal allylic moieties, which were initially clearly observed in the spectrum of **$71_3$.Eu** at 5.3 ppm and 5.9 ppm, had disappeared and were found to coalesce as a well defined singlet at 5.88 ppm. Even if the presence of several adducts could be detected, the $^1$H-NMR spectrum suggested the presence of a predominant species, which possessed a

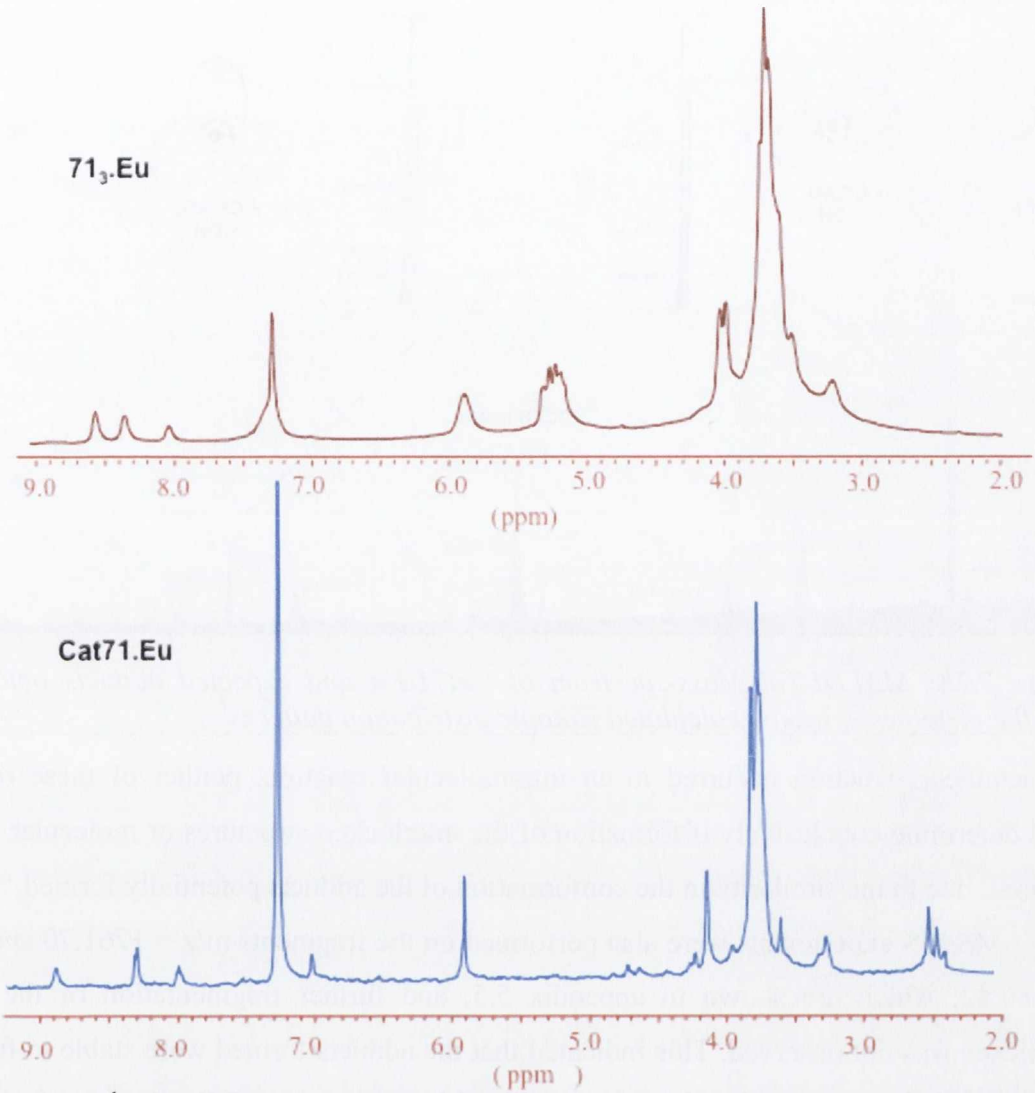


**Figure 5.37:** *$^{1}$H-NMR spectra ($CDCl_3$, 400 MHz) of the open complexe **71$_3$.Eu** and the supposed catenane **Cat71.Eu***

high degree of symmetry. This was confirmed by the simplicity of the $^{1}$H-NMR spectrum, which suggested the efficient minimisation of the potential intermolecular processes.

Further investigation of **Cat71.Eu** was also performed using MALDI-ToF mass-spectrometry in similar manner as for **Cat71**. The results of which are depicted in Figure 5.38, showed the presence of two different $Eu^{III}$ complexes. The first of these was detected at m/z = 1280.42 (calculated for $M_{72}$×2+Eu+$Tf^-$+$OH^-$ = 1281.36; with $M_{72}$ corresponding to the mass of the macrocycle **72**), which corresponded to a complex resulting from the catenation of the species **71$_2$.Eu**. The second complex, which was detected at m/z = 1761.70 (calculated for $M_{72}$×3+Eu+$Tf^-$+$OH^-$ = 1762.60), suggested the presence of architectures, such as the [3]-catenate resulting from a triple RCM.

Both of the species exhibited the typical isotopic distribution pattern of europium complexes. However, even if the mass spectrometry and the NMR analyses confirmed that

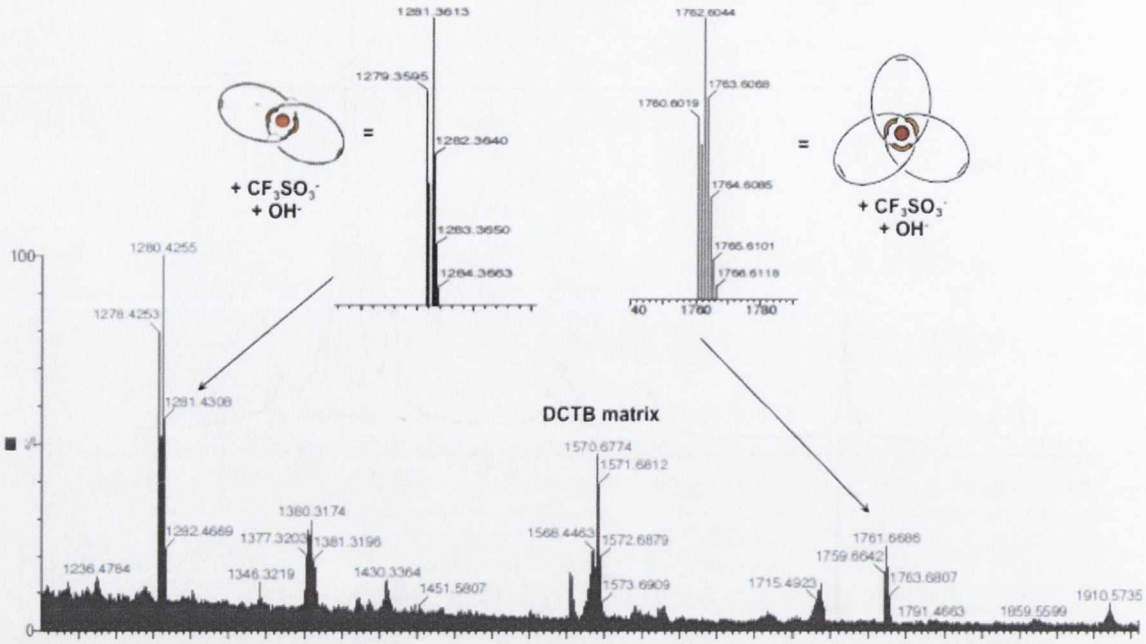


**Figure 5.38:** *MALDI-Tof Mass-spectrum of* ***Cat71.Eu*** *and expected adducts obtained after the metathesis. Insets: calculated isotopic distribution patterns*

the metathesis reaction occurred in an intramolecular reaction, neither of these results could determine conclusively if formation of the interlocked structures or molecular knots occurred, due to the similarity in the conformation of the adducts potentially formed.

MS.MS experiments were also performed on the fragments m/z = 1761.70 and m/z = 1280.42, which are shown in appendix 5.5, and further fragmentation of the $Eu^{III}$ complexes was not observed. This indicated that the adducts formed were stable to further fragmentation, suggesting that the catenation could have occurred following an intraligand process.

The stability of **Cat71.Eu** was further studied by carrying out titrations using **DTPA**, by monitoring the various spectrophotometric properties of **Cat71.Eu** and the open complex **$71_3$.Eu**. The **DTPA** titrations were performed in $CH_3OH$ solutions using **$71_3$.Eu** and **Cat71.Eu** at $1\times10^{-5}$ M. The changes observed in the UV-vis absorption spectrum for each of the compounds are shown in Figure 5.39. The UV-vis absorption band of **Cat7.Eu**, centred at 281 nm, experienced a strong decrease upon the addition of 0→4 equivalents of **DTPA**, which was indicative of decomplexation of $Eu^{III}$. The changes of the absorption at 275 nm suggested that total demetallation of the structure occurred after the addition of 4 equivalents of **DTPA**.

However, in the case of **$71_3$.Eu**, the changes in the UV-vis absorption were more pronounced showing that the decomplexation was complete upon the addition of 2 equivalents of **DTPA**, confirming the higher stability of the complex **Cat7.Eu** against **DTPA**. The corrsponding changes observed in the luminescence emission, which are

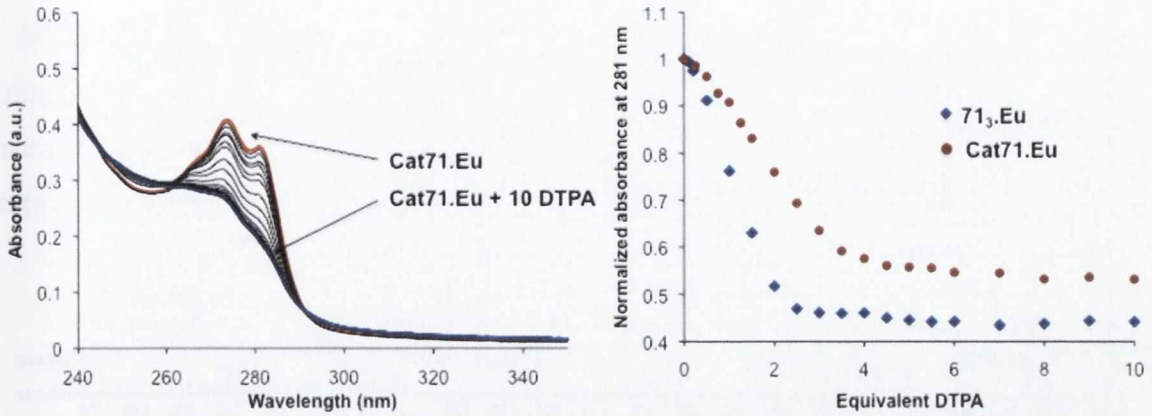


**Figure 5.39:** *Changes in the UV-vis absorption spectra of* ***Cat71.Eu*** *and* ***$71_3$.Eu*** *during the titration of* ***DTPA****.*

shown in Figure 5.40, were in agreement with that observed in the UV-vis absorption. In the case of **Cat7.Eu,** a small quenching was initially observed upon the addition of 1.5 equivalents of **DTPA**. This was followed by a more pronounced decrease upon the addition of 1.5→4 equivalents of **DTPA**. The emission of **Cat71.Eu** was totally quenched upon the addition of 10 equivalents of **DTPA**. In the case of **$71_3$.Eu** a stronger quenching was found to be taking place for quantities of **DTPA** ranging from 0→2 equivalents after which, the luminescence emission of the open complex was almost totally quenched indicating a lower stability for **Cat71.Eu** with respect to **DTPA**.

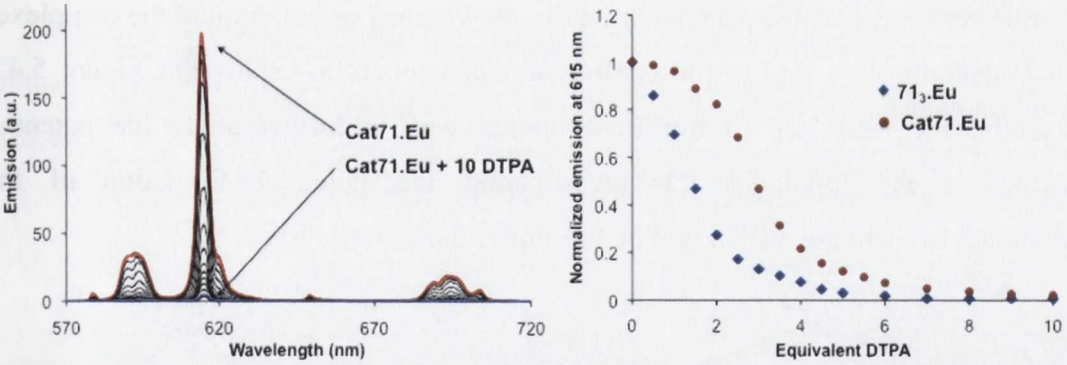


**Figure 5.40***: a) Changes occurring in the emission spectrum of* ***Cat71.Eu*** *during the DTPA titrations. b) Isotherm of decomplexation at 615 nm*

The stability of **$71_3$.Eu** and the resulting adducts **Cat71.Eu** with respect to **DTPA** were analysed by mass spectrometry. Both of the compounds **Cat71.Eu** and **$71_3$.Eu** were stirred for 1 hour in the presence of 1 equivalent of **DTPA** and the resulting samples were analysed using MALDI-ToF mass spectrometry. No major changes were observed in the mass spectrometry analyses of **Cat71.Eu** in the presence of **DTPA**, which was indicative of the high stability of the topologies obtained upon catenation. However, the analyses performed on the open complex **$71_3$.Eu,** which are shown in Figure 5.41, displayed the presence of both of the free ligand **71**, detected as two different fragments found at m/z =

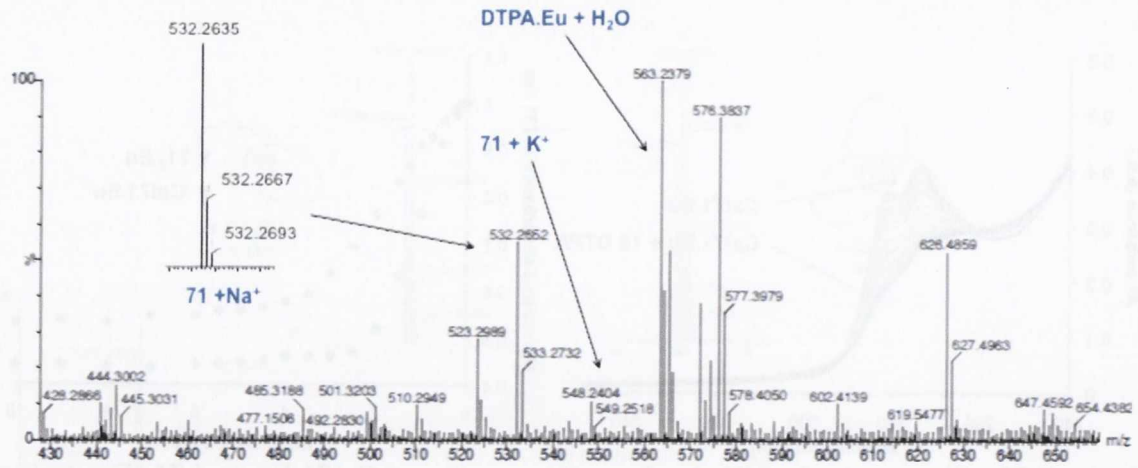


**Figure 5.41:** *MALDI-ToF Mass spectrometry analysis of* ***71$_3$.Eu*** *+ 1 equivalent of DTPA.*

532.36 and m/z = 548.24 for $M_{72}+Na^+$ and $M_{72}+K^+$ respectively, and the complex **DTPA.Eu** at m/z = 563.79. This indicated that the catenation process resulted in an increase in the complex stability, suggesting an efficient wrapping of the metal ion shielding then its access to the **DTPA** and preventing the decomplexation of $Eu^{III}$, as expected in the case of the [2]- and [3]-catenane.

The above work has shown the formation of the cyclic trimer **Cat71** resulting from an inter-strand metathesis reaction. (as any trace of **71** and **72** were detected in the mass spectrometry analyses). It is important to remember that the intra-strand methatesis can occur in different ways, as the pendant arms can be wrapped or not, around the complexes and can potentially give rise to the conformational isomers **a-f** shown in Figure 5.42. Consequently, the next step of our investigation was to further study the potential interlocking of the topologies by investigating the potential formation of the conformational isomers **c-e**, which will be the aim of the next section.

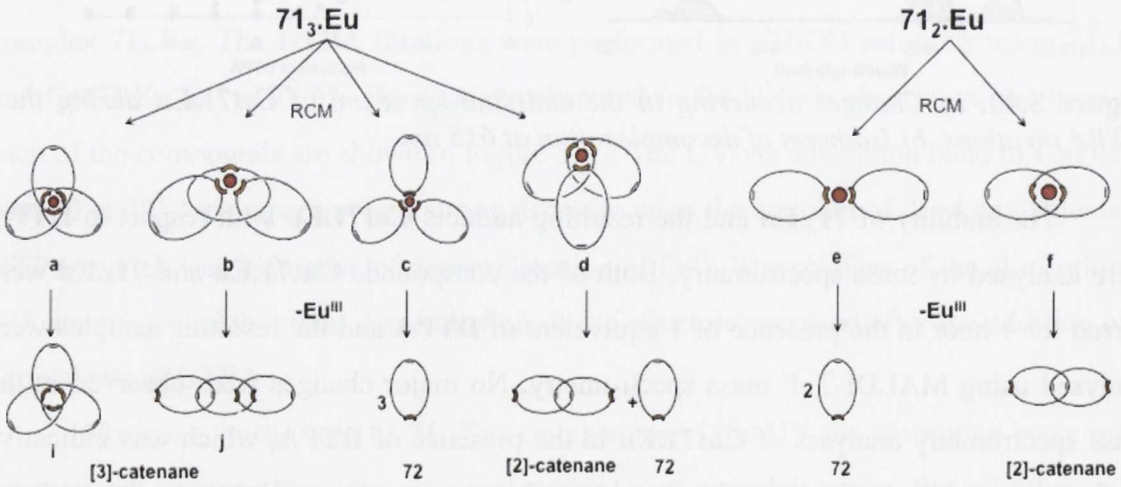


**Figure 5.42:** *Schematic representation of different isomers which could be obtained from the catenation of* ***71$_3$.Eu*** *and* ***71$_2$.Eu***

**5.4 Study of the ring closing metathesis on the free ligand 71.**

With the view of investigating the stability of the architectures resulting from an intra-strand RCM when the pendant arms were directed towards the outside of the structure, the macrocycle **72** was synthesised from **71** *via* RCM, in a similar manner as described in section 5.2 (Figure 5.41).

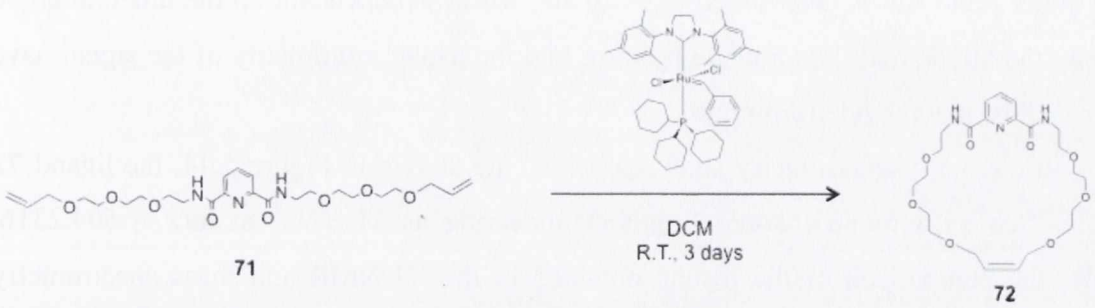


**Figure 5.43:** *Synthesis of the macrocycle 72 using RCM.*

The ligand **71**, (which was dried under vacuum for 2-3 days), was firstly dissolved in distilled dichloromethane at low concentration ($\approx 10^{-4}$ range). To this solution, the second-generation Grubbs catalyst was added slowly drop wise. The resulting mixture was stirred at room temperature for 3 days.

The macrocycle **72** was then obtained after carrying out serial acid-base washings and evaporation of the organic layer to give an orange oil in 80% yield.

The $^1$H-NMR analysis ($CDCl_3$; 400MHz) of **72**, Figure 5.44, showed the presence of a unique compound, which adopted a high degree of symmetry. Furthermore, the allylic protons of **72,** which in the case of **71** appeared as two different resonances as a multiplet

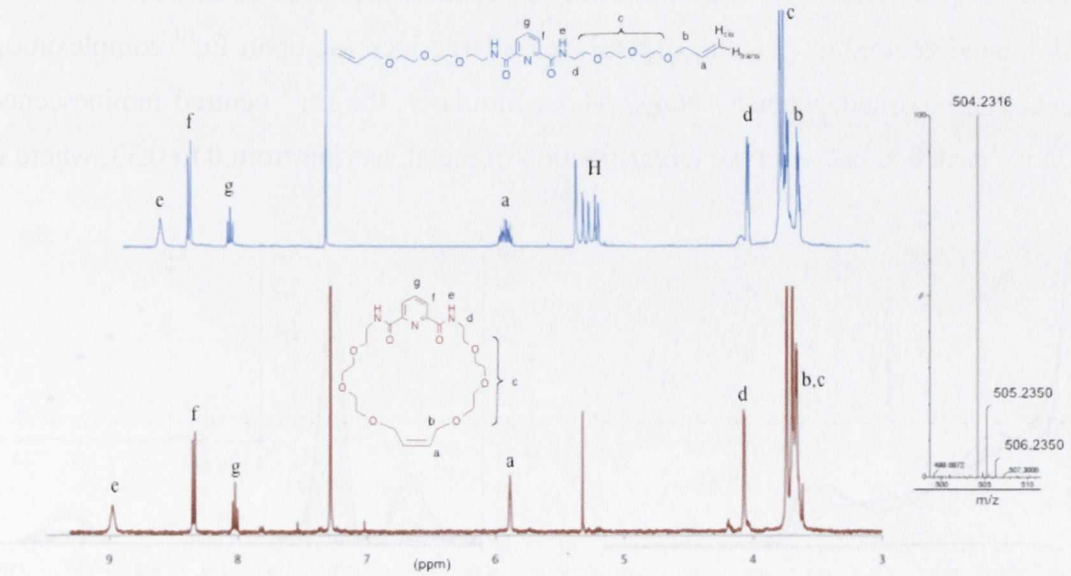


**Figure 5.44:** *$^1$H-NMR ($CDCl_3$, 400MHz) spectra of **71** (top) and **72** (bottom) and HRMS fragment found for [**72** + Na]$^+$.*

at 5.89 ppm and a doublet-doublet between 5.14 and 5.29 ppm was now observed as a unique triplet at 5.89 ppm with a weak vicinal coupling constant (*c.a.* $^3J$ = 3.0 Hz). Furthermore, the protons in the α-position of the double bond (**b**) experienced a significant shifting downfield due to the anisotropic changes in the environment of the double bond, caused by the change of the architecture geometry. The vicinal coupling constant between the protons **a** and **b** was determined $^3J$ = 3.0 Hz, which is dependant on the dihedral angle between the allylic and the aliphatic protons, and the triplet multiplicity of the signal have confirmed the macrocycle formation.

In the mass spectrometry analyses, which are shown in Figure 5.44, the ligand **72** was detected as a mono-charged fragment appearing as $M_{72}$+$Na^+$ at m/z = 504.2316. Finally, the comparison of the results obtained in the $^1$H NMR and mass spectrometry studies with those previously obtained for PEG analogues by the Grubbs group and further confirmed by the work of Monfette *et al.* suggest the stereoselective formation of the Z-isomer.[153,154] It was clear from these analyses that the macrocyle **72** was synthesised in high yields and possesses a central tridentate moiety, which can potentially form self-assemblies with lanthanide ions such as $Eu^{III}$.

### 5.4.1 Investigation of formation of the complexes $72_2$.Eu *in situ*

Initially, the preferred stoichiometry of the binding event was investigated using the job's plot experiments in $CH_3CN$ where the overall concentration of the sample was kept at $2\times10^{-5}$ M, while the molar fraction of metal was varied from 0 to 1 in a similar manner as assessed in the previous sections. The changes recorded in the UV-vis absorption and luminescence emission spectra of **72** are shown in Figure 5.43. The absorption band centred at 281 nm, experienced a large increase upon $Eu^{III}$ complexation and reached a maximum intensity at $\chi_{Eu}$ =0.33. Similarly, the $Eu^{III}$ centred luminescence emission is "switched on" with the molar fraction of metal varying from 0 to 0.33, where it

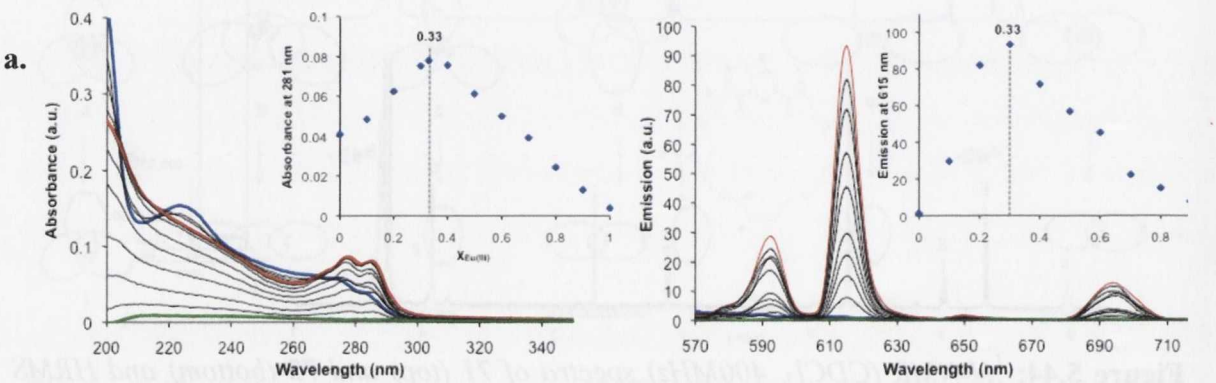


**Figure 5.45:** *Job's plot obtained in the UV-vis absorption (a) and in the lanthanide luminescence (b) for the complexation of $Eu^{III}$ by **72** in $CH_3CN$ at C = $2\times10^{-5}$M*

reached a maximum, indicating that the complex **$72_2$.Eu** was the predominant species formed in solution. Furthermore, in both cases the profile of the job's plot showed a linear decrease between $\chi_{Eu(III)}$ =0.33 to 1 suggesting the unique formation of the 1:2 species under molar thermodynamic control.

The complexation process was also investigated by performing the $Eu^{III}$ titration in $CH_3CN$ in a similar manner to that discussed for compound **71**, in section 4.2. The changes in the UV-vis absorption spectrum of **72**, which are shown in Figure 5.46, confirmed the results of the Job's plot experiments. The UV-vis absorption band at 281 nm experienced a

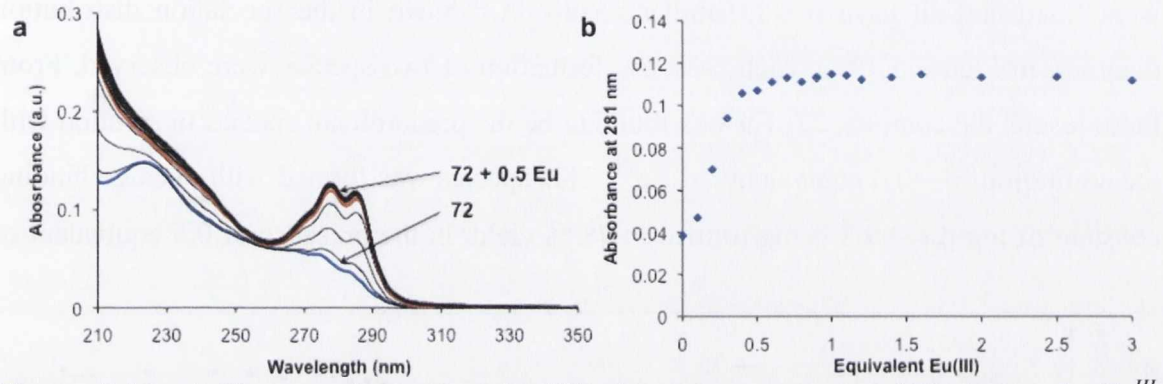


**Figure 5.46:** *a) Changes obtained in the UV-absorption spectrum of 72 during the $Eu^{III}$ titration of 72 in $CH_3CN$ at $2\times10^{-5}$ M b) Isotherm of complexation at 281 nm*

substantial hyperchromic effect upon the addition 0→0.5 equivalent of $Eu^{III}$, which was indicative of the formation of the 1:2 self-assembly. The changes observed in the $Eu^{III}$ time delayed emission ($\tau$ = 0.1 ms), which were obtained from the same solution are shown in Figure 5.47, and gave rise to a slightly different profile. The $Eu^{III}$ centred emission was switched on from the first addition of $Eu^{III}$ and the intensity at 615 nm reached a maximum upon the addition of 0.8 equivalents of $Eu^{III}$. This was followed by a significant quenching in the emission at 615 nm reaching a plateau after the addition of 2 equivalents of the lanthanide ion. The emission band centred at 585 nm ($^5D_0\rightarrow{}^7F_1$), reached a maximum at

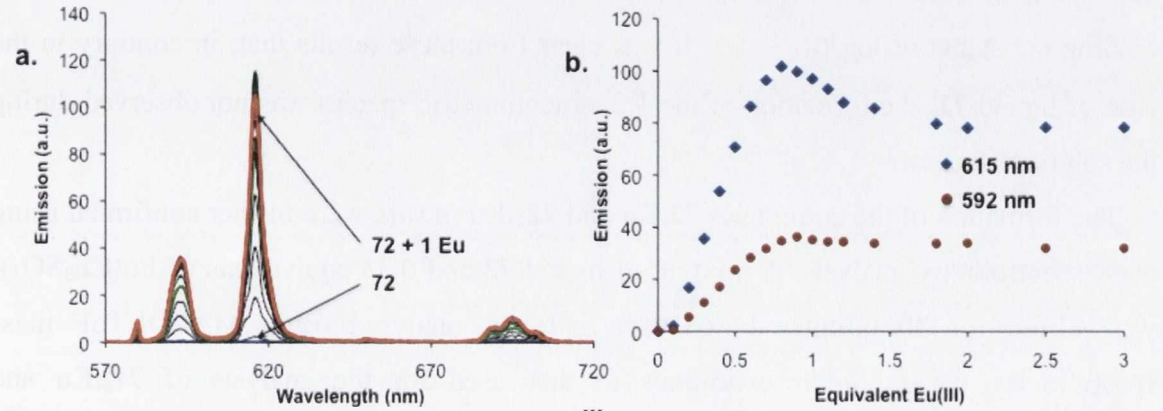


**Figure 5.47:** *(a) Changes observed in the $Eu^{III}$ emission upon the addition of $Eu(CF_3SO_3)_3$ (b) Isotherm of complexation at 615 nm.*

0.9 equivalent and experienced a less pronounced decrease, reaching a plateau after the addition of 1.5 equivalent of $Eu^{III}$. This suggests the initial formation of the 1:2 stoichiometric complex destabilised towards the formation of a second luminescent species, at higher $Eu^{III}$ concentrations. As the ratio, between the emission bands varied during the titration, this indicated a change in the coordination geometry of the luminescent species formed.

In order to understand the binding process the profiles obtained from the UV-vis absorption titration were further analysed using SPECFIT®. Several different titrations were fitted and all gave rise to similar results. As shown in the speciation distribution diagram, in Figure 5.48, in each case, the formation of two species were observed. From these results the complex **$72_2$.Eu** was found to be the predominant species in solution with the addition of 0→0.6 equivalents of $Eu^{III}$. This species was formed with average binding constant of log $\beta_{12}$ = 9.8 being formed in 78 % yield, in the presence of 0.6 equivalent of

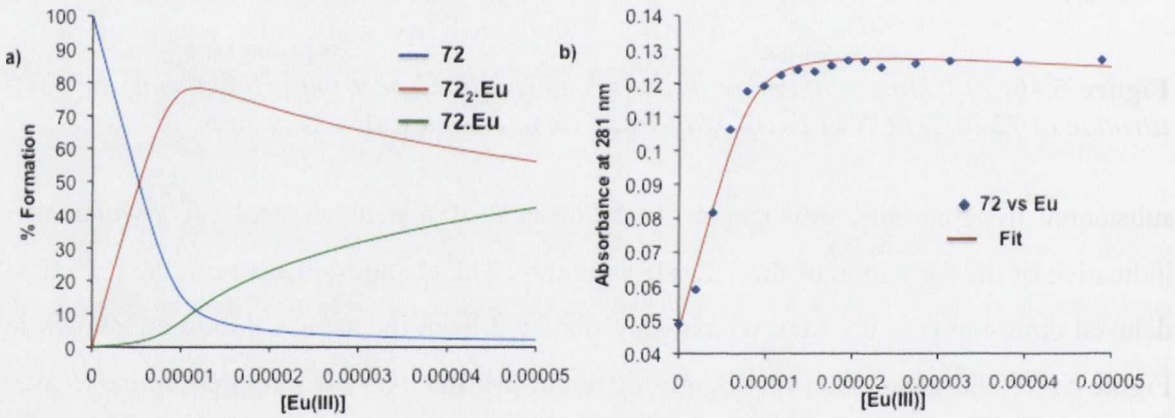


**Figure 5.48:** *a) Speciation distribution diagram of 72 derived from the fitting of the changes observed in the UV-vis absorption spectrum of 72 b) data fitting of the titration.*

$Eu^{III}$.

As predicted by the luminescence titrations the presence of the 1:1 complex was also detected and became predominant upon the addition of 10 equivalents of metal ion with binding constants of log $\beta_{11}$ = 5.7. It was clear from these results that, in contrary to the case of ligand **71,** the formation of the 1:3 stoichiometric species was not observed during the solution studies.

The formation of the complexes **72.Eu** and **$72_2$.Eu** *in situ*, were further confirmed using mass spectrometry analysis. A mixture of ligand **72** and 0.33 equivalents of $Eu(CF_3SO_3)_3$ was stirred for 30 minutes in $CH_3CN$ and was analysed using MALDI-ToF mass spectrometry using similar conditions to that used for the analysis of **$71_3$.Eu** and **Cat71.Eu**. Here, two $Eu^{III}$ complexes were observed, as shown Figure 5.49.

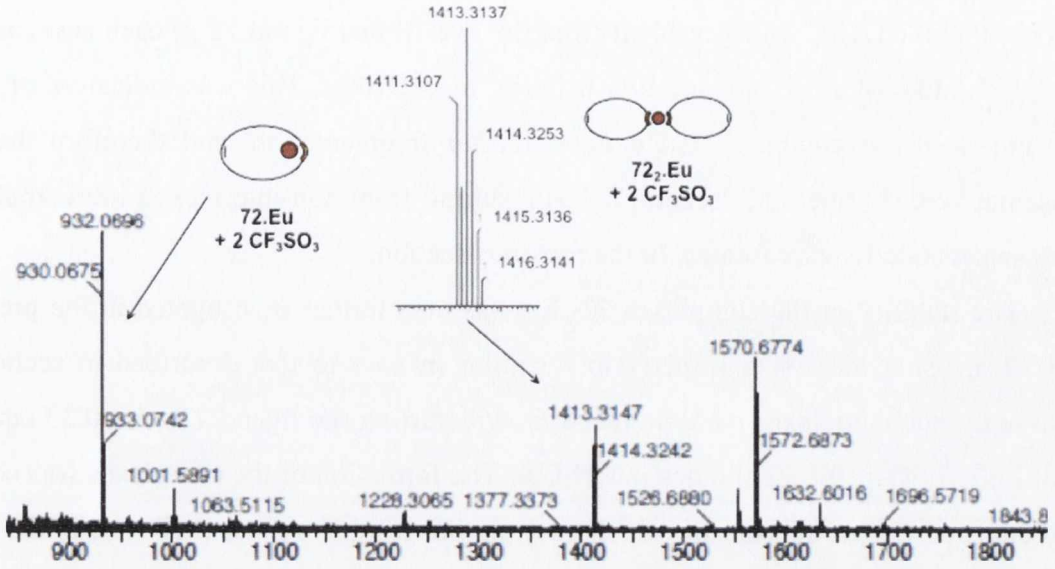


**Figure 5.49:** *MALDI-ToF Mass spectrometry analysis of 72 + 0.3 equivalent of $Eu(CF_3SO_3)_3$. Inset: Calculated Isotopic distribution pattern of* ***$72_2$.Eu***

The first species as two ions at m/z = 1413.30 and m/z = 932.03 corresponding to the **$72_2$.Eu** (found for $2M_{72}$ + Eu + 2 triflate) and **72.Eu** (found for $M_{72}$ + Eu + 2 triflate), respectively. On all occasions the observed isotopic distribution diagrams matched that of the calculated one.

The fragment at m/z = 1413.3147 assigned to **$72_2$.Eu** was further analysed using MS.MS experiments in a similar manner to that of the two fragments detected in the case of **Cat71.Eu** (section 5.3.4). In contrary to the result of **Cat71.Eu**, the spectrogram

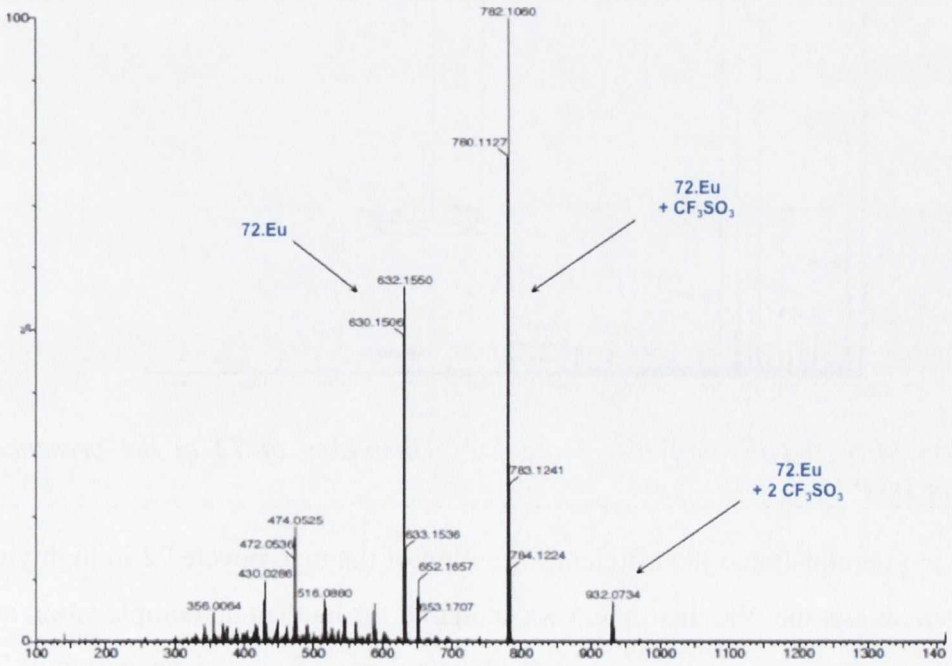


**Figure 5.50:** *MS.MS spectrum obtained for the fragmentation of the fragment at m/z = 1413.3147 attributed to* ***$72_2$.Eu***

obtained, shown in Figure 5.50, showed the presence of three species at m/z = 932.07, 782.10 and 632.15, which resulted from the loss of one ligand **72** in each case, associated with the loss of zero, one and two triflates, respectively. This was indicative of the poor stability of the complex **$72_2$.Eu** upon further fragmentation, and therefore that of the isomers **c-e** (Figure 5.42, section 5.2.5) resulting from non-interlocked intra-strand RCM, as schematically respresented, in the previous section.

The stability of the complexes **$72_2$.Eu** was also further investigated in the presence of **DTPA**, using mass spectrometry in a similar manner to that described in section 4.3.2. Initially, the complexes were prepared *in situ*, stirring the ligand **72** with 0.33 equivalents of $Eu(CF_3SO_3)_3$ for 30 minutes in $CH_3CN$. The formation of the complexes was confirmed by the analysis of the control, which gave similar results to those described in the previous paragraph. To each solution 1 equivalent of **DTPA** was added and the resulting mixture was reacted for another 30 minutes. It was clear from the spectrogram shown in Figure 5.51, that all of the complexes present in solution were demetallated upon the addition of **DTPA** as only the presence of the free ligand **72** was detected at m/z =504.22.This confirmed the poor stability of the complexes **$72_2$.Eu** and **72.Eu** with respect to **DTPA** as previously observed in the case of the of the open complex **$71_3$.Eu** and **$71_2$.Eu**.

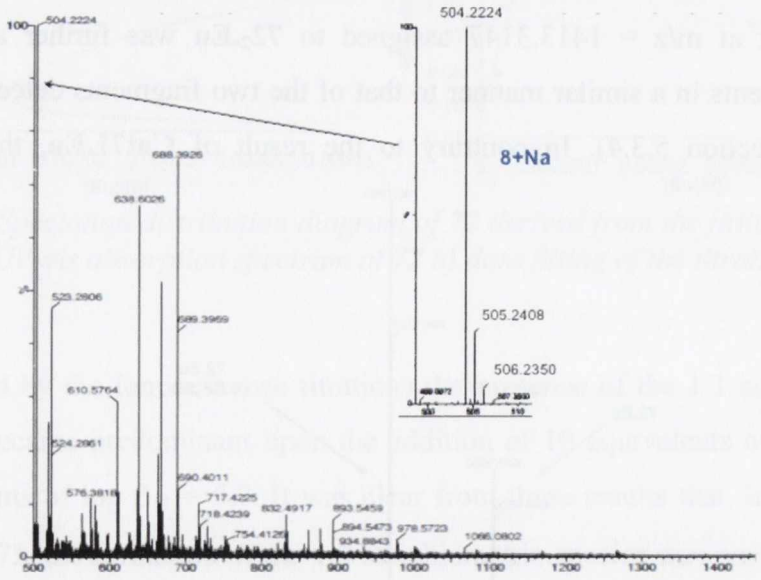


**Figure 5.51:** *MALDI-ToF analyses of the $Eu^{III}$ complexes of 72 in the presence of 1 equivalent of* ***DTPA***

Having demonstrated the efficient formation of the macrocycle **72** in high yields, it has also been shown that the this ligand was suitable for lanthanide complexation and the complexes formed were not as stable as the adducts formed from the catenation of **$71_3$.Eu** suggesting that the triple RCM process occurred following an intra-strand pathway and

gave rise to interlocked structures such as the [3]-catenanes **a**, **b** and the [2]-catenane **f** Furthermore, the macrocycle **72** offers another approach for the formation of the catenanes consisting in the $Ln^{III}$-templated double threading of **71** inside the macrocycle **72** prior to the catenation. Therefore, the next step in our research was the study of this potential threading and the investigation of the formation of the pseuso-rotaxanes needed.

### 5.4.2 Formation of the pseudo rotaxane 72.Eu.71$_2$ *in situ.*

With the view of investigating the possible interlocking of the adducts from the catenation and to develop an alternative route for the formation of a fully interlocked [3]-catenane, we have envisaged a second approach consisting in the double threading of linear ligands prior to the catenation *via* double clipping, reducing then the number of potential isomers induced by the macrocyclisation.

For that purpose the complexes **72.Eu** were formed *in situ,* stirring **72** in $CH_3CN$ in the presence of 1 equivalent of $Eu(CF_3SO_3)_3$ over 30 minutes. The potential threading of **71** within the macrocycle was firstly investigated by performing the UV-vis absorption and $Eu^{III}$ time delay luminescence emission spectrophotometric titrations in $CH_3CN$ at $C_{8.Eu}$ = $2\times10^{-5}$ M and varying the equivalents of **71** in solution from 1 to 5. The changes observed in the UV-vis absorption spectrum of **72.Eu** are shown in Figure 5.52 and displayed a strong hyperchromic effect in the $\pi$-$\pi^*$ transitions (centred at 275 nm) upon the addition of

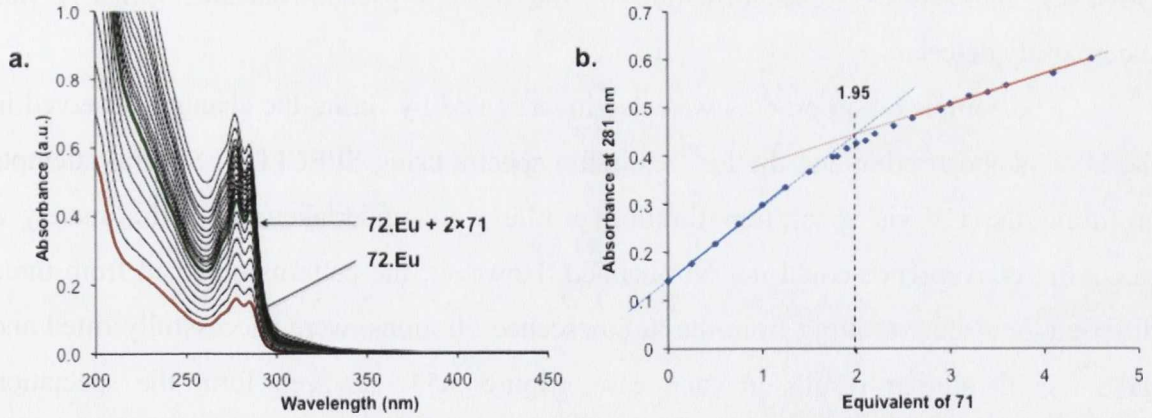


**Figure 5.52:** *Changes on the UV-vis absorption spectrum of* ***72.Eu*** *(formed in situ) upon the addition of ligand* ***71****. b) isotherm of complexation at 281 nm.*

1→2 equivalents of **71**. Further addition of **71** (form 2 to 5 equivalents of **71**) resulted in a less pronounced linear increase in the absorption spectrum due to the absorbance of ligand **71** itself. This has suggested that the system was equilibrated in the presence of ~ 2 equivalents equivalents of **71** which would suggest the formation of a complex with the stoichiometry **72.Eu.71$_2$**. Such systems fulfill the coordination requirement of the $Eu^{III}$ ion by the self-assembly of two tridentate **71** ligands and the macrocyle **72**.

This formation was further confirmed by analysing the changes observed in the $Eu^{III}$ centred emission spectrum, Figure 5.53. Contrary to the results obtained in the UV-vis absorption titrations, the formation of the 1:1 stoichiometric species was first detected by a weak increase in the luminescence emission upon the addition of 1 equivalent of **71**. However, further addition of **71** gave rise to more pronounced changes taking place upon

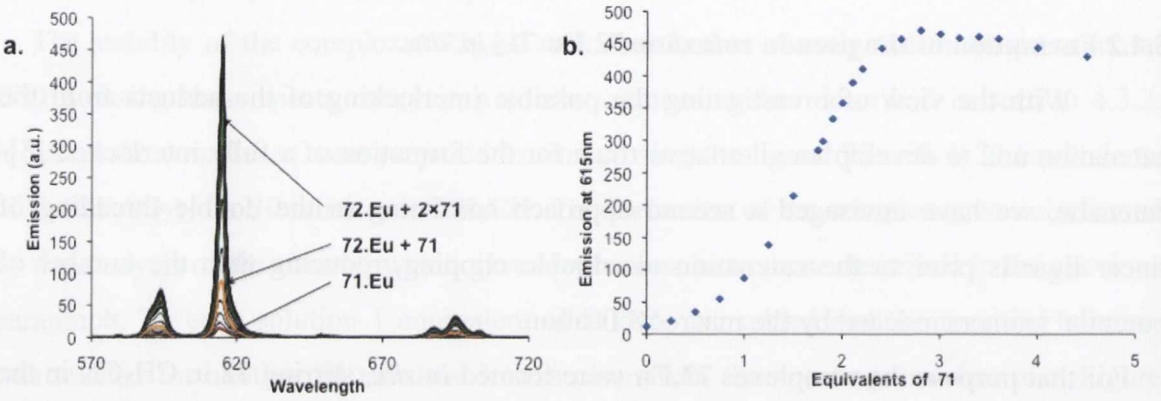


**Figure 5.53:** *Changes observed in the $Eu^{III}$ emission of* ***72.Eu*** *upon the addition of ligand* ***71****. b) isotherm of complexation at 615nm*

the addition of 1 to 2.3 equivalents of open ligand, which indicated the aforementioned formation of the complex **72.Eu.71$_2$**. Finally, the luminescence of the system experienced a small quenching upon the addition of an excess of **71** suggesting the decomplexation of the complex **72.Eu** due to the formation of the previously studied complex **71$_3$.Eu**. However, in each case the formation of the desired pseudo-rotaxane **72.Eu.7$_2$** was successfully detected.

The complexation process was also investigated by fitting the changes observed in the UV-vis abosorption and the $Eu^{III}$ emission spectra using SPECFIT®. Several attempts at fitting the UV-vis absorption titration profile were undertaken but unfortunately a satisfying convergence could not be obtained. However, the patterns obtained from three different data sets, resulting from the luminescence titrations, were successfully fitted and gave rise to similar results in each case, Figure 5.54. As seen form the speciation distribution diagram (Figure 5.54a), the formation of the **72.Eu.71** was achieved with a high binding constant of log $\beta_{11}$ = 6.7, and this species was found to be predominant upon the addition of 1 equivalent of **71,** being formed in 50%. These results have also illustrated the predominant formation of the desired pseudo-[3]-rotaxane **72.Eu.71$_2$**, with a binding constant of log $\beta_{12}$ = 13.2. This species was formed throughout the titration and reached a maximum formation of 80% in the presence of 2 equivalents of **71**. Finally, the formation of the complex **71$_3$.Eu** was also detected with binding constant in the similar range as previously mentioned.

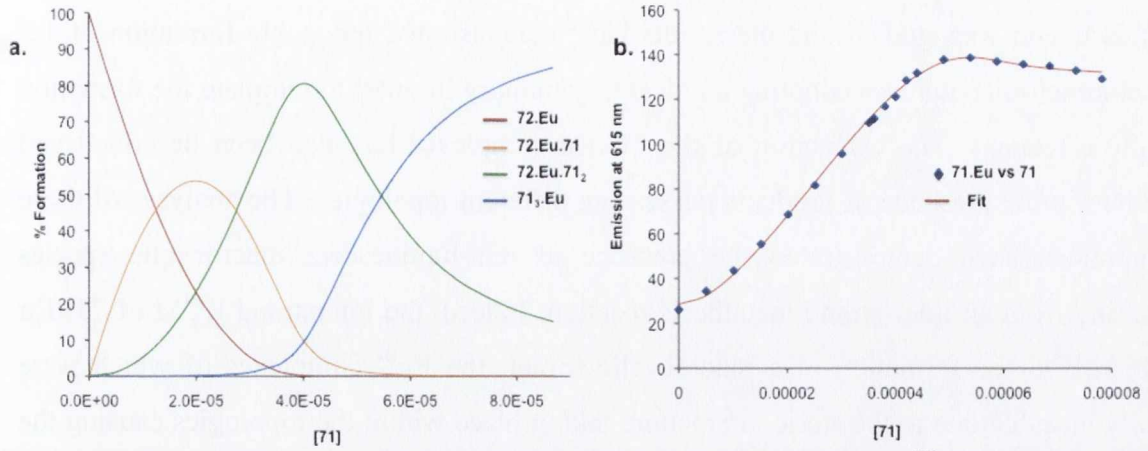


**Figure 5.54:** a*) Speciation distribution diagram obtained from the Eu$^{III}$ emission titrations of* ***72.Eu*** *with* ***71*** *b) fits resulting from these calculations.*

In summary, the results above demonstrated the possible formation of a [3]-pseudorotaxane following a Eu$^{III}$ directed threading pathway, with the formation of the complex **72.Eu.71$_2$** in good yield with high binding constants. The configuration of the adducts formed in solution could not be determined and further analysis, such as X-Ray diffraction is needed in order highlight the geometry of these species.

## 5.5 Conclusion

In this chapter, the lanthanide templated synthesis of [3]-catenanes *via* triple clipping has been studied following two different approaches varying the catenation mode. First, the synthesis, in one step of **66**, was designed in order to induce the ring closing, using the Williamson ether synthesis, was described and the complexation of **66** with lanthanide ions such as Tb$^{III}$ and Eu$^{III}$ was studied. The results of the photophysical studies and the $^1$H-NMR analyses suggested that the **66$_3$.Ln** complexes were found to adopt a $C_3$ geometry in solution, which is necessary for the preorganisation of three ligands prior to the catenation. The templation process has been also investigated in situ and demonstrated the stable formation of the complexes **66$_3$.Ln** in solution with high binding constants. The catenation has also been performed using the Williamson ether synthesis, however the characterisation of the resulting adducts remained unsuccessful. In addition, the demetallation of the adducts from the catenation was also studied using **DTPA** and this resulted in a quenching of the luminescence intensity after the addition of 10 equivalents of **DTPA**. However, the decomplexation of **66$_3$.Ln** gave rise to a similar pattern demonstrating that the catenation was unsuccessful.

A second approach based on the same design was also developed within this chapter. The ligand **71** was designed and synthesised with terminal allylic moieties in order to

induce a catenation of our systems *via* ring closing metathesis. The complexation of $Eu^{III}$ to this ligand was studied and the results have demonstrated the stable formation of 1:3 stoichiometric complexes adopting an ideal $C_3$ geometry in order to template the formation of the catenanes. The catenation of the **$71_3$.Eu** complexes has also been described and resulted in the presence of products possessing different topologies. The analyses of these compounds have demonstrated the presence of non-luminescent macrocyclic species resulting from an inter-strand metathesis reaction. Indeed, the interstrand RCM of **$71_3$.Eu** gave rise to the formation of a macrocyclic trimer, the $Eu^{III}$ complexes of which were highly unstable due to the steric interaction, taking place within the topologies causing the decomplexation of the architectures upon catenation. This suggested that the luminescent adducts, which were detected after tituration of the crude compound with dichloromethane resulted from an intra-strand ring closing process and corresponded to the catenation products of the complexes **$71_2$.Eu** and **$71_3$.Eu.** Unfortunately, we were unable to isolate these compounds using conventional methods. Further analysis of the stability of these adducts were performed using MS.MS and **DTPA** titrations were also carried out. These results illustrated that the luminescent species **[2]-Cat71.Eu** and **[3]-Cat71.Eu** showed a significant stability against further fragmentation and against **DTPA**. Comparing these results with that of the demetallation of the open complex **$71_3$.Eu** showed that the compound **Cat71.Eu** had a higher stability against **DTPA** than its open form analogues. This indicated that the metal centre was shielded preventing access to the DTPA, suggesting the potential interlocking nature of the resulting architectures. However, these studies could not confirm the formation of the [2]- or [3]-catenanes (see Figure 5.42) and further purification and analyses such as X-ray diffraction are needed.

The ring closing metathesis performed on the free ligand **71** resulted in the formation of compound **72** in high yields (>80%). The $Eu^{III}$ complexation studies on **72** showed only the formation of the complexes **$72_2$.Eu** and **72.Eu**, indicating that the fragment **[3]-Cat7.Eu** could not result from a non-interlocked intra-strand RCM giving rise to the configurational isomer **c** (Figure 5.42). The stability of the complexes **$72_2$.Eu** was further investigated using MS.MS and this resulted in the presence of fragments all resulting in the loss of one ligand **72**. This effect, which was not observed in the case of the fragments present in **Cat71.Eu,** suggested the successful formation of the [3]-catenanes **a** or **b** (Figure 5.42) and the [2]-catenane **f**. This formation has also been confirmed using mass spectrometry assisted **DTPA** studies, which showed only the presence of **72**, when 1 equivalent of **DTPA** was added whereas the decomplexation of **[3]-Cat71.Eu** and **[2]-Cat71.Eu** was not observed in the same conditions. However, the formation of the conformational isomers **a**

and **b** could not be differentiated and further analysis such as X-ray diffraction are needed in order differentiate between them.

Finally, another approach for the formation of interlocked structures was investigated where the lanthanide directed threading of two ligands into the macrocycle prior to the catenation *via* double clipping was studied. The formation of the pseudo-rotaxane has been studied and suggested the predominant formation of the [3]-pseudo-rotaxane **72.Eu.71** and **72.Eu.71$_2$** with high binding constants. However, the configuration of these could not be accurately determined and thus, the need for further studies, which are currently in process.

# Chapter 6:

# Experimental

## 6.0 Experimental section

### 6.1 General Experimental Details

All chemicals were obtained from Sigma-Aldrich, Fluka, Strem, or Chematech and unless otherwise specified were used without further purification. Deuterated solvents for NMR analysis were purchased from Apollo Scientific. Dry solvents were prepared using standard procedures, according to Vogel,[155] with distillation prior to each use. Chromatographic columns were run manually using silica gel 60 (230-40 mesh ASTM) or aluminium oxide (activated, neutral, Brockman I STD grade, 150 mesh, or activated, basic, Brockman I STD grade, 150 mesh). Chromatographic columns were also run on a Teldyne Isco Combiflash Companion Automatic machine using prepacked silica or alumina columns. Solvents for synthetic purposes were used at GPR grade unless otherwise stated. Analytical TLC was performed using Merck Kieselgel 60 $F_{254}$ silica plates or Polygram Alox N/$UV_{254}$ Aluminium oxide plates. Visualisation was by UV light (254 nm), exposure to $I_2$ on silica or by immersion in aqueous alkaline $KMnO_4$ solution. NMR spectra were recorded at 400 MHz using a Bruker Spectrospin DPX-400 instrument that operates at 400.13 MHz for $^1H$ NMR and 100.3 MHz for $^{13}C$ NMR. NMR spectra were also recored at 600 MHz, using a Bruker advance II that operates at 600.13 MHz, for $^1H$ NMR and 150.9 MHz for $^{13}C$ NMR. Shifts were referenced relevant to the internal solvent signals, with chemical shifts expressed in parts per million (ppm) downfield from the standard. Multiplicities are abbreviated as follows: singlet (s), doublet (d), triplet (t), quintet (q), multiplet (m) and broad (br). All NMR titrations were performed as 293 K. Mass Spectra were determined by detection using electrospray ionisation on a Mass Lynx NT V 3.4 on a Waters 600 Controller connected to a 996 photodiode array detector with HPLC-grade methanol, water or acetonitrile as carrier solvents. Accurate molecular weights were determined by a peak-matching method, using leucine enkephaline (H-Try-Gly-Gly-Phe-Leu-OH) as the standard internal reference (m/z = 556.2771). Samples were prepared as solutions in methanol or acetonitrile. Infrared spectra were recorded on a Perkin Elmer Spectrum One FT-IR spectrometer fitted with a universal ATR sampling accessory. Elemental analysis was carried out at the microanalysis laboratory, School of Chemistry and Chemical Biology, University College Dublin.

The lanthanide metal salts $Eu(CF_3SO_3)_3$ and $La(CF_3SO_3)_3$ were purchased from Aldrich and were dried under high vacuum over $P_2O_5$ prior to use.

### 6.2 UV-Visible Spectroscopy

UV-Visible absorption spectra were recorded with a Varian Cary 50 spectrophotometer. The solvents used were of HPLC grade. The blank used was of the solvent system the titration was undertaken in. Baseline correction measurements were used in all spectra. All stock solutions were freshly prepared before measurement.

### 6.3 Luminescence Measurements

Fluorescence and luminescence measurements were recorded using a Varian Carey Eclipse Fluorimeter with a 1.0 cm path length quartz cell. The solvents used were all of HPLC grade. The settings for the fluorimeter for the luminescence measurements carried out in all chapters are shown in Table 6.1. where the settings of PMT and the slits width were adapted with respect to the luminescence intensity of the system.

**Table 6.1:** *Luminescence settings for Varian Carey Eclipse fluorimeter.*

| | |
|---|---|
| Mode: Phophorescence | Total Decay: 0.02 ms |
| Flash: 1 | Delay: 0.1 ms |
| Gate: 10 ms | PMT Voltage: 700-800 |
| Excitation slit width: 20 nm | Emission slit width: 1-5 nm |

### 6.4 Lifetime Determination for Ln(III) Complexes

Luminescence lifetime measurements of all europium complexes were carried out in $D_2O$, $H_2O$, $CH_3CN$ $CH_3OH$ or MeOD, on a Varian Carry Eclipse fluorescence spectrophotometer. The settings for the Varian Carey Eclipse fluorescence spectrophotometer are shown in Table 6.2.

**Table 6.2:** *General Settings for Lifetime studies.*

| | |
|---|---|
| Delay time: 0.1 ms | Gate Time: 0.025-0.05 ms |
| Flash Count: 1 | No. Cycles: 10-30 |
| Total Decay: 10-30 ms | PMT Voltage: 700-800 |
| Excitation slit width: 20 nm | Emission slit width: 1-5 nm |

### 6.5 CD measurements

CD spectra were recorded in $CH_3OH$ or $CH_3CN$ on a Jasco J-810-150S spectropolarimeter. All CD spectra are represented as mDeg vs λ (nm). The baseline of the solvent was taken and substracted from all spectra.

### 6.6 CPL measurements

Circularly polarised luminescence spectra were recorded by Dr. R. Peacock at the University of Glasgow. Excitation of $Eu^{III}$ (560-581nm) was accomplished by using a Coherent 599 tunable dye laser (0.03 nm resolution) with argon ion laser as a pump source. Calibration of the emission monochromator was accomplished by passing scattered light from a low power He-Ne laser through the detection system. The optical detection system consisted of a photoelastic modulator (PEM, Hinds Int.) operating at 50 kHz and a linear polariser, which together act as a circular analyser, followed by a long pass filter, focusing lens and a 0.22 m double monochromator. The emitted light was detected by a cooled EM1-9558QB photomultiplier tube operating in photon counting mode. The 50 KHz reference signal from the photoelastic modulator was used to direct the incoming pulses into two separated counters. An up counter, which counts every photon pulse and thus is a measure of the total luminescence signal $I = I_{left} + I_{right}$, and an up/down counter, which adds pulses when the analyser is transmitting to the left circularly polarised light and substracts pulses when the analyser is transmitting right circularly polarised light. The second counter provides a measure of the differential emission intensity $\Delta I = I_{left} - I_{right}$. The helicity values or $g_{em}$ were calculated from the differential emission intensity ΔI using the formula enunciated by Richardson *et al.*: $g_{em}(\lambda) = 2\ \Delta I/I_L(\lambda)$, where $I_L(\lambda)$ is the intensty of luminescence at the given wavelength λ upon excitation with direct light.[156]

### 6.7 Molecular mechanics modelling studies

Molecular mechanics (also called MM2-3 calculation) is a mathematical method, which models molecular geometries and their energies by adjusting bond lengths and, bond and torsion angles to an equilibrium, dependent on the hybridization of the atoms and their bonding capacities.[157] his method relies on the laws of classical Newtonian physics and experimental parameters, manually introduced into the calculation, in order to predict the geometry of the molecules as a function of its steric energy.[157] The resulting set of

$$E_p = \sum E_{bd} + \sum E_{ang} + \sum E_{tor} + \sum E_{bend} + \sum E_{wi} \qquad (1)$$

equations and empirical parameters taken into account for these calculations is called field force and the MM2 and MM3 field forces have the general expression in the equation (1), in which $E_p$ corresponds to the potential energy of the molecule defined as the difference between the model and the ideal molecule. Consequently, the building of the molecular model consists of the minimization of $E_p$, monitored by its gradient, *via* the adjustment of the $E_{bd}$ (bonding energy), $E_{ang}$ (diedral angle energy), $E_{tor}$ (molecular torsion energy), $E_{bend}$ (bending energy) and $E_{wi}$ (energy of weak interactions such as Van der Waals interactions, ππ-stacking and H-bonding). Consequently, the molecular mechanics approach, which in contrast to semi-empirical methods such as the quantum mechanics and *ab-initio* methods, does not take into account any electronic effects and offers an efficient method in order to predict the shape of supramolecules.[158] The MM calculation were performed in the MM2 force field using Chem3D version 11.

### 6.8 General synthetic procedures

#### 6.8.1 Procedure 1: General procedure for the synthesis of the terbium complexes:

The calix-[4]-arene analogues were dissolved in methanol before one equivalent of $Tb(ClO_4)$ was added. The reaction mixture was refluxed for 12h. The complexes **L.Tb** were isolated as a white solid upon the addition of diethylether.

**Complex 42.Tb:**

**42.Tb** was synthesised by refluxing Ligand **42** (14.1 mg, $1.5\times10^{-5}$ mol) with $Tb(ClO_4)_3$ (11.8 mg, $1.5\times10^{-5}$ mol) in methanol (10 ml) according to **procedure 1**, to yield **42.Tb** as a white solid (14.2mg, 69%) after precipitation from methanol upon the addition of diethylether. m.p. Decomposed above 280°C; Calculated for $C_{56}H_{68}Cl_3N_4O_{20}Tb$, C, 48.65; H, 4.96; N, 4.05 found: C, 48.43; H, 4.85; N, 3.95; HRMS calculated for $C_{56}H_{68}Cl_2N_4O_{16}Tb$ $[M^{3+} + 2\ ClO_4^-]^+$ m/z = 1281.3261, Found: 1281.8023; $\delta_H$ ($CD_3CN$; 400MHz): 7.28, 6.61, 5.11, 4.89, 3.51, 3.42, 3.27; IR $\nu_{max}$: 2945, 2857, 1645, 1616, 1500, 1440, 1370, 1278, 1177, 1082, 1001, 952, 901, 856, 783.

**Complex 43.Tb:**

**43.Tb** was synthesised by refluxing Ligand **43** (8.9 mg, $0.9\times10^{-5}$ mol) with $Tb(ClO_4)_3$ (7.38 mg, $1.5\times10^{-5}$ mol) in methanol (10 ml) according to **procedure 1**, to yield **43.Tb** as a white solid (11.4 mg, 99%) after precipitation from methanol using diethyl ether. m.p. Decomposed above 280°C; Calculated for $C_{52}H_{60}Cl_3N_4O_{24}Tb$, C, 44.92; H, 4.35; N, 4.03 found: C, 44.85; H, 4.28; N, 4.01; HRMS calculated for $C_{52}H_{60}Cl_2N_4O_{20}Tb$

($M^{3+}$ + 2 $ClO_4^-$) m/z = 1289.2431, Found: 1289.8 [$M^{3+}$ + 2 $ClO_4^-$]$^+$; $\delta_H$ ($CD_3CN$; 400 MHz):, 7.28, 6.80, 6.67, 4.81, 3.61, 3.37, 3.26; IR $\nu_{max}$: 2965, 2930, 2853, 1680, 1673, 1486, 1370, 1320, 1280, 1220, 1200, 1000, 920, 780, 750.

**Complex 44.Tb:**

**44.Tb** was synthesised by refluxing Ligand **44** (20.9 mg, $1.8\times10^{-5}$ mol) with $Tb(ClO_4)_3$ (14.9 mg, $1.8\times10^{-5}$ mol) in methanol (10 ml) according to **procedure 1**, to yield **44.Tb** as a hygroscopic white solid (27.4 mg, 97%) after precipitation from methanol upon the addition of diethylether. m.p. Decomposed above 280°C; Calculated for $C_{64}H_{88}Cl_3N_8O_{20}Tb$, C, 49.44; H, 5.71; N, 7.21 found: C, 48.38; H, 5.74; N, 7.18; HRMS calculated for $C_{64}H_{88}Cl_3KN_8O_8Tb$ [$M^{3+}$ + 3 $Cl^-$ + $K^+$]$^+$: m/z = 1399.4531, Found: 1399.3651 $\delta_H$ ($CD_3CN$; 400 MHz): 7.29, 6.62, 4.53, 3.55, 2.52, 2.12; IR $\nu_{max}$: 3290, 2940, 2860, 1660, 1634, 1579, 1459, 1443, 1390, 1280, 1250, 1177, 1056, 943, 903, 856, 821, 777, 716, 691

**Complex 45.Tb:**

**45.Tb** was synthesised by refluxing Ligand **45** (28.2 mg, $2.6\times10^{-5}$ mol) with $Tb(ClO_4)_3$ (20.1 mg, $2.6\times10^{-5}$ mol) in methanol (10 ml) according to **procedure 1**, to yield **45.Tb** as a hygroscopic white solid (37.9 mg, 95%) after precipitation from methanol upon the addition of diethylether. m.p. Decomposed above 280°C; Calculated for $C_{60}H_{84}Cl_3N_{12}O_{20}Tb$, C, 46.23; H, 5.43; N, 10.78 found: C, 46.18; H, 5.40; N, 10.81; HRMS: calculated for $C_{60}H_{84}Cl_3KN_{12}O_8Tb$ [$M^{3+}$ + 3 $Cl^-$ + $K^+$]$^+$ m/z = 1403.4297, Found 1403.2623 ; $\delta_H$ ($CDCl_3$; 400 MHz): 7.31, 6.56, 4.45, 3.40; 3.22; 2.85 2.46 IR $\nu_{max}$: 3320, 3080, 2945, 2880, 2830, 1681, 1560, 1450, 1205, 880, 795, 760.

**6.8.2** Compounds **54R** and **54S** were obtained following the procedure described develeloped first by Stomeo *et al.*[112,159]

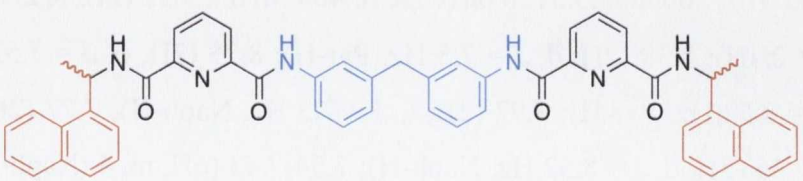

**(S,S): *N,N'*-[Methylenebis(phen-1,3-ylene)]bis(6-(*S*)-1Naphtalen-1-yl-ethylcarbamoyl)-pyridine-2 -carboxyamide) (54S):**

To a solution of 3,3'-methylene(diphenylamine) (100mg, 0.31mmol) in THF (12mL) was added HOBt (44.3mg, 0.33mmol). The solution was cooled to 0°C before being stirred for 15 minutes under an inert atmosphere. EDCI (62.8mg, 0.33mmol), DMAP

(22.1mg, 0.16mmol) and triethylamine (33.2mg, 0.33mmol) were added portionwise. After 30 minutes, the resulting suspension was allowed to warm slowly to room temperature before being reacted overnight under inert atmosphere. The solid residue was remove by filtration before the solvent was removed under reduced pressure. The resulting crude oil was dissolved in dichoromethane and washed with HCl (1M), a saturated solution of $NaHCO_3$ and finally with water. The organic layer was dried over $MgSO_4$ before the solvent was removed. Compound **54S** was collected as an off-white solid (79.2mg, 0.098mmol, 63.2%). Elemental analysis: Calculated for $C_{51}H_{42}N_6O_4 \cdot H_2O$, C, 74.62; H, 5.40; N, 10.24 found: C: 74.45; H: 5.38; N: 9.89; Calculated for $[C_{51}H_{42}N_6O_4 + Na^+]^+$ m/z = 825.3165 found 825.3137; $\delta_H$ ($CDCl_3$, 400 MHz): 9.63 (2H, s, 2NH); 8.74 (2H, d, *J* = 8.52 Hz, 2NH); 8.35 (2H, d, *J* = 7.5 Hz, Pyr-H); 8.18 (2H, d, *J* = 7.52 Hz, Pyr-H); 8.03 (2H, d, *J* = 8.52 Hz, Pyr-H); 7.92 (2H, t, *J* = 7.5 Hz, Naph-H); 7.72 (2H, d, *J* = 7.71 Hz, Naph-H); 7.58 (2H, d, *J* = 8.52 Hz, Naph-H); 7.46-7.38 (4H, m, Naph -H); 7.35 (2H, d, *J* = 7.56 Hz, Naph-H); 7.13 (2H, t, *J* = 7.52Hz, Phen-H); 7.08 (2H, s, Phen-H); 6.99-6.91 (4H, m, 2×Naph-H + 2Phen-H); 6.72 (2H, d, *J* = 7.04 Hz, Phen-H); 5.97 (2H, m, CH); 3.39 (2H, t, *J* = 7.04 Hz, $CH_2$); 1.88 (6H, d, J = 7.04 Hz, 2Me). δc ($CDCl_3$; 100 MHz): 162.2; 161.5; 148.6; 148.1; 140.8; 138.2; 137.6; 136.3; 133.2; 130.5; 128.3; 128.1; 127.5; 126.0; 125.3; 125.1; 124.5; 124.4; 122.8; 122.4; 119.2; 44.7; 27.3; 20.1. IR $\upsilon_{max}$ ($cm^{-1}$): 3292; 3040; 2977; 2934; 1654; 1589; 1521; 1488; 1445; 1316; 1229; 1167; 1119; 1074; 908; 866; 799; 739; 677.

**(*R*,*R*): *N*,*N*'-[Methylenebis(phen-1,3-ylene)]bis(6-(*R*)-1-naphtalen-1-yl-ethylcarbamoyl)-pyridine-2-carboxyamide) (54R):**

Ligand **54R (*R*,*R*)** was isolated, following the above procedure as an off-white solid (74.7mg, 0.093mmol, 59.7%). Elemental analysis: Calculated for $C_{51}H_{42}N_6O_4$, C, 76.29; H, 5.27; N, 10.47 found: C: 76.32; H: 5.35; N: 10.39; Calculated for $[C_{51}H_{42}N_6O_4 + Na^+]^+$ m/z = 825.3165 found 825.3128 $\delta_H$ ($CDCl_3$, 400 MHz): 9.52 (2H, s, 2NH); 8.54 (2H, d, *J* = 8.52 Hz, 2NH); 8.38 (2H, d, *J* = 7.5 Hz, Pyr-H); 8.25 (2H, d, *J* = 7.52 Hz, Pyr-H); 8.09 (2H, d, *J* = 8.52 Hz, Pyr-H); 7.97 (2H, t, *J* = 7.5 Hz, Naph-H); 7.77 (2H, d, *J* = 7.71 Hz, Naph-H); 7.65 (2H, d, *J* = 8.52 Hz, Naph-H); 7.54-7.43 (6H, m, 4×Naph-H+2Phen-H); 7.22 (2H, d, *J* = 7.56 Hz, Naph-H); 7.08 (2H, s, Phen-H); 7.05-7.00 (4H, m, 2×Naph-H + 2×Phen-H); 6.80 (2H, d, *J* = 7.04 Hz, Phen-H); 6.00 (2H, m, CH); 3.56 (2H, t, *J* = 7.04 Hz, $CH_2$); 1.87 (6H, d, *J* = 7.04 Hz, Me). $\delta_c$ ($CDCl_3$; 100 MHz): 162.3; 161.5; 148.5; 148.1; 140.8; 138.3; 137.7; 136.3; 133.3; 130.6; 128.3; 128.1; 127.6; 126.0; 125.3; 125.1; 124.5;

124.6; 122.8; 122.4; 119.1; 44.8; 29.3; 20.1. IR $\upsilon_{max}$ ($cm^{-1}$): 3289; 3066; 2992; 2955; 1630; 1588; 1557; 1489; 1447; 1376; 1238; 1164; 1082; 1044; 800; 777; 753; 730; 679.

**Complex $54S_3.Eu_2$:**

Ligand **54S** (15mg; $1.8\times10^{-6}$ mol) and $Eu(CF_3SO_3)_3$ (7.4mg; $1.2\times10^{-5}$ mol) were refluxed in MeOH (5 ml) for 24 hours. The solvent was removed under reduced pressure. The resulting concentrated solution was poured over diethylether and the complex **$54S_3.Eu_2$** was collected after decantation as solid oil (14.6mg; $4.0\times10^{-6}$ mol, 75%). $\delta_H$ (MeOD; 600 MHz): 8.81; 8.65; 8.25; 7.84; 7.50; 7.37; 7.00; 6.76; 6.55; 6.32; 6.19; 5.52; 4.05; 3.94; 1.81; IR $\nu_{max}$ ($cm^{-1}$): 3280; 2994; 2923; 2882; 1654; 1589; 1522; 1487; 1444; 1366; 1259; 1074; 1021; 799; 776.

**Complex $54R_3.Eu_2$:**

The complex **$54R_3.Eu_2$** was collected following the procedure described for **$54S_3.Eu_2$** (19.6mg; $5.4\times10^{-3}$ mmol, 49%): **54R** (20mg; $2.5\times10^{-5}$ mol), $Eu(CF_3SO_3)_3$ (9.9 mg; $1.66\times10^{-5}$mol). $\delta_H$ (MeOD; 600 MHz): 8.85 (3×2H, br. s., naph-H); 8.63 (3×4H, br. s., Ar-H); 8.27; 7.83; 7.49; 7.40; 6.98; 6.80; 6.54; 6.30; 6.23; 5.48; 4.03; 3.89; 1.82; IR $\upsilon_{max}$ ($cm^{-1}$): 3290; 2974; 2931; 2882; 1631; 1589; 1559; 1485; 1450; 1350; 1259; 1166; 1029; 800; 779.

### 6.8.3 2,6-Pyridinedicarboxylic acid chloride (64):

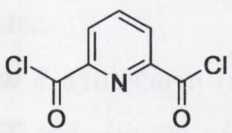


2,6-Pyridinedicarboxylic acid (5 g, 29.9 mmol) was refluxed overnight in thionylchloride (50 ml). The mixture was reduced to dryness under reduced pressure, before compound **64** was obtained as a white powder in 99% yield (5.97 g). Calculated for $C_7H_3NO_2Cl_2$: $[M+H]^+$ *m/z* = 202.9542; Found: 202.9563; $\delta_H$ (400 MHz, MeOD-$D_4$, 298.2 K) 8.39 (2H, d, *J* = 7.56 Hz, Ar-H4), 8.22 (1H, t, *J* = 7.56 Hz, Ar-H2); Selected IR bands ($cm^{-1}$): 1751s ($\upsilon_{CO}$).

### N,N'-Bis(5-hydroxy-3-oxa-pentyl)-2,6-pyridinedicarboxamide (66):[147]

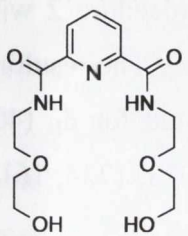


The reaction was carried out under anhydrous conditions. To a suspension of 2,6-pyridinedicarboxylic acid chloride (500mg, 2.5mmol) and triethylamine (1g, 10mmol) in dry dichloromethane at 0 °C, was added drop wise, a solution of 2(2-aminoethoxy)ethanol (575 mg, 5.5 mmol) and triethylamine (550 mg, 5.5 mmol). The mixture

was stirred at room temperature for 48 hours. The desired product (**66**) was isolated as pale yellow oil (664 mg, 1.95 mmol, 78 %). Calculated for $C_{15}H_{23}N_3O_6$ + HCl: $(M+H)^+$ *m/z* = 378.61; Found: 378.20; $\delta_H$ (400 MHz, MeOD-$D_4$, 298.2 K) 8.12 (2H, d, *J* = 8.04 Hz, Ar-H3), 7.94 (1H, t, *J* = 8.04 Hz, Ar-H4), 3.71 (8H, m, $OCH_2$-$CH_2$), 3.59 (4H, t, *J* = 4.52 Hz, HO-$CH_2$), 3.15 (4H, t, *J* = 5 Hz, HO-$CH_2$); $\delta_c$ (100 MHz, MeOD-$D_4$, 298.2 K) 171.1, 152.7, 136.8, 124.42, 71.6, 66.3, 60.2, 38.5. IR $\upsilon_{max}$ ($cm^{-1}$): 3370, 3250, 2925, 2875, 1604, 1560, 1450, 1430, 1366, 1265, 1185, 1120, 1070, 1000, 895, 765, 720.

**General procedure 2: synthesis of the complexes $66_3$.Ln (Ln = Eu, Tb, Lu):**

Ligand **66** (3 equivalents) and $Ln(CF_3SO_3)_3$ (1.1 equivalents) were refluxed for 24 hrs in dimethylformamide. The resulting precipitate was isolated by suction filtration before being washed with acetonitrile and diethyl ether.

**Complex, $66_3$.Eu:**

The synthesis of **$66_3$.Eu** was performed following the general **procedure 2** with ligand **66** (300 mg, 0.88 mmol) and $Eu(CF_3SO_3)_3$ (192 mg, 0.32 mmol). The resulting complex was obtained (264 mg, 0.162 mmol) in 18.5 % yield. Calculated for $C_{45}H_{69}N_9O_{18}Eu$: $[M+H]^+$ *m/z* = 1177.40; Found: 1177.60. $\delta_H$ (400 MHz, MeOD-$D_4$, 298.2 K) 5.37, 4.67, 3.93, 3.32. IR $\nu_{max}$: 3387, 3214, 2971, 1736, 1613, 1568, 1431, 1365, 1275, 1190, 1116, 1073, 1020, 920, 761, 728, 693, 662.

**Complex, $66_3$.Tb:**

The synthesis of **$66_3$.Tb** was performed following the general **procedure 2** with ligand **66** (500 mg, 1.47 mmol) using the $Tb(CF_3SO_3)_3$ (326 mg, 5.38 mmol). The $Tb^{III}$ complex was obtained as a white solid (407 mg, 0.25 mmol) in 17% yield. $\delta_H$ (400 MHz, MeOD-$D_4$, 298.2 K) 46.42, 31.48, 28.32, 2.65, -0.43, -3.55, -12.73, -26.38. IR (KBr) $\upsilon_{max}$ ($cm^{-1}$): 3070, 2922, 2168, 1604, 1569, 1433, 1370, 1279, 1189, 1117, 1072, 1021, 918, 897, 861, 826, 766, 731, 696, 662.

**Complex, $66_3$.Lu:**

The synthesis of **$66_3$.Lu** was performed following the general procedure 2 with ligand **2** (300 mg, 0.88 mmol) using the $Lu(CF_3SO_3)_3$ (192 mg, 0.32 mmol). The resulting complex was obtained (264 mg, 0.162 mmol) in 18.5 % yield. Calculated for $\delta_H$ (400 MHz, MeOD-$D_4$, 298.2 K) 5.37, 4.67, 3.93, 3.32. IR $\nu_{max}$ ($cm^{-1}$): 3392, 2973, 1734, 1615, 1434, 1367, 1273, 1192, 1118, 1078, 1025, 925, 758, 725, 690, 658.

**General procedure 3: "Catenation" synthesis of Cat66.Ln (Ln = Eu, Tb)[144]**

The reaction was carried out under anhydrous conditions at low concentration to avoid polymerization. A solution of diodoethoxyethylene (3.3 equivalents) was added dropwise to a stirred suspension of $Cs_2CO_3$ (9.9 equivalents) and **66$_3$.Ln** (1 equivalent) in DMF at 60°C. After 24 hours another 0.1 equivalent of diodoethoxyethylene was added before the solution was stirred at 60°C for 48 hours. The white solid was isolated by suction filtration and washed with dimethylformamide and diethyl ether yielding a mixture of several isomers.

**Catenation of 66$_3$.Tb. Complex, Cat66.Tb:**

The reaction was performed according to **procedure 3** using diodoethoxyethylene (660 mg, 0.2 mmol) and **2$_3$.Tb** (100 mg, 0.062 mmol) in presence of $Cs_2CO_3$ (198 mg, 0.61 mmol). A white solid (100 mg, 0.038 mmol) was obtained as crude compound. $\delta_H$ (400 MHz, MeOD-$D_4$, 298.2 K) 25.62, 23.74, 2.06, 1.32, 0.13, -0.94, -5.46, -7.69. IR (KBr) $\upsilon_{max}$ ($cm^{-1}$) 3346, 2161, 1620, 1585, 1506, 1429, 1380, 1365, 1276, 1190, 1158, 1111, 1080, 1022, 971, 917, 887, 857, 819, 773, 729, 700, 663.

**Catenation of 66$_3$.Eu. Complex, Cat66.Eu:**

The reaction was performed according to **procedure 3** using diodoethoxyethylene (660 mg, 0.2 mmol) and **66$_3$.Eu** (100 mg, 0.062 mmol) in presence of $Cs_2CO_3$ (199 mg, 0.61 mmol). A white solid (66 mg, 0.036 mmol) was obtained as crude compound. Calculated for $C_{59}H_{85}N_9O_{27}S_2F_6Eu$: $[M+2\times CF_3SO_3]^+$ *m/z* = 1685.62; Found: 1685.61. $\delta_H$ (400 MHz, MeOD-$D_4$) 5.72, 5.11, 4.55, 4.22, 3.87, 3.73. IR $\nu_{max}$ ($cm^{-1}$): 3390, 2255, 2982, 1738, 1619, 1589, 1429, 1380, 1275, 1189, 1116, 1079, 1020, 919, 771, 731, 696, 662.

**2-(2-(2-(allyloxy)ethoxy)ethoxy)ethanol (67):[160]**

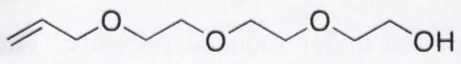

To a solution of triethylene glycol (30g, 200 mmol) in toluene (20 mL) at room temperature, allyl chloride (18.04 mL, 219.7 mmol) and NaOH (16 g, 400 mmol) were added. The resulting mixture was refluxed for 3 days. Upon filtration of a white residue and evaporation of the solvent under reduced

pressure, the brown oil was dissolved in $CH_2Cl_2$ and washed with brine (50 mL) and distilled water (50 mL). The resulting orange oil was further purified by silica column chromatography using hexane-EtOAc from 7:3 to 1:1 gradient, yielding a colourless oil (10.38 g, 54.6 mmol, 27.3% yield) HRMS (m/z) ($ES^+$) Calculated for $C_9H_{19}O_4$ $[M+H^+]^+$ m/z = 191.1286, Found 191.1286; $\delta_H$ ($CDCl_3$; 400 MHz): 5.95 (m, 1H, $CH{=}CH_2$), 5.28 (m, 2H, $CH{=}C\underline{H_2}$), 4.06 (m, 2H, $C\underline{H_2}CH{=}CH_2$), 3.62 (m, 12H, $CH_2$); $\delta_c$ ($CDCl_3$; 100 MHz): 134.6, 117.1, 72.5, 70.2-70.5, 61.6.; IR $\nu_{max}$ ($cm^{-1}$) = 3376, 2870, 1648, 1350, 1245, 1116, 1064, 934, 885.

**2-(2-(2-(allyloxy)ethoxy)ethoxy)ethyl-4-methylbenzenesulfonate (68):**[160]

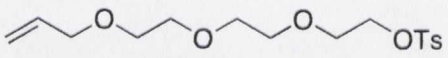


**67** (500 mg, 2.6 mmol) and 5 equivalents of TsCl (2.5 g, 13 mmol) were dissolved in dichloromethane (20 mL) before the resulting mixture was stirred for 15 minutes. To that solution, pyridine (2.13 mL, 26 mmol) was added drop wise before the resulting mixture was stirred at room temperature for 48h. The pyridine was quenched with 1M HCl (1 mL) before the solvents were removed under reduced pressure. The resulting mixture was extracted with $CH_3Cl$ (50 mL) before the organic layer was washed with $H_2O$ (2×50 mL) and dried over $MgSO_4$. **68** was isolated as a yellow oil in 45% yield (404 mg, 1.17 mmol), after purification *via* silica column chromatography using $CH_2Cl_2$-$CH_3OH$ (9-1) as eluent. HRMS (m/z) ($ES^+$) Calculated for $C_{16}H_{24}O_6S$ $[M+Na^+]^+$ m/z = 367.1191, Found 367.1132; $\delta_H$ ($CDCl_3$; 400 MHz): 7.79 (d, 2H, $^3J$ = 8.0 Hz, Ar-H), 7.33 (d, 2H, $^3J$ = 8.0 Hz, Ar-H), 5.89 (m, 1H, $C\underline{H}{=}CH_2$), 5.28 (m, 1H, $CH{=}C\underline{H_2}$), 5.18 (m, 1H, $CH{=}C\underline{H_2}$), 4.16 (m, 2H, $C\underline{H_2}$-OTs), 4.01 (m, 2H, $C\underline{H_2}CH{=}CH_2$), 3.68-3.59 (m, 12H, $CH_2$), 2.44 (s, 3H, Ar-$C\underline{H_3}$); $\delta_c$ ($CDCl_3$; 100 MHz): 144.3, 134.2, 132.5, 129.38, 127.5, 117.1, 71.8, 70.3, 70.2, 68.9, 68.8, 68.2, 21.2; IR $\nu_{max}$ ($cm^{-1}$) = 3389, 2876, 1598, 1452, 1351, 1211, 1188, 1120, 1095, 1033, 916, 816, 683, 662.

**3-(2-(2-(2-azidoethoxy)ethoxy)ethoxy)propen-1-ene (69):**[160]

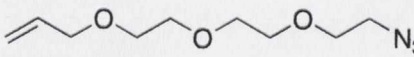


**69** was synthesised by refluxing **68** (300 mg, 0.87 mmol), with $NaN_3$ (680 mg, 10 mmol, 12 eq) in $CH_3CN$ for 4 days. The resulting white suspension was isolated by filtration before the solvent was removed under reduced pressure. The resulting yellow oil was dissolved in $CH_2Cl_2$ and washed twice with $H_2O$ (2 × 50 mL) to give **69** as a yellow oil in 74% yield (140 mg, 0.64 mmol). $\delta_H$ ($CDCl_3$; 400 MHz): 5.90 (m, 1H, $C\underline{H}{=}CH_2$), 5.28 (m, 1H, $CH{=}C\underline{H_2}$), 5.16 (m, 1H, $CH{=}C\underline{H_2}$), 4.02 (m, 2H,

$C\underline{H_2}CH{=}CH_2$), 3.68-3.59 (m, 12H, $CH_2$), 3.38 (m, 2H, $N_3$-$C\underline{H_2}$); $\delta_c$ ($CDCl_3$; 100 MHz): 134.2, 116.7, 71.8, 70.3, 70.2, 69.5, 68.9, 50.2, 42.3; IR $\nu_{max}$ ($cm^{-1}$) = 3422, 2866, 1452, 1348, 1287, 1248, 1094, 995, 927, 881, 838.

**3-(2-(2-(2-aminoethoxy)ethoxy)ethoxy)propen-1-ene (70):**[160]

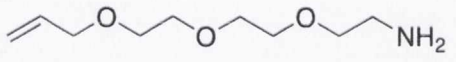

To a solution of **69** (1.24 g, 5.5 mmol) in THF (50 mL) at 0°C, $PPh_3$ (1.66 g, 6.1 mmol) was added portionwise and the resulting mixture was stirred at room temperature for 12h. The resulting oil was dissolved in $H_2O$ and washed with toluene (2 × 20mL). **70** was obtained as a yellow oil after evaporation of the aqueous layer under reduced pressure (759 mg, 4.0 mmol, 73%). $\delta_H$ ($CDCl_3$; 400 MHz): 5.89 (m, 1H, $C\underline{H}{=}CH_2$), 5.28 (m, 1H, $CH{=}C\underline{H_2}$), 5.16 (m, 1H, $CH{=}C\underline{H_2}$), 4.01 (m, 2H, $C\underline{H_2}CH{=}CH_2$), 3.65-3.49 (m, 12H, $CH_2$), 2.85 (m, 2H, $H_2N$-$C\underline{H_2}$); $\delta_c$ ($CDCl_3$; 100 MHz): 134.3, 116.7, 114.8, 71.8, 70.3, 70.2, 69.6, 69.0, 50.2, 42.3; IR $\nu_{max}$ ($cm^{-1}$)= 3360, 2666, 1665, 1565, 1445, 1348, 1297, 1248, 1091, 995, 924, 881, 818.

***N,N'*-bis(2-(2-(2-(allyloxy)ethoxy)ethoxy)ethyl)pyridine-2,6-dicarboxamide (71):**

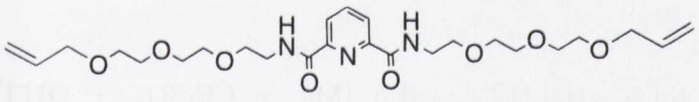

To a solution of **64** (300 mg, 1.5 mmol) and triethylamine (270 mg, 6 mmol, 4 eq) at 0°C in $CH_2Cl_2$ (50 mL) was added a solution of **70** (612 mg, 3.2 mmol, 2.2 eq) and triethylamine (148 mg, 1.6 mmol, 1.1 eq) in $CH_2Cl_2$ (20 mL) dropwise over a period of 15 min. The resulting mixture was allowed to reach room temperature before being stirred for 48h. The solvent was removed under reduced pressure before the resulting brown oil was re-dissolved in $CH_2Cl_2$ and washed with distilled $H_2O$ (2 × 50 mL). The organic layer was dried over $MgSO_4$ before the solvent was removed and **71** was then obtained as an yellow oil in 48% yield (360 mg, 0.7 mmol). HRMS (m/z) ($ES^+$) Calculated for $C_{25}H_{39}O_8N_3$ $[M+Na^+]^+$ m/z = 532.2635, Found 532.2812; $\delta_H$ ($CDCl_3$; 400 MHz):8.57 (s, 2H, N$\underline{H}$), 8.35 (d, $^3J$ = 7.6 Hz, 1H, Pyr-H), 8.03 (t, $^3J$ = 8.2 Hz, 2H, Pyr-H), 5.88 (m, 2H, $C\underline{H}{=}CH_2$), 5.26 (m, 2H, $CH{=}C\underline{H_2}$), 5.15 (m, 2H, $CH{=}C\underline{H_2}$), 3.98 (m, 2H, $C\underline{H_2}CH{=}CH_2$), 3.72-3.66 (m, 20H, $CH_2$), 3.59 (m, 2H, HN-$C\underline{H_2}$); $\delta_c$ ($CDCl_3$; 100 MHz): 169.4, 151.3, 134.6, 126.5, 117.2, 72.0, 70.3, 70.2, 70.0, 69.2, 67.3, 45.4, 39.3; IR $\nu_{max}$ ($cm^{-1}$)= 3550, 3320, 2867, 1665, 1532, 1445, 1349, 1247, 1093, 998, 926, 846, 749, 679.

**Complex, $71_3$.Eu:**

Ligand **71** (50 mg, 0.098 mmol) and $Eu(CF_3SO_3)_3$ (19.6 mg; 0.032 mmol) were refluxed in $CH_3CN$ (10 mL) for 12h. The solvent was removed under reduced pressure. The resulting concentrated solution was poured over diethylether before complex **$71_3$.Eu** was collected in 32% yield as pale yellow oil (22.2 mg; 0.012 mmol). $\delta_H$ ($CDCl_3$; 600 MHz): 8.53; 8.37; 8.05; 7.36; 5.88; 5.29; 4.04; 3.74-3.59; 3.52. IR $\nu_{max}$ ($cm^{-1}$): 3510, 3285; 1667; 1547; 1346; 1260; 1093; 1005; 980; 937; 752; 677.

**Catenation of $71_3$.Eu:**

Anhydrous complex **$71_3$.Eu** (26 mg, 0.013 mmol) was dissolved in distilled $CH_2Cl_2$ (20 mL), under an inert atmosphere. To this solution the 2nd generation Grubb's catalyst (benzylidene [1,3- bis(2,4,6-trimethylphenyl)-2- imidazolidinylidene] dichloro (tricyclohexylphosphine) ruthenium) (3.1 mg, 3.6 $\times 10^{-3}$ mmol, 0.3 eq) was added drop wise over a period of 5 minutes. The resulting mixture was stirred at room temperature for 3 days under an inert atmosphere. The $CH_2Cl_2$ was removed under reduced pressure and the resulting brown oil was dissolved in $H_2O$. The aqueous layer was washed with ethyl acetate (20 mL) before the $H_2O$ was removed under reduced pressure. The resulting orange oil was triturated in $CH_2Cl_2$ and **Cat71.Eu** was obtained as a crude white solid (7 mg). The dichloromethane was removed under reduced pressure and the compound **Cat71** was obtained as crude yellow oil (10 mg).

**Cat71.Eu:** HRMS: Calculated for $C_{70}H_{106}N_9F_9O_{28}SEu$ $[M^{3+} + CF_3SO_3^- + OH^-]^+$ 1762.6044, Found 1761.6688 $\delta_H$ ($CDCl_3$; 600 MHz): 8.93; 8.34; 7.02; 7.36; 5.88; 5.29; 4.06; 3.73-3.69; 3.50. IR $\nu_{max}$ ($cm^{-1}$): 3510, 3285; 1667; 1547; 1346; 1260; 1093; 1005; 980; 937; 752; 677.

**Cat71**: HRMS: Calculated for $C_{69}H_{105}N_9O_{24}$ $[M + Na^+]^+$ 1466.7170, Found 1466.7152 $\delta_H$ ($CDCl_3$; 600 MHz): 8.30; 8.15; 5.82; 4.00; 5.88; 5.29; 4.06; 3.73-3.71; 3.24. IR $\nu_{max}$ ($cm^{-1}$): 3552, 3314; 2865; 1665; 1532; 1445; 1345; 1310; 1245; 1099; 998; 852, 740.

**Macrocyle 72:**

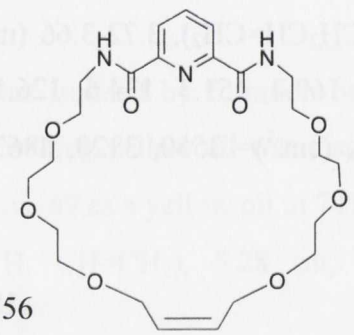

Ligand **71** (50.8 mg, 0.1 mmol) was dissolved in freshly distilled $CH_2Cl_2$ (100 mL), under inert atmosphere. To this solution the 2nd generation Grubb's catalyst (benzylidene[1,3- bis(2,4,6-trimethylphenyl)- 2-imidazolidinylidene] dichloro(tricyclohexylphosphine)

ruthenium) (12.7 mg, 1.4 $\times 10^{-3}$ mmol, 0.14 eq) was added drop wise over a period of 5 minutes. The $CH_2Cl_2$ is removed under reduced pressure and the resulting mixture is washed with $H_2O$ (2×50 mL). The organic layer was washed over $MgSO_4$ and **72** was obtained as brown oil (38.4 mg, 0.08 mmol, 80%). HRMS: Calculated for $C_{23}H_{35}N_3O_8$ [M + $Na^+$]$^+$: 504.2322, Found 504.2316; $\delta_H$ ($CDCl_3$; 400 MHz): 8.57 (s, 2H, NH), 8.34 (d, $^3J$ = 7.7 Hz, 2H, Pyr-H), 8.02 (t, $^3J$ = 7.8 Hz, 1H, Pyr-H), 5.89 (s, 2H, CH=CH), 4.07 (m, 4H, $CH_2$CH=CH), 3.74-3.66 (m, 22H, $CH_2$), 3.59 (m, 2H, HN-$CH_2$); $\delta_c$ ($CDCl_3$; 100 MHz): 163.6, 148.4, 138.2, 128.9, 124.2, 70.2, 70.1, 69.9, 69.7, 68.6, 39.0, 29.2; IR $\nu_{max}$ ($cm^{-1}$) = 3550, 3314, 2864, 1663, 1534, 1446, 1349, 1305, 1245, 1176, 1098, 999, 847, 749, 662.

# References

**References**


(1) Bünzli, J.-C. G. *Accounts Chem. Res.* **2006**, *39*, 53.

(2) Evans, W. J. *Coord. Chem. Rev.* **2000**, *206-207*, 263.

(3) Molander, G. A.; Romero, J. A. C. *Chem. Rev.* **2002**, *102*, 2161.

(4) Richman, R.; McNaughton, W. *Journal of Electronic Materials* **1997**, *26*, 415.

(5) Bünzli, J.-C. G.; Piguet, C. *Chem. Soc. Rev.* **2005**, *34*, 1048.

(6) Ozawa, L.; Itoh, M. *Chem. Rev.* **2003**, *103*, 3835.

(7) Matsumoto, K.; Yuan, J. *Metal ions in biological systems*; marcel Dekker Inc.: New-York, 2003; Vol. 40.

(8) Faulkner, S.; Pope, S. J. A.; Burton-Pye, B. P. *Appl. Spectrosc. Rev.* **2005**, *40*, 1.

(9) dos Santos, C. M. G.; Harte, A. J.; Quinn, S. J.; Gunnlaugsson, T. *Coord. Chem. Rev.* **2008**, *252*, 2512.

(10) Comby, S.; Bünzli, J.-C. G. In *Handbook of the Chemistry and Physics of Rare Earths*; Gschneider, K. A., Bunzli, J.-C. G., Pecharsky, V. K., Eds.; Elsevier: Amsterdam, The Netherlands, 2007; Vol. 37.

(11) Eliseeva, S. V.; Bünzli, J.-C. G. *Chem. Soc. Rev.* **2010**, *39*, 189.

(12) Bünzli, J.-C. G.; Comby, S.; Chauvin, A.-S.; Vandevyver, C. D. B. *Journal of Rare Earths* **2007**, *25*, 257.

(13) Bünzli, J.-C. G.; Choppin, G. R. *Lanthanide Probes in Life, Chemical and Earth Sciences: Theory and Practice*; Elsevier Science Pub. B. V.: Amsterdam, The Netherlands, 1989.

(14) Melhuish, W. H. *Pure Appl. Chem.* **1984**, *56*, 231.

(15) Parker, D.; Williams, J. A. G. In *The Lanthanides and Their Interrelations With Biosystems*; Sigel, A., Sigel, H., Eds.; Marcel Dekker Inc.: New York, 2003; Vol. 40.

(16) Carnall, W. T.; Fields, P. R.; Rajnak, K. *J.Chem.Phys.* **1968**, *49*, 4424.

(17) Beeby, A.; Clarkson, I. M.; Dickins, R. S.; Faulkner, S.; Parker, D.; Royle, L.; de Sousa, A. S.; Williams, J. A. G.; Woods, M. *J. Chem. Soc., Perkin Trans. 2* **1999**, 493.

(18) Supkowski, R. M.; Horrocks, W. d., Jr. *Inorganica Chimica Acta* **2002**, *340*, 44.

(19) Bünzli, J. C. G. In *Spectroscopic Properties of Rare Earths in Optical Materials*; Liu, G. K., Jacquier, B., Eds.; Springer Verlag: Berlin, 2005, p 462.

(20) Gunnlaugsson, T.; Stomeo, F. *Org. Biomol. Chem.* **2007**, *5*, 1999.

(21) Parker, D.; Dickins, R. S.; Puschmann, H.; Crossland, C.; Howard, J. A. K. *Chem. Rev.* **2002**, *102*, 1977.

(22) Gunnlaugsson, T.; Stomeo, F. *Org. Biomol. Chem.* **2007**, *5*, 1999.

(23) Wolbers, M. P. O.; Van Veggel, F. C. J. M.; Snellink-Räel, B. H. M.; Hofstraat, J. W.; Geurts, F. A. J.; Reinhoudt, D. N. *J. Chem. Soc., Perkin Trans. 2* **1998**, 2141.

(24) Atkins, T. J.; Richman, J. E.; Oettle, W. F. *Organic synthesis* **1978**, *58*, 86.

(25) Valeur, B. *Molecular Fluorescence - An Introduction: Principles and Applications*; Wiley-VCH Verlag GmbH, 2000.

(26) Comby, S.; Bünzli, J. C. G.; Gschneidner, K. A., Jr., Bünzli, J. C. G., Pecharsky, V. K., Eds.; Elsevier Science B.V.: Amsterdam, 2007, p 217.

(27) Dexter, D. L. *J.Chem.Phys.* **1953**, *21*, 836.

(28) Förster, T. *Ann. Phys.* **1948**, *2*, 55.

(29) Steemers, F. J.; Verboom, W.; Reinhoudt, D. N.; van der Tol, E. B.; Verhoeven, J. W. *J. Am. Chem. Soc.* **1995**, *117*, 9408.

(30) Cotton, S. *Lanthanides and actinides*; McMillan Education: London, 1991.

(31) Aspinall, H. C. *Chemistry of the f-block elements*; Gordon & Breach: Australia, 2001.

(32) Porcher, P. In *Rare earths*; Saez Puche, R., Caro, P., Eds.; Editorial Complutense: Madrid, 1998; Vol. 1st, p 43.

(33) Massue, J.; Quinn, S. J.; Gunnlaugsson, T. *J. Am. Chem. Soc.* **2008**, *130*, 6900.

(34) Bruce, J. I.; Dickins, R. S.; Govenlock, L. J.; Gunnlaugsson, T.; Lopinski, S.; Lowe, M. P.; Parker, D.; Peacock, R. D.; Perry, J. J. B.; Aime, S.; Botta, M. *J. Am. Chem. Soc.* **2000**, *122*, 9674.

(35) Montgomery, C. P.; Murray, B. S.; New, E. J.; Pal, R.; Parker, D. *Acc. Chem. Res.* **2009**, *42*, 925.

(36) Faulkner, S.; Natrajan, L. S.; Perry, W. S.; Sykes, D. *Dalton Trans.* **2009**, 3890.

(37) Leonard, J. P.; Nolan, C. B.; Stomeo, F.; Gunnlaugsson, T. *Top. Curr. Chem.* **2007**, *281*, 1.

(38) Cantuel, M.; Lincheneau, C.; Buffeteau, T.; Jonusauskaite, L.; Gunnlaugsson, T.; Jonusauskas, G.; McClenaghan, N. D. *Chem. Commun.* **2010**, *46*, 2486.

(39) Binnemans, K. *Chem. Rev.* **2009**, *109*, 4283.

(40) Gunnlaugsson, T.; Leonard, J. P.; Mulready, S.; Nieuwenhuyzen, M. *Tetrahedron* **2004**, *60*, 105.

(41) Comby, S.; Stomeo, F.; McCoy, C. P.; Gunnlaugsson, T. *Helvetica Chimica Acta* **2009**, *92*, 2461.

(42) Bünzli, J. C. G.; André, N.; Elhabiri, M.; Muller, G.; Piguet, C. *J.Alloys Comp.* **2000**, *303/304*, 66.

(43) Starynowicz, P.; Bukietynska, K.; Golab, S.; Ryba-Romanowski, W.; Sokolnicki, J. *Eur. J. Inorg. Chem.* **2002**, 2344.

(44) Sabbatini, N.; Guardigli, M.; Manet, I.; Ziessel, R. F. In *Calixarenes 2001*; Asfari, Z., Bîhmer, V., Harrowfield, J. M., Vicens, J., Eds.; Kluwer Academic Publishers: Dordrecht, 2001, p 583.

(45) Starynowicz, P.; Bukietynska, K.; Golab, S.; Ryba-Romanowski, W.; Sokolnicki, J. *Eur. J. Inorg. Chem.* **2002**, 2344.

(46) Bazzicalupi, C.; Bencini, A.; Bianchi, A.; Giorgi, C.; Fusi, V.; Masotti, A.; Valtancoli, B.; Roque, A.; Pina, F. *Chem. Commun.* **2000**, 561.

(47) Foley, T. J.; Abboud, K. A.; Boncella, J. M. *Inorg. Chem.* **2002**, *41*, 1704.

(48) Lehn, J. M. *Supramolecular Chemistry. Concepts and Perspectives*; VCH: Weinheim, New York, Basel, Cambridge, Tokyo, 1995; Vol. 1.

(49) Sastri, V. S.; Bünzli, J. C. G.; Rao, V. R.; Rayudu, G. V. S.; Perumareddi, J. R. *Modern Aspects of Rare Earths and Complexes*; Elsevier Science B.V.: Amsterdam, 2003; Vol. Chap.4b.

(50) Koshland, D. E., Jr. *Angewandte Chem. Int. Ed.* **1994**, *33*, 2375.

(51) Piguet, C.; Bünzli, J. C. G. *Chem. Soc. Rev.* **1999**, *28*, 347.

(52) Bünzli, J. C. G.; Ihringer, F.; Dumy, P.; Sager, C.; Rogers, R. D. *Dalton Trans.* **1998**, 497.

(53) Suàrez, S.; Imbert, D.; Gumy, F.; Piguet, C.; Bünzli, J. C. G. *Chemistry of Materials* **2004**, *16*, 3257

(54) Senechal-David, K.; Leonard, J. P.; Plush, S. E.; Gunnlaugsson, T. *Org. Lett.* **2006**, *8*, 2727.

(55) Senechal-David, K.; Pope, S. J. A.; Quinn, S.; Faulkner, S.; Gunnlaugsson, T. *Inorg. Chem.* **2006**, *45*, 10040.

(56) Wong, W. K.; Liang, H. Z.; Wong, W. Y.; Cai, Z. W.; Li, K. F.; Cheah, K. W. *New. J. Chem.* **2002**, *26*, 275.

(57) Izatt, R. M.; Pawlack, K.; Bradshaw, J. S.; Bruening, R. L. *Chem. Rev.* **1991**, *91*, 1721.

(58) Pope, S. J. A.; Laye, R. H. *Dalton Trans.* **2006**, 3108.

(59) Gunnlaugsson, T.; Leonard, J. P. *Chem. Commun.* **2005**, 3114.

(60) Parker, D. *Coord. Chem. Rev.* **2000**, *205*, 109.

(61) Parker, D.; Dickins, R. S.; Puschmann, H.; Crossland, C.; Howard, J. A. K. *Chem. Rev.* **2002**, *102*, 1977.

(62) dos Santos, C. M. G.; Gunnlaugsson, T. *Dalton Trans.* **2009**, 4712.

(63) Yu, J. H.; Parker, D.; Pal, R.; Poole, R. A.; Cann, M. J. *J. Am. Chem. Soc.* **2006**, 2294.

(64) Pandya, S.; Yu, J. H.; Parker, D. *Dalton Trans.* **2006**, 2757.

(65) Montgomery, C. P.; Murray, B. S.; New, E. J.; Pal, R.; Parker, D. *Account Chem. Res.* **2009**, *42*, 925.

(66) Casnati, A.; Ungaro, R. In *Calixarene in Action*; Mandolini, L., Ungaro, R., Eds.; Imperial College Press: 2000, p 62.

(67) Dozol, J. F.; Lamare, V.; Simon, N.; Ungaro, R.; Casnati, A. In *Calixarenes for Separations*; Lumetta, G. J., Rogers, R. D., Gopalan, A., Eds.; American Chemical Society: Washington D.C., 2000; Vol. 757, p 12.

(68) Sansone, F.; Fontanella, M.; Casnati, A.; Ungaro, R.; Bîhmer, V.; Saadioui, M.; Liger, K.; Dozol, J. F. *Tetrahedron* **2006**, *62*, 6749.

(69) Cadogan, F.; Nolan, K.; Diamond, D. In *Calixarenes 2001*; Asfari, Z., Bîhmer, V., Harrowfield, J. M., Eds.; Kluwer Academic Publishers: Dordrecht, 2001, p 627.

(70) Paquet, V. r.; Zumbuehl, A.; Carreira, E. M. *Bioconjugate Chem.* **2006**, *17*, 1460.

(71) Sato, N.; Shinkai, S. *J. Chem. Soc., Perkin Trans. 2* **1993**, 621.

(72) Ohto, K.; Yano, M.; Inoue, K.; Nagasaki, T.; Goto, M.; Nakashio, F.; Shinkai, S. *Polyhedron* **1997**, *16*, 1655.

(73) Oueslati, I.; SaFerreira, R. A.; Carlos, L. D.; Baleizao, C.; Berberan-Santos, M. N.; de Castro, B.; Vicens, J.; Pischel, U. *Inorg. Chem.* **2006**, *45*, 2652.

(74) Guoa, D. S.; Liu, Z. P.; Ma, J. P.; Huang, R. Q. *Tetrahedron Lett.* **2007**, *48*, 1221.

(75) Bi, Y.; Wang, X.-T.; Liao, W.; Wang, X.; Deng, R.; Zhang, H.; Gao, S. *Inorg. Chem.* **2009**, *48*, 11743.

(76) Froidevaux, P.; Harrowfield, J. M.; Sobolev, A. N. *Inorg. Chem.* **2000**, *39*, 4678.

(77) Ziessel, R. F.; Charbonniäre, L. J.; Cesario, M.; Prange, T.; Guardigli, M.; Roda, A.; Van Dorsselaer, A.; Nierengarten, H. *Supramol. Chem.* **2003**, *15*, 277.

(78) Ulrich, G.; Ziessel, R. F.; Manet, I.; Guardigli, M.; Sabbatini, N.; Fraternali, F.; Wipff, G. *Chem.-Eur. J.* **1997**, *3*, 1815.

(79) Glover, P. B.; Ashton, P. R.; Childs, L. J.; Rodger, A.; Kercher, M.; Williams, R. M.; De Cola, L.; Pikramenou, Z. *J. Am. Chem. Soc.* **2003**, *125*, 9918.

(80) Lewis, D. J.; Day, T. M.; MacPherson, J. V.; Pikramenou, Z. *Chem. Commun.* **2006**, 1433.

(81) Fatin-Rouge, N.; Toth, E.; Perret, D.; Backer, R. H.; Merbach, A. E.; Bünzli, J. C. G. *J. Am. Chem. Soc.* **2000**, *122*, 10810.

(82) Davies, G. M.; Adams, H.; Pope, S. J. A.; Faulkner, S.; Ward, M. D. *Photochem. Photobiol. Sci.* **2005**, *4*, 829.

(83) Piguet, C.; Borkovec, M.; Hamacek, J.; Zeckert, K. *Coord. Chem. Rev.* **2005**, *249*, 705.

(84) Charbonnière, L. J.; Ziessel, R. F.; Guardigli, M.; Roda, A.; Sabbatini, N.; Cesario, M. *J. Am. Chem. Soc.* **2001**, *123*, 2436.

(85) Renaud, F.; Piguet, C.; Bernardinelli, G.; Hopfgartner, G.; Bünzli, J. C. G. *Chem. Commun.* **1999**, 457.

(86) Tanase, S.; Gallego, P. M.; de Gelder, R.; Fu, W. T. *Inorganica Chimica Acta* **2007**, *360*, 102.

(87) Lawrence, D. S.; Jiang, T.; Levett, M. *Chem. Rev.* **1995**, *95*, 2229.

(88) Swiegers, G. F.; Malefetse, T. J. *Chem. Rev.* **2000**, *100*, 3483.

(89) Beer, P. D.; Hayes, E. J. *Coord. Chem. Rev.* **2003**, *240*, 167.

(90) Lama, M.; Mamula, O.; Kottas, G. S.; Rizzo, F.; De Cola, L.; Nakamura, A.; Kuroda, R.; Stoeckli-Evans, H. *Chem.-Eur. J.* **2007**, *13*, 7358.

(91) Comby, S.; Imbert, D.; Chauvin, A. S.; Bünzli, J. C. G.; Charbonniere, L. J.; Ziessel, R. F. *Inorg. Chem.* **2004**, *43*, 7369.

(92) Comby, S.; Scopelliti, R.; Imbert, D.; Charbonnière, L. J.; Ziessel, R.; Bünzli, J. C. G. *Inorg. Chem.* **2006**, *45*, 3158.

(93) Mazzanti, M.; Chen, X. Y.; Bretonniere, Y.; Pecaut, J.; Imbert, D.; Bünzli, J. C. G. *Inorg. Chem.* **2007**, *46*, 625.

(94) Wang, C.-G.; Xing, Y.-H.; Li, Z.-P.; Li, J.; Zeng, X.-Q.; Ge, M.-F.; Niu, S.-Y. *Cryst. Growth Des.* **2009**, *9*, 1525.

(95) Guo, D.; Duan, C.-y.; Lu, F.; Hasegawa, Y.; Meng, Q.-j.; Yanagida, S. *Chem. Commun.* **2004**, 1486.

(96) Sabbatini, N.; Guardigli, M.; Lehn, J. M. *Coord. Chem. Rev.* **1993**, *123*, 201.

(97) Xue, Q.; Chen, P.; Lu, J.; Xie, G.; Hou, J.; Liu, S.; Zhao, Y.; Zhang, L.; Li, B. *Solid-State Electron.* **2009**, *53*, 397.

(98) Tanabe, S. *Comptes Rendus Chimie* **2002**, *5*, 815.

(99) Gassner, A.-L.; Duhot, C.; Bünzli, J.-C. G.; Chauvin, A. S. *Inorg. Chem.* **2008**, *47*, 7802.

(100) Muller, G.; Riehl, J. P.; Schenk, K. J.; Hopfgartner, G.; Piguet, C.; Bünzli, J. C. G. *Eur. J. Inorg. Chem.* **2002**, 3101.

(101) Piguet, C.; Williams, A. F.; Bernardinelli, G.; Bünzli, J. C. G. *Inorg. Chem.* **1993**, *32*, 4139.

(102) Leonard, J. P.; Jensen, P.; McCabe, T.; O'Brien, J. E.; Peacock, R. D.; Kruger, P. E.; Gunnlaugsson, T. *J. Am. Chem. Soc.* **2007**, *129*, 10986.

(103) Piguet, C.; Bünzli, J. C. G.; Bernardinelli, G.; Bochet, C. G.; Froidevaux, P. *Dalton Trans.* **1995**, 83.

(104) Petoud, S.; Bünzli, J. C. G.; Renaud, F.; Piguet, C.; Schenk, K. J.; Hopfgartner, G. *Inorg. Chem.* **1997**, *36*, 5750.

(105) Muller, G.; Bünzli, J. C. G.; Schenk, K. J.; Piguet, C.; Hopfgartner, G. *Inorg. Chem.* **2001**, *40*, 2642.

(106) Lessmann, J. J.; Horrocks Jr, W. d. *Inorg. Chem.* **2000**, *39*, 3114.

(107) Albrecht, M. *Chem. Rev.* **2001**, *101*, 3457.

(108) Elhabiri, M.; Scopelliti, R.; Bünzli, J. C. G.; Piguet, C. *Chem. Commun.* **1998**, 2347.

(109) Piguet, C.; Bünzli, J. C. G.; Bernardinelli, G.; Hopfgartner, G.; Williams, A. F. *J. Am. Chem. Soc.* **1993**, *115*, 8197.

(110) Floquet, S.; Borkovec, M.; Bernardinelli, G.; Pinto, A.; Leuthold, L. A.; Hopfgartner, G.; Imbert, D.; Bünzli, J. C. G.; Piguet, C. *Chem. -Eur. J.* **2004**, *10*, 1091.

(111) Bassett, A. P.; Magennis, S. W.; Glover, P. B.; Lewis, D. J.; Spencer, N.; Parsons, S.; Williams, R. M.; De Cola, L.; Pikramenou, Z. *J. Am. Chem. Soc.* **2004**, *126*, 9413.

(112) Stomeo, F.; Lincheneau, C.; Leonard, J. P.; O'Brien, J. E.; Peacock, R. D.; McCoy, C. P.; Gunnlaugsson, T. *J. Am. Chem. Soc.* **2009**, *131*, 9636.

(113) Deiters, E.; Song, B.; Chauvin, A. S.; Vandevyver, C. D. B.; Gumy, F.; Bünzli, J.-C. G. *Chem.-Eur. J.* **2009**, *15*, 885.

(114) Fernández-Moreira, V.; Song, B.; Sivagnanam, V.; Chauvin, A.-S.; Vandevyver, C. D. B.; Gijs, M.; Hemmilä, I.; Lehr, H.-A.; Bünzli, J.-C. G. *The Analyst* **2010**, *135*, 42.

(115) Albrecht, M.; Osetska, O.; Bünzli, J.-C. G.; Gumy, F.; Fröhlich, R. *Chem. -Eur. J.* **2009**, *15*, 8791.

(116) Redshaw, C. *Coord. Chem. Rev.* **2003**, *244*, 45.

(117) Paquet, V. r.; Zumbuehl, A.; Carreira, E. M. *Bioconjugate Chemistry* **2006**, *17*, 1460.

(118) Hoppe, E.; Limberg, C.; Ziemer, B. *Inorg. Chem.* **2006**, *45*, 8308.

(119) Quinlan, E., Trinity College Dublin, 2007.

(120) Aspinall, H. C. *Chem. Rev.* **2002**, *102*, 1807.

(121) Seitz, M.; Moore, E. G.; Ingrarn, A. J.; Muller, G.; Raymond, K. N. *J. Am. Chem. Soc.* **2007**, *129*, 15468.

(122) Montgomery, C. P.; New, E. J.; Parker, D.; Peacock, R. D. *Chem. Commun.* **2008**, 4261.

(123) Muller, G. *Dalton Trans.* **2009**, 9692.

(124) Flapan, E. *When Topology Meets Chemistry: A Topological Look at Molecular Chirality*; Cambridge University Press: Cambridge, 2000.

(125) Murray, N. S., Trinity College Dublin, 2008.

(126) Chauvin, A. S.; Gumy, F.; Imbert, D.; Bünzli, J. C. G. *Spectroscopy Letters* **2004**, *37*, 517.

(127) Stomeo, F., Trinity College Dublin, 2006.

(128) Yeh, R. M.; Ziegler, M.; Johnson, D. W.; Terpin, A. J.; Raymond, K. N. *Inorg. Chem.* **2001**, *40*, 2216.

(129) Otero, A.; Lara-Sánchez, A.; Fernández-Baeza, J.; Alonso-Moreno, C.; Tejeda, J.; Castro-Osma, J.; Márquez-Segovia, I.; Sánchez-Barba, L.; Rodríguez, A.; Gómez, M. *Chem. -Eur. J.* **2010**, *16*, 8615.

(130) *IUPAC Compendium of chemical terminology* **1995**, *67*, 1327.

(131) Hudson, B.; Vinograd, J. *Nature* **1967**, *216*, 647.

(132) Frisch, H. L.; Wasserman, E. *J. Am. chem. Soc.* **1961**, *83*, 3789.

(133) Kidd, T. J.; Leigh, D. A.; Wilson, A. J. *J. Am. chem. Soc.* **1999**, *121*, 1599.

(134) Credi, A. *J. Phys.: Condensed Matt.* **2006**, 1779.

(135) Stoddart, J. F.; Colquhoun, H. M. *Tetrahedron* **2008**, *64*, 8231.

(136) Ikeda, T.; Stoddart, J. F. *Science and Technology of Advanced Materials* **2008**, 14104.

(137) Haussmann, P. C.; Stoddart, J. F. *The Chemical Record* **2009**, *9*, 136.

(138) Amabilino, D. B.; Perez-Garcia, L. *Chem. Soc. Rev.* **2009**, *38*, 1562.

(139) Sauvage, J. P.; Dietrich-Bucheker, C. *Molecular catenane, rotaxane and knot: a journey through the world of molecular topology*; Wiley-VCH, 1999.

(140) Wasserman, E. *J. Am. chem. Soc.* **1960**, *82*, 4433.

(141) Walba, D. M.; Richards, R. M.; Haltiwanger, R. C. *J. Am. chem. Soc.* **1982**, *104*, 3219.

(142) Schill, G.; Lüttringhaus, A. *Angewandte Chem. Int. Ed.* **1964**, *3*, 546.

(143) Stoddart, J. F. *Chem. Soc. Rev.* **2009**, *38*, 1802.

(144) Dietrich-Bucheker, C.; Sauvage, J. P. *J. Am. chem. Soc.* **1984**, *106*, 3043.

(145) Chambron, J.-C.; Dietrich-Bucheker, C.; Sauvage, J. P. *Top. Curr. Chem.* **1993**, *165*, 131.

(146) Chichak, K. S.; Cantrill, S. J.; Pease, A. R.; Chiu, S.-H.; Cave, G. W. V.; Atwood, J. L.; Stoddart, J. F. *Science* **2004**, *304*, 1308.

(147) Costero, A. M.; Jose Banuls, M.; Jose Aurell, M.; Ward, M. D.; Argent, S. *Tetrahedron* **2004**, *60*, 9471.

(148) Astruc, D. *New J. Chem.* **2005**, *29*, 42.

(149) Biefeld, C. G.; Eick, H. A.; Grubbs, R. H. *Inorg. Chem.* **1973**, *12*, 2166.

(150) Hérisson, J.-L.; Chauvin, Y. *Macromol. Chem.* **1971**, *141*, 161.

(151) Kotha, S.; Singh, K. *Eur. J. Org. Chem.* **2007**, *2007*, 5909.

(152) Brändli, C.; Ward, T. *Helvetica Chimica Acta* **1998**, *81*, 1616.

(153) Monfette, S.; Crane, A. K.; Duarte Silva, J. o. A.; Facey, G. A.; dos Santos, E. N.; Araujo, M. H.; Fogg, D. E. *Inorganica Chimica Acta* **2010**, *363*, 481.

(154) Clark, P. G.; Guidry, E. N.; Chan, W. Y.; Steinmetz, W. E.; Grubbs, R. H. *J. Am. Chem. Soc.* **2010**.

(155) Vogel, A. I.; Tatchell, A. R.; Furnis, B. S.; Hannaford, A. J.; Smith, P. W. G. *Vogel's Textbook of Practical Organic Chemistry*; 5th ed.; Prentice Hall: New York, 1996.

(156) Richardson, F. S.; Riehl, J. P. *Chem. Rev.* **1977**, *77*, 773.

(157) Allinger, N. L.; Burkert, U. *Molecular Mechanics*; American Chemical Society: Washington D.C., 1982.

(158) Frey, S. T.; Chang, C. A.; Carvalho, J. F.; Varadarajan, A.; Schultze, L. M.; Pounds, K. L.; Horrocks Jr, W. d. *Inorg. Chem.* **1994**, *33*, 2882.

(159) Lincheneau, C.; Peacock, R. D.; Gunnlaugsson, T. *Chem -Asian J.* **2010**, *in press*.

(160) Chien, Y.-Y.; Jan, M.-D.; Avijit, K.; Tzeng, H.-S.; Lin, Y.-P.; Chen, Y.-Y.; Wang, K. T.; Chen, C.-T.; Chein, C.-C.; Chen, C.-C.; Lin, C.-C. *Chem. Bio. Chem.* **2008**, *9*, 1100.

# Appendixes

**Appendixes:**

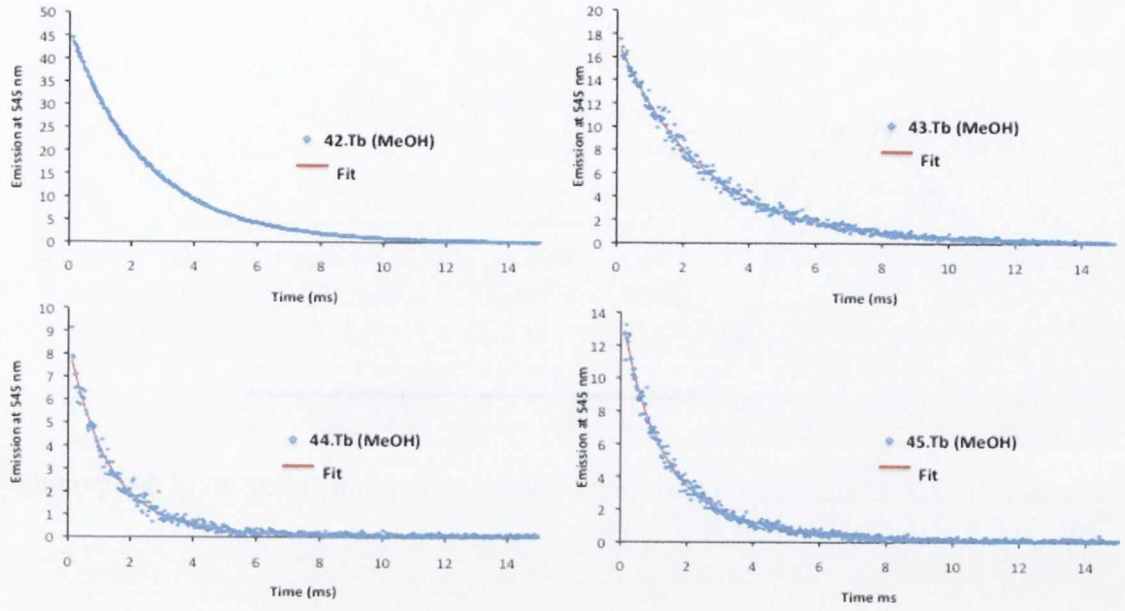


**Appendix 2.1:** Luminescence decays of L.Tb (L=42-45) in MeOH and resulting mono-exponential fits

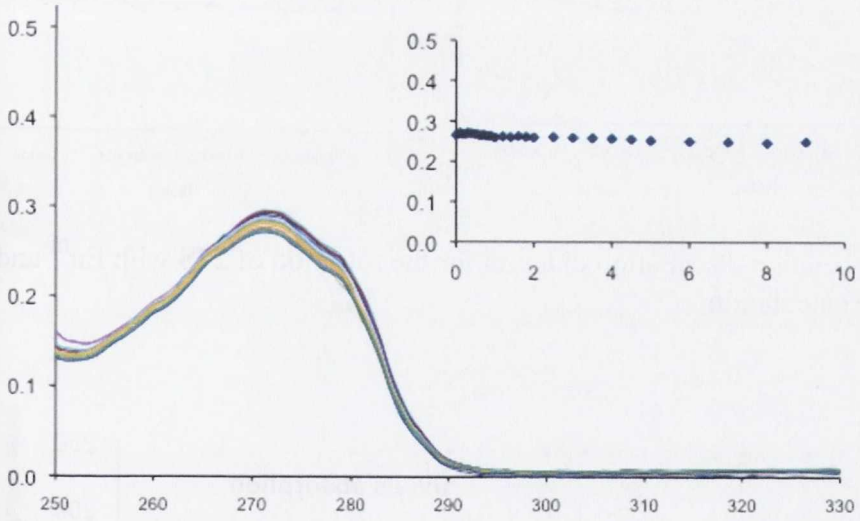

**Appendix 2.2:** Changes observed in the UV-vis absorption spectrum of 44 upon the addtion of $Tb(ClO_4)_3$ Inset: Variation at 271 nm

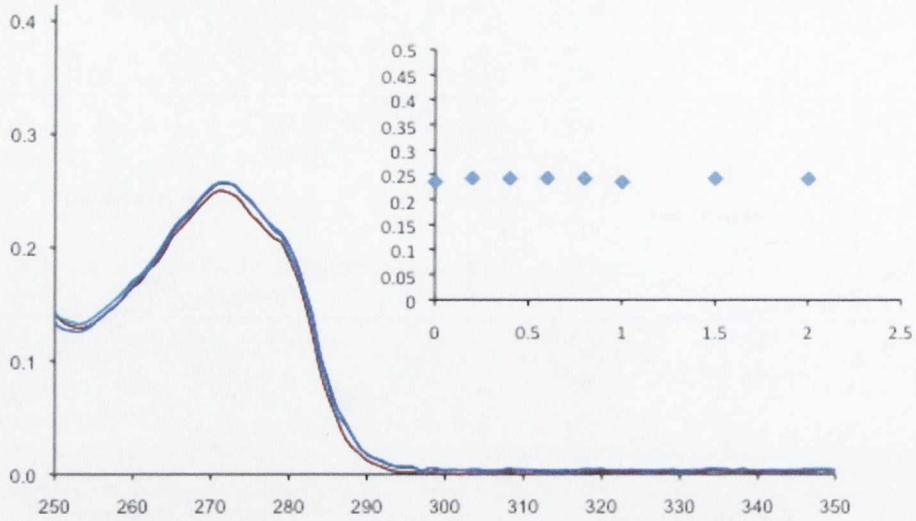


**Appendix 2.3**: Changes observed in the UV-vis absorption spectrum of **44** upon the addtion of $Tb(ClO_4)_3$ inset: changes at 271 nm

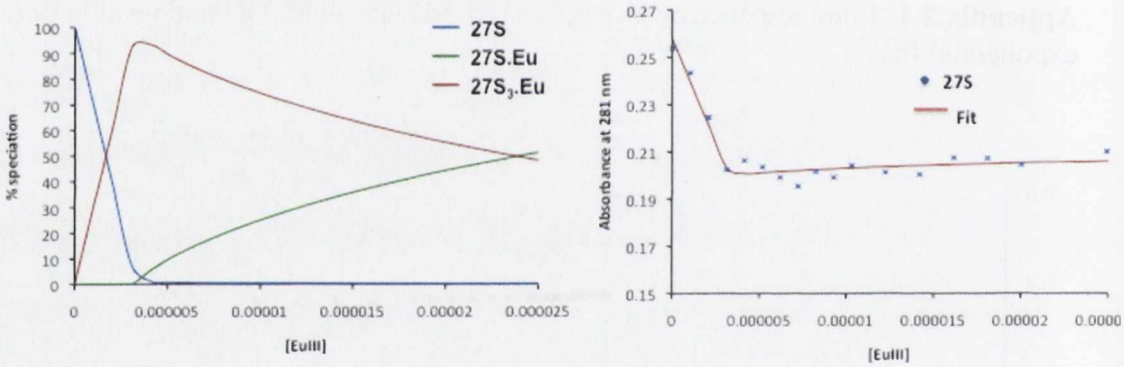


**Appendix 3.1:** Speciation distribution diagram for the ttitration of **27S** with $Eu^{III}$ and fit resulting from the calculation

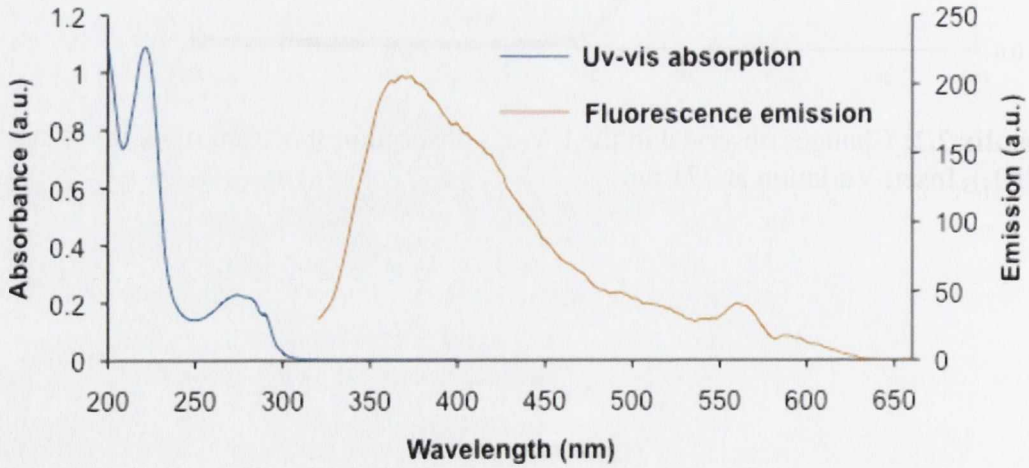


**Appendix 3.2:** UV-vis absorption spectrum and fluorescence emission of **47D$_2$.Eu** ($\lambda$exc = 271 nm)

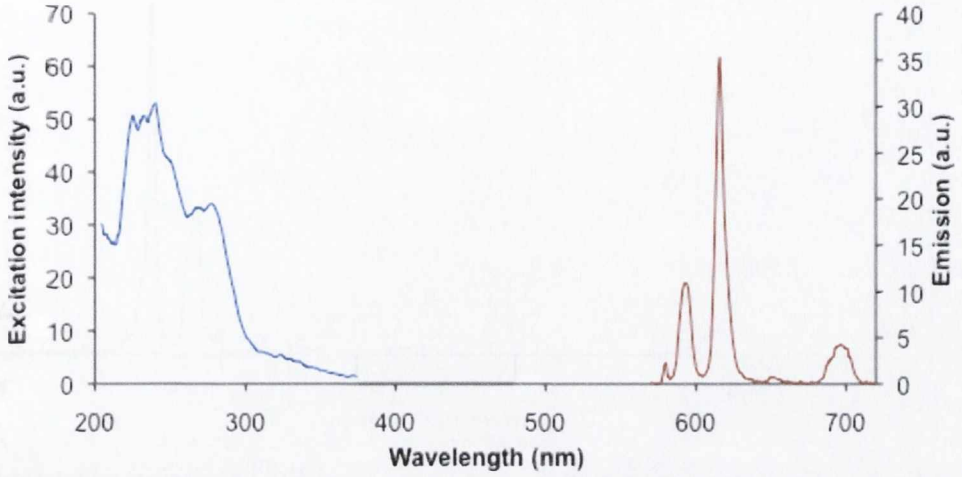


**Appendix 3.3:** Excitation spectrum ($\lambda_{em}$ =615 nm) and $Eu^{III}$ emission spectrum ($\lambda_{ex}$ = 271 nm) of **47D$_2$.Eu**

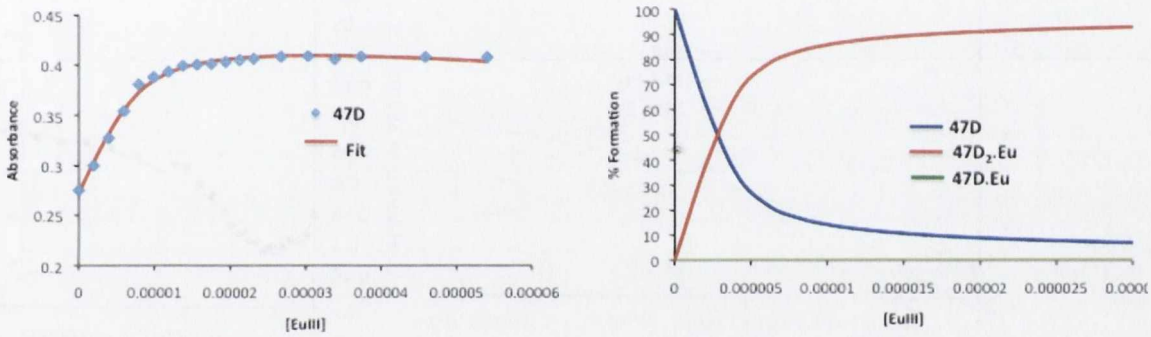


**Appendix 3.4:** Speciation distribution diagram for the titration of **47D** with $Eu^{III}$ and fit resulting from the calculation

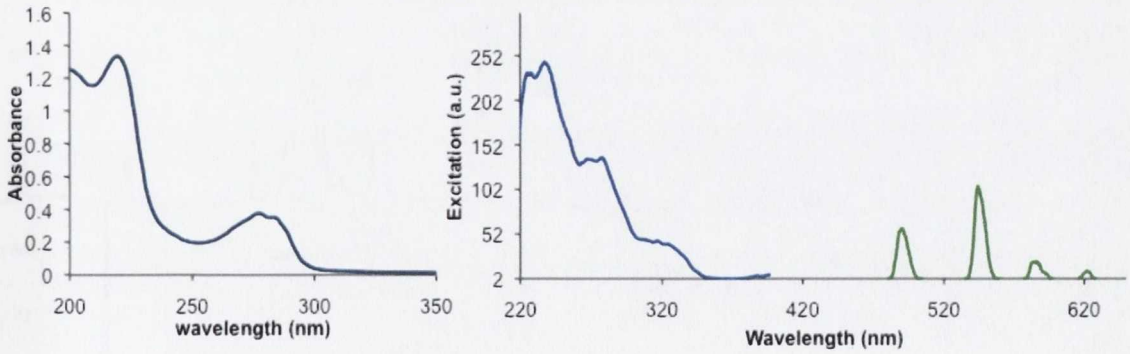


**Appendix 3.5:** UV-vis absorption spectrum (left) Excitation spectrum ($\lambda_{em}$ =615 nm) and $Eu^{III}$ emission spectrum ($\lambda_{ex}$ = 271 nm) of **47D$_2$.Tb** in $CH_3CN$

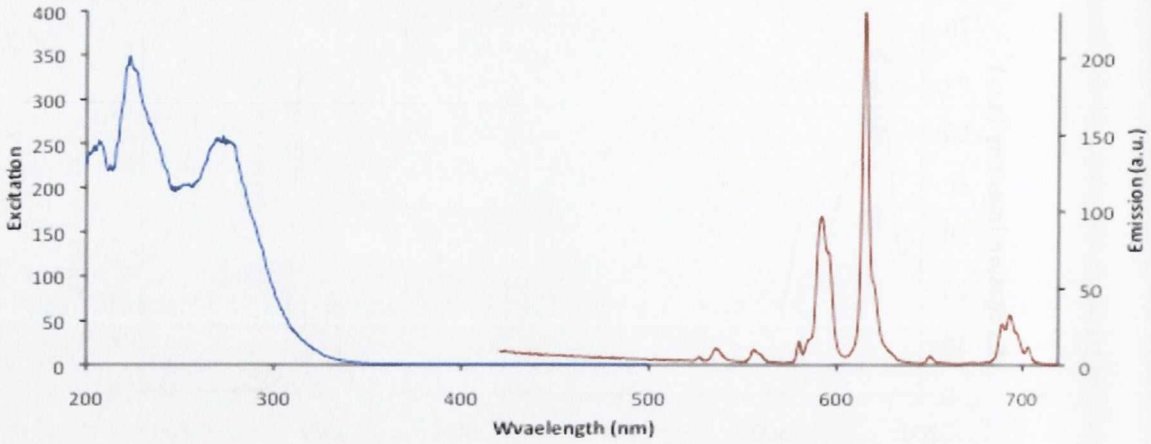


**Appendix 3.6:** Excitation spectrum ($\lambda_{em}$ =615 nm) and $Eu^{III}$ emission spectrum ($\lambda_{ex}$ = 271 nm) of **51S$_3$.Eu**

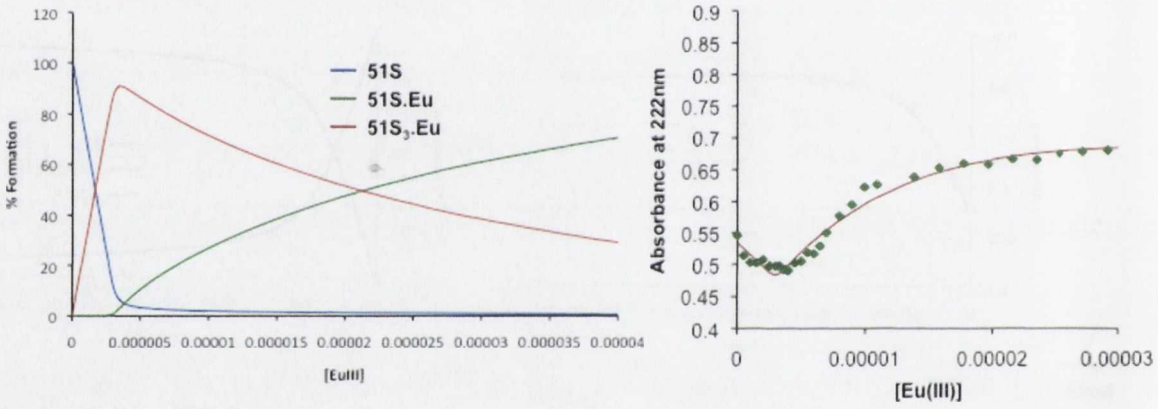


**Appendix 3.7:** Speciation distribution diagram for the titration of **52S** with $Eu^{III}$ and fit resulting from the calculation

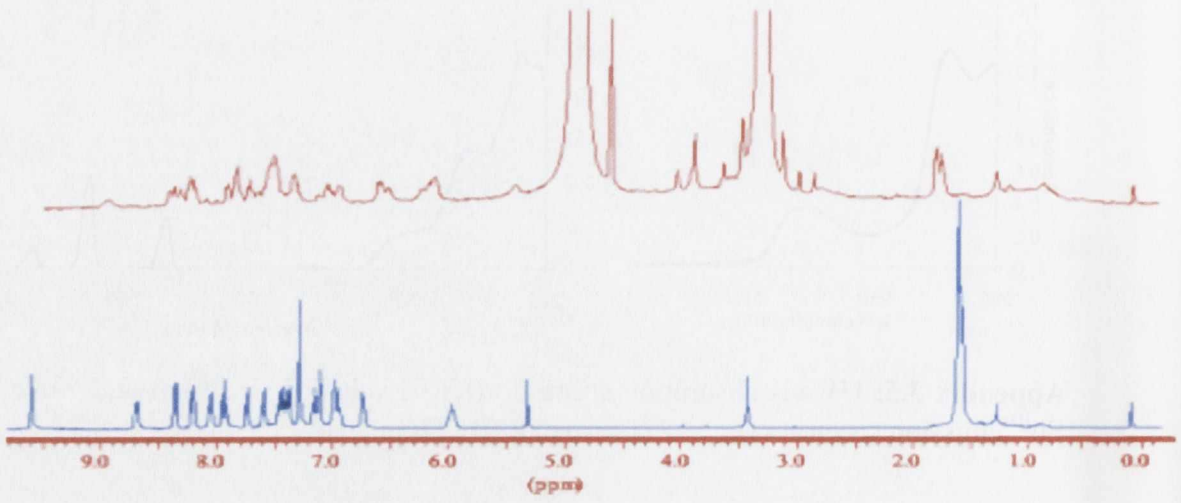


**Appendix 4.1:** $^1$H-NMR ($CDCl_3$) spectrum of **54R** (blue) and $^1$H-NMR spectrum (MeOD, 400MHz) of **54R$_3$.Eu$_2$**

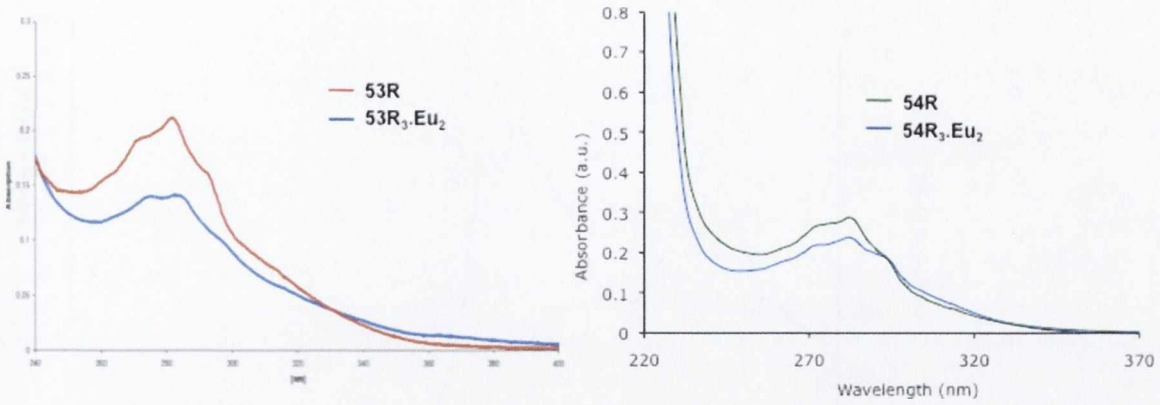


**Appendix 4.2:** UV-vis absorption spectra of **53R** and **$53R_3.Eu_2$** (left) and of **54R** and **$54R_3.Eu_3$** (right) in CH3OH at $1\times10^{-5}$M.

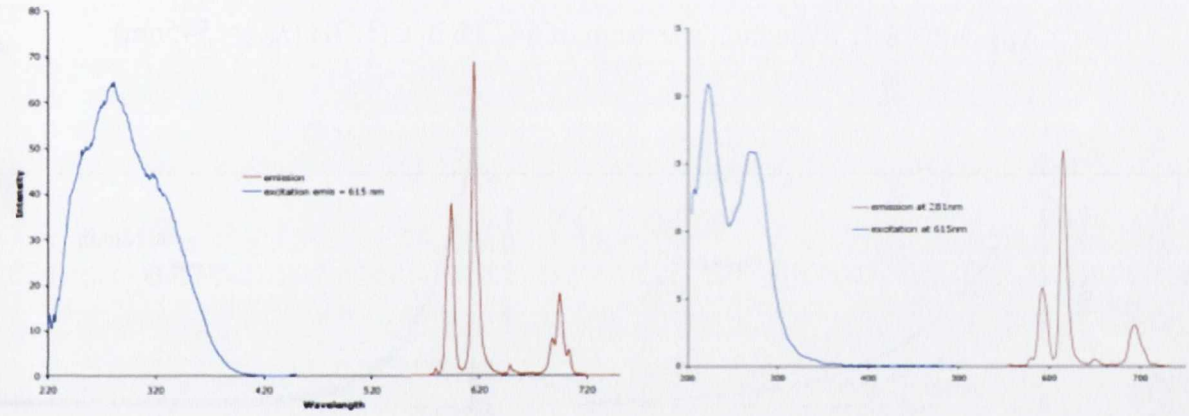

**Appendix 4.3:** Excitation ($\lambda_{em}$= 615 nm) and emission spectra ($\lambda_{ex}$ = 281nm) of **$53R_3.Eu_2$** (left) and **$54R_3.Eu_3$** (right) in $CH_3CN$ at $1\times10^{-5}$M.

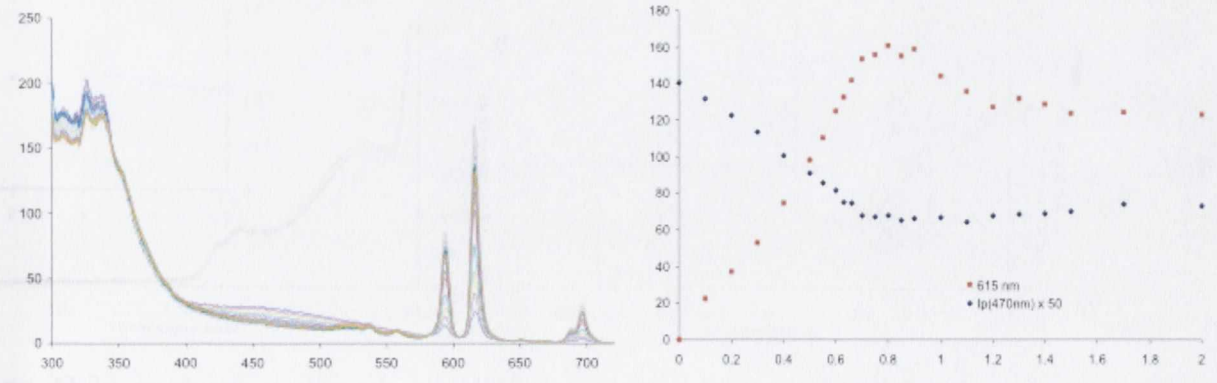


**Appendix 4.4:** Changes observed in the fluorescence emission during the titration of **54** (C = 1×10-5 M) upon the addition of $Eu(CF_3SO_3)_3$ and isotherm of complexation at 615 nm and 470 nm.

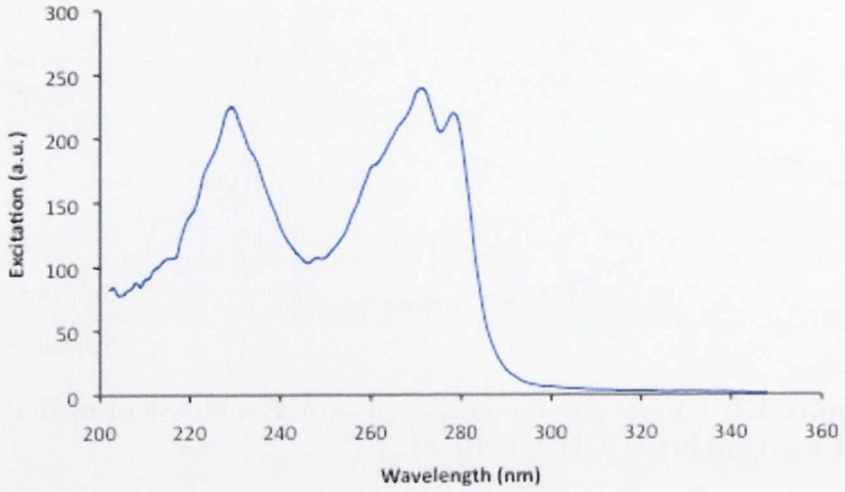


**Appendix 5.1:** Excitation spectrum of **66$_3$.Tb** in $CH_3OH$ ($\lambda_{em}$ = 545nm)

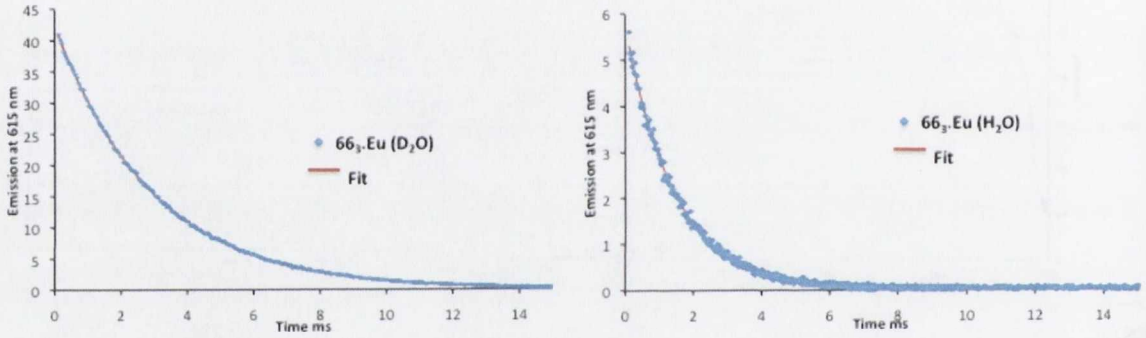


**Appendix 5.2:** Luminescence emission decays at 615 nm ($\lambda$ex = 281 nm) of **66$_3$.Eu** in $D_2O$ (left) and in $H_2O$ (right) and resulting mono- and bi-exponential fits, repectively (red).

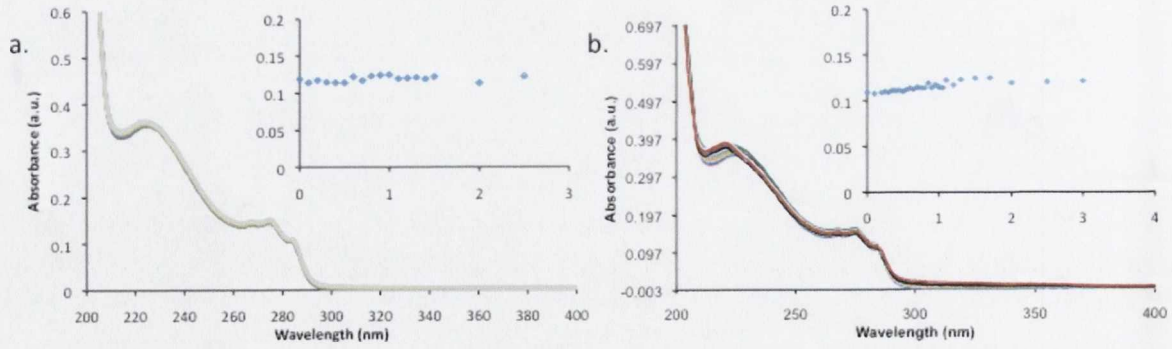


**Appendix 5.3:** Changes observed in the UV-vis absorption spectrum of **66** upon the addition of $Eu^{III}$ (a) and $Tb^{III}$ (b) in MeOH (C = $2\times10^{-5}$M) insets: variation of the absorbance at 281 nm.

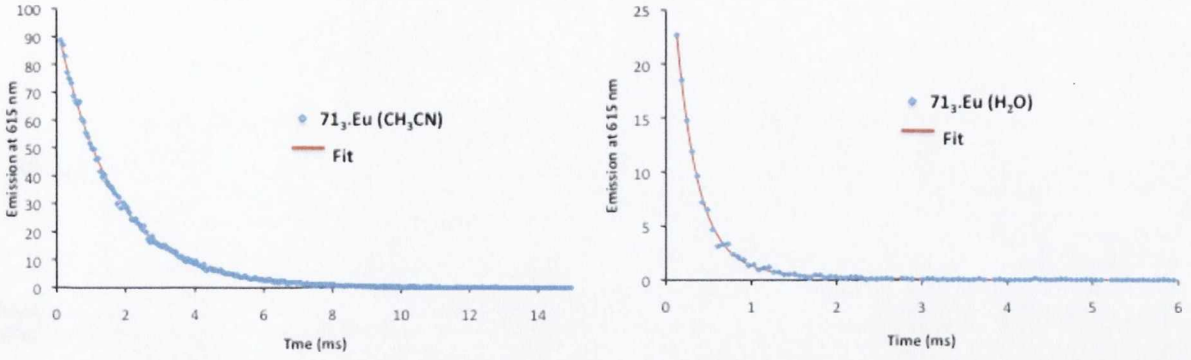


**Appendix 5.4:** Luminescence emission decays at 615 nm (λex = 281 nm) of **71$_3$.Eu** in $CH_3CN$ (left) and in $H_2O$ (right) and resulting mono- and bi-exponential fits (red),

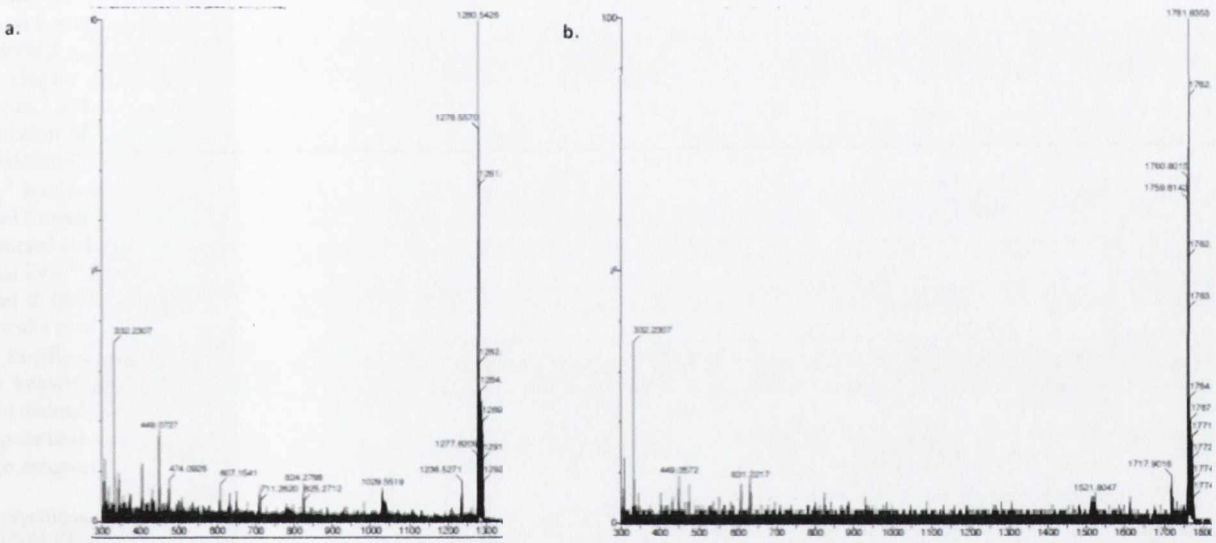


**Appendix 5.5:** Results obtained using MS.MS mass spectrometry on the fragments found at (a) m/z = 1280.54 and (b) m/z = 1761.85 in **Cat71.Eu**